Structure des Couches d'InN et d'alliages (In,Al)N

Arantxa Vilalta-Clemente

UNIVERSITÉ de CAEN BASSE-NORMANDIE
U.F.R. SCIENCES

ECOLE DOCTORALE : Structure, information, matière et matériaux

THESE

présentée par

Arantxa VILALTA-CLEMENTE

et soutenue

Le 25 Avril 2012

En vue de l'obtention du

DOCTORAT de L'UNIVERSITE DE CAEN

Spécialité : Génie des matériaux

Arrêté du 07 août 2006

Structure des Couches d'InN et d'alliages (In,Al)N

JURY

Mr. Patriarche Gilles, Directeur de Recherche CNRS, LPN, Marcoussis, France, **Rapporteur**

Mr. Vickridge Ian, Directeur de Recherche CNRS, INSP Paris, **Rapporteur**

Mr Giesen Christoph, Ingénieur Aixtron SE, Aachen, Germany

Mr. Grandjean Nicolas, Professeur Ecole Polytechnique de Lausanne, Switzerland

Mr. Levalois Marc, Professeur Université de CAEN

Mr. Tuomisto Filip, Professeur Université Aalto, Finland

Mme Morales Magali, Maître de conférences HDR Université de CAEN, **Co-directeur de thèse**

Mr. Ruterana Pierre, Directeur de Recherche CNRS, CIMAP, **Directeur de thèse**

"La vida és risc;
l'aventura és novetat radical;
la creació es produeix cada dia, quelcom absolutament nou
i imprevisible"

Raimon Panikkar

"Life is risk,
adventure is radical innovation;
creation takes place everyday, something absolutely new
and unpredictable"

Raimon Panikkar

Acknowledgments

During many years I have made a long travel in the research world, and this part of the manuscript gives me the opportunity to express my thanks to many people that I have met along this journey until I wrote my PhD thesis.

First, I would like to thank my advisor, Pierre Ruterana for giving me the opportunity to join the RAINBOW Project at CIMAP laboratory in Caen and for his support, guidance and encouragement over the development of my PhD investigation, and especially for introducing me in the world of the dislocations and defects of the materials and for having his office door always open for me. I am very grateful to Magali Morales, my co-advisor, for her contribution and guidance to the RSM measurements and IBA analysis.

I convey my thanks to the members of the PhD committee: the President Prof. Marc Levalois (Université de Caen); the reviewers: Drs. Gilles Patriarche (LPN) and Ian Vickridge (INSP); examinators Prof. Nicolas Grandjean (EPFL), Prof. Filip Tuomisto (University Aalto) and Dr. Christoph Giesen (Aixtron); invited: Dr. Marie-Antoinette Di Forte-Poisson (Thales III-V Labs) and Prof. Evgenia Valcheva (University of Sofia) for having kindly accepted to judge my work, amidst their busy schedule. I greatly benefited from their constructive comments which greatly improved the manuscript.

I have to acknowledge, evidently, all the family of RAINBOW project: Professor, Supervisors, ESRs and ER for contributing with their talks during the numerous workshops and conferences that we attended together, the long discussions about the materials that we characterized and for the numerous hours that we enjoyed together in different countries and places.

Several collaborations have contributed to the InAlN and InN results in a significant way, and I had the opportunities of scientific visits which became a crucial point in my thesis and I would like to mention some of them. In particular, I would like to thank Marie-Antoinette Poisson (III-V Labs) for the MOVPE InAlN samples, and for her explanations on how this material is difficult to grow; Slawomir Kret (IFPAN) for the introduction to Optimas software and simulations; Evgenia Valcheva for the Raman measurements, Gilles Patriarche (LPN) for his critical and kind contribution of HAADF-TEM along with the important discussions on semiconductors materials and characterization; Ian Vickridge (INSP) for the measurements and discussions on IBA techniques.

For this work, the sample preparation was a crucial step for TEM observations, so I owe special thanks to Marie Pierre and Yadira for teaching me the preparation of the TEM samples and of course many thanks also to the growers (III-V lab, Aixtron, EPFL, TUB and UPM), who have provided me the samples without which I could not have been able to carry out this work.

I would always remember the nice moments I spent in CIMAP, my second home during all this time, and the friends I leave. I want to thank very specially Bertrand "ja ja", for his patience and listening to all my questions, for his generosity and to encourage me in the research and of course: "je suis contente". I thank my co-workers Geeta, Claire, Yi and Elodie for sharing different experiences during these years. I would like to thank Cédric, Michael and Stefan for lunch time and their patience with my French. I also enjoyed the companionship of the NIMPH group members at CIMAP and the coffee time with them.

Thanks to the Spanish Community: Diana, Elsa, Sheila, Luis and Western for the weekends and evenings; and French Community: Burcu, Olivier, Thomas, Delphine and Florent pour vos soirées.

I cannot forget my first stay abroad in Thessaloniki with another Marie Curie Project (SYNTORBMAG, Sept. 2007-Oct.2008). Thanks to Makis Angelakeris for giving me the opportunity to start as an ESR and to have the patience for my talks together with Kostas. Ευχαριστω Stefanos for teaching me the synthesis of nanoparticles and how a precursor or a different solvent can change their shape,

thank you also for the φραπε μετριος με γαλα. Ευχαριστίες to all the κορίτσια: Kathrin, Maya, Lata, Julita, Alkyoni, Aria, and Eleni for the time that we spent together and for encouragement to continue with the research.

I would like to thank especially the friends that I know from FiCMA group where I did my master: Cinta, Joan, Sandra, Òscar (you always will be with us), Montse, Isabel and Ana. Thanks for all the time that we spend together, for all the trips together and for your visits to me in Thessaloniki and Caen, and for the scientific discussions and long conversations by skype helping me to feel close to home. Thanks Sandra and Frida for the first six months that we were living together in Caen.

To my colleagues and friends at Servei de Recursos Científics i Tècnics (SRCiT) de Tarragona perque m'heu ajudat i m'heu donat ànims en totes les decisions que vaig pendre i prenc, mai podré oblidar el temps que vam treballar junts, gràcies Pepi, Lucia, Cristina, Carme, Ester, Francesc i Toni.

Naturally, I can not forget the chemistry group, for which we just celebrated our 20 years of existence, so thanks: Dolors, Angelina, Sílvia, Eva, David, xatos, xata and petits. I want to thank my friends Geni and Noèlia, amb vosaltres vaig començar a viure a Tarragona i en tot moment heu estat al meu costat, gràcies per les xerrades telefòniques, per tots els moments i experiències viscudes i que són molt difícils d'explicar en dues línies. También le quiero agradecer a Jose su confianza depositada desde que empecé a trabajar como técnica del AFM, y por su empuje constante para la investigación. My special thanks to all the friends and colleagues, whom I have met during this trip, and who, for small reason, kindly helped me to become the person and researcher I am now.

Thanks, finally, to my family, for dedicating so much time and effort in my education and for always standing by me, for their love, trust and support all the way. This is a small reward after so long time. And thanks to Στεφανος, for patiently listening to me, for keeping me strong, but most for all, for sharing many moments.

Arantxa Vilalta-Clemente

To my parents: Joan and Marina
To my sisters and brother: Ruth, Nuria and Angel
To my brother-in-law and sister-in-law: Patricio and Marta
To my nieces and nephew: Marina, Leire, and Ignacio

Content

Résumé

Etant donné que cette thèse est rédigée en anglais, vous trouverez ici un résumé en français des différents chapitres qui la composent. La structure de ce résumé est donc la même que celle du manuscrit, avec, premièrement, une introduction générale, suivi d'une courte chronologie concernant l'étude des nitrures et des applications associées ainsi que des techniques expérimentales mises en oeuvre. Les différents résultats sont ensuite exposés selon l'ordre des chapitres, pour finir par les conclusions et perspectives de ce travail.

Introduction

Au cours des 50 dernières années, la recherche et les avancées technologiques dans les matériaux semi-conducteurs ont considérablement modifié notre mode de vie. Les outils tels que les ordinateurs personnels, les téléphones portables et les diodes électroluminescentes (LEDs) ne sont que quelques exemples de la multitude de dispositifs électroniques utilisés au quotidien. Les LEDs et diode laser à base de nitrures semiconducteurs sont le résultat d'une percée technologique qui a provoqué une révolution dans l'optoélectronique dès 1994.

Les nitrures d'éléments III: InN, GaN, AlN et leurs alliages se sont imposés pour le développement de dispositifs optoélectroniques de très bonne efficacité. La récente réévaluation de la bande interdite d'InN de 1.89 eV à seulement ~0.65 eV a permis d'envisager la production de dispositifs luminescents émettant dans

le rouge et le proche infrarouge (IR) et couvrir l'ensemble du spectre visible (de l'infrarouge à l'ultraviolet). Ces matériaux trouvent aussi des applications dans la réalisation de transistors à haute mobilité électronique (HEMTs). Bien évidemment, la production de dispositifs nitrures efficaces dépendra principalement de la qualité structurale des couches disponibles. La croissance des couches minces de nitrures pose encore de très nombreux problèmes. En effet, l'absence de substrats adaptés en paramètres de maille et/ou coefficients de dilatation thermique constitue un problème majeur pour la croissance d'hétérostructures de ses composés et de leurs alliages.

Au cours de ce travail, j'ai étudié des échantillons venant de trois techniques de croissance: épitaxie par jets moléculaires assistée par plasma (Plasma-Assisted Molecular Beam Epitaxy, PAMBE), épitaxie en phase vapeur à base d'hydrures (Hydride Vapour Phase Epitaxy, HVPE) et épitaxie en phase vapeur aux organométalliques (Metalorganic Vapour Phase Epitaxy, MOVPE). Dans le cas d'InN, la technique PAMBE a produit les couches de meilleure qualité réalisées à ce jour, avec cependant de faibles vitesses de croissance. La méthode MOVPE présente des avantages importants pour la fabrication de dispositifs commerciaux car elle permet des vitesses de croissance et de production élevées. Cependant, elle possède des limitations pour la croissance de l'InN, en effet, elle nécessite une température de croissance relativement élevée pour obtenir un craquage effectif de NH_3.

Ce travail s'est inscrit dans le cadre du projet européen RAINBOW intitulé "High Quality Material and intrinsic Properties of InN and Indium rich Nitride Alloys". L'objectif scientifique de ce projet est d'obtenir des couches de semiconducteurs nitrures d'indium et leurs alliages de bonne qualité cristalline, et comprendre leurs mécanismes de croissance afin d'améliorer leurs propriétés opto- et micro- électroniques. Ma contribution à ce projet a été focalisée sur l'analyse détaillée de la structure d'InN et d'InAlN, en utilisant différentes techniques de caractérisation complémentaires. Il a été mené en étroite collaboration avec des partenaires qui faisaient la croissance des couches et ceux

qui fabriquaient les dispositifs, ceci dans le but d'aider à l'amélioration de la qualité des matériaux et les performances des dispositifs.

Le manuscrit est divisé en quatre chapitres:

Chapitre 1 III-Nitrures propriétés et applications

Le premier chapitre présente une courte chronologie de l'état de l'art dans les semiconducteurs nitrures et des applications de InN et InAlN. Après avoir décrit la principale phase dans laquelle ces matériaux cristallisent (structure wurtzite), nous nous sommes intéressée plus particulièrement aux caractéristiques structurales (polarisation spontanée et piézoélectrique, contraintes et déformations, épaisseur critique, défauts dans la structure wurtzite (défauts ponctuels, dislocations et fautes d'empilement) et aux propriétés optiques. Nous avons examiné plus particulièrement les problèmes liés au choix du substrat. Enfin, nous avons finalement discuté des diagrammes de croissance pour InN et InAlN.

Chapitre 2 Techniques expérimentales

Dans une première partie, nous avons décrit les trois techniques de croissance qui ont été employées par les différents collaborateurs. Les couches d'InAlN ont été réalisées par MOVPE dans deux entreprises, III-V labs (Marcoussis) et Aixtron (Allemagne), ainsi qu'à l'Ecole Polytechnique de Lausanne (EPFL-Lausanne). Les échantillons d'InN ont été élaborés par différentes méthodes de dépôt dans trois différent laboratoires: par MBE (Instituto de Sistemas Optoelectrónicos y Microtecnología à Universidad Politécnica de Madrid, ISOM-UPM), par MOVPE (Technische Universität Berlin-TUB) et par HVPE (EPFL).

La deuxième partie de ce chapitre est dédiée à la description des principaux équipements utilisés dans ce travail. Les morphologies de surface et la rugosité des InN et InAlN ont été caractérisées par la microscopie à force atomique (AFM).

La diffraction de rayons X haute résolution (DRXHR) a permis de déterminer les paramètres de maille, et de connaître les contraintes et la composition en indium dans InAlN. En outre, la densité de dislocations a également été examinée par DRXHR à partir des mesures de l'inclinaison (tilt) et de torsion (twist).

La microscopie électronique en transmission a été utilisée pour la caractérisation des défauts cristallins en champs clair et sombre, ainsi qu'en faisceau faible qui permet d'optimiser le contraste pour une meilleure identification des défauts.

Par la suite, nous avons eu l'occasion d'utiliser, de façon extensive, la microscopie électronique en transmission à balayage en mode champ sombre annulaire à grand angle (HAADF-STEM). Cette technique présente un intérêt considérable car le contraste dans les images est sensible à la composition chimique locale.

La microscopie électronique en transmission nécessite la préparation d'échantillons pour être transparents aux électrons. Nos lames minces ont été préparées en section transverse ou plane. Deux méthodes de préparation ont été utilisées: la méthode du tripode et l'amincissement mécanique.

Les méthodes d'analyses par faisceau d'ions (IBA) constituent un ensemble de techniques dérivées des interactions ion-matière. Dans ce travail, nous avons utilisé deux méthodes: la spectrométrie par rétrodiffusion de Rutherford (RBS) et l'analyse par réaction nucléaire (NRA). La RBS est une technique d'analyse des matériaux solides qui permet de séparer les éléments en fonction de leur masse atomique, d'obtenir des informations sur la composition chimique et les concentrations de chaque espèce, et de déterminer leur distribution en profondeur. La NRA est une variante de la RBS qui permet d'étudier les éléments légers, comme l'azote.

En plus des rayons X, nous avons utilisé la spectroscopie RAMAN pour accéder à la déformation dans les couches et déterminer la densité des porteurs résiduels dans les couches InN.

Chapitre 3 Couches d'InN

La première partie de ce chapitre a été utilisée pour comparer la microstructure des couches obtenus par les trois techniques de croissance: HVPE, MOVPE et MBE. Pour se faire, nous avons corrélé les résultats de spectroscopie RAMAN avec les analyses par microscopie électronique en transmission. Avec la spectroscopie Raman, les couches MOVPE-InN et MBE-InN ont une meilleure qualité cristalline que HVPE-InN. Les couches MOVPE sont caractérisées par un mode de croissance en îlots avec de nombreuses cavités au niveau des interfaces. Bien évidemment, cette structure est préjudiciable à la fabrication de dispositifs. Comme les couches MBE présentaient des surfaces planes et une microstructure uniforme, nous procédé à leur caractérisation détaillée. Un des buts était de corréler la morphologie de surface des échantillons et conditions de croissance (température, le rapport V/III, l'épaisseur des couches). Par microscopie à force atomique, nous avons mis en évidence que les échantillons fabriqués dans des conditions riches en indium avaient une rugosité plus faible que ceux riches en azote. Pour les échantillons produits à des températures de croissance plus basses (400 °C), la rugosité augmente rapidement. Nous avons observé que pour de meilleurs résultats, la croissance devait être faites autour du rapport V/III le plus proche possible de un, mais dans la région riche en indium à des températures d'environ 470 ° C.

Nous avons réalisé l'étude des contraintes dans ces couches MBE-InN. Pour ce faire, la diffraction des rayons X s'est révélée un outil particulièrement adapté; nous avons pu mettre en évidence une contrainte résiduelle de compression pour tous les échantillons déposés sur GaN/Al_2O_3, alors que pour les échantillons déposés sur Si, nous avons une déformation en expansion lorsque la couche InN est déposée sur AlN/Si, alors qu'elle devient compressive sur GaN/AlN/Si. Après avoir comparé les résultats de la déformation de nos échantillons avec la littérature, on a déduit que des couches MBE-InN présentent deux composantes de déformation: l'une biaxiale et l'autre hydrostatique, cette dernière est souvent liée à la présence défauts ponctuels (donnée vérifiée par les analyses NRA et RBS).

Par la suite nous avons déterminé les densités de dislocations en comparant les résultats de DRXHR et les données obtenues par les analyses en MET. Il en découle que le pourcentage de dislocation *c* et *a*+*c* sont en faible proportion. Dans ces couches, les dislocations coin (type *a*) prédominent; et les résultats de MET sont conformes aux calculs DRXHR d'après le modèle mosaïque lorsque l'on utilise une petite taille de grains (≤90nm).

Chapitre 4 InAlN hétérostructures

Dans ce quatrième chapitre, nous avons caractérisé deux types d'hétérostructures: InAlN/AlN/GaN (avec une couche ultrafine d'AlN pour l'amélioration du gaz d'électrons à deux dimensions-2DEG) et InAlN/GaN.

Les couches ont été préparées par MOVPE dans différentes conditions de croissance (la température, le rapport V/III, des flux de gaz, etc..,) dans trois laboratoires (Aixtron, EPFL et III-Vlab). La croissance d'alliages d'InAlN est difficile à cause des grandes différences entre InN et AlN: paramètre de maille, énergies de liaison et températures de croissance. Son contrôle très précis est critique pour l'obtention de couches de bonne qualité. Par exemple, la croissance d'AlN requiert une haute température (>1000 °C), une basse pression, et un faible flux de NH_3. Par contre, pour la croissance d'InN, il faudra une basse température (~500 °C), une pression partielle élevée de NH_3 et une pression total relativement élevée pour optimiser l'incorporation d'In.

Dans une première partie, nous avons analysé l'influence de l'épaisseur de la couche intermédiaire d'AlN (hétérostructures InAlN/AlN/GaN) sur la structure de la couche d'InAlN avec AFM et MET. Dans cette étude il a été observé que l'épaisseur de la couche d'AlN a une influence sur les défauts dans InAlN et sa morphologie. Par exemple, une épaisseur d'AlN de 6.9 nm conduit à l'apparition d'une très forte densité de défauts en forme de V dans la couche d'InAlN. Donc, le contrôle exact de l'épaisseur de la couche AlN est un facteur important pour la qualité cristalline de l'InAlN. Dans le même sens, l'étude a été réalisée pour différentes épaisseurs de la couche InAlN directement sur GaN et nous avons

montré que lorsque l'épaisseur devient trop grande, la crystallinité de l'alliage se dégradait très fortement.

Ce chapitre a aussi eu pour but une étude exhaustive de la composition en In dans ces hétérostructure InAlN/GaN et InAlN/AlN/GaN en utilisant DRXHR, RBS et EDS. Par DRXHR, nous avons pu déterminer à chaque fois une composition moyenne, qui dans les couches les plus minces correspondait parfaitement à la loi de Végard corrigé en accord avec les mesures RBS. Par microscopie analytique, on contaste des fluctuations locales qui s'amplifient avec l'augmentation de l'épaisseur de l'InAlN.

Enfin, un point importante dans ce chapitre (grâce à l'analyse EDS) est l'observation de la présence du Ga dans la plus part des couches intermédiaires d'AlN. De plus, dans certains échantillons, le Ga a même été incorporé dans toute la couche d'InAlN.

Conclusions et Perspectives

Au cours de notre travail, cinq techniques complémentaires (AFM, IBA, Raman, MET, DRXHR) ont été utilisées pour la caractérisation des couches d'InN (UPM, TUB, EPFL) et des hétérostructures InAlN/GaN and InAlN/AlN/GaN (III-V Labs, Aixtron, EPFL) dans le but de contribuer à l'optimisation des procédés. Les principaux résultats sont résumés dans ce qui suit.

Les couches d'InN

Dans un premier temps, nous avons mis en évidence que les échantillons MBE-InN disposent de la meilleure qualité cristalline, avec des densités raisonnables de porteurs libres résiduels. Ensuite, leur morphologie, état de déformation et densités de dislocations traversantes (TD) ont été étudiées en fonction des conditions de croissance (rapport V/III, la vitesse de croissance, la température, les conditions de croissance riche en In ou N). Tous les échantillons présentent deux composantes de déformation: l'une biaxiale, l'autre

hydrostatique. Par ailleurs, deux tendances typiques ont été observées, dans des conditions de croissance riches en N: on aboutit à une croissance en 3D (rugosité rms ~7nm) et les plus grandes densités de porteurs libres (8 et 17 x 10^{18} cm^{-3}). Sur substrat silicium, cette croissance donne des couches aux contraintes résiduelles et densités de dislocation plus basses (1.8-3.2 x 10^{10} cm^{-2}).

Concernant les échantillons déposés dans des conditions de croissance riches en In, une croissance avec marches atomique a été obtenue (rugosité rms <1 nm). Dans ce cas, nous avons pu mettre en évidence le rôle important de la température de croissance: à basse température (T = 400 °C), la densité TDs mesurée est la plus forte (5.5 x 10^{10} cm^{-2}) tout comme la densité de porteurs libres. Pour le reste des échantillons (à une température située entre 420 et 480 °C), les densité des TDs étaient comparables (3.6-4.4 x 10^{10} cm^{-2}) tout comme la morphologie de surface (en 2D).

Les couches d'InAlN

En parallèle, nous avons étudié deux séries d'hétérostructures dont la croissance a été obtenue par MOVPE: InAlN/AlN/GaN/sapphire et InAlN/GaN.

Nous avons pu observer que lorsqu'on fait croître une couche intermédiaire AlN, on génère des défauts dans l'InAlN en forme de V (v-shape), leur densité augmente avec l'épaisseur de l'AlN. De plus, dans les échantillons où la couche intermédiaire AlN est la plus épaisse (3 et 6.9 nm), s'est formée une double couche, dont la partie la plus proche de l'interface est riche en Ga, indépendamment de la température de croissance (850 et 790 °C). Dans le cas où la croissance de la couche intermédiaire a été faite à 1200°C, cette couche intermédiaire était systématiquement riche en Ga avec une épaisseur entre 3 à 4.6 nm selon l'échantillon au lieu de 1 à 2nm qui était l'objectif de départ. Dans les hétérostructures déposées 790 °C, nous avons observé une forte concentration en Ga, environ 50 % dans la barrière InAlN. En accord avec la littérature, lorsque la couche intermédiaire était de AlGaN, la densité 2DEG (1.16-1.50 x 10^{13} cm^{-2}) est

légèrement inférieure à celle obtenue avec une couche intermédiaire AlN (2.49-2.98 x 10^{13} cm^{-2}).

Concernant les barrières InAlN les plus fines (t_{InAlN} < 33 nm), les couches montrent une bonne cristallinité par RBS avec χ_{min}=7-30 % selon les conditions de croissance. Lorsque les barrières deviennent épaisses (t_{InAlN} > 90 nm), la RBS montre une formation de deux couches avec une teneur en indium différente. La couche en surface d'InAlN a un χ_{min} of 100 % indiquant qu'elle est polycristalline. Cette dégradation progresse vers l'interface avec le GaN lorsque l'épaisseur de la barrière augmente.

Une analyse de la composition locale a ensuite permis d'expliquer cette dégradation structurale. En effet, nous avons trouvé des fluctuations de la composition locale à l'échelle du nanomètre dès l'interface avec le GaN. L'amplitude de cette fluctuation est faible à l'interface, elle augmente fortement vers la surface des barrières.

Suggestions pour compléter ce travail

Concernant la croissance de couches InN, ce travail a montré qu'il reste une marge importante d'amélioration de la qualité des matériaux. Une première suggestion serait de tester pour toutes le techniques étudiées: l'utilisation de substrats de GaN de polarité N dont certains auteurs ont montré qu'ils sont intéressants pour la croissance d'InN par MBE. De plus, les conditions de croissance riches en N devraient être évitées, car elles conduisent à des couches avec des densités de porteurs libres plus importantes. Les résultats obtenus avec des couches MBE-InN sont plutôt intéressants dans les conditions de croissance riches en In. On a pu observer une corrélation entre la densité de porteurs résiduels et les dislocations traversantes. Cependant, la plus faible densité de porteurs obtenue reste encore assez élevée, il reste donc beaucoup de place pour une amélioration de la qualité du matériau. Pour ce faire, on peut suggérer les tâches suivantes:

♦ La croissance des échantillons étudiés s'est faite avec des variations de températures importantes (variations pouvant aller jusqu'à 50 °C pendant la croissance d'une couche). Il est évident qu'un contrôle plus précis de la stabilité de la température lors de la croissance serait la première étape à effectuer.

♦ On a vu que les échantillons que l'on a fait croître avec un rapport V/III = 0.8-0.88 montrent une croissance en 2D. Selon nos données, il est clair qu'une étude sur le vitesse de croissance pourrait apporter d'importantes améliorations.

Dans le cas des hétérostructures InAlN, trois conditions de croissance différentes ont été étudiées.

♦ A une température de dépôt plus basse, nous avons observé l'incorporation de Ga de ~ 43-50% à l'intérieur de l'InAlN, et ces échantillons présentent une bonne qualité cristalline en RBS. De telles conditions devraient être davantage explorées par la fabrication de dispositifs et la caractérisation afin de connaître les performances de façon précise.

♦ Lorsqu'on a fait croître une couche intermédiaire AlN à 1200 °C et V/III = 2200, le Ga s'est incorporé à l'AlN et aucun défaut en forme de V n'a été observé dans la couche InAlN. Ce résultat pourrait contribuer à la croissance d'hétérostructures avec une densité de défauts réduite. Par exemple, il serait intéressant de tester la croissance d'une double couche intermédiaire AlGaN/AlN.

♦ Dans tous les cas, l'uniformité de l'InAlN nécessite encore une recherche approfondie.

List of abbreviations

2DEG	Two dimensional electron gas
α_{twist}	Twist angle
α_{tilt}	Tilt angle
a_0, c_0	unstrained lattice parameters
a_f	Lattice parameter film
a_s	Lattice parameter substrate
AECi	Thales samples
AFM	Atomic Force Microscopy
Aiii	EPFL samples
Aixii	Aixtron samples
b	Burger vector
b	dilatation coefficients
BF	Bright field
c	Lattice parameter
C_{ij}	Stiffness coefficients
d_0	grain diameter
$\Delta\omega$	Raman Shift
DBR	Distributed Bragg Reflectors
DF	Dark field
e_{ij}	piezoelectric tensor coefficients
ε_∞	high-frequency dielectric constant
ε_{xx}	in-plane strain tensor
ε_{zz}	out-plane strain tensor

E	Young modulus
EDS	Energy dispersive spectroscopy
ECCI	Electron channelling contrast imaging
φ	azimuthal angle rotation
Φ	Flux
f_m	misfit parameter
FvdM	Frank-van der Merwe mode
FWHM	Full width at half maximum
GB	grain boundaries
HAADF	High Angle Annular Dark Field
HEMT	High Electron Mobility Transistors
HFET	Heterojunctions Field Effect Tansistors
HRXRD	High Resolution x-Ray Diffraction
HVPE	Hydride Vapour Phase Epitaxy
I_x and I_{ref}	Intensity in an area unknown and know, respectively
IBA	Ion Beam Analysis
IDB	inversion domain boundary
IR	Infrared
K^H	Hydrostatic linear pressure
$L_{\parallel}$	Lateral coherence length
$L_{\perp}$	Vertical length
LED	Light Emitting diode
μ_e	Electron mobility
m*	effective electron mass
MBE	Molecular Beam Epiatxy
MOVPE	Metalorganic Vapour Phase Epitaxy
n_s	Sheet carrier density
N	concentration point defects
N_{edge}	Dislocations with edge component
N_m	concentration of lattice sites of the host matrix
N_{screw}	Dislocations with screw component

NRA	Nuclear Reaction Analysis
PAMBE	Plasma Assisted Molecular Beam Epitaxy
PIPS	Precision Ion Polishing System
PLD	Pulsed Laser Deposition
P_{pz}	Piezoelectric polarization
P_{sp}	Spontaneous polarization
r_h	covalent tetrahedral radius
rms	root mean square
r_s	radius of solute atoms
R^B	Biaxial relation coefficient
R^H	Hydrostatic relation coefficient
R_s	Sheet resistance
RBS	Rutherford Backscattering Spectroscopy
RC	Rocking curve
RHEED	Reflection high energy electron diffraction
RLP	Reciprocal lattice point
RSM	Reciprocal space map
σ_{kl}	stress tensor component
SAED	Selected area electron diffraction
SF	stacking faults
SK	Stranski-Krastanov mode
STM	Scanning tunnelling microscope
SEM	Scanning electron microscopy
t_{AlN}	Thickness AlN
t_c	Critical thickness
t_{InAlN}	Thickness InAlN
TD	Threading dislocation
TEM	Transmission Electron Microscopy
TMA	Trimethylaluminium
TMG	Trimethylgallium
TMI	Trimethylindium

UHV	Ultrahigh vacuum
UV	Ultraviolet
V/III	Ratio of the NH_3 molar versus group III molar flow
VCSELS	Vertical Cavity surface Emitting Lasers
WBDF	Weak Beam Dark Field
χ	tilt angle rotation
χ_{min}	minimum yield
XRD	x-Ray Diffraction
Y	Biaxial Modulus

Introduction

Research and technological advancements in electronic materials have modified, in the last 50 years, our views, our attitudes and our way of living. Tools and gadgets like personal computers, mobile phones and Light Emitting Diodes (LEDs) are just some examples of the vast number of electronic devices. In this context, the nitride based LEDs and laser diode are clear examples: the blue light was the result of a technological breakthrough in 1994 and caused a revolution in optoelectronics.

Group-III nitride semiconductors InN, GaN, AlN and their alloys represent a unique materials family for the development and mass production of numerous electronic and optoelectronic devices. The recent revision of the InN band gap, down to only ~ 0.65 eV, allows the development of LEDs for the red and near-infrared spectral region and carries an important opportunity for covering the whole visible and UV spectral range using one family of compounds (group-III nitrides). Furthermore, such materials find applications in electronic devices like high electron mobility transistors (HEMTs). The performance of III-nitride devices depends critically on their structural quality. A related important issue for the growth of InN and In-rich alloys is the large lattice mismatches and thermal expansion coefficient with the available substrates (sapphire, Si, SiC) or even bulk GaN. As a consequence, thin epitaxial films usually contain a high density of structural defects which are detrimental to their physical properties. Suitable growth methods to reduce the threading dislocation density in InN materials have to be developed in order to improve the crystalline quality of the InN towards the fabrication of high efficiency devices, like solar cells or light emitters.

This work has been investigated three growth techniques: Plasma Assisted Molecular Beam Epitaxy (PAMBE), Hydride Vapour Phase Epitaxy (HVPE) and Metalorganic Vapour Phase Epitaxy (MOVPE). While PAMBE has produced the highest quality InN achieved so far, growth rates are typically lower than in MOVPE. The latter method has significant advantages for commercial device fabrication since it enables high growth rates and high volume production, but it also has some limitations as MOVPE requires relatively high growth temperature to thermally crack NH_3, which is a particular challenge in the case of InN growth. Indeed, thick InN layers are needed and HVPE is a most appropriate technique for this purpose. Two of the key objectives for the epitaxial growth development are the reduction of dislocation density and impurity concentrations in InN and its alloys and to realize high-quality In-rich alloys.

This work was carried out within the 'RAINBOW ITN' European project with the title "High quality Material and intrinsic Properties of InN and indium rich Nitride Alloys". This thesis results from a detailed structural characterization of InN and InAlN heterostructures, using a number of complementary methods in close collaboration with the growers and device makers, with the aim of helping towards the improvement of the materials quality and device performances. Some of the results included in this manuscript have been obtained in collaboration with the other RAINBOW partners.

The manuscript is divided into four chapters. In the *first Chapter*, we present a brief history of the III-nitrides semiconductors and the applications of InN and InAlN. We describe the basic properties of wurtzite nitride semiconductors: residual strain, polarity, etc,... We discuss more specifically the problem for the choice of substrate and the structural defects in these materials. Finally, we present growth diagrams for InN and InAlN heterostructures as found in the literature.

In the *second Chapter*, a short description of the growth methods is reviewed; the characterization techniques employed in this work are also presented.

In the *third Chapter* the results of our detailed investigation of the InN layers are discussed. First, we compare the InN grown by the three different techniques:

PAMBE, HVPE and MOVPE and the rest of the chapter is focused on MBE-InN samples which are previously shown to have the best quality. The InN layers surface was analysed with atomic force microscopy (AFM). The residual strain of these layers was determined by high resolution x-ray diffraction (HRXRD). As already reported in GaN, the presence of a hydrostatic strain component in these InN layers is correlated to excess of nitrogen as shown by nuclear reaction analysis (NRA) and Rutherford backscattering spectroscopy (RBS). The determination and observations of dislocation densities by HRXRD and transmission electron microscopy (TEM) are also discussed. As would be expected due to large lattice mismatch between InN and the used substrates/templates, the ***a***- edge type threading dislocations are predominant, while a lower percentage of mixed type dislocations is observed.

In the *fourth Chapter* the In composition of InAlN/GaN and InAlN/AlN/GaN is studied using HRXRD mapping, RBS and EDS, as well as high angle annular dark field imaging (HAADF). The potential of these techniques for the analysis of composition in inhomogeneous or heterogeneous layer systems as well as compositional fluctuations is demonstrated. The important finding in this chapter is the non intentional gallium incorporation in the AlN interlayer and for some samples it was even seen to be present all over the InAlN barrier.

In the end, the results of this work are summarized and an outlook to future work is given.

Chapter 1

III-Nitrides properties and applications

Since the dawn of civilization, the human being tried to understand and use the phenomena related to light. People had constantly wondered how to illuminate the night until they discovered with the use of fire. For the two last centuries, the lighting technology has taken more and more room and nowadays this field is one of the most interesting sectors of optical technologies.

The development of semiconductors has been crucial for technological applications. For last years, the research and applications of the III-nitride semiconductors have been highly extensive for materials without native substrates. Indeed, their synthesis for even better performances is still a challenge as the structural defects generated in the epitaxial growth are responsible for the low efficiency of the devices. The objective of this chapter is to present the structural properties of InN and InAlN compounds which are at the basis of this work.

1.1 Brief history of nitrides

Historically, the most important periods of Humanity have been designated as the different types of materials. Thus, Stone Age ranges from the Lower Paleolithic Period, about 2.5 million years to the Neolithic; Bronze Age begins around 3000 years BC, and from 1500 years BC until the Roman Period is the Iron Age. When, in the mid-seventies of last century, the number of publications on semiconductors materials exceeded at on steel, some historians began to call the period as the "Age of Semiconductors". This strong growth is still underway until today, and semiconductors have led to a revolution, at least, comparable to that produced by the steam engine. Today, semiconductors based electronics has a clear impact on everyday life, at our work and in our home.

Group III-Nitrides (GaN, AlN, InN and their alloys) have remarkable properties, the first is their direct bandgap spanning from 0.65 eV (InN) to 6.2 eV (AlN) at room temperature, which should allow emission and detection of wavelengths ranging from infrared to deep ultraviolet. Other properties such as their high thermal and mechanical stability, large piezoelectric constants, or spontaneous polarization make them good candidates for the fabrication of

electronic and optoelectronic devices able to operate at high temperature, high frequency and high power densities.

Among this III-nitride family, GaN is the compound that has been most investigated in the literature. The first report of III-nitride synthesis was in 1938 by Juza *et al*.[1] for GaN and InN crystals. Then 30 years later, Maruska *et al*.[2] grew GaN layers by vapour phase deposition on sapphire substrates and measured its bandgap at 3.39 eV. Epitaxial layers were also reportd in the late 1960s using hydride vapour phase epitaxy (HVPE). In 1971, Pankove *et al*.[3] reported the first blue GaN-based diode consisting of a metal/insulating device. However most of this early research was eventually abandoned due to the high defect density and poor surface morphology of the available heteroepitaxial films. These problems began to be overcome in the mid-1980s and good quality of GaN thin films were obtained in 1986 by Amano *et al*.[4] with the optimized two steps growth method using metal organic vapour phase epitaxy (MOVPE). In this procedure, a thin AlN buffer layer was first grown on sapphire at low temperature (~600 °C), followed by GaN layer growth at a higher temperature (~1040 °C). The AlN buffer provided high density nucleation centers and promoted the lateral growth of the main layer, resulting in better quality of GaN thin films.[4] Later, Nakamura[5] reported that a GaN buffer layer had a similar effect.

III-nitrides research increased in 1990s when Nakamura *et al*.[6] working for the Japanese company Nichia, announced the first blue light emitting diode (LED) based on GaN and $In_xGa_{1-x}N$.[6,7] After that the progress of manufacturing devices based on III-group nitrides was accelerated. In 2002, Nichia announced the development of high power InGaN LED's for white, blue and green light emission with expected lifetime of 100000h. From the heterostructure LED and laser diode up to high electron mobility transistor (HEMT), all devices are now investigated using the nitride compounds and alloys.

In the early 1990s, it was discovered also that the III-nitride material exhibit strain induced and spontaneous piezoelectric polarization effects, leading to the demonstration of the two-dimensional electron gas (2DEG) at an $Al_xGa_{1-x}N/GaN$, and demonstration of an $Al_xGa_{1-x}N/GaN$ HEMTs.[8,9]

In 2001, Kuzmík[10] proposed the use of the ternary InAlN in order to replace AlGaN and improve the reliability of HEMTs. Indeed, InAlN/GaN systems have many predicted advantages over AlGaN/GaN heterostructures, in particular, by changing the Al to In ratio, the strain can be varied, while maintaining high electron sheet density, and devices degradation due to strain relaxation observed in AlGaN/GaN HEMTs can be reduced. The strain can be completely eliminated by growing InAlN/GaN lattice matched heterostructures. Many more details can be found in the reviews by Jan *et al.*[11], Bhuiyan *et al.*[12], and Vurgaftman *et al.*[13]

There are two fundamental reasons to choose the III-nitride system for light sources. First, as mentioned above, their direct band gap covers the entire visible spectrum from the UV to the IR. This is in a contrast to the (Ga,Al)As based LEDs (1.5–2.2 eV) or (Al,Ga,In)P based LEDs (1.3–2.5 eV) that cover only the IR to yellow region (Fig 1.1). The other advantage of the III-nitride semiconductors is their strong chemical bond, which makes them very stable and resistant to degradation under high electric currents and high temperatures.

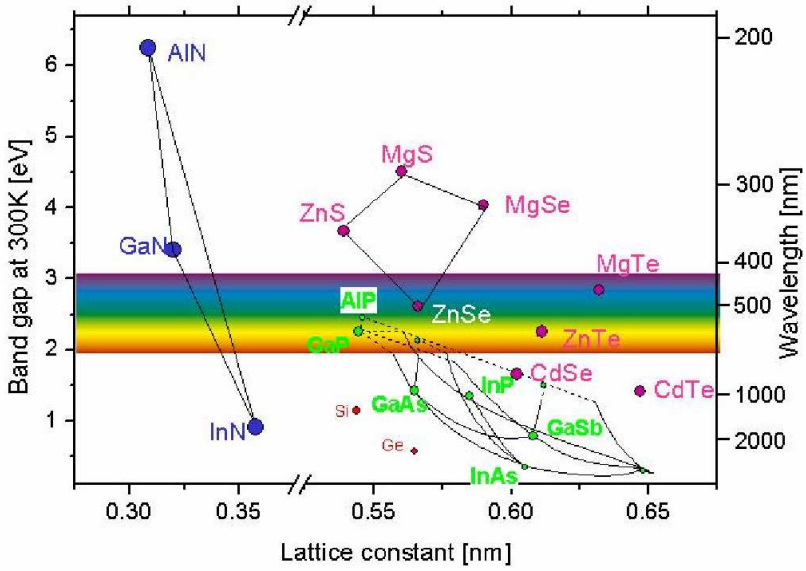

Fig 1.1 Room temperature bandgap energy versus lattice constant of the nitrides and other common semiconductors.[14]

However, despite intense research efforts worldwide, there still remains a strong need to improve the nitride based devices quality. In particular, in contrast to AlAs/GaAs system, they suffer from lattice-mismatches and from the absence

of suitable substrates leading to strong built-in strains and to the formation of cracks or dislocations detrimental for optical and electrical properties.

1.2 InN: Introduction and applications

Research on the growth and characterization of InN has increased tremendously in last years, mainly, due the recent redefinition of its band gap at 0.65 eV, in contrast to the earlier admitted value of 1.89 eV.[15] The controversy associated with the discovery of its narrow band gap has led to intense research efforts.[15,16] Several reports have shown since that oxygen incorporation (oxynitride) was one of the reasons for the earlier measured bandgap.[17,18] It became then very interesting to explore the AlN-GaN-InN alloy system for device applications in solid-state lighting, spintronics, and terahertz devices. Indeed InN is a key elemental in InGaN based LED as it exhibits smallest effective mass, the largest mobility and highest peak and saturation velocities of the III-nitrides.[19] It was also reported that InN rich alloys could be resistant to radiation damage[20] and therefore be used in a variety of device applications (including high efficiency multi-junction solar cells,[21] high-brightness light emitting diodes[22] and high electron mobility transistors,[10]...).

Until now, integration of InN into device applications has been limited by a number of growth difficulties:

- low dissociation temperature
- high equilibrium vapor pressure of nitrogen molecules
- lack of suitable substrate material for InN

1.3 InAlN: Introduction and applications

InAlN is the least characterised of the ternary nitride alloys: much less is known about its properties, compared to AlGaN and InGaN, due to its unstable growth conditions. The attractive features of InAlN are the wide bandgap range from 0.65 eV to 6.2 eV and the lattice matching of $In_{0.18}Al_{0.82}N$ to GaN. This lattice matched alloy has a large refractive index contrast to GaN and a direct band gap around 5 eV, which is larger than that of GaN (3.5 eV).

In contrast to other heterojunctions field effect transistors (HFETs) fabricated from the conventional cubic III-V semiconductors, the band gap discontinuities and polarization effects in nitride allow the HFETs without the need to dope the barrier. In this instance, the two dimensional electron gas (2DEG) from which originates the name of such devices (high electron mobility transistor or HEMT) is due to polarization and piezoelectric fields. However, in theses heterostructures, the lattice mismatch between AlGaN and GaN results in strain causing device degradation through defect generation. The possibility of growing lattice-matched InAlN/GaN removes the strain induced degradation of GaN-based HEMTs and piezo-polarization, potentially improving the heterostrucure stability. InAlN/GaN HEMTs exhibit a high 2DEG density (n_s), together with good mobility (μ_e) and low sheet resistance (R_s), solely due to spontaneous polarization effects.[23] Such devices show high temperature stability, and the inclusion of an AlN ultrathin interlayer was shown to improve the 2DEG mobility.[10] In such a device, (Fig 1.2), the current between drain (D) and source (S) is controlled by the voltage on the gate contact (G), it flows through an ultra thin channel defined by the two dimensional electrons gas distribution.[24]

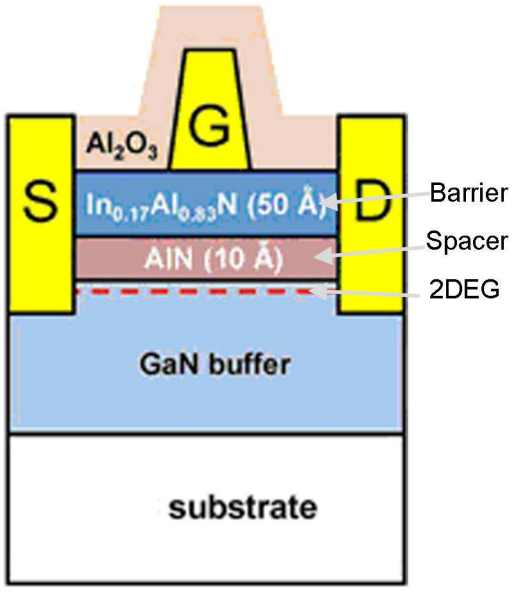

Fig 1.2 Schematic cross section of $In_{0.17}Al_{0.83}N$/AlN/GaN HEMT.[24]

Apart from HEMTs, InAlN ultrathin layers are used in distributed Bragg reflectors (DBRs)[25,26] such heterostructures are essential building blocks for advanced optoelectronic devices (i.e. vertical cavity surface emitting lasers (VCSELS)). They consist in multilayer structures exhibiting a high reflectivity around a desired wavelength. In this instance, the InAlN lattice-matched DBRs prevents cracking.[27] Other applications of InAlN consist in realization of prototypes such as thermoelectric device,[28] and ultraviolet photodiode.[29]

1.4 Structural properties

1.4.1 Crystalline structure

Group III-V nitrides (GaN, AlN, InN and their alloys) may take three crystalline structures: the wurtzite, zincblende and rock salt.[30] For these nitrides semiconductors (GaN, AlN, InN), the most stable structure is the wurtzite structure (space group $P6_3mc$) with four atoms per unit cell. The metal (Ga, Al or In) element is surrounded by four nitrogen atoms, at the edges of a tetrahedron, this makes two translated compact hexagonal (HCP-hexagonal close packed) structures, which project along the $[11\bar{2}0]$ direction as an ABAB layered structure, where A, and B form III-N pairs (Fig 1.3).

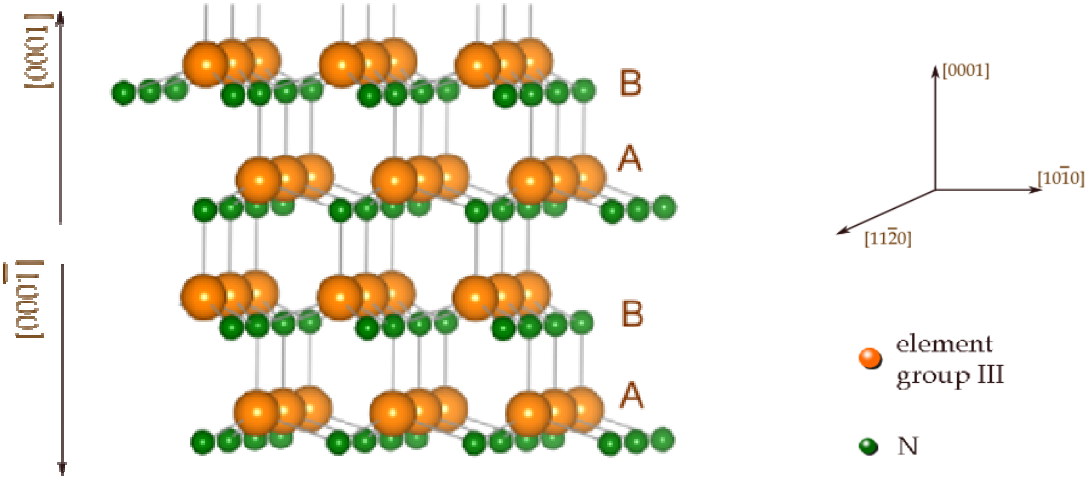

Fig 1.3 Schematic illustration of wurtzite structure.

In this structure, the bond length along the [0001] direction between N and the metal atoms is larger than the three other bonds of the basic tetrahedron, and its length as related to the *c* parameter is named *u*. This parameter is different for each compound. Taking an appropriate origin, the atoms inside the unit cell are then located at (1/3, 2/3, 0) and (2/3, 1/3, ½) (group III) and (1/3, 2/3, *u*) and (2/3, 1/3, ½+*u*) N.

1.4.2 Polarity and piezoelectric properties

Conventionally, the [0001] axis is defined as the direction which connects the metal to the N atoms, and if the crystals is cut along the A-B bond, as can be seen in Fig 1.3, the (0001) surface will be terminated by III atoms type, whereas the $(000\bar{1})$ surface will be only populated by N atoms: the <0001> and $<000\bar{1}>$ directions correspond to III and V polar directions, respectively. One of the consequences of this polarity is a spontaneous polarization (P_{sp}) which may take place at interfaces. In addition to this P_{sp}, the III-nitrides show a large piezoelectric (P_{pz}) response to elastic strain. This results in a piezoelectric polarization when their heterostructures are submitted to strain. The nitrides having different lattice parameters, their epitaxial heterostructures are either under tensile or compressive strain. At the interface of the heterostructures, the total polarization is then the sum of the spontaneous polarization due to the net difference of charges along the *c* axis and of the strain induced piezoelectric polarization.

$$\vec{P}_{Total} = \vec{P}_{sp} + \vec{P}_{pz} \tag{1.1}$$

Table 1.1 lists the spontaneous and piezoelectric polarization of group III nitrides. As can be seen, the P_{sp} of the III-nitrides is negative. In a theoretical study, Bernardini *et al.*[31] reported a strong nonlinear dependence of spontaneous polarization on composition in chemically disordered alloys. Assuming that ternary nitride alloys have random microscopic structure, the same authors

expressed the piezoelectric parameter to second order in the composition parameter x as [32]

$$P_{sp}\,(In_xAl_{1-x}N) = -0.090\,(1-x) - 0.042\,x + 0.071\,x\,(1-x) \qquad (1.2)$$

for the $In_xAl_{1-x}N$ compounds C/m^2. The first two terms are the usual linear interpolation parameters between the binary compounds, and the third term is the so called bowing parameter.

Table 1.1 Spontaneous (P_{sp})[32] and piezoelectric (P_{pz})[32] polarization for the group III nitrides, piezoelectric tensor coefficients[30] and stiffness coefficients.

Material	**GaN**	**AlN**	**InN**
P_{sp} (C/m^2)	-0.034	-0.90	-0.042
P_{pz} (C/m^2)	1.8765	-3.1963	0.4448
e_{33} (C/m^2)	0.73	1.46	0.97
e_{31} (C/m^2)	0.49	0.60	0.57
C_{11}	367 [33]	411 [30]	223 [33]
C_{12}	135 [41]	149 [30]	115 [33]
C_{13}	103 [41]	99 [30]	92 [33]
C_{33}	405 [41]	389 [30]	224 [33]

For biaxial strained III-V nitride epitaxial layers grown in the (0001) orientation, the piezoelectric polarization occurring along the <0001> direction is given by:[34]

$$P_{pz,z} = 2\varepsilon_{xx}\left(e_{31} - e_{33}\frac{C_{13}}{C_{33}}\right) \qquad (1.3)$$

where C_{13} and C_{33} are the stiffness elastic coefficients of the film, related to Young's modulus and Poisson's ratio of the crystal, e_{31} and e_{33} are the piezoelectric

tensor coefficients[30] (Table 1.1) and ε_{xx} corresponds to the in-plane strain tensor components, which is defined as

$$\varepsilon_{xx} = \frac{a_{subtrate} - a_{film}}{a_{film}} \quad (1.4)$$

Applying the numbers in Table 1.1 to the case of $In_xAl_{1-x}N$ grown on GaN, it can be seen that P_{pz} (equation 1.3) is positive for compressive strain and negative for tensile strain (as example: for In content 0.1 the P_{pz} is 0.030 C/m^2, when x_{In}= 0.18 the P_{pz}=0 C/m^2 and x_{In}=0.3 then the P_{pz} = -0.07 C/m^2).

The polarization related properties are obviously important for devices because the electric fields influence the shape of the band edges and the carrier distribution inside nitride-based heterostructures. As was reported many times, spontaneous and piezoelectric polarization can influence the radiative recombination in light-emitting devices as well as the electrical properties in transistors.[35]

1.4.3 Substrates

As no bulk nitride substrates are commonly available in the nature, III-nitrides growth has been performed on a number of different substrates and crystal orientations. Growing heteroepitaxially requires the choice of a substrate with a surface template that matches the crystal symmetry of the desired material. The lattice mismatch between the substrate and the film leads to the generation of misfit dislocations at the interfaces in order to release the mismatch. Unfortunately the relaxation is never completely confined inside the interface and the dislocations usually propagate inside the interfacial layer. During such heteroepitaxial growth, not only the lattice parameters difference plays an important role, but also it is necessary to manage the thermal behaviour of the substrate and the epitaxial layers. Indeed at cooling down from the growth temperature, the substrate and film will relax in significantly different way depending on the differences in their thermal expansion coefficients. In this work

the investigated nitride layers were grown on [0001]-sapphire and Si substrates. As can see in Table 1.2, the lattice parameters, mismatch and thermal expansion coefficients are quite different between the nitrides and the used substrates. Therefore, one expects, if no special care is taken, the generation of large defect densities following heteroepitaxy of nitride layers on these substrates.

The main criteria for the substrate choice is that the substrate has a low lattice mismatch this is measured by the misfit parameter (f_m) defined as

$$f_m = \frac{a_{substrate} - a_{film}}{a_{substrate}} \tag{1.5}$$

and $a_{substrate}$ and a_{film} are the lattice constant for the substrate and the film, respectively (Table 1.2).

Table 1.2 Parameters of III-V nitrides and substrates.

Material		**GaN**	**AlN**	**InN**	**Al_2O_3**	**SiC**	**Si**
Structure		Wurtzite	Wurtzite	Wurtzite	Rhombohedral	Wurtzite	Cubic (111)
Lattice constant	***a***	3.185 [36]	3.111 [37]	3.5378 [38]	4.765 [39]	3.0806 [39]	a = b = c = 5.431 [39]
	c	5.188 [36]	4.98 [37]	5.7033 [38]	12.982 [39]	15.1173 [39]	
Mismatch to GaN (%)		0	~ 2.3	~ -11	~ 16	~ -3.1	~ 21
Mismatch to InN (%)		~ 11	~ 13.7	0	~ 29.2	~ 14.8	~ -7.8
Thermal expansion ($10^{-6}K^{-1}$)[40,41]	‖ ***a*-axis**	3.17	4.2	3.09	5.0	4.3	3.59
	‖ ***c*-axis**	5.59	5.3	2.79	9.03	4.7	

If the film consists on an alloy, such as $In_xAl_{1-X}N$ grown on GaN, its lattice constant depend on the composition x. Assuming that Vegard's law is valid, the lattice constants of the films are given by[42]

$$a\ (In_xAl_{1-x}N) = x \cdot a\ (InN) + (1-x) \cdot a\ (AlN) \quad (1.6)$$

$$c\ (In_xAl_{1-x}N) = x \cdot c\ (InN) + (1-x) \cdot c\ (AlN) \quad (1.7)$$

Although its strict validity is under constant questioning, Dridi *et al.*[43], using first principle calculations, reported that the Vegard's law holds for AlGaN (both lattice constants) and the *a*-lattice constant for InGaN and InAlN. The authors predicted a small deviation from Vegard's law for the *c*-lattice parameter of the latter alloys. More recently, Darackchieva *et al.*[44] used the ab initio program VASP[45] which uses the generalized gradient approximation and reported for InAlN, that both *a*-and *c*-lattice parameters exhibit essentially a linear dependence on the In composition with very small deviations from Vegard's rule. They concluded that even such small deviations could have influence on the strain calculations as carried from HRXRD and Raman data. They proposed the following equation for *a* and *c*:

$$\xi(x) = x\xi(InN) + (1-x)\xi(AlN) - \delta_\xi x(1-x) \quad \text{and} \quad \xi = a, c \quad (1.8)$$

where δ_a = 0.0412 ± 0.0039 Å and δ_c = -0.060 ± 0.010 Å are the corresponding deviation values respectively for the *a*- and *c*-cell parameters.

Fig 1.4 shows the lattice constants and thermal expansion coefficients for common substrates and III-N semiconductors. The plot gives an indication of how various substrates match indium nitride in terms of lattice constant and thermal expansion coefficient. It is interesting to note that the most common III-N substrate, sapphire, has the worst lattice and thermal expansion match to InN, as well as for the other nitrides (AlN, GaN). The use of sapphire substrates for the growth of nitride layers appears to have only been possible when the use of buffer layers was discovered.[46]

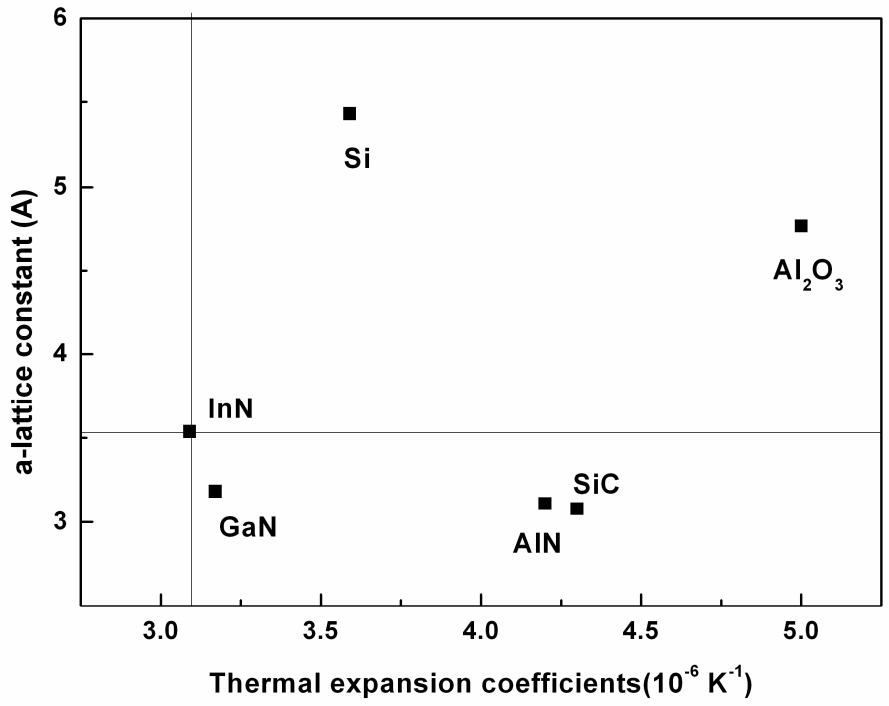

Fig 1.4 The *a*-plane lattice constant and *a*-plane thermal expansion coefficients for common indium nitride substrates and III-N semiconductors.

1.4.3.1 *Sapphire (Al_2O_3)*

Sapphire is the most extensively substrate used for the epitaxial growth III-nitrides although it has large lattice and thermal expansion match to nitrides Several orientations, such as *c*-(0001), *a*-$(11\bar{2}0)$, *m*-$(1\bar{1}00)$ and *r*-$(1\bar{1}02)$, have been used for nitride. In this work, the investigated InN layers were growth on *c*-orientation. Usually, the InN is grown on top of a GaN/*c*-Al_2O_3, in this instance, the unit cell of GaN is rotated by 30° around the *c*-axis with respect to the sapphire unit cell (Fig 1.5) and the lattice mismatch is ~ 16 % (Table 1.2) whereas for the non rotated GaN on sapphire is about 32 %.[39] In fact, this rotation not only permits to decrease the lattice mismatch between sapphire and GaN, but it also allows the alignment between the oxygen and III-element sub-lattices of the two materials.[47] In this instance, the mismatch between sapphire and GaN lattice parameters is thus calculated using the following equation:

$$f_m = \frac{a_{substrate} - \sqrt{3}a_{GaN}}{\sqrt{3}a_{substrate}} \qquad (1.9)$$

If InN is grown directly on sapphire, two kinds of in-plane rotated domains can be observed with epitaxial relationships of $[10\bar{1}0]InN//[11\bar{2}0]Al_2O_3$ and $[11\bar{2}0]InN//[11\bar{2}0]Al_2O_3$ where the lattice mismatch are 29.2 % and -25.4 %, respectively.[48]

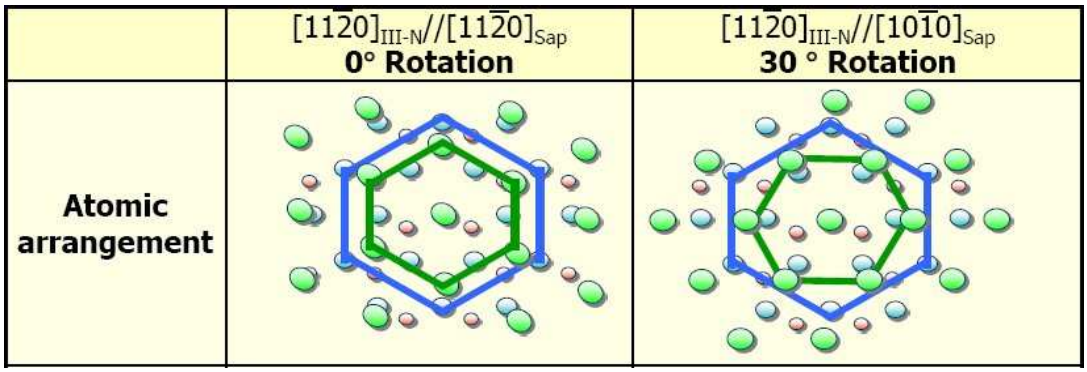

Fig 1.5 Schematic diagram of the plane crystal structure for a III-N/sapphire with the two atomic arrangement. The blue atom is oxygen and the green atom is the III-element.[49]

1.4.3.2 *SiC*

Recently,[50] InN epitaxial films were grown by PA-MBE at 450 °C on 4H- and 6H-SiC substrates using low-temperature InN nucleation layers. It was shown that InN films grown under the In-rich regime show improved crystal quality, surface morphology, and optical properties. Photoluminescence measurements showed emission up to room temperature; the deduced band gap values as low as 0.64 eV at T = 10 K, and carrier concentrations were of the order of $8 \times 10^{17} cm^{-3}$.

1.4.3.3 *Si*

The interest of using Si as a substrate for nitride growth includes the crystalline quality and low cost, as well its highly dominant technological applications in the microelectronic field. Since Si has a diamond structure, the (111) Si substrates are usually used for GaN epitaxy. Silicon is also an alternative substrate for InN growth. Indeed, the lattice mismatch between InN/Si(111) is ~8 %, which is smaller than InN/Al_2O_3, and the low cost substrate as well as

availability of large size wafers, and high thermal conductivity offers advantages compared with the sapphire substrates.[51]

InN nitride has already been grown on most of the above substrates. As was shown by Noia *et al.*[52], when it is directly deposited on (0001) sapphire, InN layers take the N polarity. Otherwise, the temperature for successful growth of InN is strongly dependent on the substrate polarity: InN grows at 550 °C on N-face GaN and C-face SiC substrates, while the growth is only realized at a decreased temperature around 450 °C on Ga-face GaN and Si-face SiC substrate.

1.4.4. Mosaic model

Heteroepitaxial films with large lattice mismatch to the substrate commonly exhibit a high density of threading dislocations (TD). TDs can evolve from the coalescence of neighboring misoriented islands affecting the microstructure and crystalline quality of the InN epilayer. A mosaic model is widely used to describe the epilayer microstructure in which the in-plane and out-of-plane rotations of grains are quantified by the mosaic twist and tilt, respectively.[53] In this model, the layer is assumed to consist of single crystals, called mosaic blocks with certain mean vertical and lateral dimensions. Since the crystallites are assumed to be free of dislocations, they can coherently scatter the x-rays, and their dimensions are called vertical and lateral coherence length.

These terms are related to directions perpendicular and parallel to the growth plane, respectively. For systems with defects mainly running parallel to the surface normal, the vertical coherence length is related to the thickness of the layer.

As shown in Fig 1.6, in the mosaic model, the hexagonal layers such as wurtzite InN and/or InAlN alloys can be characterized by four different parameters: tilt angle, $\alpha_{tilt,}$ or out-of-plane misorientation; twist angle, α_{twist}, or in-plane misorientation; lateral coherence length, $L_{\parallel}$; and the vertical length ($L_{\perp}$) which is related to the thickness of the layer, in case of thin films as in our case.[54] These four characteristic parameters can be accessed using high resolution x-ray diffraction.

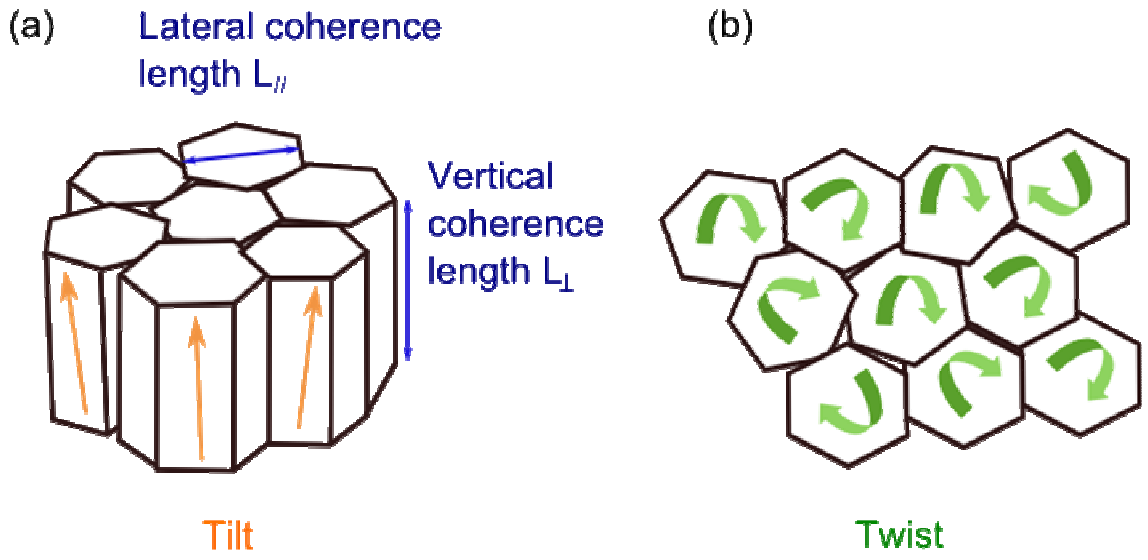

Fig 1.6 A mosaic layer structure with the four characteristics parameters: (a) lateral and vertical length, and tilt (b) twist.

1.4.5 Strain and stress

1.4.5.1 *Critical thickness*

The generation of misfit dislocations is a well-known phenomenon in heteroepitaxy.[55] A layer grown on a substrate with a different lattice constant and a different thermal expansion coefficient, as it is the general case for III-nitrides layer, is usually strained and the strain may depend on the layer thickness. Below a certain thickness, called the critical thickness t_c, the film can be grown pseudomorphically on a substrate, meaning that the in-plane lattice constants of the substrate ($a_{substrate}$) and the film (a_{film}) are equal (Fig 1.7(a)), whereas for $t > t_c$, the layer relaxes (Fig 1.7(b)) forming misfit dislocations.[56]

For a partially relaxed layer, two cases are possible:

- $a_{substrate} > a_{film}$ the layer is under tensile strain
- $a_{substrate} < a_{film}$ the layer is under compressive strain

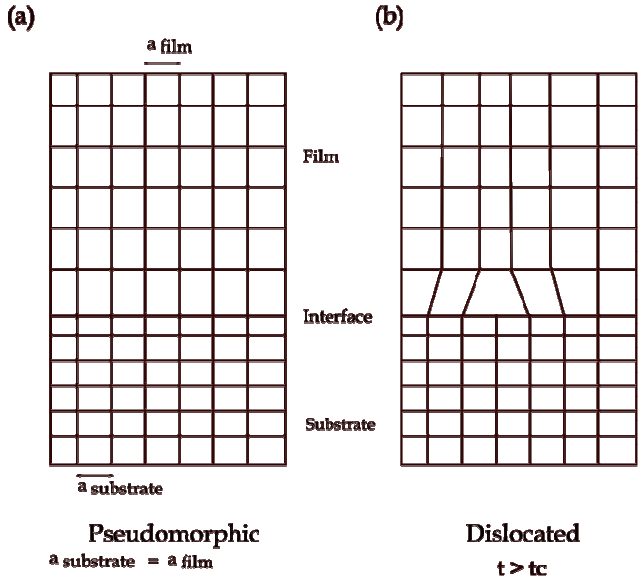

Fig 1.7 Film grown on a substrate: (a) $a_{substrate} = a_{film}$, (b) $t > t_c$, the biaxial strain is accommodated by the introduction of misfit dislocations.

Matthews *et al.*[57], People *et al.*[58], and Fisher *et al.*[59] proposed different theoretical models for calculating the critical thickness in isotropic materials. The first introduced a force balance model using layers of GaAs and $GaAs_{0.5}P_{0.5}$. They identified two forces (misfit force and tension of the dislocation line) which act on the dislocations and the critical thickness was determined by their equilibrium. People *et al.*[58] investigated a strained Ge_xSi_{1-x} layer on Si substrate and they calculate the t_c based on an energy balance of the dislocation self-energy and the elastic energy. Fisher *et al.*[59] proposed an estimate for the t_c, namely $t_c \sim b\ \varepsilon_{xx}$, where b is the length of the Burgers vector of the misfit dislocations. Holec *et al.*[60] provided a model based on the energy balance of hexagonal symmetry for an InGaN epitaxial layer on a GaN substrate and they predicted lower t_c by about 10-20 % for the range of In content $0 < x < 0.3$ when compared to the corresponding isotropic approximation.

1.4.5.2 *Residual stress*

In heteroepitaxy, the mismatches between lattice constants and thermal expansion coefficients of film and substrates (Table 1.2) as well as point defect incorporation lead to residual stress. The stress-strain relations for a hexagonal crystal (C_{6v}) is given from Hooke's law and can be expressed by a 6x6 matrix: σ_i

$= \sum_j C_{ij}\, \varepsilon_j$ where C_{ij} represents the elastic stiffness coefficients (Table 1.1), developing the matrix, the expression displays:

$$\begin{pmatrix} \sigma_{xx} \\ \sigma_{yy} \\ \sigma_{zz} \\ \sigma_{yz} \\ \sigma_{zx} \\ \sigma_{xy} \end{pmatrix} = \begin{pmatrix} C_{11} & C_{12} & C_{13} & 0 & 0 & 0 \\ C_{12} & C_{11} & C_{13} & 0 & 0 & 0 \\ C_{13} & C_{13} & C_{33} & 0 & 0 & 0 \\ 0 & 0 & 0 & C_{44} & 0 & 0 \\ 0 & 0 & 0 & 0 & C_{44} & 0 \\ 0 & 0 & 0 & 0 & 0 & \frac{C_{11}-C_{12}}{2} \end{pmatrix} \times \begin{pmatrix} \varepsilon_{xx} \\ \varepsilon_{yy} \\ \varepsilon_{zz} \\ \varepsilon_{yz} \\ \varepsilon_{zx} \\ \varepsilon_{xy} \end{pmatrix} \quad (1.10)$$

where σ_{kl} are the stress tensor components and ε_{kl} corresponds to the strain tensor components. The in-plane strain ε_{xx} and out of plane ε_{zz} are given by:

$$\varepsilon_{xx} = \frac{a - a_0}{a_0} \quad (1.11) \qquad \text{and} \qquad \varepsilon_{zz} = \frac{c - c_0}{c_0} \quad (1.12)$$

where a, c and a_0, c_0 are the strained and unstrained lattice parameters, respectively. Due to hexagonal symmetry $\varepsilon_{xy} = \varepsilon_{yz} = \varepsilon_{zx} = 0$, which leads to:

$$\sigma_{xx} = \sigma_{yy} = (C_{11} + C_{12}) \cdot \varepsilon_{xx} + C_{13} \cdot \varepsilon_{zz} \quad (1.13) \qquad \sigma_{zz} = 2 \cdot C_{13} \cdot \varepsilon_{xx} + C_{33} \cdot \varepsilon_{zz} \quad (1.14)$$

The InN growth is a complex phenomenon and various parameters during the growth or the subsequent cooling can result in a combination of hydrostatic and biaxial strain states.[61]

Biaxial Stress

During heteroepitaxy of III-nitrides on the (0001) plane, biaxial strain arises from the lattice mismatch with the substrate and from the film–substrate thermal expansion coefficient. If the crystal is stressed in the (0001) plane and is free to relax in the [0001] direction, the in-plane residual stress is uniform ($\sigma_{xx} = \sigma_{yy}$) and

there is no stress along the *c* axis ($\sigma_{zz} = 0$). In this biaxial stress situation, the strain tensor components are given by

$$\varepsilon_{yy} = \varepsilon_{xx} \qquad (1.15) \qquad \varepsilon_{zz} = -2 \cdot (C_{13}/C_{33}) \cdot \varepsilon_{xx} \qquad (1.16)$$

where R^B ($-2\ (C_{13}/C_{33})$) is called the biaxial relation coefficient, then $\varepsilon_{zz}=R^B\ \varepsilon_{zz}$ (1.17).

Using equations (1.13) and (1.14)

$$\sigma_{xx} = \left(C_{11} + C_{12} - 2\frac{C_{13}^2}{C_{33}} \right) \varepsilon_{xx} \qquad (1.18)$$

and $Y=(C_{11} + C_{12} - 2\frac{C_{13}^2}{C_{33}})$ is called the biaxial modulus; $\sigma_{xx}=Y\varepsilon_{xx}$ (1.19)

Using the equation (1.17) and (1.19): $\sigma_{xx} = (Y/R^B)\ \varepsilon_{zz}$ (1.20)

Hydrostatic Stress

A crystal under hydrostatic stress does not change the shape of its unit cell: it will be enlarged or reduced but will maintain the same ratio of lateral to vertical lattice constant, *c*/*a*. In InN, hydrostatic stress has been related to the homogeneous incorporation of point defects.[62]

Under hydrostatic pressure p, the stress becomes: $\sigma_{xx}=\sigma_{yy}=\sigma_{zz}=-p$

$$\varepsilon_{zz} = (C_{11}+C_{12}-2C_{13})/(C_{33}-C_{13})\varepsilon_{xx} \qquad (1.21)$$

For the nitrides $R^H = (C_{11}+C_{12}-2C_{13})/(C_{33}-C_{13})$ is close to 1 (R^H=1.24, 0.98 and 1.16 for AlN, GaN and InN, respectively); this fact has led a number of authors who dealt with the hydrostatic strain to use the approximate relationship: $\varepsilon_{zz}=\varepsilon_{xx}$,[63] which gives for the corresponding strain.

$$\varepsilon = b \cdot N = \frac{\Delta c}{c_0} = \frac{\Delta a}{a_0} \tag{1.22}$$

where N is the concentration of the point defects and b describes the dilatation coefficient given by[64]

$$b = 1/3\ [1-(r_s/r_h)^3]N_m^{-1} \tag{1.23}$$

here, N_m is the concentration of lattice sites of the host matrix, r_h is the covalent tetrahedral radius of host atoms and r_s is the radius of solute atoms.

Uniaxial Stress

An uniaxial stress (linear stress) may arise for instance when point defects incorporated uniformly in the basal plane, in which case $\sigma_{zz} \neq 0$ and the other stress components are zero; the non-zero strain components are:

$$\varepsilon_{xx} = -[C_{13} / (C_{11}+C_{12})]\varepsilon_{zz} \tag{1.24}$$

with $C_{13}/(C_{11}+C_{12})$ corresponds to the Poisson ratio ν

$$\sigma_{zz} = (C_{33}-2C_{13}^2/(C_{11}+C_{12}))\varepsilon_{zz} = E\varepsilon_{zz} \tag{1.25}$$

with E the Young modulus.

1.4.6 Structural defects

The electrical and optical properties of a semiconductors material are highly sensitive to the presence of defects and impurities. Defects can greatly affect carrier mobility, electrical and thermal conductivity, etc,... The commonly observed defects in III-nitrides films can be divided in three types: point, line and planar. The point defects are vacancies, interstitial and substitutional impurities, the line defects are dislocations and the planar ones are staking faults.

1.4.6.1 *Point defects*

Point defects in a semiconductor crystal occur when an atomic site is vacant (atom missing from lattice sites) or substituted (cation on anion sites or vice versa), or an interstitial (additional atoms in between the lattice sites) site is occupied (Fig 1.8). For InN, isolated and complexes of In[65] and N point defects have been investigated.[66,67] Point defects often contribute to an increased background doping[68] and/or reduce the mobility of the free carriers in the semiconductors.[64]

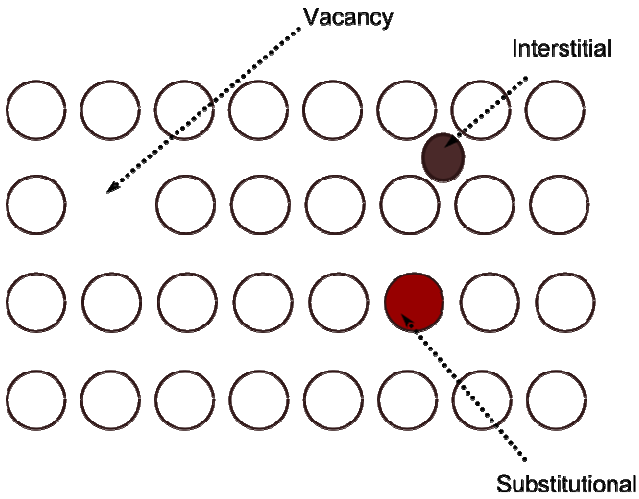

Fig 1.8 Main point defects presence in a film.

In the case of compound semiconductors such as InN, also antisite defects can be formed by atoms occupying opposite sub-lattice sites. Frenkel defects are nearby pairs of vacancies and interstitials. Schottky defects are vacancy pairs created by the simultaneous removal of a two opposite atoms in compound semiconductors.

1.4.6.2 *Dislocations*

A dislocation is a line defect in a crystal, completely determined by two quantities: an oriented line direction, l, and a displacement vector $\boldsymbol{b}$, (known as the Burgers vector of the dislocation), which corresponds to the displacement introduced in the crystal along its line.[69] A dislocation is perfect when its Burgers

vector corresponds to lattice parameter; it is partial, when the displacement is a fraction of a lattice parameter.

Based on the relation of l and $\boldsymbol{b}$, three dislocation types are distinguished:

(1) Pure *edge* - type dislocation, where $l \perp \boldsymbol{b}$. Schematically, this corresponds to the insertion of an additional half lattice plane in the crystal between two adjacent lattice planes. The end of the additional half plane is the dislocation line and $\boldsymbol{b}$ is the lattice vector that virtually connects the atoms along the line (Fig 1.9)

(2) Pure *screw* - type dislocation with $l \parallel \boldsymbol{b}$. In this case, all along the line, a quarter of the crystal is moved for instance downward by the amount of a lattice parameter (Fig 1.9), and as can be seen no additional plane is inserted.

(3) *mixed* – type dislocation where l and $\boldsymbol{b}$ do not have a particularly well defined angular relationship.

In the hexagonal lattice, there are three possible Burgers vectors for perfect dislocations $\boldsymbol{a}$, $\boldsymbol{c}$, and $\boldsymbol{a}+\boldsymbol{c}$, and depending on their line directions, the corresponding dislocation may have respectively an edge, screw or mixed character. For instance, in the nitride epitaxial layers the $\boldsymbol{a}$ dislocation is either edge or of mixed type when its line is in the basal plane and it become of edge type when it propagates inside the epitaxial layer where it becomes a threading dislocation TD (l=[0001]). A particular case is the $\boldsymbol{a}+\boldsymbol{c}$ dislocation which is always a TD in such layers, and therefore of mixed type. Indeed, the $\boldsymbol{c}$ dislocation is always screw as a TD, but it may become edge type when its line bends in the basal plane for instance in case of epitaxial lateral overgrowth.[70]

The density of threading dislocation can be measured directly by transmission electron microscopy. Unfortunately, this process is destructive. Alternatively, non-destructive x-ray diffraction is a widely applied method to evaluate the crystalline perfection of epitaxial layers and the density of dislocation may also be estimated.[71]

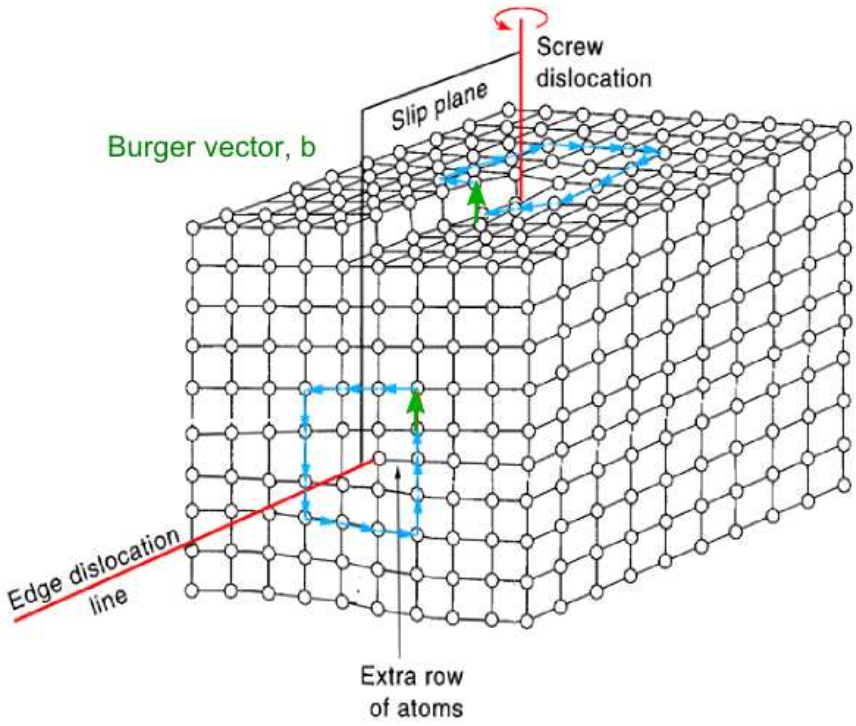

Fig 1.9 Schematic diagram showing edge and screw dislocation.[72]

1.4.6.3 *Planar defects*

In a crystal, the local periodicity can be disrupted along a planar boundary which then constitute a planar defect. Such defects have been largely investigated and in nitride layers, stacking faults (SF), inversion domain boundary (IDB), and grain boundaries (GB) have been identified.[73] The three types of planar defects are characterized by the crystallographic operation that connects the two sides of the crystal separated by the boundary. In a SF, there is a simple displacement which corresponds to a fraction of a crystal translation vector. In the wurtzite structure, three types of stacking faults may form in the c planes with R: $1/3<10\bar{1}0>$, $1/2<0001>$ and $1/6<20\bar{2}3>$, respectively (Fig 1.10). A stacking fault can be terminated inside the crystal by a partial dislocation having the same displacement vector.

In wurtzite crystals, there is no center of symmetry, therefore, the growth may give rise to different domains which may be related by an inversion operation, such domains are separated by an IDB. As compared to SFs and IDBs, grain boundaries connect the two sides of the crystal through more complex

crystallographic operations such as rotations and translations.[74] A stacking fault is any defect that alters the periodic sequence of layers. These defects may be a wrong layer inserted into the sequence, a change of the layer sequence or a different translation between two subsequent layers. These defects may affect the whole crystal or a finite region. The schematic diagram of the stacking sequence of wurtzite and the main basal stacking faults of the hexagonal lattice are exhibited in Fig 1.10, respectively.

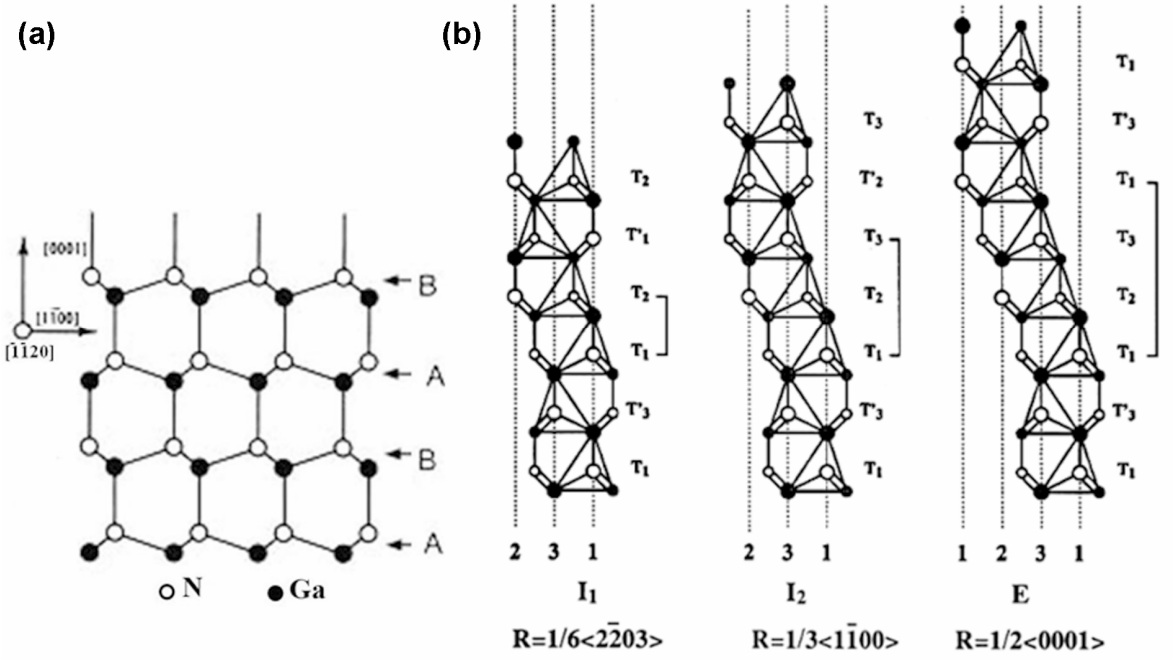

Fig 1.10 Diagram of (a) wurtzite, (b) stacking faults in the wurtzite structure.[75]

1.5 InN and InAlN growth

1.5.1 InN

Nowadays, InN is heteroepitaxially grown on various substrates and templates. Although most results have been obtained on sapphire, there are also reports on GaAs,[76] on Si-face and C-face SiC substrates with In-polarity and N-polarity, respectively,[77] on GaP.[78] The common epitaxial techniques used are Molecular Beam Epitaxy (MBE),[79] Metal Organic Vapour Phase Epitaxy (MOVPE),[80] and Hydride Vapour Phase Epitaxy (HVPE).[81]

In the late 1980's, sputtering was the only technique available to grown InN.[82] Single crystalline InN was reported by Matsuoka *et al.*[83] and Wakahara *et al.*[84] for the first time in 1989 using MOVPE. The first attempt to grow single-crystalline InN by the RF-MBE method was reported by Hoke *et al.*[85] (1991). In fact, for this low temperature material (400-550 °C), MBE has shown an advantage over MOVPE for obtaining high quality InN. As nitrogen can be activated using plasma (PA-MBE), the MBE technique has the possibility to select the growth temperature without considering the requirements of NH_3 pyrolysis.

The growth of InN is the most problematic among III-nitrides due to its low dissociation temperature, extremely high equilibrium vapour pressure of nitrogen and the lack of lattice-matched substrates. InN epilayers start to decompose at temperatures above 550 °C and In-droplets form on the surface.[12]

Gallinat *et al.*[79] reported a MBE growth diagram for In-face InN using a constant nitrogen flux (Φ_N = 10.5 nm/min). Fig 1.11 shows that two growth regimes exist: the first corresponds to N-rich condition and the second to In-rich regime or also called In-droplet.[65]

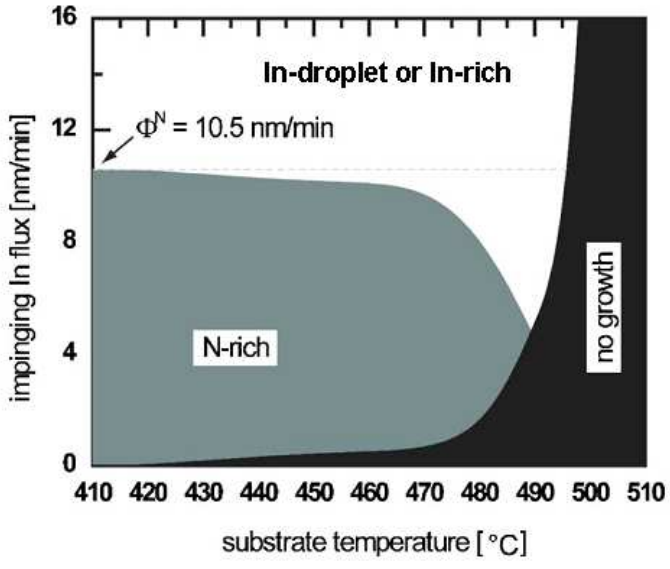

Fig 1.11 The PAMBE growth diagram for In-face (0001) InN.

They showed that for $\Phi_{In}/\Phi_N > 1$, growth occurs in the In-droplet regime and the layer surface morphology shows spiral hillocks characteristic of step flow growth in the areas between In droplets. Whereas, for $\Phi_{In}/\Phi_N < 1$, they reported a

degradation of the growing layer with rough surfaces and three dimensional features.[79]

1.5.2 InAlN

The first growth of InAlN by rf magnetron sputtering was reported by Starosta[86] in 1981 and later for Kubota *et al*.[87] Theoretically, Teles *et al*.[88] used first principle ab initio techniques to calculate the phase diagram for cubic $In_xAl_{1-x}N$, and the result can be seen on Fig 1.12 where is plotted the growth temperature versus In composition (x). The spinodal curve in the phase diagram marks the equilibrium solubility limit, and as can be seen, there is a large miscibility gap in which no solid solution can be obtained. For instance if the growth was to be carried out at 800 °C, a large decomposition tendency is seen between 9 % and 85 % In.

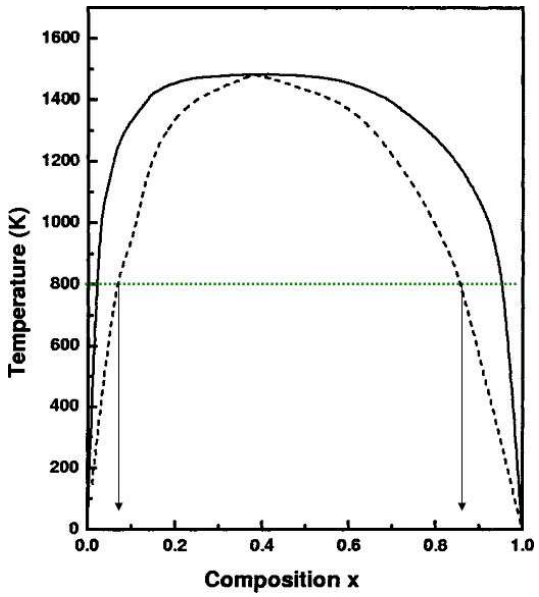

Fig 1.12 Phase diagram of unstrained cubic $In_xAl_{1-x}N$ alloys. The solid line indicates the binodal curve, and the dashed line indicates the spinodal curve.[88] The green dashed shows the T = 800 °C at which temperature spinodal descomposition is predicted for alloys with In content between 0.09 and 0.85 %.

Recently, a systematic study of InAlN growth by MBE was reported in which the ternary alloys were grown on GaN templates.[89] Indium incorporation was analysed as a function of the growth temperature and metal fluxes and a

growth diagram (Fig 1.13) was proposed.[90] In this figure, four regimes can be distinguished as a function of the impinging flux Φ_{In} and the substrate temperature, namely: In droplets, N-rich, intermediate In-rich, and no In regimes.

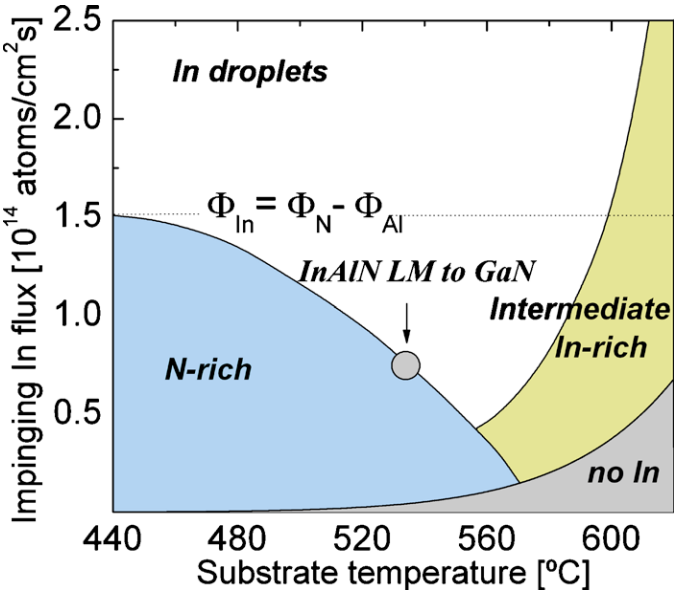

Fig 1.13 MBE growth diagram for InAlN.[90]

1.5.3 Growth modes

The epitaxy is a complex process, especially, as we try to produce thin layers for specific applications, on top of completely different substrates. The way the growth takes place depends upon many parameters, one may site a few which probably are rather critical: the energies of surfaces that we are aiming at connecting, the symmetry of these surfaces, the lattice misfit between the substrate and film, the supersaturation (flux) of the crystallizing phase, the growth temperature, etc,... A classification in three main growth modes has been proposed by Ernst Bauer in 1958.[91] At the nucleation stage, the film starts to grow in one of these three basic modes;[91] they are illustrated schematically in Fig 1.14.

1.5.3.1 *Frank-van der Merwe mode (FvdM)*

Two dimensional grown (2D) occurs when the adatoms of the film are strongly attracted to the substrate. Therefore, the first adatoms condense on the substrate surface and form a complete monolayer (Fig 1.14(a)). Subsequently, the next adatoms constitute the following monolayers and the growth takes place

layer by layer. This is the ideal case, and it happens when the two materials have close or highly equal characteristics (symmetry, lattice parameters, surface energies, growth temperatures, etc...).

1.5.3.2 *Stranski-Krastanov mode (SK)*

This is an intermediate case: after forming the first monolayer, or a few monolayers, subsequent layer by layer growth becomes unfavourable and the growth continues in the form of islands (Fig 1.14(b)). The lattice mismatch between film and substrate induces a strain in the film and can explain the transition from 2D layer to 3D islands growth modes.[91]

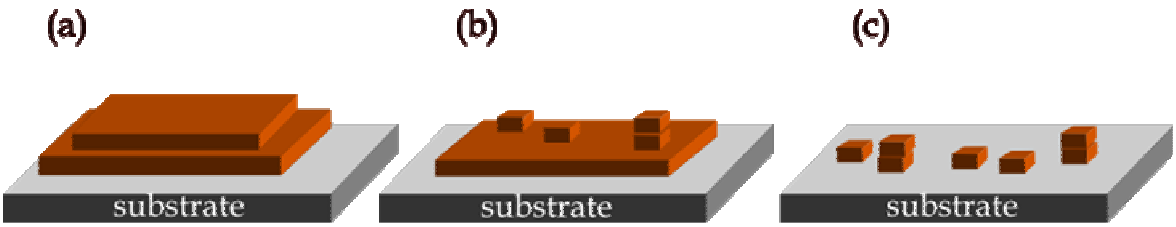

Fig 1.14 The three modes of thin films, (a) Frank-van der Merwe, (b) Stranski-Krastanov, and (c) Volmer–Weber.

1.5.3.3 *Volmer-Weber mode*

This is the island growth, also known as three-dimensional growth mode. It occurs when the impinging atoms (adatoms) forms clusters on the substrate which then grow into individually islands. In this growth mode the bonds between the adatoms are stronger than the bonds between the adatoms and the substrate surface (Fig 1.14(c)). This mode will govern the heteroepitaxial growth when the two materials have completely different symmetries, surface energies, large lattice mismatch, etc,...

1.6 A brief review of the optical properties of nitrides

The III-nitrides are direct band gap semiconductors, which makes them suitable for the fabrication of optoelectronic devices. Fig 1.15 shows the band gap of GaN, AlN and InN, plotted versus their *a* lattice parameter. With band gap energies ranging from 0.65 eV (InN)[15] to 6.25 eV (AlN),[13] devices can be in

principle designed to emit light of any colour in the visible spectrum, and from the near infra-red to deep UV. The composition dependences of the band gaps for the binary nitride alloys are assumed to follow a simple quadratic form, as proposed by Vurgaftman and Meyer:[13]

$$E_g\,(A_{1-x}B_x) = (1-x)E_g(A) + xE_g(B) - x\,(1-x)C \qquad (1.26)$$

where *Eg* is the band gap energy, and C is the bowing parameter, which describes the deviation from a linear interpolation between the band gap values of the two members, A and B.

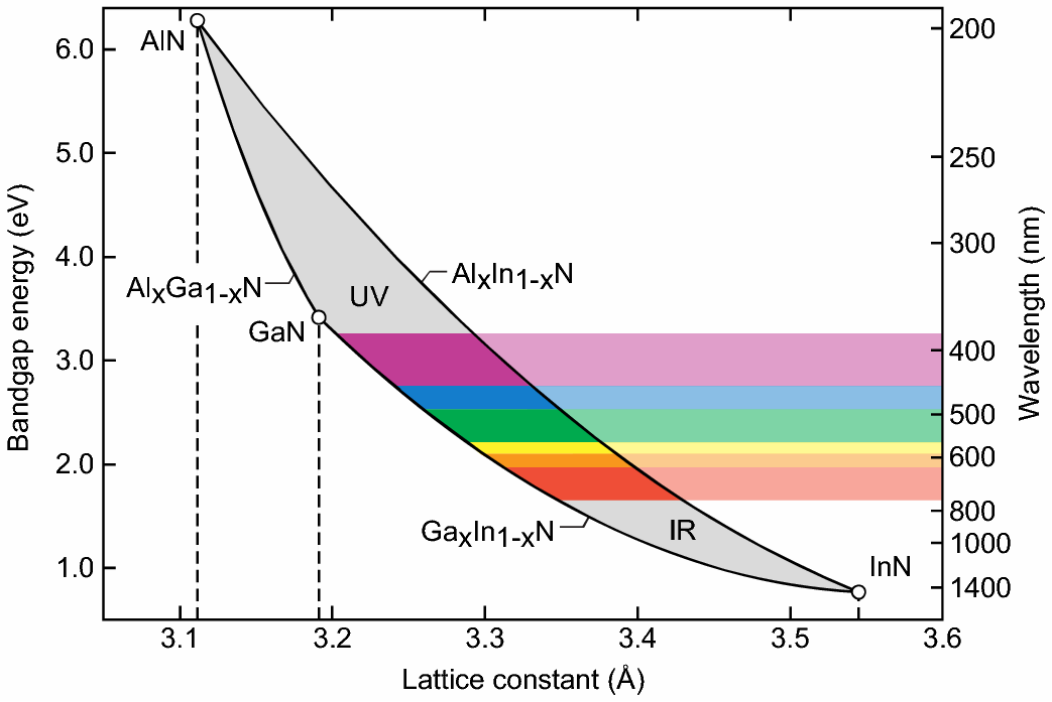

Fig 1.15 Diagram showing the band gaps of AlN, GaN and InN, as a function of their *a* lattice parameter. For comparison, the visible colours in the solar spectrum are shown.[92]

The compositional dependence of the bandgap of InAlN can be expressed with the following expression using a bowing parameter, b_{InAlN}, as:[93]

$$E^{g}_{In_xAl_{1-x}N} = 6.1\cdot x + 0.7\cdot(1-x) - b_{InAlN}\cdot x\cdot(1-x) \qquad (1.27)$$

1.7 Aim of this work

This work has been performed in the framework of the European RAINBOW project. The goal of this project is to obtain high quality indium nitrides materials and its alloys, to understand their growth mechanisms and to improve their opto- and micro-electronic properties. In the consortium, the growth as well as the structural, optical and electrical investigations have been done in collaboration with different research laboratories and industries. My contribution to this project has been focused on the structural characterization of InN and InAlN layers grown by the partners of RAINBOW, using different complementary techniques.

References

[1] R. Juza, and H. Hahn. *Über die kristallstrukturen von Cu_3N, GaN und InN metallamide und metallnitride*, Z. Anorg. Allgem. Chem. **234**, 282 (1938).

[2] H. P. Maruska, and J. J. Tietjen. *The preparation and properties of vapor-deposited single crystal line GaN.* Appl. Phys. Lett. **15**, 327 (1969).

[3] J.I. Pankove, E.A. Miller, and J. E. Berkeyheiser. *GaN electrolumiscent diodes*. RCA Rev. **32**, 383 (1971).

[4] H. Amano, M. Kito, K. Hiramatsu, and I. Akasaki. *P-type conduction in Mg-doped GaN treated with Low-Energy Electron Beam Irradiation (LEEBI).* Jpn. J. Appl. Phys. **28**, L2112 (1989).

[5] S. Nakamura. *In situ monitoring of GaN growth using interference effects.* Jpn. J. Appl. Phys. **30**, 1620 (1991).

[6] S. Nakamura, T. Mukai, and M. Senoh. *High-power GaN p-n junction blue-light-emiiting diodes.* Jpn. J. Appl. Phys. Part 2, **30**, L1998 (1991).

[7] S. Nakamura, M. Senoh, and T. Mukai. *p-GaN/n-InGaN double-heterostructure blue-light-emitting diodes.* Jpn. J. Appl. Phys. Part 2, **32**, L8 (1993).

[8] M. A. Khan, J. M. Van Hove, J. N. Kuznia, and D. T. Olson. *High electron mobility GaN/$Al_xGa_{1-x}N$ heterostructures grown by low-pressure metalorganic chemical vapor deposition*. Appl. Phys. Lett. **58**, 2408 (1991).

[9] M.A. Khan, A. Bhattarai, J.N. Kuznia, and D.T. Olson *High electron mobility transistor based on a GaN-$Al_xGa_{1-x}N$ heterojunction.* Appl. Phys. Lett. **63**, 1214 (1993).

[10] J. Kuzmík. *Power electronics on InAlN/(In)GaN: Prospect for a record performance.* IEEE Electron Device Lett. **22**, 510 (2001).

[11] S. C. Jain, M. Willander, J. Narayan, and R. Van Overstraeten. *III-nitrides: Growth, characterization, and properties.* J. Appl. Phys. **87**, 965 (2000).

[12] A. G. Bhuiyan, A. Hashimoto, and A. Yamamoto. *Indium nitride: A review on growth, characterization, and properties.* J. Appl. Phys. **94**, 2779 (2003).

[13] I. Vurgaftman, and J. R. Meyer. *Band parameters for nitrogen-containing semiconductors.* J. Appl. Phys. **94**, 3675 (2003).

[14] http://www.grin.com/en/doc/272493/molecular-beam-epitaxy-growth-of-indium-nitride-and-indium-gallium-nitride

[15] V. Y. Davydov, A. A. Klochikhin, V. V. Emtsev, D.A. Kurdyukov, S. V. Ivanov, V. A. Vekshin, F. Bechstedt, J. Furthmüller, J. Aderhold, J. Graul, A. V. Mudryi, H. Harima, A. Hashimoto, A. Yamamoto, and E. E. Haller. *Band gap of hexagonal InN and InGaN alloys.* Phys. Stat. Sol. b **234**, 787 (2002).

[16] J. Wu, and W. Walukiewicz. *Band gaps of InN and group III nitride alloys.* Superlattices and Microstruct. **34**, 63 (2003).

[17] Motlan, E. M. Goldys, and T.L. Tansley. *Optical and electrical properties of InN grown by radio-frequency reactive sputtering*. J. Cryst. Growth **241**, 165 (2002).

[18] M. Yoshimoto, H. Yamamoto, W. Huang, H. Harima, J. Saraie, A. Chayahara, and Y. Horino. *Widening of optical bandgap of polycrystalline InN with a few percent incorporation of oxygen.* Appl. Phys. Lett. **83**, 3480 (2003).

[19] B. E. Foutz, S. K. O'Leary, M. S. Shur, L. F. Eastman. *Transient electron transport in wurtzite GaN, InN, and AlN*. J. Appl. Phys. **85**, 7727 (1999).

[20] J. Wu, W. Walukiewicz, K. M. Yu, W. Shan, and J. W. Ager III, E. E. Haller, Hai Lu, W. J. Schaff, W. K. Metzger, and S. Kurtz. *Superior radiation resistance of $In_{1-x}Ga_xN$ alloys: Full-solar-spectrum photovoltaic material system*. J. Appl. Phys. **94**, 6477 (2003).

[21] A. Yamamoto, M. Tsujino, M. Ohkubo, and A. Hashimoto. *Metalorganic chemical vapour deposition growth of InN for InN/Si tandem solar cell*. Sol. Energy Mater. Sol. Cells **35**, 53 (1994).

[22] T. Mukai, M. Yamada, and S. Nakamura. *Characteristics of InGaN-Based UV/Blue/Green/Amber/Red Light-Emitting Diodes*. Jpn. J. Appl. Phys. **38**, 3976 (1999).

[23] M. Gonschorek, J.-F. Carlin, E. Feltin, M. A. Py, and N. Grandjean. *High electron mobility lattice-matched AlInN/GaN field-effect transistor heterostructures.* Appl. Phys. Lett. **89**, 062106 (2006).

[24] http://www.semiconductor today.com/features/SemiconductorToday_AprMay2011_InAlNHEMT.pdf

[25] J.-F. Carlin, and M. Ilegems. *High quality AlInN for high index contrast Bragg mirrors lattice matched to GaN.* Appl. Phys. Let. **83**, 668 (2003).

[26] J.-F. Carlin, J. Dorsaz, E. Feltin, R. Butté, N. Grandjean, M. ilegims, and M. Laügt. *Crack-free fully epitaxial nitride microcavity using highly reflective.* Appl. Phys. Lett. **86**, 031107 (2005).

[27] T. Sadler. *Nitride distributed Bragg reflectors for single photon source applications*. PhD University of Cambridge (2009).

[28] S. Yamaguchi, R. Izaki, N. Kaiwa, S. Sugimura, and A. Yamamoto. *Thermoelectric devices using $Al_{1-x}In_xN$ thin films prepared by reactive radio-frequency.* Appl. Phys. Lett. **84**, 5344 (2004).

[29] S. Senda, H. Jiang, and T. Egawa. *AlInN-based ultraviolet photodiode grown by metal organic chemical vapour deposition.* Appl. Phys. Lett. **92**, 203507 (2008).

[30] H. Morkoç. *Handbook of nitride semiconductors and Devices.* Vol 1. Wiley-VCH 2008.

[31] F. Bernardini, and V. Fiorentini. *Nonlinear behaviour of spontaneous and piezoelectric polarization in III-V nitride alloys.* Phys. Stat. Sol a **190,** 65 (2002).

[32] V. Fiorentini, F. Bernardini, and O. Ambacher. *Evidence for nonlinear macroscopic polarization in III-V nitride alloy heterostructure.* Appl. Phys. Lett. **80**, 1204 (2002).

[33] A. F. Wright. *Elastic properties of zinc-blende and wurtzite AlN, GaN, and InN*. J. Appl. Phys. **82**, 2833 (1997).

[34] N. Sarrazin. *HEMTs à base de nitrure de Gallium: évolution vers un nouveau système de matériaux, une nouvelle génération de composants*. Thèse Doctorat de l'Université des Sciences et Technique de Lille, N°4028 (2007).

[35] O Ambacher. *Growth and applications of Group III-nitrides.* J. Phys. D: Appl. Phys. **31** 2653 (1998).

[36] K. Lorenz, N. Franco, E. Alves, S. Pereira, I. M. Watson, R. W. Martin, and K. P. Donnell. *Relaxation of compressively strained AlInN on GaN*. J. Cryst. Growth **310**, 4058 (2008).

[37] M. Tanaka, S. Nakahata, K. Sogabe, H. Nakata, and M. Tabioka. *Morphology and X-ray Diffraction Peaks widths aluminium nitride single crystals prepared by the sublimation method*. Jpn. J. Apply. Phys. **36**, L1062 (1997).

[38] W. Paszkowicz. *X-ray powder diffraction data for indium nitride.* Powder Diffraction **14**, 258 (1999).

[39] L. Liu, and J. H. Edgar. *Substrates for gallium nitride epitaxy*. Mat. Scien. and Eng. R **37**, 61 (2002).

[40] B. Gil. *Group III nitride Semiconductor Compounds. Physics and Applications.* Clarendon Press (1998).

[41] W. Paszkowicz, R. Cerny, and S. Krukowski. *Rietveld refinement for indium nitride in the 105-295 K range*. Powder Diffr. **18**, 114 (2003).

[42] S. C. Jain, M. Willander, J. Narayan, and R. Van Overstraeten. *III-nitrides: Growth, characterization, and properties.* J. Appl. Phys. **87**, 965 (2000).

[43] Z. Dridi, B. Bouhafs, and P. Ruterana. *First-principles investigation of lattice constants and bowing parameters in wurtzite $Al_xGa_{1-x}N$, $InGa_{1-x}N$ and $In_xAl_{1-x}N$ alloys.* Semicond. Sci. Technol. **18**, 850 (2003).

[44] V. Darakchieva, M. –Y. Xie, F. Tasnádi, I. A. Abrikosov, L. Hultman, B. Monemar, J. Kamimura, and K. Kishino. *Lattice parameters, deviations from Vegard's rule, and E_2 phonons in InAlN.* Appl. Phys. Lett. **93**, 261908 (2008).

[45] G. Kresse, and J. Furthmüller. *Efficient iterative schemes for ab initio total-energy calculations using a plane-wave basis set.* Phys. Rev. B **54**, 11169 (1996).

[46] H. Amano, N. Sawaki, I. Akasaki, and Y. Toyoda. *Metalorganic vapor phase epitaxial growth of a high quality GaN film using an AlN buffer layer*. Appl. Phys. Lett. **48**, 353 (1986).

[47] K. Dovidenko, S. Oktyabrsky, J. Narayan, and M. Razeghi. *Aluminium nitride films on different orientations of sapphire and silicon.* J. Appl. Phys. **79** 2439 (1995).

[48] X. Wang, and A. Yoshikawa. *Molecular beam epitaxy growth of GaN, AlN and InN.* Progress in Crys. Growth and Charact. Mat. **48/49**, 42 (2004).

[49] Y. Nanishi presentation in Rainbow Workshop. Madrid. Spain (2009). http://rainbow.ensicaen.fr/

[50] M. Losurdo, M. M. Giangregorio, G. Bruno, T.H. Kim, P. Wu, S. Choi, A. Brown, F. Masia, M. Capizzi, and A. Polimeni. *Characteristics of InN grown on SiC under the In-rich regime by molecular beam heteroepitaxy*. Appl. Phys. Lett. **90**, 011910 (2007).

[51] C. C. Huang, R. W. Chuang, S. J. Chang, J. C. Lin, Y. C. Cheng, and W. J. Lin. *MOCVD Growth of InN on Si(111) with various buffer layers.* J. Electr. Mat. **37**, 1054 (2008).

[52] H. Naoi, F. Matsuda, T. Araki, A. Suzuki, Y. Nanishi. *The effect of substrate polarity on the growth of InN by RF-MBE*. J. Cryst. Growth **269**, 155 (2004).

[53] R. Chierchia, T. Böttcher, H. Heinke, S. Einfeldt, S. Figge, and D. Hommel. *Microstructure of Heteroepitaxial GaN revealed by x-ray diffraction.* J. Appl. Phys. **93**, 8918 (2003).

[54] V. Srikant, J. S. Speck, and D. R. Clarke. *Mosaic structure in epitaxial thin films having lattice mismatch*. J. Appl. Phy. **82**, 4286 (1997).

[55] I. A. Ovid'ko. *Misfit dislocation walls in solid films.* J. Phys.: Condens. Matt. **11**, 6521 (1999).

[56] S. C. Jaint, A. H. Harker, and R. A. Cowler. *Misfit strain and misfit dislocations in lattice mismatched epitaxial layers and other systems.* Phil. Mag. A **75**, 1461 (1997).

[57] J. W. Matthews, and A. E. Blakeslee. *Defects in Epitaxial Multilayers. I. Misfit dislocations*. J. Cryst. Growth **27**, 118 (1974).

[58] R. People, and J. C. Bean. *Calculations of critical layer thickness versus lattice mismatch for* Ge_xSi_{1-x}/Si *strained-layer heterostructures.* Appl. Phys. Lett. **47**, 322 (1985).

[59] A. Fisher, H. Kühne, and H. Richter. *New Approach in Equilibrium Theory for Strained Layer Relaxation.* Phys. Rev. Lett. **73**, 2712 (1994).

[60] D. Holec, P. M. F. J. Costa, M. J. Kappers, and C. J. Humphreys. *Critical thickness calculations for InGaN/GaN.* J. Cryst. Growth **303**, 314 (2007).

[61] D. Y. Song, M. E. Holtz, A. Chandolu, A. Bernussi, S. A. Nikishin, M. W. Holtz, and I. Gherasoiu. *Effect of stress and free-carrier concentration on photoluminescence in InN.* Appl. Phys. Lett. **92**, 121913 (2008).

[62] K. S. A. Butcher, A. J. Fernandes, P. P.-T. Chen, M. Wintrebert-Fouquet, H. Timmers, S. K. Shrestha, H. Hirshy, R. M. Perks, and B. F. Usher. *The nature of nitrogen related point defects in common forms of InN*. J. Appl. Phys. **101**, 123702 (2007).

[63] C. Kisielowski, J. Krüger, S. Ruminov, T. Suski, J. W. Ager III, E. Jones, Z. Liliental-Weber, M. Rubin, E. R. Weber, M. D. Bremser, and R.F. Davis. *Strain-related phenomena in GaN thin films.* Phys. Rev B. **54**, 17745 (1996).

[64] K. Yagi, N. Miyamoto, and J. Nishizawa. *Anomalous diffusion of Phosphorus into silicon.* Jpn J. Appl. Phys. **9**, 246 (1970).

[65] F. Reurings, F. Tuomisto, C. S. Gallinat, G. Koblmüller, and J. S. Speck. *In vacancies in InN grown by plasma-assisted molecular beam epitaxy*. Appl. Phys. Lett. **97**, 251907 (2010).

[66] X. M. Duan, and C. Stampfl. *Nitrogen vacancies in InN: Vacancy clustering and metallic bonding from first principles*. Phys rev. B **77**, 115207 (2008).

[67] A. Terentjevs, A. Catellani, and G. Cicero. *Nitrogen vacancies at InN (100) surfaces: A theoretical study*. Appl. Phys. Lett. **96**, 171901 (2010).

[68] Y. Ishitani, K. Kato, H. Ogiwara, S.B. Che, A. Yoshikawa, and X. Wang. *Carrier recombination processes in In-polar n-InN in regions of low residual electron density*. J. Appl. Phys. **106**, 113515 (2009).

[69] S. Amelinckx. *The characterization of defects in crystals.* J. Cryst. Growth **24/25**, 6 (1974).

[70] P. Gibart. *Metal organic vapour phase epitaxy of GaN and lateral overgrowth* Rep. Prog. Phys. **67** 667 (2004).

[71] M. J. Hordon, and B. L. Averbach. *X-ray measurements of dislocation density in deformed copper and aluminium single crystals.* Acta Metall. **9,** 237 (1961).

[72] http://www.google.fr/imgres?q=dislocations+screw+and+edge&um=1&hl=fr&client=firefox-a&rls=org.mozilla:fr:official&biw=1024&bih=585&tbm=isch&tbnid=5jd9uQDSYHD6LM:&imgrefurl=http://courses.eas.ualberta.ca/eas421/lecturepages/microstructures.html&docid=Hkp7FZDeC_L_cM&imgurl=http://courses.eas.ualberta.ca/eas421/diagramspublic/bergerslarge.gif&w=807&h=611&ei=5-4rT9q5MIqcOonx2ZcO&zoom=1&iact=rc&dur=331&sig=111764880061757961352&page=1&tbnh=113&tbnw=149&start=0&ndsp=18&ved=1t:429,r:4,s:0&tx=95&ty=65

[73] V. Potin, P. Vermaut, P. Ruterana, and G. Nouet. *Extended defects in wurtzite nitride semiconductors.* Electronic Materials **27**, 266 (1998).

[74] V. Potin, P. Ruterana, G. Nouet, R.C. Pond, and H. Morkoç. *Mosaic growth of GaN on (0001) sapphire: a high resolution electron microscopy and crystallographic study of dislocations from low angle to high angle grain boundaries*. Phys. Rev. B **61**, 5587 (2000).

[75] V. Potin. *Structure atomique des défauts dans les films minces de nitrure de gallium sur substrat alumine par microscopie électronique en transmission.* Thèse Doctorat de l'Université de Caen. (1999).

[76] A. Yamamoto, Y. Yamauchi, M. Ohkubo, and A. Hashimoto. *A comparative study of OMVPE-grown InN heteroepitaxial layers on GaAs(111)B and a-Al_2O_3 (0001) substrates.* J. Crys. Growth **174**, 641 (1997).

[77] H. Naoi, F. Matsuda, T. Araki, A. Suzuki, and Y. Nanishi. *The effect of substrate polarity on the growth of InN by RF-MBE.* J. Crys. Growth **269**, 155 (2004).

[78] A. G. Bhuiyan, A. Yamamoto, A. Hashimoto, and Y. Ito. *High temperature growth of InN on GaP (111)B substrate using a new two-step growth method.* J. Cryst. Growth **236**, 59 (2002).

[79] C. S. Gallinat, G. Koblmüller, J. S. Brown, and S. Speck. *A growth diagram for plasma-assisted molecular beam epitaxy.* J. Appl. Phys. **102**, 064907 (2007).

[80] Q. Guo, O. Kato, and A. Yoshida. *Thermal stability of indium nitride single crystal films.* J. Appl. Phys. **73**, 7969 (1993).

[81] Y. Kumagai, J. Kikuchi, Y. Nishizawa, H. Murakami, and A. Koukitu. *Hydride vapour phase epitaxy of InN by the formation of $InCl_3$ using In metal and Cl_2.* J. Cryst. Growth **300**, 57 (2007).

[82] T.L. Tansley and C. P. Foley. *Electron mobility in indium nitride.* Electonic Lett. **20**, 1066 (1984).

[83] T. Matsuoka, H. Tanaka, and A. Katsui Int. Symp. on GaAs and related compounds, Karuizawa, Japan (1989).

[84] A. Wakahara and A. Yoshida. *Heteroepitaxial growth of InN by microwave-excited metalorganic vapour phase epitaxy.* Appl. Phys. Lett. **54**, 709 (1989).

[85] W.E. Hoke, P. J. Lemonias, and D. G. Weir. *Evaluation of a new plasma source for molecular beam epitaxial growth of InN and GaN films.* J. Cryst. Growth **111**, 1024 (1991).

[86] K. Starosta. *RF sputtering of $Al_xIn_{1-x}N$ thin films.* Phys. Stat. Sol a **68** K55 (1981).

[87] K. Kubota, Y. Kobayashi, and K. Fujimoto. *Preparation and properties of III-V nitride thin films.* J.Appl. Phys. **66**, 2984 (1981).

[88] L. K. Teles, L. M. R. Scolfaro, and J. R. Leite. *Phase diagram, chemical bonds, and gap bowing of cubic $In_xAl_{1-x}N$ alloys: Ab initio calculations.* J. Appl. Phys. **92**, 7109 (2002).

[89] S. Fernández-Garrido, Ž. Gačević, and E. Calleja. *A comprehensive diagram to grow InAlN alloys by plasma-assisted molecular beam epitaxy.* Appl. Phys. Lett. **93**, 191907 (2008).

[90] Ž. Gačević, S. Fernández-Garrido, D. Hosseini, S. Estradé, F. Peiró, and E. Calleja. *InAlN/GaN Bragg reflectors grown by plasma-assisted molecular beam epitaxy.* J. Appl. Phys. **108**, 113117 (2010).

[91] W. K. Liu, and M.B. Santos. *Thin films: heteroepitaxial systems.* Vol 15. Ed World Scientific Publishing (1999).

[92] http://www.grin.com/en/doc/275972/overcoming-the-efficiency-droop-in-gallium-indium-nitride-light-emitting

[93] J. Wu. *When group-III nitrides go infrared: New properties and perspectives.* J. Appl. Phys. **106**, 011101 (2009).

Chapter 2

Experimental Techniques

In this chapter, we describe the fundamentals of the techniques that have been used along our work. The presented experimental equipments were available in different laboratories: CIMAP and CRISMAT in Caen, Institut des Nanociences de Paris, Laboratoire de Photonique et de Nanostructure (LPN) in Marcoussis, and Faculty of Physics in Sofia.

The InAlN samples studied in this work have been grown by metal organic vapour phase epitaxy (MOVPE) either in III-V labs (Marcoussis), and Aixtron (Germany) companies and Ecole Polytechnique de Lausanne (EPFL-Lausanne). The InN samples were grown using different deposition methods: molecular beam epitaxy (MBE) in Instituto de Sistemas Optoelectrónicos y Microtecnología (ISOM), Universidad Politécnica de Madrid (UPM-Madrid), MOVPE in Technische Universität Berlin (TUB-Berlin) and hydride vapour phase epitaxy (HVPE) in EPFL.

2.1 Growth techniques

As already discussed in *Chapter 1*, due to the lack of III-nitrides substrates, nearly all III-nitride based devices realised up to now have been grown on foreign substrates. Such heteroepitaxial growth is most often achieved using *c*-plane sapphire (α-Al_2O_3) substrates, and it was the majority of the samples investigated in this work.

2.1.1 Metal Organic Vapour Phase Epitaxy (MOVPE)

The MOVPE of III-nitrides became important in the early 1990s when Akasaki[1] and Nakamura[2] first demonstrated nitride-based light emitting diodes (LEDs). These results motivated a lot of groups to embark on research into the MOVPE of III-nitrides.

In MOVPE, organometallic precursors are transported using a carrier gas to a heated substrate where after decomposition they react to form a crystalline film with an epitaxial relationship to the substrate heated at high temperature (~950 °C). The precursors used for the group-III elements are trimethylgallium (TMG, $Ga(CH_3)_3$), trimethylaluminium (TMA, $Al(CH_3)_3$), and trimethylindium (TMI,

$In(CH_3)_3$),…. The organometallics are stored in bubblers, where the temperature is carefully selected to control the vapour pressure over the source material. A carrier gas, usually nitrogen or hydrogen, flows through the bubbler, saturating with the organometallic vapour and transporting it to the substrate. At the substrate surface, the group-III precursor reacts with a nitrogen source, most commonly ammonia (NH_3). The ratio of the NH_3 molar flow versus that of group III elements is called the V/III ratio, and constitutes an important parameter in MOVPE.

2.1.2 Molecular Beam Epitaxy (MBE)

MBE is one of the most advanced thin film deposition techniques, invented in the late 1960s in Bell Telephone Laboratories by A. Y. Cho and J. R. Arthur.[3]

Essentially, MBE is a well-controlled thermal deposition in an ultrahigh vacuum (UHV) chamber: the evaporated atoms should not interact with each other until they react at the substrate surface. Generally, the evaporation sources either solids or liquids kept in crucibles, and the vapour pressure can be controlled with the temperature; as it is possible to measure the resulting flux accurately, a very precise control of composition and growth rate is possible.

The UHV environment in an MBE system is achieved through a combination of various pumping technologies and cryopanels filled with liquid nitrogen, which tends to trap impinging molecules. The result is a background pressure below 10^{-10} torr. MBE also permits the use of in-situ monitoring techniques such as reflection high energy electron diffraction (RHEED), which are used to monitor the growth at the monolayer level.

The most important difference between MBE and MOVPE for growth of InN is the nitrogen source and lower growth temperature (500-580 °C). While MOVPE uses ammonia, MBE typically uses a nitrogen plasma. However, one of the problems associated with MBE is the difficulty to decompose the NH_3 at low growth temperature (700-800 °C) to form the nitrides alloys. To solve this problem, the classical MBE technique is modified to allow sources of active nitrogen species,

for instance by generating a nitrogen plasma, in which case it is called plasma assisted MBE (PA-MBE).

2.1.3 Hydride Vapour Phase Epitaxy (HVPE)

HVPE was the technique used by Maruska and Tietjen in 1969 to grow the first epitaxial GaN layers. At that time, a HCl vapour was flown over metallic gallium to form metallic chloride GaCl at high temperature about 900 °C :

$$2HCl_{(g)} + 2Ga \leftrightarrow 2GaCl_{(g)} + H_2\,(g)$$

Then GaCl reacted at the substrate with NH_3 to form the III-V compound (GaN, InN, AlN):

$$GaCl\,(g) + NH_3\,(g) \leftrightarrow GaN\,(s) + HCl\,(g) + H_2\,(g)$$

In general, the growth rate is determined by the HCl flux and probably by the source temperature. High growth rates (several microns per minute) can be achieved offering the possibility of preparing substantially thick films.[4] This process is a chemical vapour deposition method, which is usually carried out around the atmospheric pressure. For InN, the source materials generally used are indium monochloride (InCl) or indium trichloride ($InCl_3$)[5,6] and the growth temperatures are around 500 °C.

2.2 Characterisation techniques

2.2.1 Atomic Force Microscopy (AFM)

The surface morphologies and the roughness of InN and InAlN alloys were characterized by AFM. The AFM belongs to a series of scanning probe microscopes invented in the 1980s. This series started with the scanning tunnelling microscope (STM), which was invented by Binning *et al.*[7], and later, Binning, Quate and Gerber[8] developed the AFM.

In this technique, a tip is attached to the free end of a cantilever and is brought very close to a surface in order to scan the surface. The cantilever is typically silicon or silicon nitride. The movement of the tip or sample is performed by a device that provides precise control of position via piezoelectric ceramics.

Interatomic forces between the tip and the surface sample cause the deflection of the cantilever. The magnitude of the deflection is captured by a laser light reflected from the back of the cantilever. A plot of the laser deflection versus tip position on the samples provides information on the sample surface topography.[9]

There are three different modes that can be used to study the samples surface: (1) contact mode (the tip makes soft contact with the surface of the sample), (2) non-contact mode (the tip operates in the attractive region and the tip-sample interaction is minimized), and (3) tapping mode.

The tapping mode was developed by Digital Instruments (Fig 2.1). The cantilever oscillates on the sample surface at a frequency close to the resonance frequency of the tip (f_o = 271-319 kHz). Following the surface morphology, a constant oscillation amplitude is used as the feed back signal via the z displacement of the piezo ceramics. The amplitude image is obtained recording the variation of the root mean square (rms) of the amplitude before the feedback loop. The surface topography is represented by a height image.

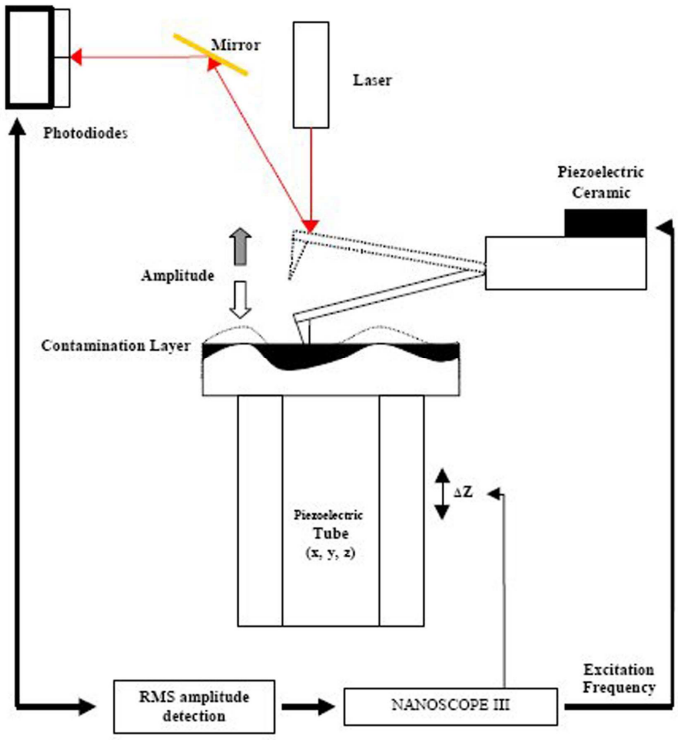

Fig 2.1 Schematic diagram of the tapping mode used for surface roughness measurements in AFM.[10]

The roughness parameters are determined on each image obtained in tapping mode (height image) and are defined as *Rq*, corresponding to the standard deviation of the z values within a given area and it is calculated by:

$$Rq = \sqrt{\frac{\sum (z_i - \bar{z})}{N}} \tag{2.1}$$

where $\bar{z}$ is the average of the z values within the given area, z_i is the z value of point i, and N the number of points i within the given area.

The instrument used in this work is a Nanoscope III from Digital Instruments and a silicon cantilever type was used.

2.2.2 High-Resolution X-Ray Diffraction (HRXRD)

In order to obtain information on the structural quality, on the lattice parameters, on the strain state of the layer, and on the composition of the InN and InAlN heterostructures, high resolution X-ray diffraction measurements using a triple axis diffractometer are necessary. Additionally, information about dislocation density was also obtained by HRXRD through the measurements of the tilt and twist. The notation high resolution refers to a low λ dispersion of the used x-ray beam ($\Delta\lambda/\lambda = 10^{-5}$-$10^{-4}$), a limited beam divergence ($\Delta\omega$ = 0.001-0.008°) and a very good 2θ resolution ($\Delta\theta$ = 0.001-0.003°).

2.2.2.1 Set up

The x-ray diffraction measurements were carried out using a Philips X'Pert MRD high-resolution diffractometer (Fig 2.2) at CRISMAT laboratory in Caen and requires:

(1) an X-ray beam is given by a ceramic tube (in general used with a point focus); if the x-ray tube is used with a line focus, an x-ray mirror can be placed after the x-ray source to collect the photons emerging from the line focus of the tube within an acceptance angle, forming an intense parallel beam with a very low divergence.

(2) Receiving slits are used to control the height and width of the incident X-ray beam or an analyser crystal between sample and detector can be inserted to limit the beam divergence (~3.5 x 10^{-3} °); indeed, the analyser crystal will only accept scattered x-rays that fall within its intrinsic diffraction width.

(3) 4-bounce (220)-Ge monochromator is used to obtain a monochromatic parallel incident beam with a x-ray wavelength corresponding to Cu$K_{\alpha 1}$ (λ = 1.54056 Å) and reaching a maximal resolution $\Delta\lambda/\lambda = 10^{-5}$.

(4) A goniometer where the sample under investigation is mounted.

(5) An x-ray detector.

The simplest kind of X-ray diffraction arrangement is the double crystal diffraction scheme which consists on a monochromator crystal and a sample crystal from which the diffracted intensity signal is registered depending on the angle of rotation of the sample. The addition of a further crystal to that scheme, a so called analyser crystal, makes it possible to resolve with high resolution the angular distribution of the beam diffracted by the sample. Such a diffraction scheme is called triple-axis diffraction setup.

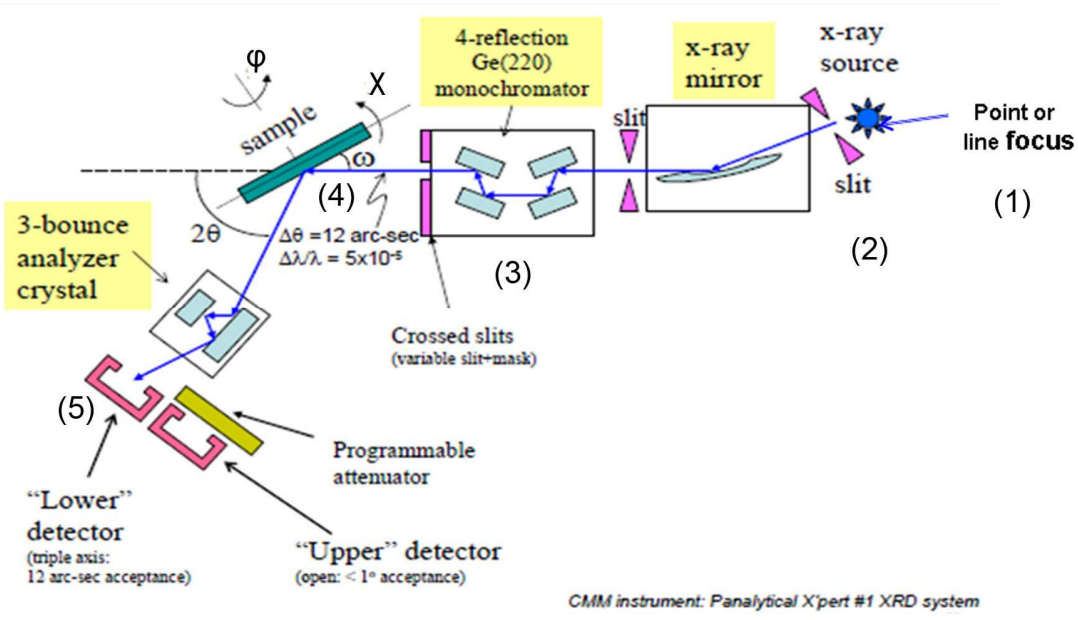

Fig 2.2 Schematic figure of the used HRXRD diffractometer.

The sample is mounted on the center of a platine making possible (x,y,z) translations inside an Eulerian Craddle allowing tilt (χ) and azimuthal (φ) sample rotations: χ is defined as the angle between sample surface and the horizontal plane (in the 0-90° range) and the azimuthal φ angle (in the 0-360° range) measures the rotation around the surface normal of the sample. The incident ω and diffracted 2θ angles are defined respectively between the X-ray source and the sample and between the incident beam and the detector angle.

2.2.2.2 *Scans in reciprocal space*

Fig 2.3 shows the different scan modes which can be used in HRXRD.

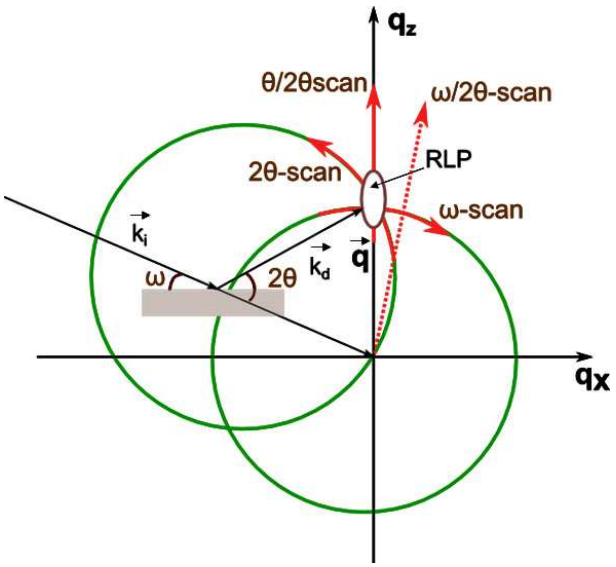

Fig 2.3 Schematic representation of the different scan modes of a reciprocal lattice point (RLP).

The scan modes available on high resolution diffractometers are described here, where $\vec{q}$ is the momentum transfer vector or the scattering vector defined as $\vec{q} = \vec{k}_d - \vec{k}_i$:

a) ***ω*-scan or rocking curve**: the sample is rotated at a fixed 2θ position and this corresponds to a scan perpendicular to the scattering vector $\vec{q}$ in the reciprocal space. In this configuration, $|\vec{q}|$ is constant but its direction changes slightly (related with the tilt angles).

b) ***ω-2θ*-scan or radial scan:** the scattering vector is moved radially. This requires a coupled movement of the sample (ω) and the detector (2θ). In reciprocal space, $\vec{q}$ moves outwards from the origin. The length of $\vec{q}$ changes , but its direction remains the same and depends on the offset = θ–ω. In this case, the orientation of the probing $\vec{q}$ vector has the same tilt angle with respect to the sample surface normal during the whole measurement. In the special case of $\omega = \theta$, the scan runs parallel to the normal surface (offset = 0 and tilt angle = 0).

c) ***θ -2θ*-scan:** it is a specific radial scan. In this geometry the incident beam hits the surface under the angle ω and the diffracted beam is detected under the same outgoing angle. By increasing the angle of incidence and the angle of detection simultaneously, the scattering vector, $\vec{q}$, is always normal to the surface but $|\vec{q}|$ is varied (Fig 2.4).

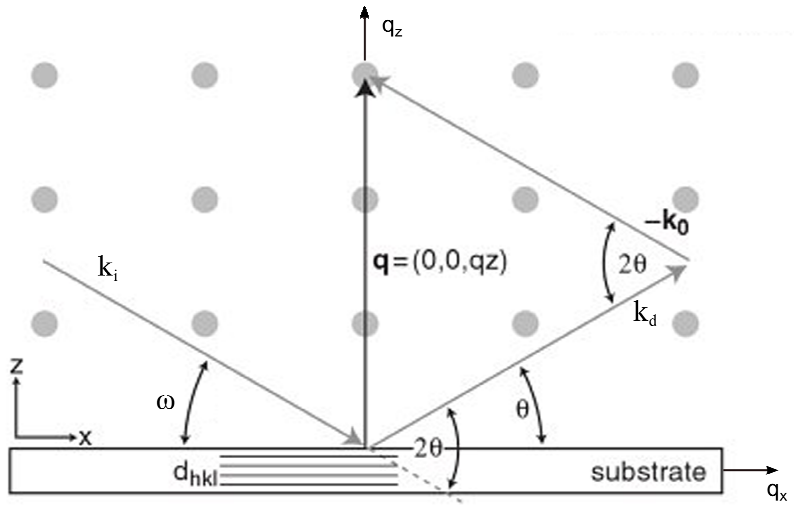

Fig 2.4 Representation θ-2θ scan in the reciprocal space.

Due to this geometry only the planes which are parallel to the surface of the sample can contribute to the diffraction ($\vec{q}$ has non zero component in the direction of the substrate normal noted q_z).

d) ***2θ*-scan:** in this configuration the 2θ is changing for a given ω angle.

e) **Reciprocal space map** (RSM) have recently gained attention due to the need for accurate determination of epitaxial structures quality. Indeed defects introduced in the structure will broaden a reciprocal lattice points (RLP) in two ways. First, compositional variations and/or strain in the lattice will locally change the lattice parameters, this change will be detected in θ-2θ-scan. Secondly mosaic spread in the sample will create extra intensity away from Bragg angle when rotating the sample axes (ω, 2θ). So, the shape of a given RLP carries information about the sample quality and is measured by RSM.

One way of mapping consists in performing various rocking curves with increasing scattering angle 2θ. Another technique makes use of successive radial scans (ω-2θ scans). In both cases, intensity map of the momentum transfer $\vec{q}$ area (RLP) around the Bragg reflection is obtained. The resulting data is plotted as a 2D contour plot with one axis representing a rotation in ω and the other representing the movement in $\theta/2\theta$. The contours represent equal diffracted intensity regions in reciprocal space.

f) φ-scan: Rotation of the sample about the φ axis (in the plane of the sample).

g) χ-scan: In this case the sample is rotated about the χ-axis.

A pole figure is a scan obtained by measuring the diffracted intensity (I) at different (χ, φ) angles for a specific Bragg angle. It is essentially a series of φ-scans at different χ-angles with the diffractometer Bragg angle value of (000ℓ) or $(h0\bar{h}\ell)$ reflections. The results I(χ,φ) are presented in 2D map and the HWHM of the (000ℓ) and $(h0\bar{h}\ell)$ pole figure will give access to the tilt and twist. Poles figures can be used to obtain orientation relationship between film and substrate. However, epitaxial relationship between InN or InAlN and their substrate are well known. So, pole figures of symmetric (000ℓ) and asymmetric $(h0\bar{h}\ell)$ reflections have been performed on InN films in order to determine respectively the tilt and twist in this films.

In this work, HRXRD has been used to extract:

(i) the *a* and *c* lattice parameters of the samples in order to calculate their residual stress (absolute lattice parameters measurements[11]).

(ii) the tilt and twist mosaic parameters in order to determine the screw and edge dislocation density, respectively.

2.2.3 Electron Microscopy

Defects in a crystalline material and their influence on its properties are essential to know. Thus, it is necessary to characterize both composition and microstructure at the highest levels of resolution in order to understand materials behaviour and to help towards the growth of improved materials. Such a characterization requires advanced methods of analysis using microscopic, diffraction, and spectroscopic techniques. In this regard the electron transmission microscope allows to obtain quantitative information on the crystal structure and chemical composition profiles of materials systems.

2.2.3.1 *Conventional Transmission Electron Microscope (TEM)*

There are two modes of TEM operation: diffraction and imaging.[12] As the beam of electrons passes through a crystalline specimen, it is scattered according to the Bragg's law. As the corresponding θ angles are very small, the Bragg law can be then written $2\, d_{h'k'l'}\, \theta = \lambda$. A schematic representation of the objective lens of the microscope is a convergent lens. Therefore, in its back focal plane, the transmitted electron beam gives an image of the sample at infinity which corresponds to the diffraction pattern. In order to see the diffraction pattern we have to adjust the imaging system lenses so that the back focal plane of the objective lens acts as the object plane for the intermediate lenses. Then the diffraction pattern is projected onto the viewing screen (Fig 2.5(a)). While for the imaging mode, we adjust the intermediate lens so that its object plane is the image plane of the objective lens. The image is then projected onto the viewing screen (Fig 2.5(b)).

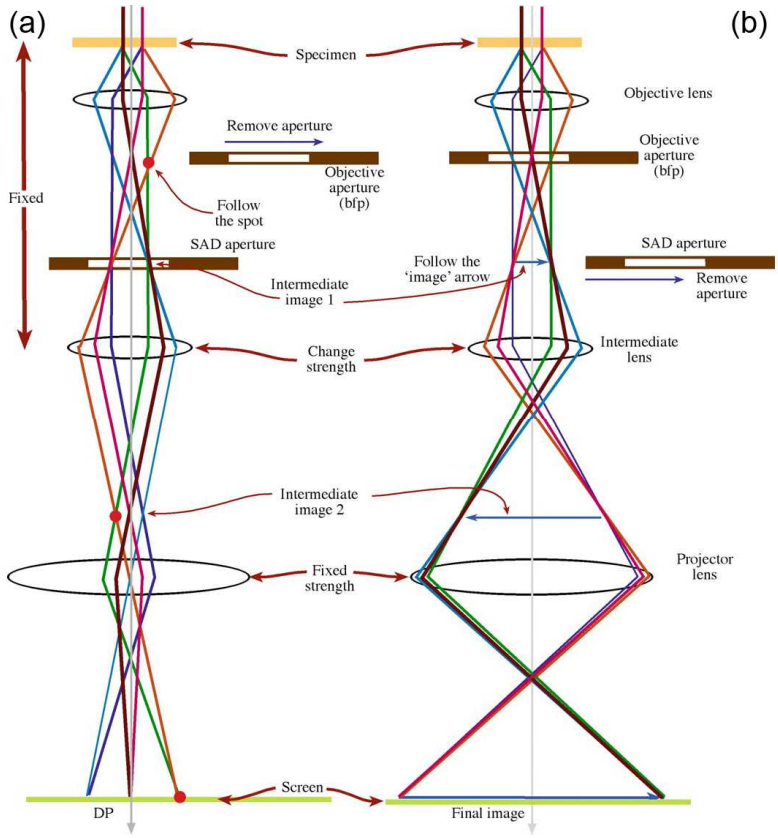

Fig 2.5 The two basic operations of TEM imaging system (a) diffraction pattern (b) image code.[12]

From the Fig 2.5(a), the diffraction pattern contains electrons from the whole area of the specimen that it is illuminated with the beam. There are two ways to reduce the illumination area: making the beam smaller or inserting an aperture above the specimen which would only permit electrons that pass through it to hit the specimen. In the real microscopes, this is done by inserting a diaphragm in a conjugate plane below the specimen (for instance the image plane of the objective lens). This operation is called selected area electron diffraction (SAED) and is performed in the following way: the specimen is first examined in the image mode until a region of interest is found. The aperture is then inserted in the image and positioned around the region interest. The microscope is then switched to the diffraction mode.

A) Bright field and dark field image

When the SAED pattern is projected onto the viewing screen, it is possible to use this pattern to perform the two basic operations in TEM: bright and dark field imaging which use only one spot in a diffraction pattern. The SAED pattern

contains a central spot, which corresponds to the direct electron beam. In order to form the bright and dark images, one uses respectively the central (transmitted) and a diffracted beam, respectively (Fig 2.6). In order to choose which electrons which finally form the image, an aperture is inserted in the objective lens back focal plane, blocking out most of the beams except those the visible through the aperture.

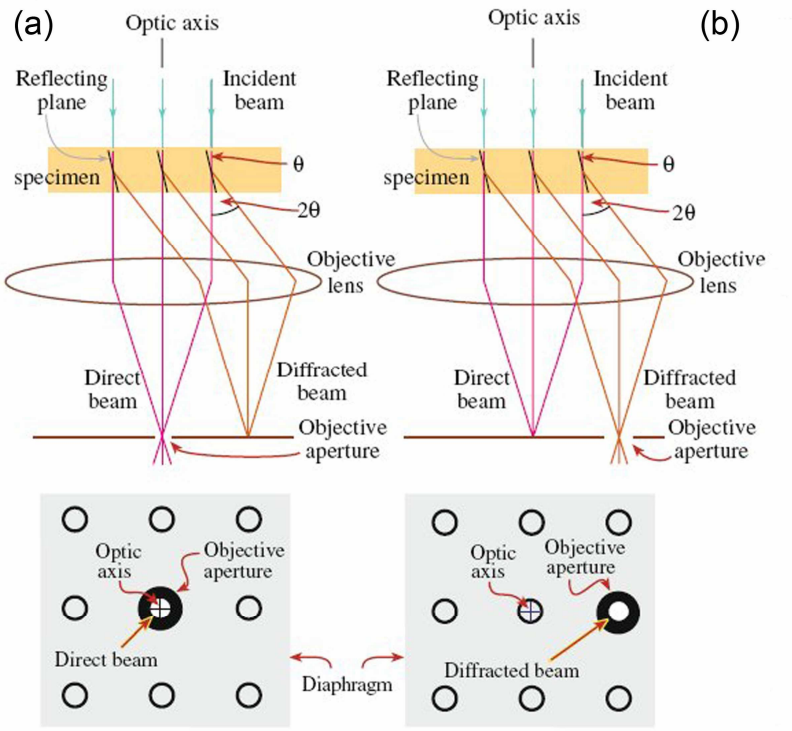

Fig 2.6 Ray diagrams showing (a) bright field image formed from the direct electron beam and (b) dark field image.[12]

B) Two beam and weak beam conditions

In order to obtain specific diffraction contrast in both bright and dark field images, the specimen has to be tilted to the so called two beam conditions, in which only one diffracted beam is strong along with the direct beam in the pattern. The electrons in the strongly excited *hkl* beam (**g**) is diffracted by the family of (*hkl*) planes at the Bragg conditions. This is realized by tilting the sample accordingly; in these conditions, the electron beam oscillates only between the two beams along its way through the samples. Such conditions are adequate for investigating the defect such as dislocations, as for instance those having a Burgers

vector perpendicular to the (*hkl*) will be visible in the images. However, such images exhibit strong contrast and rather poor resolution even for conventional TEM. The fine details of defect in conventional TEM are better imaged in weak beam conditions, especially when the so called –g/3g condition is realized. In this instance, the sample is first set to two beam conditions where +g and 0 are strongly excited, and then it is tilted further so that higher order beams are more excited than +g, in this instance +3g. The steps necessary to form a weak beam image are outlined in Fig 2.7 using the Ewald sphere construction and the Kikuchi lines in the bright and dark field. The sample is tilted away until the corresponding Kikuchi line crosses the 3g reflection. In this instance, the *g* reflection becomes weak and instead, the 3*g* reflection is strong (Fig 2.7(c)-(d)). Finally, the dark field corresponding image is formed using –g.

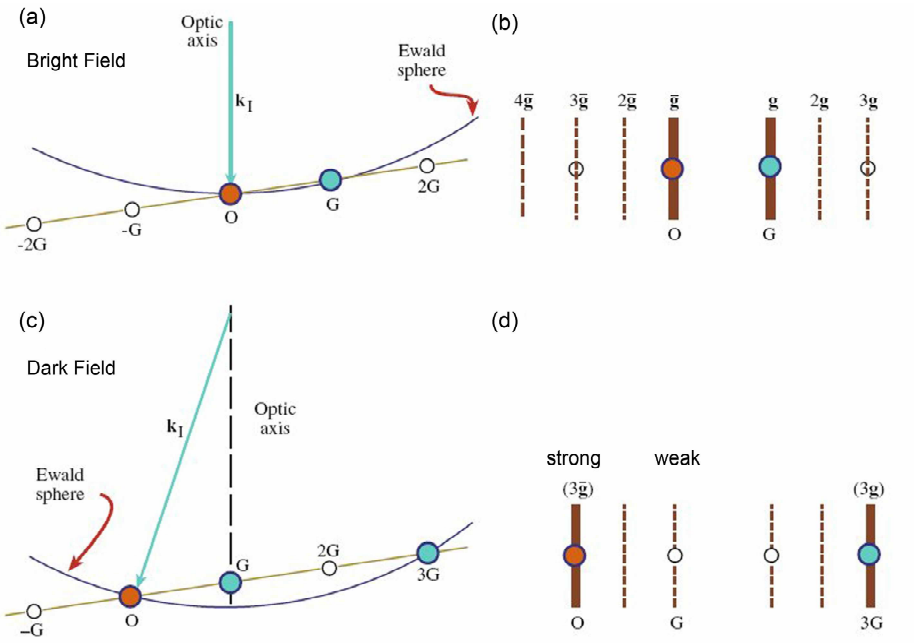

Fig 2.7 Relation between Ewald sphere and Kikuchi lines (a)-(b) bright field and (c)-(d) dark field.[12]

Important information which we need to extract from TEM images concerning dislocations is:

(i) the direction and magnitude of the Burgers vector, **b**, which is normal to the (*hkl*) diffracting planes

(ii) the line direction and therefore the character of the dislocation (edge, screw, or mixed)

(iii) the glide plane

(iv) the density of the dislocations

A general rule that used to determine the Burgers vector is the so called "**g**·**b** rule", which states that if the Burgers vector of the dislocation is perpendicular to the active diffraction vector, i.e. **g**·**b** = 0, there is no diffraction contrast from the dislocation, and it is thus not visible in the images (bright field and dark field).[13]

In the nitride epitaxial layers, the line direction of the threading dislocations is <0001>, then it is possible to determine the types of dislocations: the dislocations with Burgers vector of [0001], 1/3 $[11\bar{2}0]$, and 1/3 $[11\bar{2}3]$ are screw, edge and mixed type dislocations, respectively. Table 2.1 summarizes the visible and invisible criteria for these dislocations using the different *g* vectors, which are used for these dislocations analysis in cross section samples of nitrides samples.

Table 2.1 Values of **g**.**b** for perfect dislocations in wurtzite structure.

	g = 0001		**g** = $11\bar{2}0$		**g** = $10\bar{1}0$	
b = 1/3 $[11\bar{2}0]$	0	Invisible	2	Visible	1	Visible
b = 1/3 $[\bar{2}110]$	0	Invisible	-1	Visible	-1	Visible
b = 1/3 $[1\bar{2}10]$	0	Invisible	-1	Visible	0	Invisible
b = [0001]	1	Visible	0	Invisible	0	Invisible
b = $[000\bar{1}]$	-1	Visible	0	Invisible	0	Invisible
b = 1/3 $[\bar{2}113]$	1	Visible	-1	Visible	-1	Visible
b = 1/3 $[11\bar{2}3]$	1	Visible	2	Visible	1	Visible
b = 1/3 $[11\bar{2}3]$	1	Visible	2	Visible	1	Visible

The TEM analysis in this work was performed at CIMAP using a JEOL-2010 TEM operating at 200 kV.

2.2.3.2 *Scanning TEM (STEM)/High Angle Annular Dark Field (HAADF)*

The sensitivity of STEM-HAADF imaging to the specimen chemistry makes it a powerful tool for analytical application at the highest spatial resolution. One of the interest of this technique is the possibility to investigate the chemical composition in a film (for instance in our case InAlN), or in the study of the chemistry of the interface between two materials.

STEM-HAADF imaging offers Z contrast which is directly related to the atomic number. To form a STEM image, the beam is scanned on the specimen. Fig 2.8 shows a schematic of a STEM-HAADF system. The scattered beam is collected by an annular detector to form dark field (ADF) STEM image, and the direct beam can be selected by a bright field detector to form BF-STEM images. When the inner angle of an annular detector is more than three times larger than the objective aperture, called high angle annular dark field (HAADF) detector, the intensity of the image can be directly correlated to atomic number Z (Z-contrast).[14] Such a detector gives an image that integrates the total scattered intensity reaching it for each position of the electron probe.[15] The dependence of Z contrast on the detector geometry was investigated theoretically by Hartel *et al.*[16], who pointed out that, for thin objects, an analytical expression for Z dependence of image intensity can be approximated by an exponential function of the form $I \sim Z^{\alpha}$, where α is smaller than 2 and in the range 1.6-1.9 for most cases.[13]

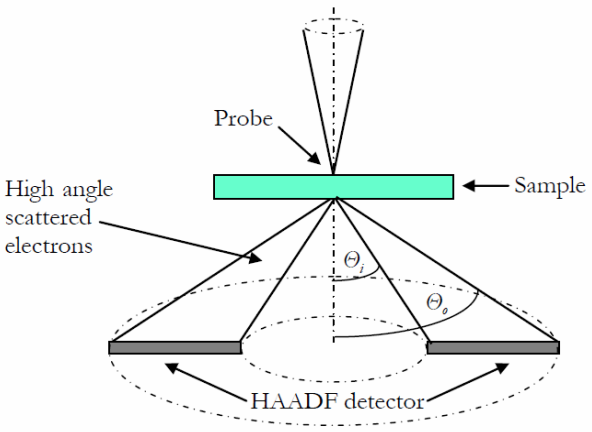

Fig 2.8 Schematic of the STEM-HAADF system configuration. The probe is rastered across the sample and high angle scattered electrons are collected by an annular detector with an inner collection angle θ_i and an outer collection angle θ_0.

In a HAADF micrograph, bright spots typically represent atomic columns, and the intensity is higher at columns of heavy atoms.

STEM-HAADF experiments were performed in a Jeol 2200 FS TEM, equipped with a corrector of the spherical aberration of the probe in Marcoussis.

2.2.3.3 *Energy Dispersive Spectroscopy (EDS)*

EDS analysis carried out at the same time as the STEM observations, and it is used to determine the specimen local composition. The impact of the electron beam on the sample produces X-rays that are characteristic of the atoms which interact with the beam. The EDS detector measures the number of emitted X-rays versus their energy. For quantification at 1% accuracy, known references should be used, and the best results will be obtained when the reference composition and structure are not very different from the analyzed samples, as it helps to correct the matrix effects on the fluorescence and absorption of the X-rays.

2.2.3.4 *TEM sample preparation*

The sample preparation is an important prerequisite for TEM observations, because the specimen has to be transparent to the electron beam. During this work the samples were prepared by two different ways. The first called mechanical polishing and the second, the tripod polishing. There are common steps in both methods.

Mechanical polishing

For the cross sectional sample, first the InN or InAlN specimen is cut in two pieces with the desired dimensions (2.1 mm wide and 1 cm long). The two pieces are glued by the top surface constituting the "sandwich structure" (Fig 2.9(a)). This sandwich is introduced in a press in order to reduce the thickness of the glue. After this procedure the sandwich is introduced into a hollow cylinder, and fixed inside it with glue (Fig 2.9(b)-(c)). The whole is then slipped into another hollow cylinder (Fig 2.9(d)) and fixed again with glue (Fig 2.9(e)). Finally 800 μm slices are cut by diamond wire giving small disks of 3 mm diameter.

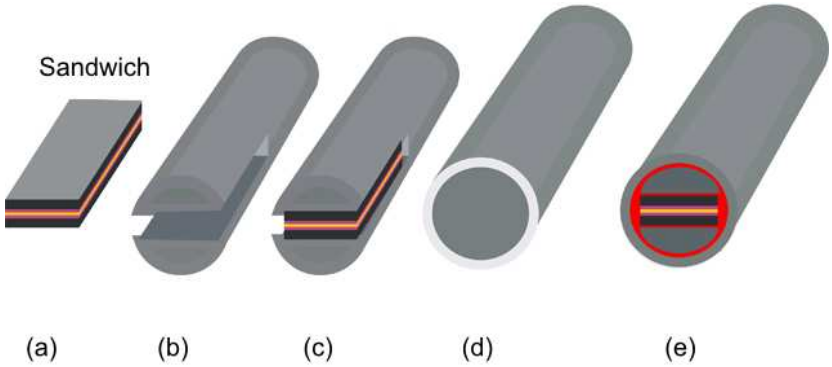

Fig 2.9 Illustration cross section sample mounting(a) sandwich (b) first cylinder (c) sandwich into the cylinder (d) in this second cylinder is put the first cylinder with the sample (d) final mounting.[17]

The next step is to polish the slices using silicon carbide paper with decreasing grade to minimize surface scratches until the specimen has a ~380 μm thickness, then, the second side is polished in the same way, until the specimen is 80 μm thick. Finally, the slice is dimpled from both sides by a Gatan Dimple Grinder down to less than 10 μm.

For plan view samples, one square piece (2.1 mm x 2.1 mm) is cut out and polishing until 40 μm, in this type of sample preparation, only the back side is dimpled until 10 μm.

Tripod polishing

In this method, the sandwich is prepared from two pieces with dimensions: 800 μm wide and 3 mm long. This time the structure is piece-glue-piece. The sandwich is mounted on the tripod polisher in order to polish the first side (Fig 2.10(a)). This polishing is carried out with the use of a diamond paper with different grain size (30 μm, 15 μm, 9 μm, 6 μm, 3 μm, 1 μm and 0.5 μm). After attaining a mirror polished surface, the specimen is turned over and the polishing is resumed in the same way, until the thickness becomes less than 10 μm with no scratches. Finally, the sample is glued on a copper grid (Fig 2.11).

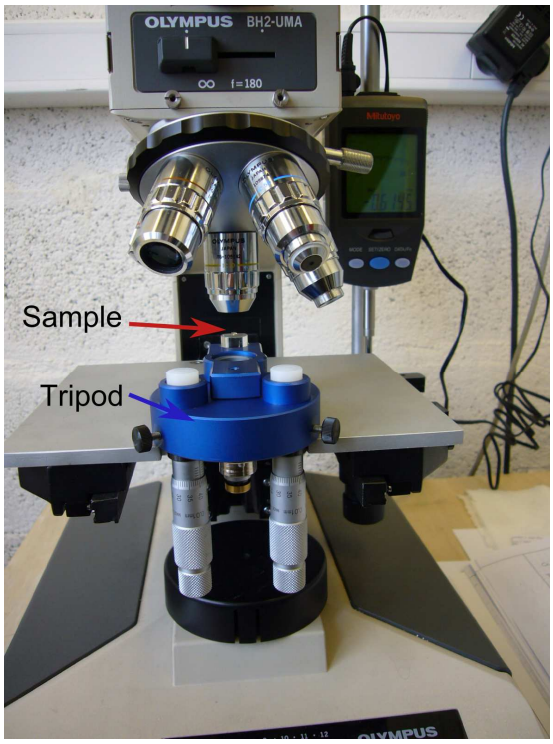

Fig 2.10 Tripod used for the sample preparation.

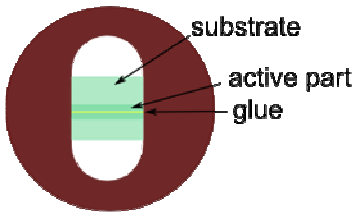

Fig 2.11 Sample glued on a copper ring.

The last step of TEM sample preparation is ion beam milling in the Gatan PIPS (precision Ion Polishing System) equipped with a LN_2 cooling stage to prevent sample damage. The ion beam energy and incident angle (top/bottom) are 5 keV and 5 ° with until the sample has an electron transparent area, respectively. Finally, the specimens are cleaned using 0.7 keV at room temperature in order to decrease the thickness of amorphous layer produced during the ion beam.

2.2.4 Ion Beam Analysis

Ion beam analysis (IBA) comprises a suite of analytical techniques based on ion-matter interactions. The techniques use high-energy ion beams (MeV) of light elements (H^+, H_2^+, He^+....) provided by particle accelerators. In this work, we used two techniques: Rutherford backscattering spectroscopy (RBS) and nuclear reaction analysis (NRA).

2.2.4.1 *Rutherford Backscattering Spectroscopy (RBS)*

Rutherford Backscattering (RBS) is based on collisions between atomic nuclei and derives its name from Lord Ernest Rutherford, who in 1911 was the first to present the concept of atoms having nuclei. It involves measuring the number and energy of ions in a beam which backscatter after colliding with atoms in the near-surface region of a sample at which the beam has been targeted.

RBS is the most popular IBA technique because of its versatility and power. Actually, RBS is fast, non destructive and quantitative for the composition depth-profiling of materials, and it can be performed in the channelling geometry for probing the single crystal structural quality (RBS/C).[18]

In RBS, monoenergetic incident beam particles ($^4He^+$) hit target atoms (sample) and are scattered into a detector located at certain angle θ (scattering angle) in order to measure their energies (Fig 2.12).

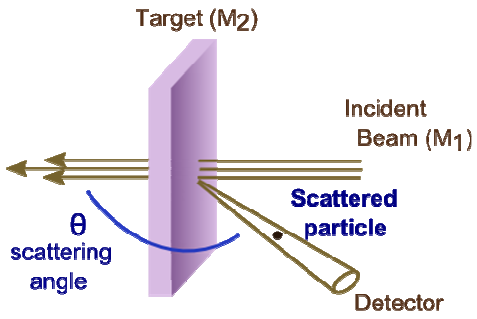

Fig 2.12 Experimental setup RBS.

In a collision event, the energy is transferred from the incident particle (M_1) to the target atom (M_2), and the resulting reduction in energy of the scattered particle depends on the masses of incident particles and target atoms.

The energy transfers or kinematics in elastic collisions between two isolated particles (M_1 and M_2) can be solved by applying the principles of conservation of energy and momentum. After the elastic collision, the values of the velocities v_1 and v_2 and energies E_1 and E_2 of the incident ion beam and target atoms are determined by the scattering angle θ and recoil angle Φ. The notations and geometry are given in Fig 2.13.

Such elastic processes can be treated within the classical mechanics framework since the involved velocities are not too high (for a 2 MeV incident ion the beam we have velocities of 0.033c).

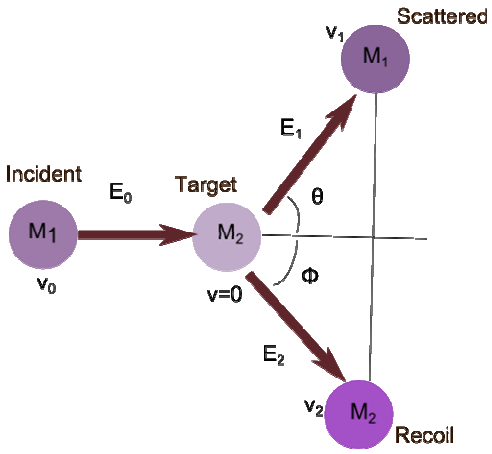

Fig 2.13 Illustration about the collisions.

The conservation of energy and momentum leads then to the relations:

$$E_1 = k\,E_2 \quad (2.2) \quad \text{with} \quad k = \frac{E_1}{E_0} = \left[\frac{\left(M_2^2 - M_1^2 \sin^2\theta\right)^{1/2} + M_1\cos\theta}{M_2 + M_1}\right] \qquad (2.3)$$

where k is the kinematic factor (lower than 1), E_0 is the energy of the incident ion with mass M_1, E_1 the energy of the backscattered ions, M_2 the mass of the target atom and θ the scattering angle. The angular dependence of k for different atoms indicates that the largest separation between elements is obtained for θ = 180 ° (best mass resolution); this is why in the experimental chambers the detectors are placed in backscattering geometry (in general ~165 °).

The identification of target atoms is then made by the analysis of the energy of the scattered particles following the elastic collision. Once the identification of the individual elements of the target is known, the second aspect to consider in RBS is how to quantify their concentration. The number of detected backscattered particles (called yield, Y) will be proportional to the number of incident particles or dose (Q), to the solid angle of the detector (Ω), and to the layer thickness (Ns) in

at/cm^{-2}. All these factors can be determined experimentally; moreover, this yield also depends on the scattering probability (in atoms/cm^2) : $Y(\Omega) = Q\left(\frac{d\sigma}{d\Omega}\right)\Delta\Omega$ Ns (2.4). Indeed, atoms with different masses have different scattering probabilities because the Coulombic potential depends on the atomic number and, therefore, the repulsing force will be higher for heavy elements than for light ones. The physical quantity representing the scattering probability is the differential scattering cross section (dσ/dΩ), and it is the essential parameter to consider for the calculation of the target element concentration. The differential cross section can be expressed as:[1920]

$$\frac{d\sigma}{d\Omega} = \left(\frac{Z_1 Z_2 e^2}{4E}\right)^2 \frac{4\left(\left(1-\left((M_1/M_2)\sin\theta\right)^2\right)^{1/2}+\cos\theta\right)^2}{(\sin\theta)^4\left(1-\left((M_1/M_2)\sin\theta\right)^2\right)^{1/2}} \qquad (2.5)$$

where Z_1 and Z_2 are the atomic numbers of the incident ion and the target atom, E is the energy of the incident ion immediately before scattering, and e is the electronic charge. A rule of thumb is that the scattering cross section is basically proportional to the square of the atomic number Z of the target species. This means that RBS is more than a hundred times more sensitive for heavy elements than for light elements, such as nitrogen. Then, for the simplest case of RBS on a thin film under normal incidence, N_s can be calculated as $N_s = Y/Q\sigma\Omega$, where σ is the average cross section coinciding with dσ/dΩ for low Ω.

So, in the case of one layer with two elements A and B, it is possible to determine its composition with the relation:

$$\frac{N_A}{N_b} = \frac{Y_A}{Y_B} \times \frac{\sigma_B}{\sigma_A} \qquad (2.6)$$

where N_A and N_B is the atomic number of A and B elements per surface, respectively. Y_A and Y_B correspond to the area under the well separated peaks of

each element (A and B constituting the target) and σ_i are the cross section for both elements (i= A or B).

However, this formula is a surface approximation where a constant energy of particles is assumed. To take into account this effect, the stopping power variable that is the energy loss per length (ΔE) due to the interaction with the surrounding atoms as the particles penetrate in the sample, must be introduced. The stopping power is the physical link between energy and depth and therefore is the mechanism providing depth resolution to RBS (Fig 2.14).

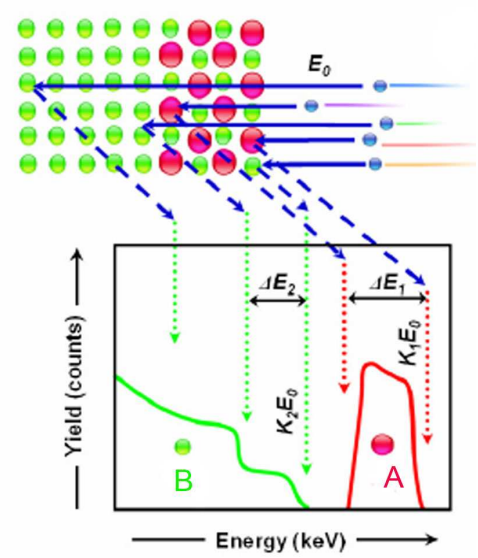

Fig 2.14 Representation of an RBS spectrum for the simple case of two layers.[19]

As shown in Fig. 2.14, for a complete analysis of an RBS spectrum obtained in the simple case of a bilayer with two elements $M_1 > M_2$, with M_2 belonging to the two layers, the kinematic factor, the stopping power and the cross section must be considered. To this end, there are many commercial programs that are available in order to simulate the experimental data such as SIMNRA, RBX etc,... In this work, the SIMNRA software has been used for which the fitting is done by a certain layer structure and comparing the simulation result with the experimental data in an iterative process. The main fitted data obtained in SIMNRA using a simplex algorithm are layer thicknesses and compositions.

The RBS measurements in this work were performed using the 2.5 MeV Van de Graaff–type accelerator located at the Institute of NanoSciences in Paris

(INSP). The RBS data were obtained using a 1.6 MeV $^4He^+$ with a normal incidence and a scattering angle (θ) of 165 °. In this work, a standard sample consisting on Bi implanted in Si layer with N_{SiBi} = 5.6 x 10^{15} at·cm^{-2} is used as reference in order to establish in particular the relationship between the detector channel and the ion energy, and to determine the solid angle (Ω) of the detector.

Ion channelling (RBS/C)

When measuring single crystalline materials, RBS can be carried out with the beam aligned along a major crystallographic direction (RBS/C). Then, in addition to elemental composition information, RBS also can be used to study the crystal quality of epitaxial films and their strain state. When a sample is channelled (Fig 2.15), the rows of atoms in the lattice are aligned parallel to the incident He ion beam. The bombarding He will be backscattered from the first few monolayers of material at the sample rate as a non-aligned sample, but backscattering from buried atoms in the lattice will be drastically reduced, since these atoms are shielded from the incident particles by the atoms in the surface layer. By measuring the reduction in backscattering when a sample is channelled, it is possible to quantitatively access to the sample crystal perfection.

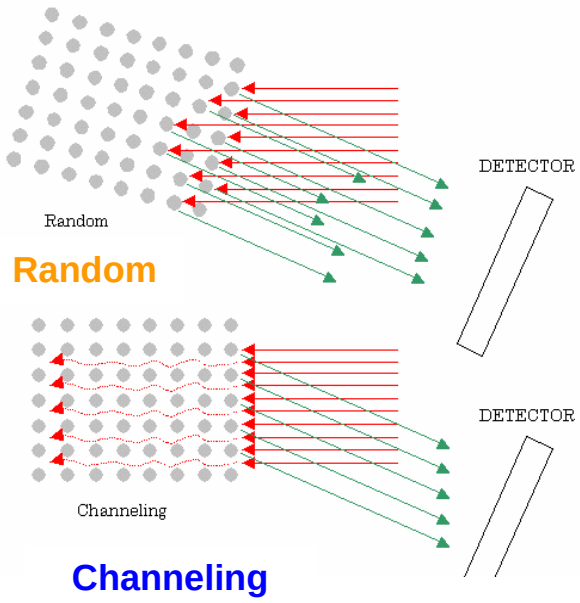

Fig 2.15 Illustration about the random and channelling conditions.

The ratio of the backscattered yield of aligned and random yields is called minimum yield, χ_{min}. The determination of χ_{min} requires only two spectra, one in random configuration and the other in aligned geometry. Since this calculation can be carried out for different elements and at different energy window, RBS/C provides very useful information about crystal quality with depth resolution. In our layers, the growth direction was <0001>, therefore, the crystal quality was checked for this direction. The χ_{min} is determined by the integration of the aligned and random yields for a given energy (so for a given element). χ_{min} calculation provides method to highlight the crystalline quality. Indeed, channelling based techniques have a high sensitivity to any lattice perturbation such as extended defects, strain, impurities, phase separation or implantation damage.[19]

2.2.4.2 Nuclear Reaction Analysis (NRA)

The sensitivity and resolution of RBS to specific light elements can be greatly enhanced by NRA. This method uses accelerated particles which induce nuclear reactions with specific target atoms in the sample. The energy of detected reaction product (secondary ion) is characteristic of target nucleus. Such reactions can be considered as the counterpart of RBS for light target nuclei and the difference between the two techniques is the method by which the particles entering the detector are produced. Despite these differences, the analysis of the data is similar. So, as in RBS, from the yield of the peak one is able to determine the concentration of the light elements and the width of the peak can be correlated to the target depth. Most of the reactions use deuteron beams because they provide the highest yield. In this work, the ion-ion nuclear reaction $^{14}N(d,\alpha)^{12}C$ was used for the determinations of the depth profile of N in our InN epitaxial layers. The corresponding spectra recorded with incident deuteron energy of 1450 KeV were fitted using also the SIMNRA program.

2.2.4 Raman Spectroscopy

Raman spectroscopy is an optical characterization technique which determine the lattice vibrations of a material by analyzing the inelastic scattered

radiation generated during the interaction with an incident laser light. Such vibrational frequencies (Raman active modes) provide a unique insight on the forces responsible for the chemical bonding. Therefore, Raman spectroscopy is a powerful technique to investigate the quality of all types of materials from elemental molecules to crystalline solids. In a particular layer, shifts in position of each mode as well as additional modes can take place. They may originate from stress, carrier concentration, polarization condition and quality of the crystal in general, etc,...

The wurzite structure (space group-$P6_3mc$; point group C_{6v}) has six optical Raman-active phonons modes: E_2 (high), E_2 (low), E_1 (LO), E_1 (TO), A_1 (TO) and A_1 (LO). In Table 2.2, the position of these Raman active phonons are shown for wurtzite InN, GaN and AlN.

Table 2.2 First order Raman active phonon frequency (cm^{-1}) of wurtzite InN, GaN, and AlN.

C_{6v}	Active in	InN frequency mode (cm^{-1})[21]	GaN frequency mode (cm^{-1})[22]	AlN frequency mode (cm^{-1}) [21]
A_1 (TO)	IR, Raman	447	531.8	611
A_1 (LO)	IR	586	734	890
B_1 (low)	silent			
B_1 (high)	silent			
E_1 (LO)	IR, Raman	593	741	912
E_1 (TO)	IR, Raman	476	558.8	670.8
E_2 (low)	Raman	87	144	6
E_2 (high)	Raman	488	567.6	657.4

(LO= longitudinal Optical; TO = Transverse Optical, IR = Infrared)

The two InN-related modes observed at 488 and 586 cm^{-1} have been assigned to the long wavelength E_2 and A_1 (LO) phonons of InN, respectively.[23] In particular, to analyze the structural quality, the strain as well as free carrier concentration in InN layers, the two optical phonon modes of hexagonal InN, E_2 and A_1(LO), have been studied in more detail in *Chapter 3.* Indeed, on one hand

the FWHM of the E_2 (high)-phonon mode is an indicator of the crystalline quality (when this valour decreases, the crystalline quality of InN is improved) and it is also known to be sensitive to strain. On the other hand, the A_1 mode strongly interacts with the conduction band electrons and the magnitude of this interaction depends on the free electron concentration.[24]

MicroRaman measurements were carried out using a Labram 800HR facility, equipped with an optical microscope. The excitation source was a He-Ne diode laser that emits at 633 nm. The experiments were conducted in the backscattering $z(x,-)\bar{z}$ configuration, with the InN film *c*-axis parallel to the *z* direction at the Faculty of Physics of Sofia University (Bulgaria).

References

[1] I. Akasaki, H. Amano, K. Iitoh, H. Sakai, T. Tanaka, and K. Manaba. *Inst. Phys. Conf. Ser.* **129**, 851 (1992).

[2] S. Nakamura, T. Mukai, and M. Senoh. *Candela-class high-brightness InGaN/AlGaN double heterostructure blue-light-emitting diodes.* Appl. Phys. Lett. **64**, 1687 (1994).

[3] A. Y. Cho, and J. R. Arthur. *Molecular beam epitaxy.* Progress in Solid State Chemistry **10,** 157 (1975).

[4] P. Gibart. *Metal organic vapour phase epitaxy of GaN and lateral overgrowth.* Reports on Progress in Physics **67**, 667 (2004).

[5] N. Takahashi, J. Ogasawara, and A. Koukitu. *Vapor phase epitaxy of InN using InCl and $InCl_3$ sources.* J. Cryst. Growth. **172**, 298 (1997).

[6] Y. Kumagai, J. Kikuchib, Y. Nishizawab, H. Murakamia, and A. Koukitua. *Hydride vapour phase epitaxy of InN by the formation of $InCl_3$ using In metal and Cl_2.* J. Cryst. Growth. **300**, 57 (2007).

[7] G. Binning, H. Rohrer, Ch. Gerber, and E. Weibel. *Surface studies by scanning Tunneling Microscopy* Phys. Rev. Lett. **49**, 57 (1982).

[8] G. Binning, C. F. Quate, and Ch. Gerber. *Atomic Force Microscope.* Phys. Rev. Lett. **56**, 930 (1986).

[9] B. Bhushan. *Springer Handbook of Nanotechnology.* Ed. Springer (2005).

[10] http://www.biophyresearch.com/pdf/afm_uk.pdf

[11] P. F. Fewster, and N. L. Andrew. *Strain analysis* by X-ray diffraction. Thin solid film. **318**, 1 (1998).

[12] D. B. Williams, and C. B. Carter. *Transmission Electron Microscopy.* Ed. Springer. (2009).

[13] B. Fultz, and J. M. Howe. *Transmission electron microscopy and diffractometry of material.* Ed. Springer (2009).

[14] S. J. Pennycook. *Z-contrast STEM for materials science.* Ultramicroscopy **30**, 58 (1989).

[15] P. Hartel, H. Rose, and C. Dinges. *Conditions and reasons for incoherent imaging in STEM.* Ultramicroscopy **63**, 93 (1996).

[16] S.J. Pennycook, and P. D. Nellist. Scanning Transmission Electron Microscopy. Ed. Springer (2011).

[17] www.temsamprep.in2pe.fr

[18] L. C. Feldman, J. W. Mayer, and S. T. Picraux. *Materials analysis by ion channelling.* Academic Press, New York (1982).

[19] W.-K. Chu, J.W. Mayer, M.A. Nicolet.*BackscatteringSpectrometry*, Academic Press, Boston, (1978).

[20] A. Redondo-Cubero. *Structural and compositional characterization of wide bandgap semiconductor heterostructures by ion beam analysis,* PhD Universidad Autónoma de Madrid, (2010). http://digital.csic.es/bitstream/10261/32095/1/ARC_PhD_100709.pdf

[21] V. Y. Davydov, Y. E. Kitaev, I. N. Goncharuk, A. N. Smirnov, J. Graul, O. Semchinova, D. Uffmann, M. B. Smirnov, A. P. Mirgorodsky. *Phonon dispersion and Raman scattering in hexagonal GaN and AlN.* Phys. Rev. B **58**, 12899 (1998).

[22] V. Y. Davydov, V. V. Emtsev, I. N. Goncharuk, A. N. Smirnov, V. D. Petrikov, V. V. Mamutin, V. A. Vekshin, and S. V. Ivanov. *Experimental and theoretical studies of phonons in hexagonal InN.* Appl. Phys. Lett. **75**, 3297 (1999).

[23] V. Y. Davydov, N. S. Averkiev, I. N. Goncharuk, D. K. Nelson, I. P. Nikitina, A. S. Polkovnikov, A. N. Smirnov, M. A. Jacobson, and O. K. Semchinova. *Raman and photoluminescence studies of biaxial strain in GaN epitaxial layers grown on 6H-SiC.* J. Appl. Phys. **82**, 5097 (1997).

[24] F. Demangeot, C. Pinquier, J. Frandon, M. Gaio, O. Briot, B. Maleyre, S. Ruffenach, and B. Gil. *Raman scattering by the longitudinal optical phonon in InN: wave-vector nonconserving mechanisms.* Phys. Rev. B **71**, 104305 (2005).

Chapter 3

InN layers

The first part of this chapter deals with the Raman and TEM measurements of InN films grown by different techniques (HVPE, MOVPE and PA-MBE). The second part deals with the characterization of InN-MBE films using HRXRD, IBA techniques and TEM. The strain of the InN films is analysed and attempt is made to correlate the density of dislocations measured by TEM and that extracted from the mosaic structure model by HRXRD.

3.1 Introduction

One of the main issues with the development of InN is the ability to grow single crystalline films. The large lattice mismatch of InN with the available substrates (GaN (11 %), AlN (13.7 %), sapphire (29.2 %), Si (8 %),...), its low dissociation temperature, coupled with its tendency to form misoriented domains, makes the epitaxy of this material complicated.[1]

Despite the problems inherent to InN growth, some works have been reported on InN films deposited by various techniques such as sputtering,[2,3] HVPE,[4,5] pulsed laser deposition (PLD),[6] MOVPE;[7] until now, the best results have been attained by MBE.[8] However, the choice of the optimum growth process, the ideal substrate and the respective growth parameters are still under discussion.

In MOVPE, a relatively high reactor pressure, and V/III ratio in the 3300-24000 range and a growth temperature of 550 °C have been reported to lead to the highest MOVPE InN crystalline quality.[7,9] In HVPE, growth temperatures of around 450-510 °C with V/III ratios of 500 to 2000 have been used for the synthesis of InN layers.[5,10] In MBE, due to the much lower growth pressures (~10^{-7} Torr), the deposition needs to takes place as close as possible to the V/III stoichiometric ratio, the temperature being close or just below 500 °C.

The knowledge of strain in these films is of crucial importance for device fabrication since lattice strain generating point and/or extended defects has a strong impact on band gap energy, dielectric tensor and carrier mobility.[11]

3.2 The samples

The investigated samples in this chapter were grown by three different techniques: HVPE, MOVPE and PA-MBE. The thickness of the InN ranged from 0.64 to 2 μm for HVPE samples, from 100 to 300 nm for MOVPE, and from 150 to 750 nm for the MBE layers. All the samples were grown on Al_2O_3 substrates or GaN/Al_2O_3 buffer layer, except for two where Si (111) substrate was used. In this case, Si substrates were used in order to test the adequacy of InN/Si heterostructures for possible integration in the standard Si based technological platform. However the corresponding films exhibit bad crystalline quality in comparison to the ones deposited on sapphire. An AlN buffer layer has been added in order to improve their quality (R117 and R135). Table 3.1 describes all the studied samples, as well as a number of experimental data (nominal thickness, growth rate and temperature).

Table 3.1 Samples under study.

	Delivered Number	Description	Nominal InN thickness (nm)	Growth rate (nm/h)	Temperature growth (°C)
HVPE	1267	$InN/GaN/Al_2O_3$	2000	2000	520-567
	1269	$InN/GaN/Al_2O_3$	1000		
	1270	$InN/GaN/Al_2O_3$	1500		
	1273	$InN/GaN/Al_2O_3$	1500		
	1278	InN/Al_2O_3	640		
MOVPE	EG1937	InN/Al_2O_3	100	100	530-560
	EG1779	InN/Al_2O_3	200		
	EG1822	InN/Al_2O_3	250		
	EG1859	$InN/GaN/Al_2O_3$	300		
PA-MBE	R374	$InN/GaN/Al_2O_3$	150	480	400-490
	R593 (N-rich)	$InN/GaN/Al_2O_3$	250		
	R489	$InN/GaN/Al_2O_3$	250		
	R338	$InN/GaN/Al_2O_3$	400		
	R512	$InN/GaN/Al_2O_3$	750		
	R117	InN/AlN/Si (111)	350		
	R135	InN/GaN/AlN/Si (111)	450		

3.2.1 Raman and microstructure analysis

In order to investigate the structural quality of the InN layers, Raman spectroscopy was carried out in all the epilayers. We investigated the E_2 and A_1 (LO) phonon modes of wurtzite InN.[12] The energy position of the E_2 phonon mode is sensitive to the strain. The value of 491.0 cm^{-1} has been proposed as strain-free peak position for E_2 by many authors.[13,14] This value will be used for the calculation of the residual stress in our samples.

Moreover, this phonon mode can also be used to characterize the crystalline quality of the InN layers. Indeed, a detailed E_2 mode shape analysis gives information on the sample quality: for example, the presence of extended defects (such as dislocations, stacking faults,...)[15] and the loss of long range periodicity results in phonon confinement causing a considerable broadening of this peak.

In the wurtzite structure, the polar A_1 (LO) mode is very sensitive to doping effects via the interaction between collective oscillations of free electrons and phonons. The investigation of the coupled modes, denoted LO phonon–plasmon coupled mode ($LOPC^+$ and $LOPC^-$ for upper and lower frequency branches, respectively), has already been used for the estimation of free electron concentration in GaN.[16] In this instance, the Raman spectrum of the system (lattice and electrons) exhibits two additional modes $LOPC^+$ and $LOPC^-$, the corresponding peak positions are then given by:

$$\omega_{\pm}^2 = \left\{ \omega_L^2 + \omega_p^2 \right\}/2 \pm \left\{ \left[\omega_p^2 - \omega_L^2 \right]^2 + 4\omega_p^2 \left[\omega_L^2 - \omega_p^2 \right] \right\}^{1/2}/2 \qquad (3.1)$$

where ω_L is the uncoupled phonon frequency and ω_p corresponds to the plasmon frequency given by:

$$\omega_p = \left\{ 4\pi n e^2 / \left(\varepsilon_\infty m^* \right) \right\}^{1/2} \qquad (3.2)$$

where m^* is the effective electron mass, n is the free electron concentration, and ε_∞ is the high-frequency dielectric constant. When coupled modes are observed in Raman spectra, the plasmon frequency is calculated from equation (3.1) and then the concentration is calculated from equation (3.2).

For a more precise evaluation of the carrier density n, a line-shape fitting is needed as shown in references 17,18. However, it should be noted that the dielectric constant and the effective mass are necessary for the calculations and using different values available in the literature may lead to discrepancies.[19] The Raman investigation was carried out in close collaboration with Professor E. Valcheva of Sofia University.

In the Raman scattering geometry configuration used in this work, $z(x,-)\bar{z}$, only E_2 and A_1 modes are allowed (*Chapter 2*). Starting with the five HVPE-InN samples (Table 3.1), the Raman spectra are shown from 450 cm^{-1} to 650 cm^{-1} (Fig 3.1). Two broad peaks are visible: the first which extends between 480-500 cm^{-1} corresponds to E_2 mode and has very low intensity. The second peak is even larger; for all the samples, it goes from 510 cm^{-1} to 600 cm^{-1} and corresponds to the A_1 mode. It is therefore clear that the crystalline quality of these HVPE layers is poor as has been reported by Kuball *et al.*[20] for other types of InN layers.

Due to these large peaks, it is not possible to extract any quantitative information (the residual stress and free carrier density) for these samples.

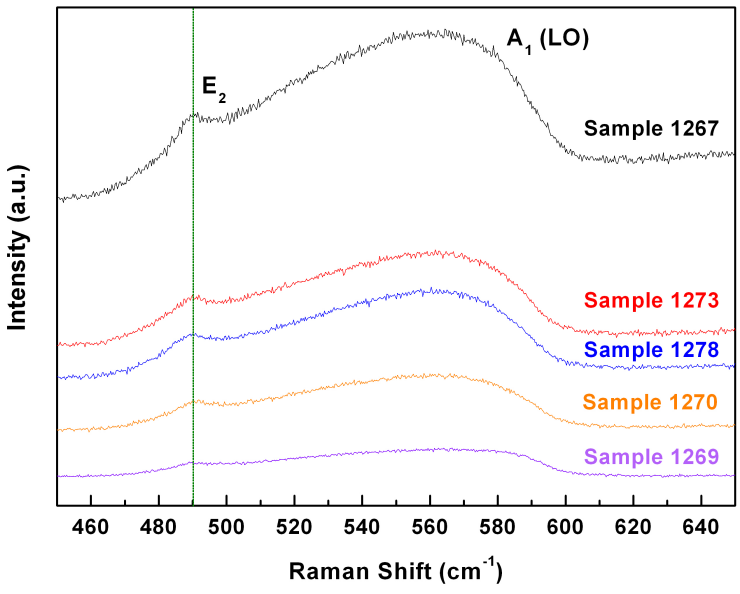

Fig 3.1 Raman spectra of the HVPE samples. The vertical line represents the position of the strain free E_2 mode at 491 cm^{-1}.

Two samples (1269 and 1273, Table 3.1) were selected for checking the layer structure using cross-section TEM observations. Fig 3.2(a) corresponds to a dark

field TEM micrograph taken with **g** = $10\bar{1}0$ for 1269 sample. In this image, we observed high density of stacking faults in the basal planes and many dislocations can be seen along the *c*-axis. As shown in Fig 3.2(b), similar density of defects is visible in 1273 sample using **g** = 0002, meaning that we have also huge amounts of defects (with displacement vectors along the *c*-axis) in agreement with the observed large Raman peaks.

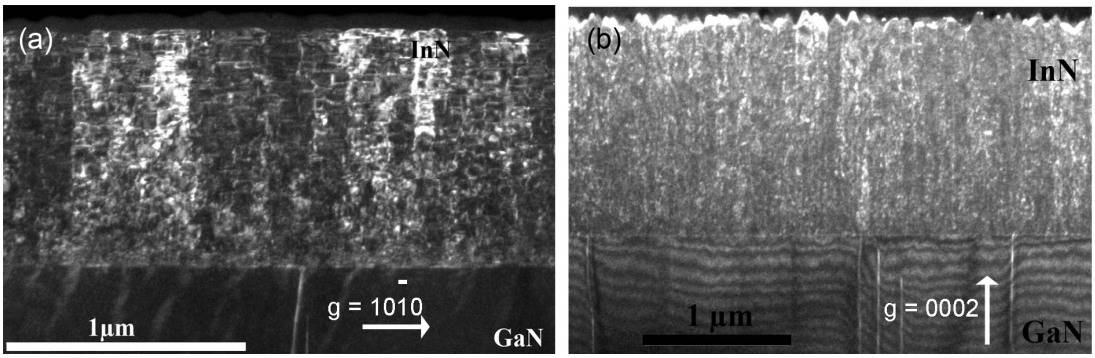

Fig 3.2 Cross sectional TEM images: (a) sample 1269, **g** = $10\bar{1}0$ (high density of stacking faults), (b) sample 1273, **g** = 0002.

A similar investigation was carried out on the four MOVPE-InN samples (Table 3.1). In this case, the Raman spectra exhibited narrow peaks for the two active InN phonon modes: the first E_2 mode at ~ 491.5–494.1 cm^{-1} and the second A_1 (LO) at 596.7-600.7 cm^{-1} (Fig 3.3).

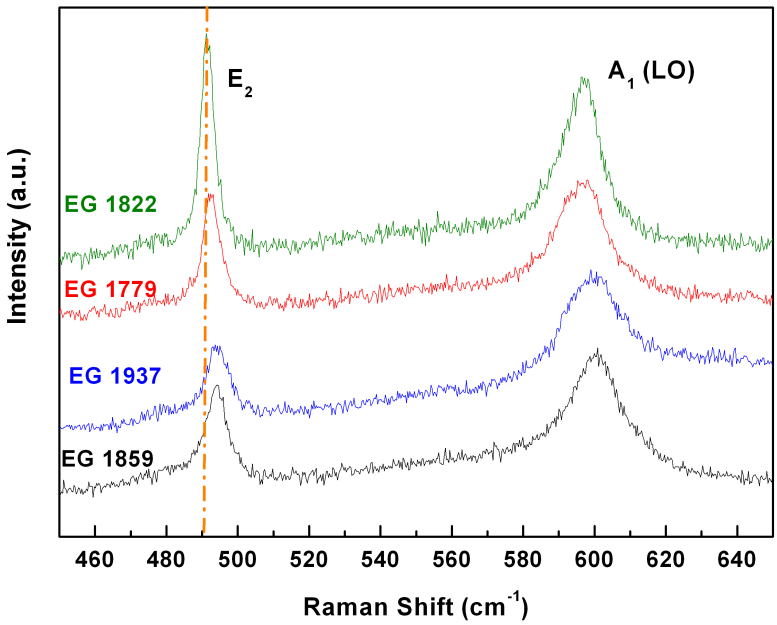

Fig 3.3 Raman spectra for MOVPE-InN samples. The dash dotted line represents the position of the strain free E_2 mode at 491 cm^{-1}.

All these samples have positive Raman Shift $\Delta\omega = \omega E_2^{measured} - \omega E_2^{strain\ \ free}$ showing that MOVPE-InN samples exhibit compressive in plane strain. The three samples deposited on Al_2O_3 exhibit a linear Raman shift behaviour with the thickness (Fig 3.4).

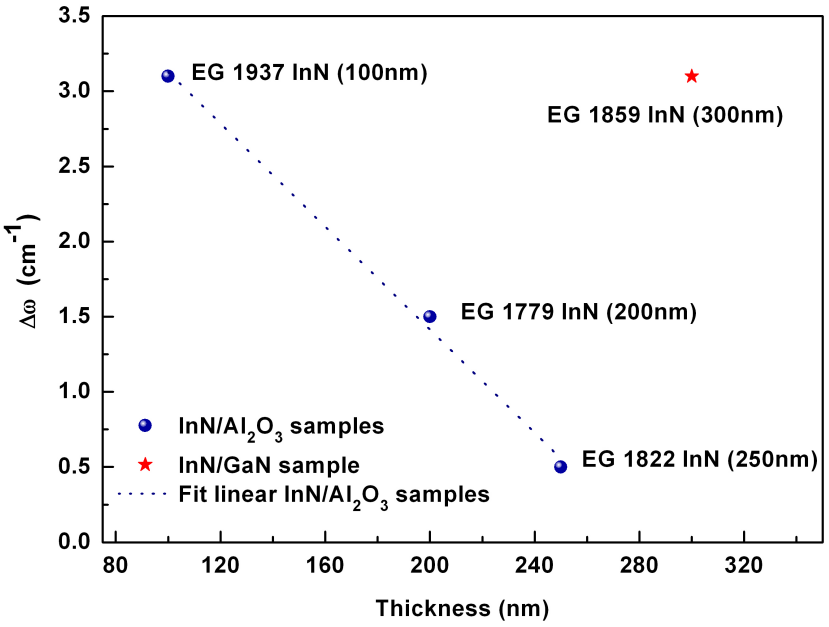

Fig 3.4 Raman shift evolution with the InN layer thickness. The dashed line represents a linear fit for the samples grown on sapphire.

As in general biaxial strain is reduced by increasing the thickness of the layers, we can suppose that these samples are under pure biaxial strain. Assuming biaxial strain, the Raman shift is given by $\Delta\omega = 2\,(a\text{-}C_{13}\cdot b/C_{33})\cdot\varepsilon_{xx}$, where ε_{xx} is the strain tensor component perpendicular to the *c*-axis (*z*-axis for the used configuration), and a = -610 cm^{-1} and b = -857 cm^{-1} correspond to the deformation potentials of the E_2 phonons of InN.[14] Then the in-plane residual stress was calculated using:

$$\sigma_{xx(Raman)} = \frac{\omega E_2^{measured}(cm^{-1}) - \omega E_2^{strain\ \ free}(cm^{-1})}{K^H} \qquad (3.3)$$

where K^H is the hydrostatic linear pressure coefficient which can be derived from the equation:[21]

$$K^H = -\frac{2\cdot(C_{33}-C_{13})\cdot a + (C_{11}+C_{12}-2C_{13})\cdot b}{C_{33}\cdot(C_{11}+C_{12})-2\cdot C_{13}^2} \quad (3.4)$$

Using the stiffness constants C_{ij} of Kim *et al.*[22] the calculated K^H is 5.6 $cm^{-1}GPa^{-1}$. The corresponding calculated residual stress values are given in Table 3.2. These values, which are smaller than 0.6 GPa, are in the same range than those reported by Gherasoiu *et al.*[23] for MBE-InN samples (0.18–0.48 GPa). In general, biaxial compressive stress is due to difference in thermal expansion coefficients between InN and GaN or InN and Al_2O_3 and to lattice mismatch (see *Chapter 1-Table 1.1*). For sample EG1859 (300 nm) grown on GaN/Al_2O_3 the same Raman shift was observed for EG1937 (100 nm) grown directly on Al_2O_3. Therefore, the measured stress in sample EG1859 whose thickness is three times larger than for sample EG1937 cannot be attributed to a built-in pure biaxial stress.

Table 3.2 Thickness, carrier density, E_2 mode position and in plane residual stress values for MOVPE samples.

	Thickness (nm)	**Carrier density ($x10^{18}$ cm^{-3})**	**$\Delta\omega$ (cm^{-1})**	**E_2 (cm^{-1})**	**σ_{xx} (GPa)**
EG1937	100	4	3.1	494.1	0.53
EG1779	200	0.9	1.5	492.5	0.25
EG1822	250	1	0.5	491.5	0.06
EG1859	300	2	3.1	494.1	----

The small FWHM values for the E_2 peak (in the 4.35–7.48 cm^{-1} range) suggests better crystalline quality for these layers in comparison with the HVPE samples. However, these values are larger than the best value of 3.7 cm^{-1} reported in the literature for MBE samples.[24] Moreover, the lowest carrier density was measured in the two samples exhibiting the smallest residual stress.

The InN-MOVPE samples were also investigated by TEM. Fig 3.5(a)-(b) displays the cross-sectional bright field images (**g** = 0002) for two representative samples. The surface of InN films exhibits a large roughness with voids at the interface with the substrate, suggesting a 3D growth mode (Volmer-Weber). However, a close observation of the islands shows that they are mainly defect free.

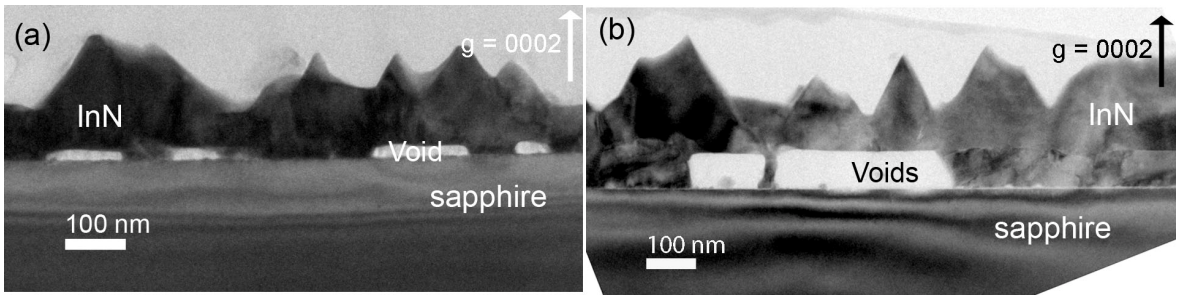

Fig 3.5 Cross-sectional TEM images on MOVPE-InN samples: (a) EG1779, (b) EG 1822.

Therefore, in agreement with the Raman results, we can point out, that although, the MOVPE samples have a poor surface morphology, the islands are of good crystalline quality.

The MBE-InN samples exhibit narrow Raman peaks at 490.6-496.2 cm^{-1} for the E_2 and 588.6-592.3 cm^{-1} for the A_1 (LO) modes (Fig 3.6), respectively. An additional peak is observed for R489 and R374 samples at 571 cm^{-2} (denoted by *); in these samples where the InN layers are thinner, this peak corresponds to the E_2 mode of the underlying GaN (567.6 cm^{-1}). The used laser was at 633 nm, and the detection of the GaN E_2 mode is due to its penetration depth in InN.[20] All the samples exhibit in plane compressive strain, except R117 deposited on Si (111) substrate with an AlN interlayer (Table 3.2), which also shows the smallest Raman shift.

In Fig 3.7 is plotted the Raman shift $\Delta\omega$ versus the thickness; as can be seen a non linear behaviour with the thickness is exhibited for the MBE-InN samples, meaning that a possible non pure biaxial strain is present in these samples. This point will be investigated later in detail by analysing the residual stress using HRXRD (*section 3.3.2*).

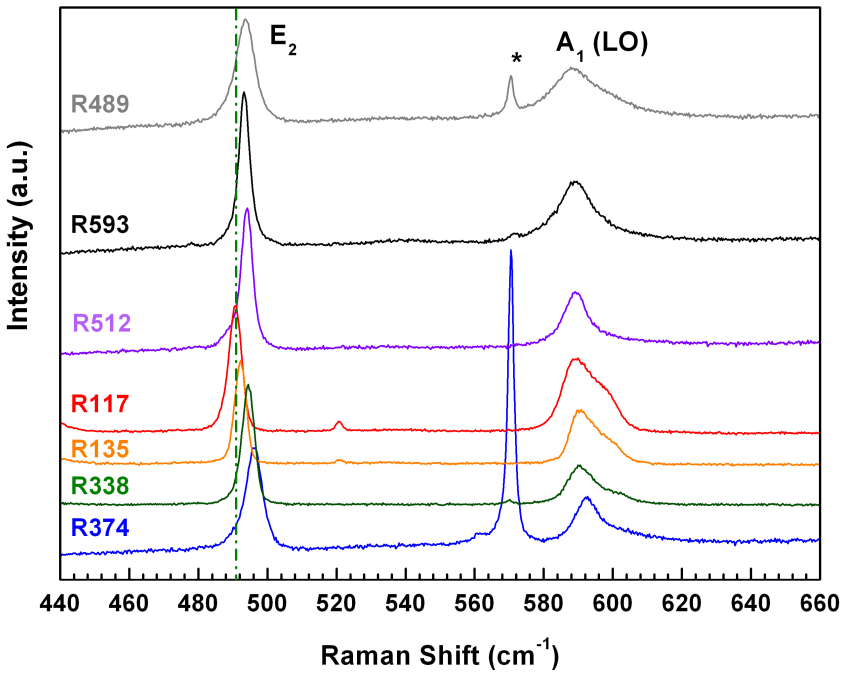

Fig 3.6 Raman spectra for MBE samples in $z(x,-)\bar{z}$ configuration. The dash dotted line represents the position of the strain free E_2 mode at 491 cm^{-1}.

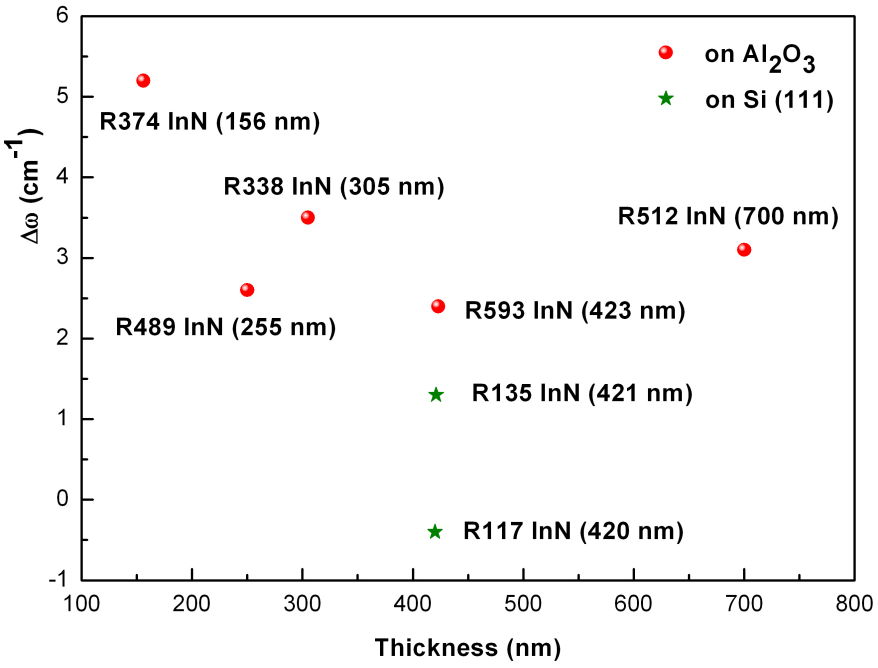

Fig 3.7 Raman shift evolution with the InN layer thickness.

In the samples deposited on Si (111), there is a shoulder in the high wave number side of A_1(LO) at around 590 cm^{-1}. Kuball *et al.*[20] have reported a similar

feature in MBE samples and attributed it to defect or impurity activated E_1(LO) mode. As can be seen in Table 3.3, this feature is observed particularly in two samples R117 and R135, grown on Si and in which our estimated carrier concentrations are 17 x 10^{18} cm^{-3} and 8 x 10^{18} cm^{-3}, respectively.

Table 3.3 MBE samples: InN thickness, and Raman results.

	Thickness (nm)		**Carrier density**	**Δω**	**E_2**
	Nominal	**Measured by TEM**	**(x10^{18} cm^{-3})**	**(cm^{-1})**	**(cm^{-1})**
R374	150	156	3.2	5.2	496.2
R593	250	423	3	2.4	493.4
R489	250	255	4.3	2.6	493.6
R338	400	305	1.5	3.5	494.5
R512	750	700	2	3.1	494.1
R117	350	420	17	-0.4	490.6
R135	450	421	8	1.3	492.3

For these MBE samples, the peak width of E_2 ranges from 3.25-5.24 cm^{-1} which indicates their good crystalline quality. Cross-sectional TEM observations were performed in order to verify the internal structure of the samples. As can be seen in Fig 3.8(a) which is a (**g** = 0002) weak beam micrograph recorded from sample R512, there are no additional screw or mixed type dislocations generated at the InN/GaN interface. However, the dislocations from the GaN layer cross the interface until the InN top surface without being deviated or annihilated (white asterisks). Throughout the InN layer, continuous thickness fringes can be noticed, attesting the layer good quality in agreement with the Raman observations.

However, as expected from the large mismatch between InN and GaN, many edge dislocations are generated at the interface, and most propagate towards the surface as can be seen in Fig 3.8(b).

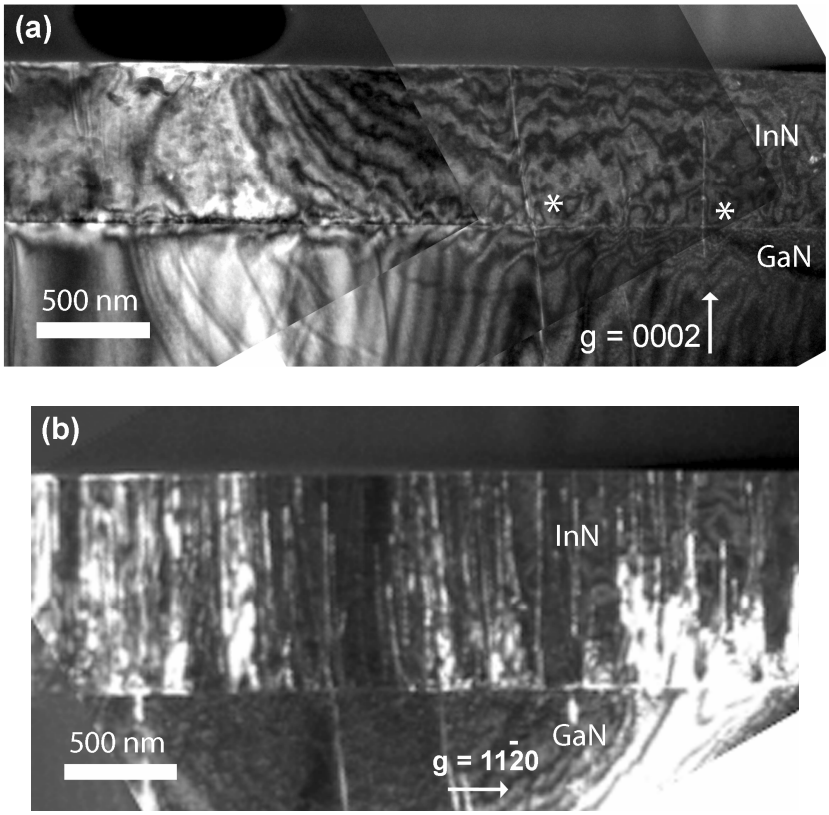

Fig 3.8 Cross-sectional TEM micrograph of R512 sample (a) **g** = 0002 (b) **g** = 11$\bar{2}$0 .

In summary, the InN films grown by MOVPE and MBE techniques show better crystalline quality than HVPE-InN as attested by Raman spectroscopy. However, the MOVPE layers are characterized by a strong island growth mode and numerous voids have formed at the interfaces, for all the samples; notwithstanding the layer quality, it is clear that this particular structure should be detrimental to device fabrication. In contrast, as the MBE layers exhibit good microstructure and quite flat surfaces, we will now focus on them for a detailed investigation.

3.3 InN films grown by PA-MBE

The layers quality can be modified due to various parameters: thickness, indium or nitrogen flux, the growth rate, substrate temperature, etc. during MBE growth.[25,26] Table 3.4 lists the growth conditions for the MBE samples. In contrast to the MOVPE where the V/III ratio can be varied in orders of magnitude, in this instance (Table 3.3) V/III ratio is closed to 1. Our samples were grown in slightly

N-rich (R593, R117, R135) or slightly In-rich (R374, R489, R338, R512) conditions (Table 3.4).

Table 3.4 Growth parameters for MBE-InN samples.

	Thickness measured by TEM	**In flux Φ_{In} (nm/min)**	**N flux Φ_N (nm/min)**	**Growth rate (nm/min)**	**T (°C)**
R374	156	11.2	9	7.5	470-480
R593	423	6.9	8.33	4.16	485-495
R489	255	9.5	8.33	8.33	400
R338	305	10.5	9	8.8	440-465
R512	700	9.5	8.33	8.3	420-470
R117(*)	420	8	8.33	8	475-480
R135(*)	421	8	8.33	8	475-480

(*) Si substrate

3.3.1 The surface morphology by AFM

Looking at the Table 3.4, the investigated samples may be divided in two sets according to the nitrogen flux used during the growth (9 and 8.33 nm/min). The first case is made of samples R374 and R338 grown with a nitrogen flux of 9 nm/min. As shown in Fig 3.9, the dominant growth mode is 2D and we can clearly observe spiral growth hillocks, atomic terraces and a few small pinholes (arrows) for R374. In R338, the terraces appear to be in one direction and in this area a large hexagonal shaped (diameter = 95 nm) defect is present (see arrow). The measured root mean squared (rms) surface roughness for the two samples is quite similar, at around 0.7 nm.[27]

The second set is made of samples R512, R489, R593 deposited on GaN/Al_2O_3 and R117 and R135 on Si, where the used nitrogen flux was Φ_N = 8.33 nm/min. Among the samples deposited on sapphire (Fig 3.10(a)-(c)), the first two were grown using the same In flux (Φ_{In} = 9.5 nm/min) and the third was under N-rich conditions (Φ_N = 6.9 nm/min). Obviously, there is a large morphological difference between the three samples. The difference between samples R512 and R489 grown exactly with the same fluxes (In,N) can be probably attributed to the

change in the growth temperature, higher for sample R512 which exhibits steps flow surface. This is in agreement with the report of Nanishi *et al.*[8] who showed that the best quality MBE-InN layers can be obtained by a precise control of the V/III ratio, in conjunction with the highest temperature within the decomposition limit.

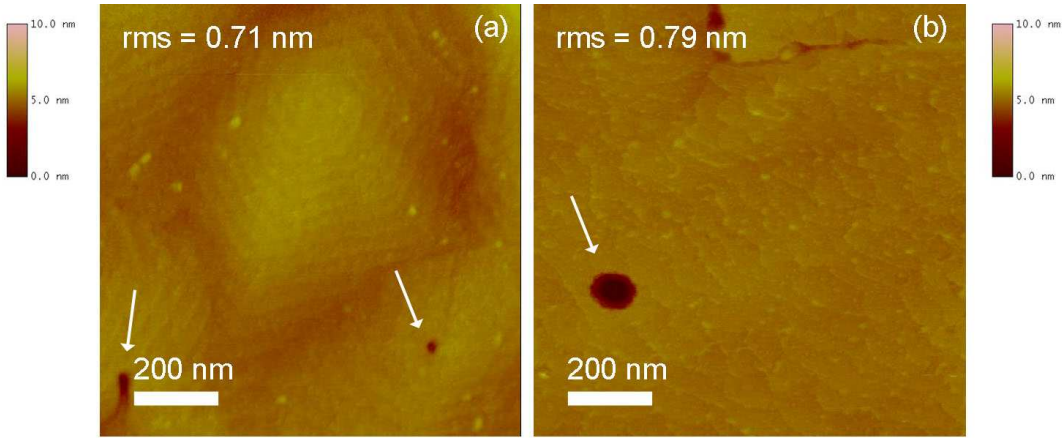

Fig 3.9 AFM image of samples InN/GaN/sapphire with Φ_N = 9 nm/min: (a) R374 (t_{InN} = 156 nn) (b) R338 (t_{InN} = 305 nm). The white arrows show the pinholes.

In contrast, the third sample (R593) exhibits a much higher roughness in comparison with the two previous, most probably due to N-rich growth conditions. This is agreement with Gallinat *et al.*[28] who reported that when Φ_{In} becomes lower than the Φ_N flux, the surface looses the step flow growth which appears to be characteristic of slightly indium rich conditions.

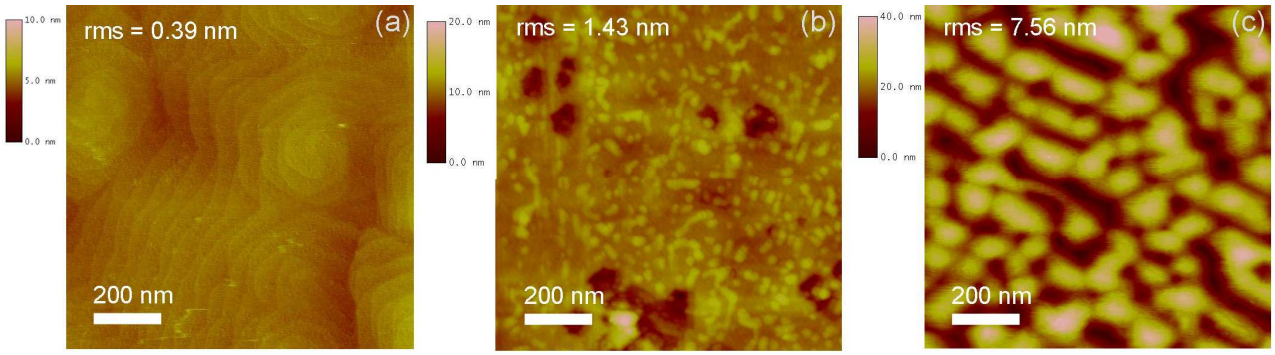

Fig 3.10 Surface morphologies (AFM images) for InN film with Φ_N = 8.3 nm/min: (a) R512 (t_{InN} = 700 nm) (b) R489 (t_{InN} = 255 nm), (c) R593 (t_{InN} = 483 nm).

In Fig 3.11, the 5 x 5 μm² AFM scans show the morphology of samples grown on Si(111) which have been also grown in slightly N-rich conditions. Both samples exhibit platelets propagating in a zigzag manner and surrounded by deep trenches which leads to the observed large surface roughness (around 7 nm). Therefore the insertion of GaN buffer layer before the InN growth (R135) does not seem to improve the surface morphology, as would be expected if we consider the lattice mismatches.

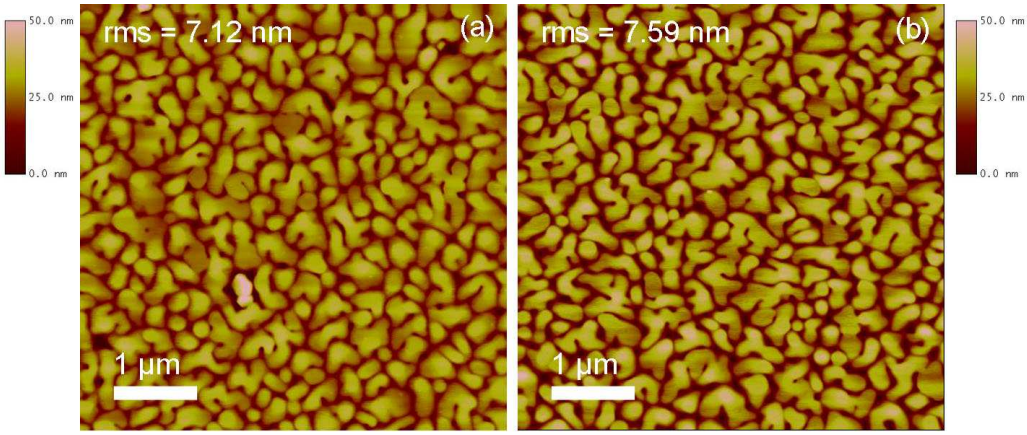

Fig 3.11 AFM 5 x 5 μm² micrographs of (a) R117 and (b) R135.

Using STM, the 2D growth mode of InN on GaN was first reported by Ng *et al.*[29] where they explained that such a mode was controlled by the growth conditions, with low temperature or high N flux favouring 3D growth, whereas high temperature and In flux led to 2D mode. In our case for In-rich conditions, if we considered the N/In fluxes ratio, the optimal surface morphology was obtained for sample R512 grown at high temperature (470 °C). When the growth temperature was lowered to 400 °C (R489), the surface roughness became more than three times larger. If the N/In fluxes ratio is decreased (sample R374) keeping the same temperature (470 °C), the roughness increased almost by two times and small pinholes appeared. With a slight increase of the flux ratios and slight decrease of the temperature (R512 and R338), we obtained large pinholes and the roughness is also two times larger. Therefore, the best growth condition was for the V/III ratio closest to 1 in the indium rich region at temperatures around 470 °C.

For N-rich conditions, the differences in morphology between the two samples grown on Si (R117 and R135) and R593 can be explained by the fact that in R593 we are further away from stoichiometry (V/III = 1.21) compared with the samples grown on Si (V/III = 1.04). Koblmüller *et al.*[26] reported that the samples grown closed at V/III = 1 show homogeneous surface, and large separated InN islands are observed when the ratio increases.

3.3.2 Residual stress

In the literature[30,31,32,33,34] the lattice parameters of the wurtzite InN structure which have been reported covers a wide range of values. Such dispersion may be attributed to the lack of high quality and the difficulty to grow bulk samples. As previously mentioned the biaxial stress can be due to lattice mismatch and thermal expansion coefficients with the substrate, whereas hydrostatic and uniaxial stress are related respectively to point and linear defects (*Chapter 1, section 1.4.3.6*). Thus, as was explained in *Chapter 1*, in order to access to residual stress by HRXRD, the *a* and *c* lattice parameters were extracted using RSM. To access the *c* lattice parameter, we have measured (000ℓ) symmetrical reflections, whereas *a* lattice parameters were extracted from the $(10\bar{1}1)$, $(10\bar{1}2)$, and $(10\bar{1}3)$ asymmetrical reflections.

Typical (0002) and $(10\bar{1}1)$ RSM for sample R489 are presented in Fig 3.12. The RLP center coordinates allows to access the $2\theta_{0002}$ and $2\theta_{10\bar{1}1}$ Bragg angles.

Then the *c* and *a* lattice parameters are extracted using the Bragg's law ($2\, d_{hkl} \sin\theta = n\,\lambda$) and the following equations:

$$c = d_{0002} * 2 \qquad (3.5) \qquad\qquad a = \frac{2 \cdot d_{10\bar{1}1} \cdot c}{\sqrt{3 \cdot c^2 - 3 \cdot d_{10\bar{1}1}{}^2}} \qquad (3.6)$$

The measured cell parameters are given in Table 3.5 and correspond to the mean value of the *c* and *a* cell parameters given respectively by (0002) and (0004) symmetric and $(10\bar{1}1)$, $(10\bar{1}2)$, $(10\bar{1}3)$ asymmetric reflections RLP centers.

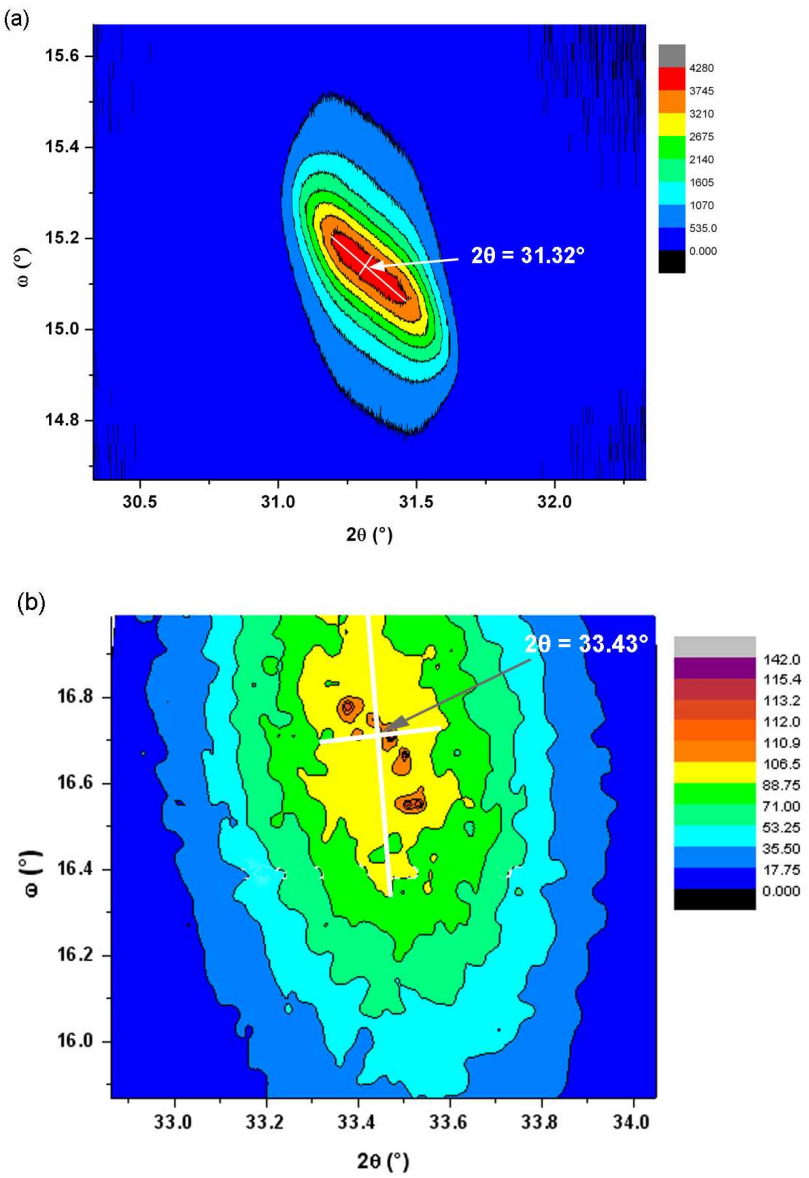

Fig 3.12 RSM: (a) (0002) symmetric and (b) $(10\bar{1}1)$ asymmetric reflections (no coplanar reflection) for InN R489 sample. In each RSM are indicated the center of the RLP.

Table 3.5 Cell parameters extracted by RSM measurements, in- and out-plane strain tensor components and the corresponding in-plane residual stress σ_{xx} values.

	a (Å)	**c (Å)**	**ε_{xx}**	**ε_{zz}**	**σ_{xx} (GPa)**
R374	3.508	5.725	-0.008	0.004	-2.336
R593	3.492	5.716	-0.013	0.002	-4.21
R489	3.498	5.710	-0.011	0.001	-3.626
R338	3.496	5.715	-0.012	0.002	-3.872
R512	3.498	5.708	-0.011	0.001	-3.626
R117	3.530	5.699	-0.002	-0.001	-0.768
R135	3.526	5.708	-0.003	0.001	-0.922

The two InN layers on Si substrate exhibit lattice parameters closest to the strain free ones reported by Paszkowicz[31] (a = 3.5378 Å and c = 5.7033 Å) as extracted by Rietveld refinement on InN powder. The in- and out-plane strain tensor components were calculated respectively from the following equations $\varepsilon_{xx} = \frac{a - a_0}{a_0}$ and $\varepsilon_{zz} = \frac{c - c_0}{c_0}$ (see *Chapter 1*, *section 1.4.3.6*).

Under the assumption of biaxial strain, there is a linear correlation between both strains tensor components given by the equation $\varepsilon_{zz} = -2 \cdot (C_{13}/C_{33}) \cdot \varepsilon_{xx}$, using stiffness coefficients of InN as reported by Wright[35] (C_{13} = 92 GPa and C_{33} = 224 GPa), the relation becomes $\varepsilon_{zz} = -0.82 \cdot \varepsilon_{xx}$. However, we must point out that the C_{13}/C_{33} ratio is sensitive to the uncertainties of the stiffness coefficients[22,35,36] as well as of the unstrained InN lattice parameters used for the calculation of strain tensor components.

In Fig 3.13, we have plotted the out-plane strain tensor component versus the in-plane for all the MBE samples.

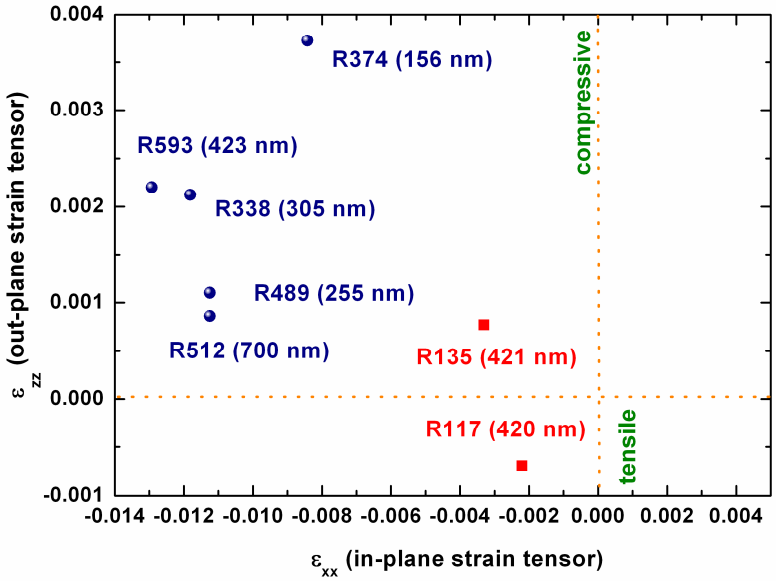

Fig 3.13 Out-plane and in-plane strain tensor components for the investigated MBE-InN samples. The dashed lines indicate the situation where the strains are zero, at their intersection is the strain free case. The in-plane compressive (ε_{xx}<0) and tensile (ε_{xx}>0) regions are indicated.

As can be seen, there is no linear relationship between ε_{zz} and ε_{xx}, therefore the strain in these layers is not purely biaxial, in agreement with the above Raman

investigations (*section 3.2.1*). For sample R117, ε_{zz} and ε_{xx} are smallest, and it is the only one to exhibit tensile strain. A similar behaviour has been noticed by Darakchieva *et al.*[14] on samples grown on top of sapphire using an AlN interlayer, however the overall strain was purely biaxial in their case. The in-plane residual stress tensor is given by $\sigma_{xx\ (HRXRD)} = (C_{11}+C_{12}) \cdot \varepsilon_{xx} + C_{13} \cdot \varepsilon_{zz}$ and the calculated values are summarized in Table 3.5. In Fig 3.14, we show the evolution of the σ_{xx} in-plane residual stress obtained by HRXRD as well as the Raman shift. As can be seen, the two exhibit a similar behaviour.[27]

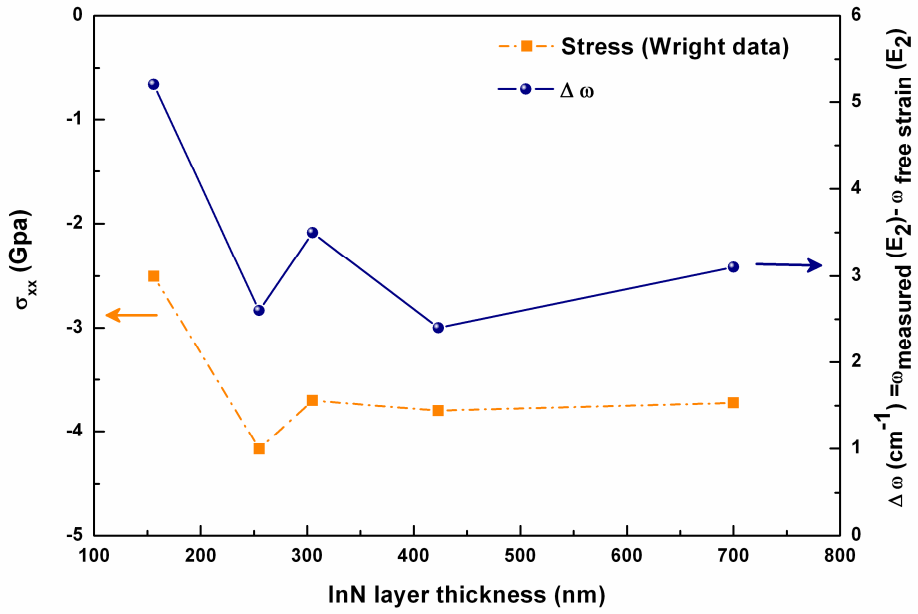

Fig 3.14 In-plane residual stress σ_{xx} as deduced from HRXRD and $\Delta\omega$ Raman shift versus the InN layer thickness.

We observe compressive in-plane residual stress for all the samples deposited on GaN/Al_2O_3, whereas for samples deposited on Si, tensile (R117: AlN/Si) or compressive (R135: GaN/AlN/Si) residual stress is obtained.

In the literature, a number of reports have been published on strain investigation in InN layers grown by MBE as well as MOVPE. In Fig 3.15, we have collected some of these data along with our results. In the MBE reports, Cimalla *et al.*[37] studied InN layers grown on AlN/sapphire with thicknesses up to 1 µm, using XRD, Specht *et al.*[38] used also XRD, AFM and TEM, on InN/Al_2O_3 of similar thickness, whereas, Dimakis *et al.*[39] used XRD and AFM, on InN/GaN/Al_2O_3 films

of thicknesses up to 10 µm; in their growth conditions, the residual stress was purely biaxial. In contrast, Kadir *et al.*[40] reported from their XRD investigations of InN/GaN/Al_2O_3 layers grown by MOVPE, with thickness around 0.2 µm, that the stress was pure hydrostatic.

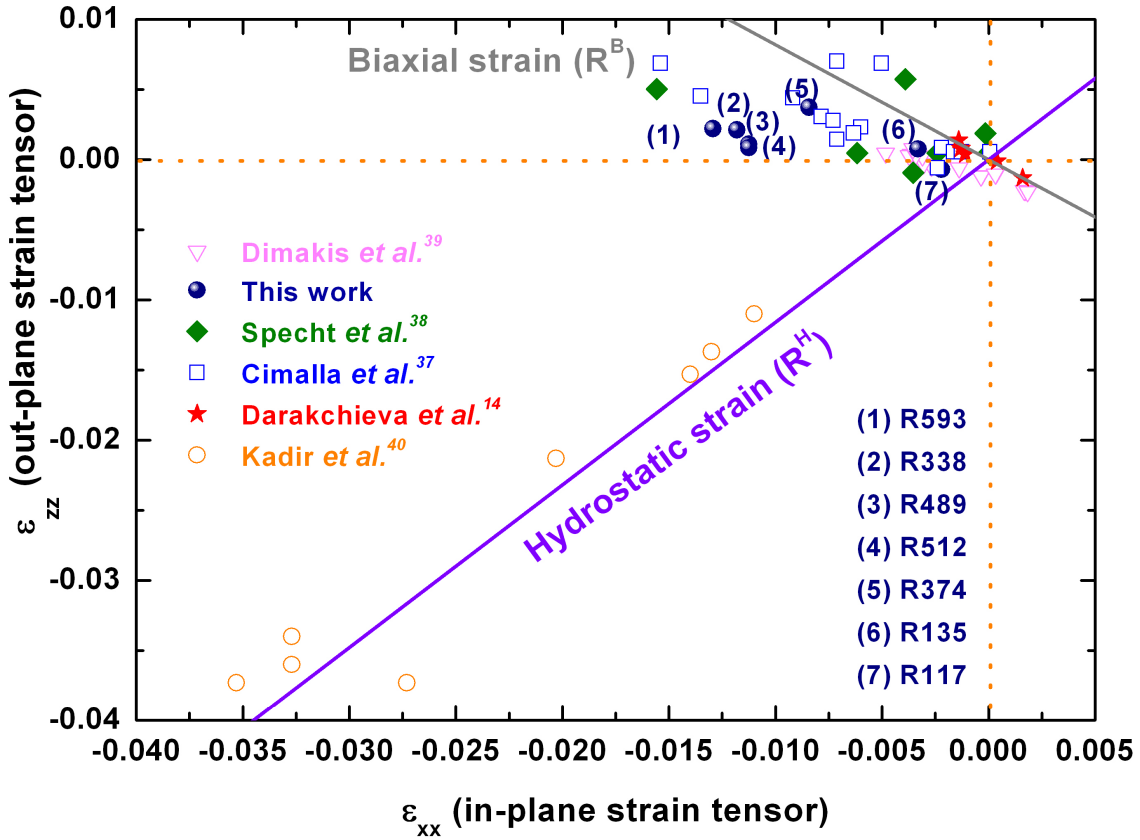

Fig 3.15 Comparison of our data with the literature and using the strain free InN cell parameters of Paszkowicz,[31] the gray line stands for biaxial strain using R^B = -0.82 and the purple line stand for hydrostatic strain R^H = 1.16.

As can be seen in Fig 3.15, when our data is plotted along with the above, it is clear that all the MBE layers are scattered within the same region, meaning that most of the layers may not be considered as under pure biaxial strain (see gray line). In this figure only the layers which have been investigated by Darakchieva *et al.*[14], appear to be closest to this condition (red star in Fig. 3.15).

For our samples, we note that only R374 and R135 are closest to a pure biaxial strain state, whereas for the other samples, a hydrostatic component should be superimposed to the biaxial one. This is leading to a deviation from the biaxial state as observed by Kadir *et al.*[40] in MOVPE-InN layers. Butcher *et al.*[41] observed

the same behaviour in InN films where the presence of hydrostatic strain component was attributed to In vacancies and nitrogen-on-In anti-site defects. In our samples, due to experimental limitations (film thickness) an attempt of positron annihilation experiments was made on sample R512 (700 nm) in collaboration with Aalto University (Finland); however, no indium point defects were detected. Therefore RBS and NRA measurements have been performed in order to look for any presence of nitrogen excess which would help to explain this hydrostatic strain component (*see §3.3.3*).

3.3.3 The layers stoichiometry

In this study, RBS and NRA were employed to obtain detailed stoichiometry and depth composition of 420 nm thick InN epilayers grown on GaN/AlN/Si (111) (sample R135). NRA was used to access the total nitrogen content of the films whereas RBS was used for In content determination.

Fig 3.16(a) shows the experimental RBS spectrum for R135 sample; the labels with In, Ga and Al indicate the backscattered energy from these elements at the surface. The three In, Ga and Al signals are completely separated allowing precise measurements of their concentration. As evidenced, there is an excess of In content in the top film part of the R135. In Fig 3.16(b) the corresponding NRA spectrum exhibits two peaks at 5600 KeV and 9000 KeV, respectively and related to $^{15}N(d,\alpha_0)^{13}C$ and $^{14}N(d,\alpha_1)^{12}C$ reactions. Using SIMNRA, we have tried to find a unique film composition leading, simultaneously, to a good agreement between RBS and NRA experimental and simulated spectra. Such an agreement for both experimental RBS and NRA spectra has been reached for a three layers structure consisting on:

- a top film layer of 28 nm thick with a large In content of 72 %.
- an intermediate layer of 201 nm thick with an In content of 49 %.
- an interface layer of 190.6 nm thick with In content of 45 %.

The most probable explanation of the large excess of In inside the 28 nm surface layer maybe the oxidation of the samples which may have generated a mixture of InN and In_2O_3 phases. The two other layers have an In/N ratio smaller

than 1 and lowering close to the interface. This excess of N could lead to the presence of point defects in the InN structure which may explain the deviation from the biaxial strain as observed using HRXRD.

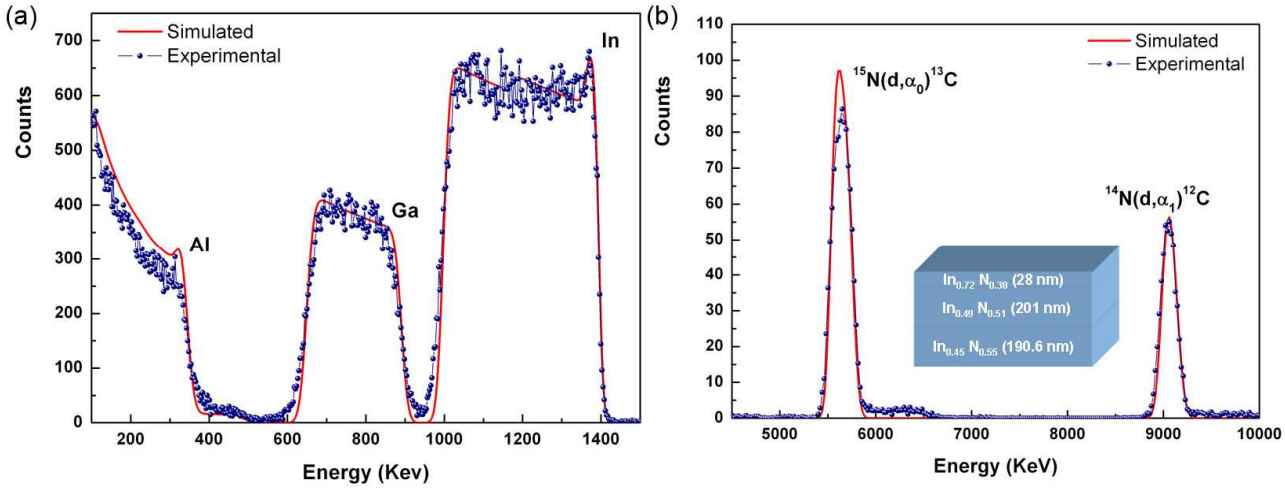

Fig 3.16 Ion beam analysis in R135 sample: (a) experimental (blue circles) and simulated (red solid line) RBS spectra of InN film (b) NRA spectrum, a schematic structure of the three InN layers fitted in SIMNRA is inserted.

3.3.4 Dislocation density

Heteroepitaxial thin films with large lattice mismatch in respect to the substrate commonly exhibit a large number of dislocations that can be examined using TEM and AFM observations, but also using HRXRD. Indeed, HRXRD has become recently a popular method for probing dislocation density in various thin films grown on foreign substrates as it is a non-destructive technique which gives a general view in contrast to TEM and AFM, which cover smaller areas.

3.3.4.1 *HRXRD: tilt and twist*

As described in *Chapter 1-Section 1.4.3.4*, four parameters (tilt, twist, lateral and vertical coherence lengths) are necessary in the mosaic model in order to determine the microstructure of the samples. In this model, the out-of-plane rotation of the blocks perpendicular to the film surface normal is called tilt, and the in-plane rotation around the surface normal is called twist; tilt and twist thus define the full width at half maximum (FWHM) of the corresponding distribution

of crystallographic orientations. Moreover, a limited coherence length causes a RLP broadening in the (q_x and q_y) plane, while a limited vertical coherence length is correlated with a RLP broadening along the q_z direction. These parameters can give rise to a broadening of elliptical shaped RLP, i.e. a distribution of the scattered intensity in reciprocal space around the RLP. Therefore, the influence of the mosaicity on the broadening of RLP can be analyzed and a pronounced broadening of the RLP along a certain direction in reciprocal space indicates the predominance of a particular parameter of the mosaic structure. The impact of the various mosaicity parameters on the RLP broadening is illustrated in Fig 3.17 and Fig 3.18.

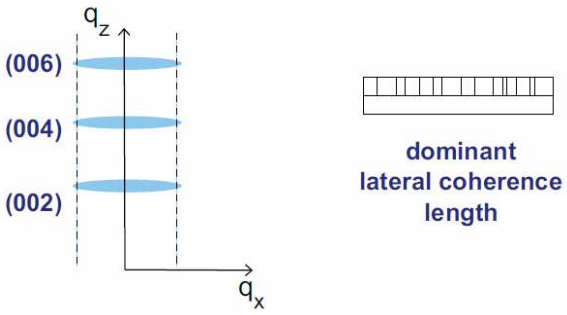

Fig 3.17 Influence of a limited lateral coherence length on symmetric reflections[42] where q_x and q_z are respectively the in-plane and out-of-plane scattering vector components. For symmetric reflections, they can be calculated considering the equations:

$$q_x = (4\pi/\lambda)\,[\sin(\theta) \cdot \sin(\omega - \theta)] \qquad (3.7)$$

$$q_z = (4\pi/\lambda)\,[\sin(\theta) \cdot \cos(\omega - \theta)] \qquad (3.8)$$

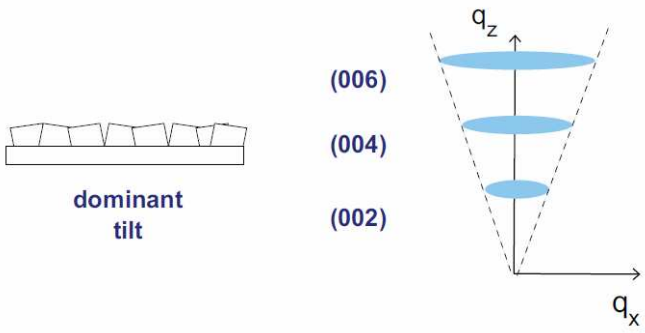

Fig 3.18 Influence of a dominant tilt effect on symmetric reflections.[42]

As shown in these Fig 3.17 and Fig 3.18, the tilt modifies the RLPs with q_z = 0 whereas the twist broadens the RLP in the (q_x,q_y) plane. The superposition of a

rotational disorder and a limited lateral coherence length is shown in Fig 3.19 for a symmetrical reflection and in Fig 3.20 for an asymmetrical reflection (arrow).

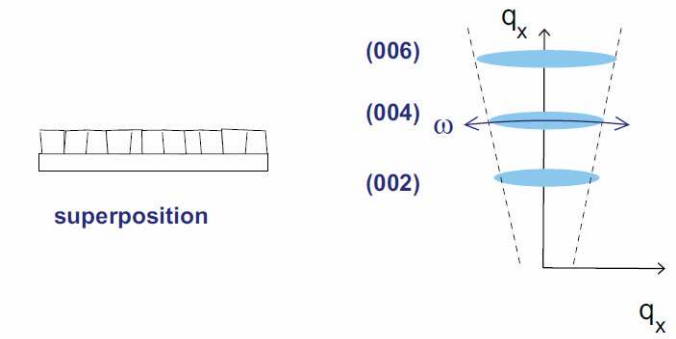

Fig 3.19 Influence of the superimposition of a limited lateral coherence length and tilt.[42]

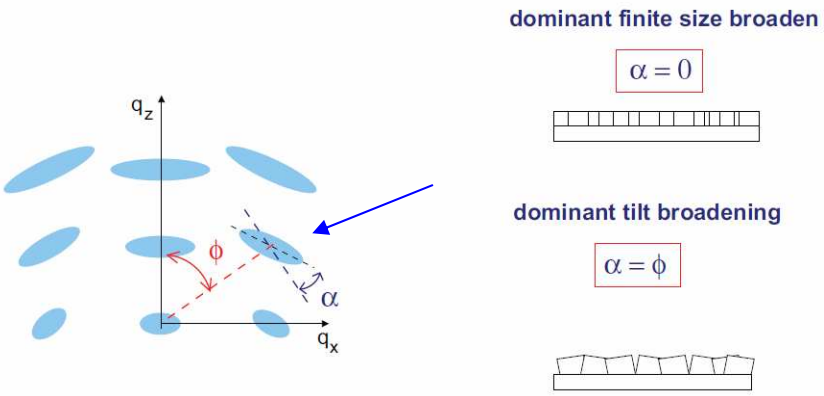

Fig 3.20 Influence of the mosaic structure on the orientation of RLPs.[42]

In III-nitride films, twist and tilt are directly related to the dislocation density and each dislocation type is associated with a local lattice distortion: for dislocations running along [0001], edge dislocations accommodate a lattice twist; screw dislocations accommodate a lattice tilt and mixed dislocations both. According to Metzger *et al.*[43], the tilt of (0001) oriented InN layers can be correlated to the screw and mixed threading dislocations (TD) which have a component of the Burger vector along [0001], while the twist is connected to the those which have an edge component with $\mathbf{b} = \frac{1}{3}\langle 11\bar{2}0\rangle$. Assuming a random dislocation density distribution, the density of the dislocations with a screw component N_{screw} can be obtained using the equation of Dunn *et al.*[44] as follows:

$$N_{screw} = \frac{\alpha_{tilt}^2}{4.36 b^2} \tag{3.9}$$

where b is c-lattice lattice.

The number of dislocation with an edge component is calculated from the equation (3.10)

$$N_{edge} = \frac{\alpha_{twist}^2}{4.36 b^2} \tag{3.10}$$

where b is the a-lattice parameter.

In the case that the dislocations are not randomly distributed but localized at the grain boundaries, their individual strain fields overlap and the grain diameter d_0 ,that is essentially the lateral coherence length, has to be taken into account: [43]

$$N_{edge} = \frac{\alpha_{twist}}{2.21 \cdot b \cdot d_0} \tag{3.11}$$

As observed in GaN films by Metzger *et al.*[43], for a system where dislocations are neither completely randomly distributed nor completely piled up in grain boundaries, the real TD dislocation density lies between the two values given by equations (3.10) and (3.11). The same trend has been observed by Dimakis *et al.*[45] for a 10 μm thick MBE-InN layers and for which the TEM measured density of edge dislocations was between 2.0 x 10^{10} cm^{-2} using a random distribution and 2.7 x 10^{9} cm^{-2} for a non random distribution dislocation model.

So in order to estimate TD dislocations density using HRXRD, a determination of the tilt and twist parameters must be done. This is achieved using different approaches and different x-ray diffraction geometries (see C*hapter 2* and Fig 3.21).

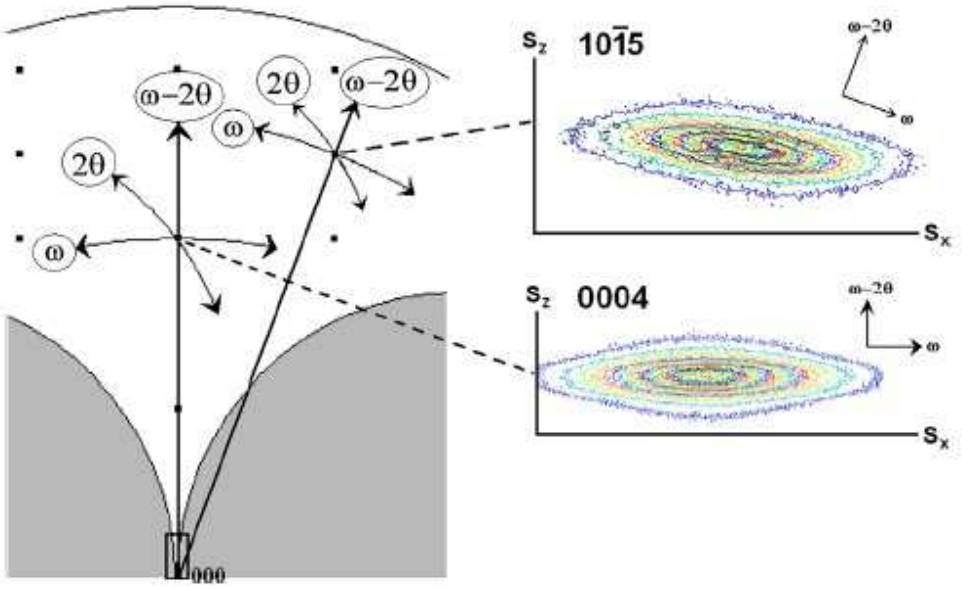

Fig 3.21 The directions taken by different scan types (*ω*, 2*θ* and *ω*-2*θ*) in reciprocal space. Inset show the reciprocal space map of the (0004) symmetric and $(10\bar{1}5)$ asymmetric reflections.[46]

To access to the tilt angle value (α_{tilt}), HRXRD rocking curves as well as measurements of (000ℓ) symmetric reflections can be done. Indeed, as previously mentioned, the broadening of the RLP due to tilted crystallites in reciprocal space and perpendicular to the q_z axis is proportional to the scattering order, while the broadening perpendicular to the q_z axis in reciprocal space due to a limited lateral coherence length is independent of the scattering order. A separation of the two effects is possible by recording rocking curves (ω-scan) of (0002), (0004) and (0006) symmetric reflections and using a Williamson-Hall plot.[47] In this latter, the integral breadth (β) (for Gaussian peaks, β is the FWHM whereas for Lorentzian peaks, β is to 0.62 times the FWHM)[46] of the measured $2\theta_{000\ell}$ Bragg peak is plotted in reciprocal space units ($\beta \cdot \frac{\sin\theta}{\lambda}$) versus the reflection order in reciprocal space units (Fig 3.22(a)). The corresponding fit using a linear regression $y = y_0 + \alpha_{tilt} \cdot \sin\theta/\lambda$ gives y-intersection y_0 of the fitted line which corresponds to the lateral coherence length $L_{//} = 1/2y_0$ and the slope (α_{tilt}) is a direct measure of the tilt angle (Fig 3.22(a)).

Rocking curves (RC) of the (0002), (0004) and (0006) symmetric reflections were measured for all our MBE-InN samples and their broadening (FWHM = β) was analysed in a Williamson-Hall plot.

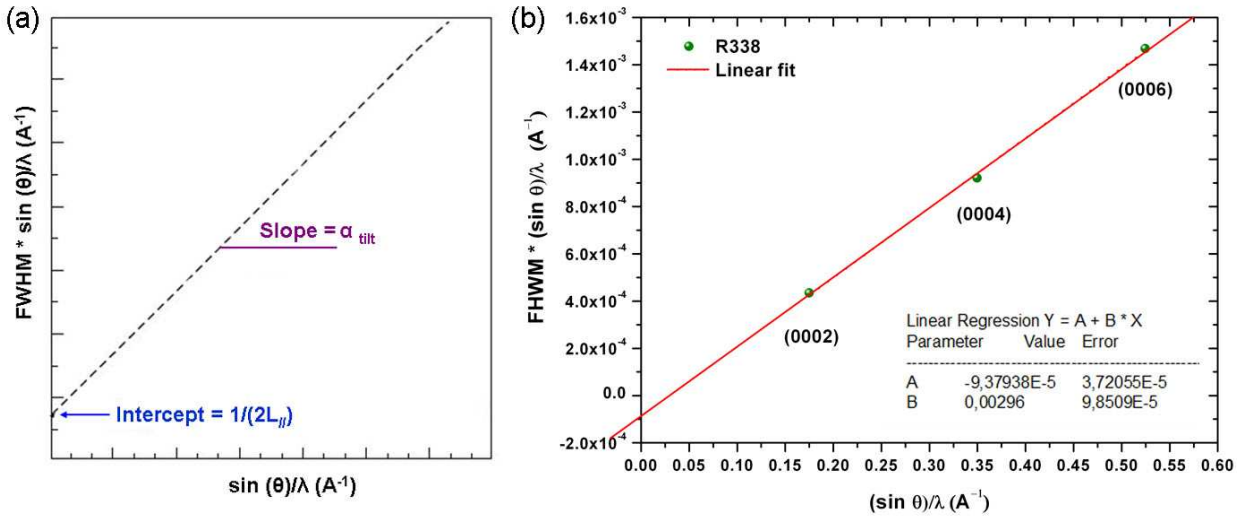

Fig 3.22 (a) Schematic Williamson-Hall plot for the determination of tilt (α_{tilt}) and lateral coherence length of mosaic structure ($L_{//}$) (b) Williamson-Hall plot for sample R338. Triple-axis rocking curves were measured for (000ℓ) reflections as indicated in the figure. The line results from a linear data fit.

Fig 3.22(b) shows a typical linear fit for R338 sample. We can clearly notice that using a linear interpolation, the intercept (y_0) is negative, meaning that we should have a negative lateral coherence length $L_{//}$ (no possible). The same trend has been observed for all our MBE samples. Many other works have shown that lateral coherence length determination using RC based Williamson Hall plots give rather large error.[48] Moreover, it is suggested in the literature that the best way to access this lateral coherence length with a good accuracy is to simulate the RSM using the model of Holý *et al.*[49] which assumes a mean block size lateral coherence length and an average tilt. As in our samples, it may be questionable to use the deduced tilt of 0.00296 rad for the calculation of the dislocation density, (000ℓ) symmetric pole figure measurements have been performed in order to access the tilt angle. To this end, (χ,φ) scans at fixed $2\theta_{000\ell}$ Bragg angle were recorded. Two typical (0002) InN (χ,φ) scans are shown in Fig 3.23(a)-(b) for sample R338 for χ = φ = 0° and χ = 0° and φ = 98°, respectively. In these scans (0002) InN and (0002)

GaN peaks are clearly visible. However, two additional peaks can be seen respectively at 2θ = 30.37° for an azimuthal φ angle of 0° and at 2θ = 32.25° for an azimuthal φ angle of 98°. These two reflections have been attributed to the (222) reflection of In_2O_3 and to the (111) reflection of metallic indium, respectively. The observations of such In rich secondary phases at different azimuthal angle shows that the two have been grown with different epitaxial relationships with the substrate (same χ angle but different φ azimuthal angle for the two extra phases).

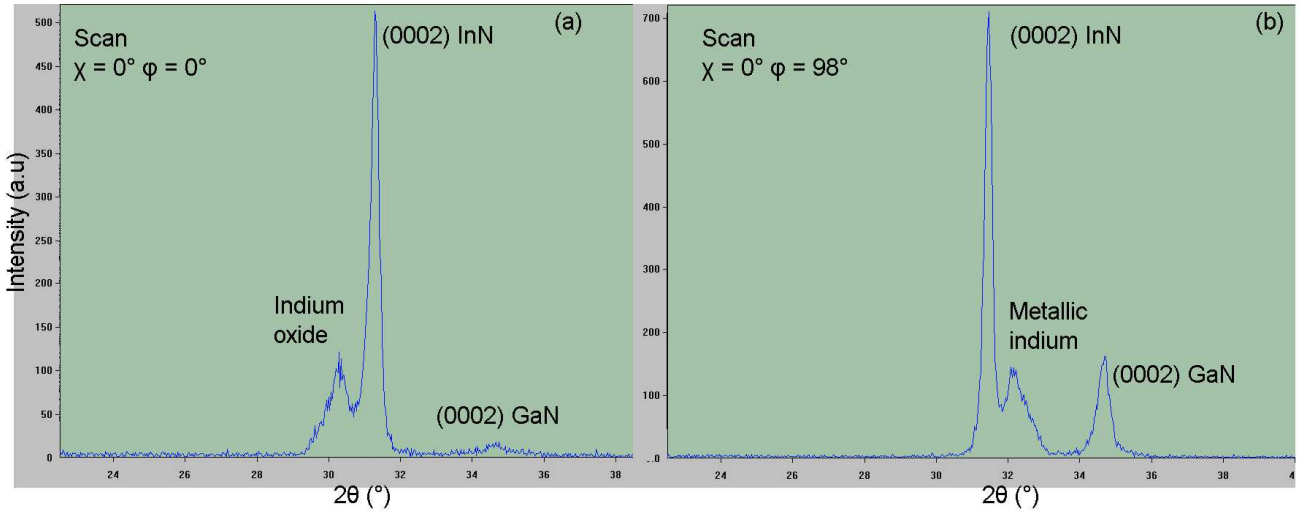

Fig 3.23 (χ,φ) scans measurements for (0002) InN reflections of samples R338: (a) with χ = φ = 0° (b) with χ = 0° and φ = 98°.

(0004) InN (χ,φ) scans have been also performed and no secondary indium phases were found around the (0004) InN reflection (Fig 3.24(a)). However, the asymmetry of the (0004) reflections at χ = φ = 0° suggests that there is still a small contribution of the In_2O_3 phases in the (0004) reflections (Fig 3.24(b)). Such asymmetry is no more observed for (0006) InN (χ,φ) scans where no extra phases are then evidenced around the (0006) InN reflections. As the (0004) and (0006) InN reflections probe a larger film thickness compared to the (0002) one, we can conclude that the In_2O_3 and metallic In extra phases are located in the top film part.

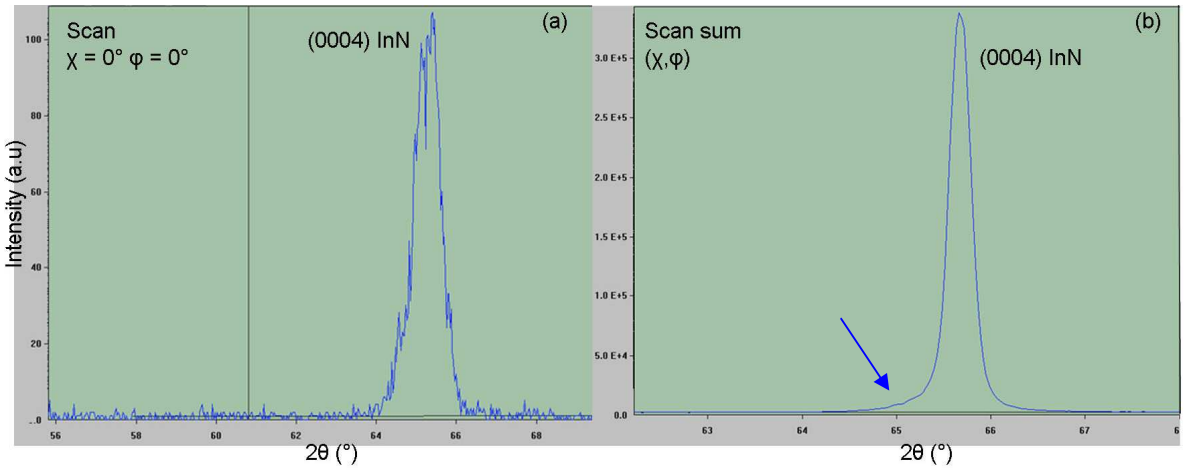

Fig 3.24 For (0004) InN reflection: (a) (χ,φ) scan with χ = φ = 0° and (b) summed scan of all χ and φ angles showing the asymmetry at the left side of the peak (see arrow).

This sample was also investigated with RBS and as seen in Fig 3.25, the RBS indium signal revealed a non homogeneous depth Indium profile with a large amount of In towards the surface of the layer. According to the previous pole figure observations, this latter can be correlated to indium oxide and metallic indium impurity phases. A two layers structure model used in SIMNRA gave a refined In contents at around of 0.86 % for the top layer and 0.59 % for interface layer (Fig 3.25).

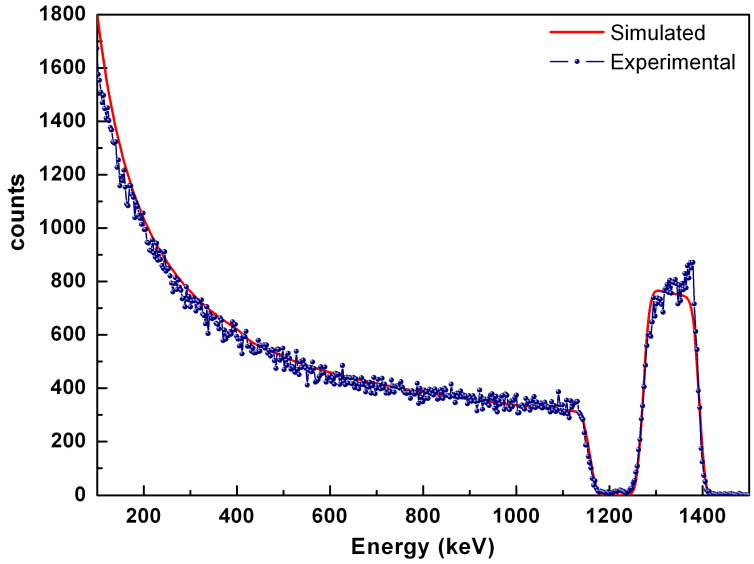

Fig 3.25 Experimental and simulated RBS spectra of InN/GaN/Al_2O_3 (R338 sample).

(0002) and (0004) InN pole figures corresponding respectively to the measured intensity integration of the 29–34° and 63–67° angular ranges of each (χ,φ) scans are displayed in Fig 3.26(a)-(b). In these pole figures, an asymmetric pole with two lobes is clear and we noticed a variation on the location of each pole: for (0002) pole figure the pole centre was located at φ ≈ 64.74° with χ = 1° whereas for the (0004) pole figure it was at φ ≈ 54.75°, with χ = 1°. This difference in φ angular location for the (000l) pole is due to the contribution of the two previously mentioned In-rich extra phases, both are present along the (0002) InN pole; however, only In oxide phase still contributes to the (0004) pole whereas the (0006) pole figure is free impurity contribution (pole located at χ = 1° and φ ≈ 0.49° not shown here). The contributions of these phases give rise to a tilt profile which is not homogeneous in depth inside the layer. The measured tilt (α_{tilt}) was 1°, 0.88° and 0.59° for (0002), (0004) and (0006) pole figures, respectively. This inhomogeneous tilt profile, which is present in all the samples, has probably a strong contribution to the negative lateral coherence length obtained using Williamson-Hall plots. So in such situation where impurity phases are present in the top part of film, the tilt can not be determined using HRXRD rocking curves measurements.

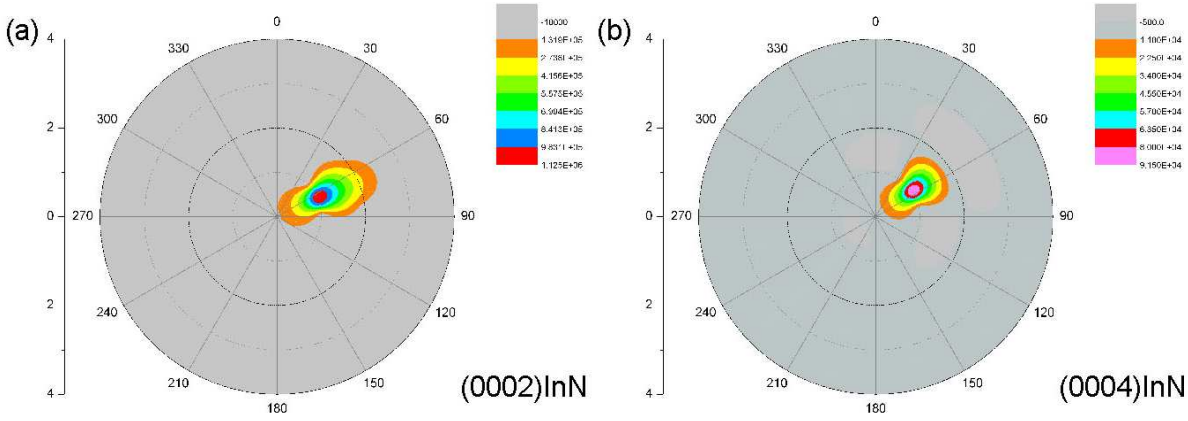

Fig 3.26 (a) (0002) InN and (b) (0004) InN pole figures with an HWHM distribution (α_{tilt}) of 1 and 0.88° respectively.

Using the above tilt values and assuming a random dislocation distribution model, for each reflection, the TD densities were then calculated using the

equation (3.9) and the Burger vector is the *c* lattice parameter extracted for each sample using RSM (Table 3.5). The corresponding tilt values for the three reflections as well as the TD densities are listed in Table 3.6 for all the studied samples. Tacking into account the tilt values calculated using the (0006) pole figure (free from impurity extra phases), we see that higher density of dislocations with a screw component were obtained in comparison with the 3 x 10^8 cm^{-2} reported in the literature using HRXRD,[50] where the authors investigated 10 µm thick MBE InN layer. Of course this discrepancy may be explained in terms of the defect reduction with the film thickness, as all our samples are under 1 µm.

Table 3.6 Thickness, *c* lattice parameter, tilt for the three (000ℓ) reflections and the deduced screw dislocation density.

		R374	R489	R338	R593	R512	R135	R117
Thickness (nm)		156	255	305	423	700	421	420
c (Å)		5.725	5.710	5.715	5.716	5.708	5.708	5.699
Tilt	**α_{0002} (rad)**	0.0175	0.0686	0.0175	0.0179	0.0166	0.0189	0.0208
	α_{0004} (rad)	0.0077	0.0071	0.0077	0.0072	0.0073	0.0078	0.0077
	α_{0006} (rad)	0.0044	0.0043	0.0051	0.0041	0.0052	0.0050	0.0052
Screw component TD Density ($x10^{10}$ cm^{-2})	**(0002)**	2.150	2.072	2.156	2.263	1.938	2.527	3.061
	(0004)	0.419	0.356	0.417	0.364	0.380	0.424	0.421
	(0006)	0.136	0.131	0.183	0.118	0.192	0.174	0.191

As seen in the table, for all the samples, the calculated dislocations densities can be more than ten times larger towards the surface, and this due to the inhomogeneous depth distribution in the tilt profile.

In order to access to the twist measurement (α_{twist}), pole figure or φ-scan measurements of $(10\bar{1}1)$, $(10\bar{1}2)$, $(10\bar{1}3)$, $(10\bar{1}4)$, $(10\bar{1}5)$ reflections have been used. A typical $(10\bar{1}2)$ pole figure of sample R338 recorded at χ = 44° with φ=32° and 91 ° is displayed in Fig 3.27. The asymmetric pole exhibits a HWHM distribution (twist value) of 0.78 °.

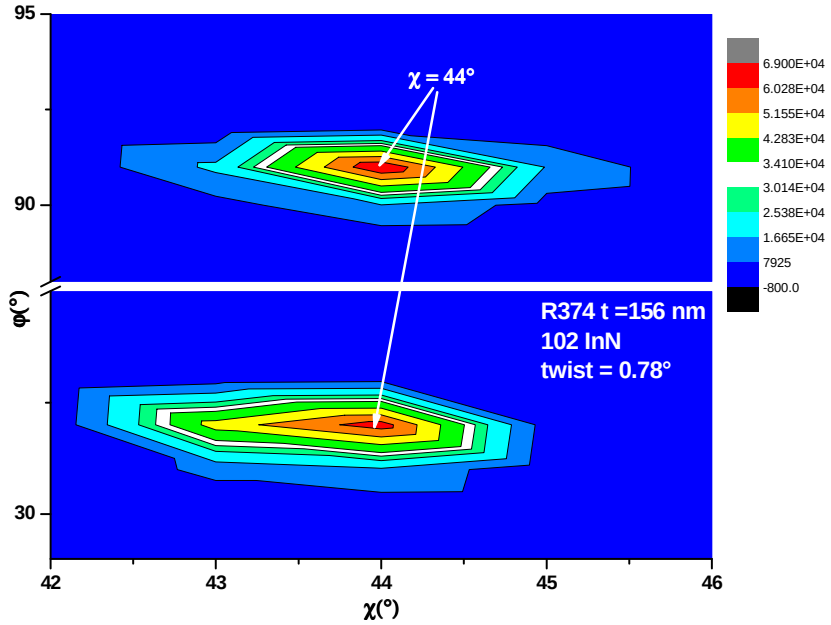

Fig 3.27 Two equivalent $(10\bar{1}2)$ poles are represented located at the same χ of 44° but at different φ angle of (a) 32° and (b) 91°.

The corresponding twist values as well as the edge and mixed dislocations density calculated using equation (3.10) are summarized in Table 3.7. For this calculation, only the screw-mixed TD extracted from the (0006) tilt reflection value have been taken into account in order to be free of the surface In rich contributions. The corresponding screw-mixed dislocations density, found in the 5-19 % range show that our MBE-InN epitaxial layers contained a high concentration of edge-component dislocations, up to 19 times than the screw component dislocations.

Table 3.7 Summary: *a* lattice parameters, twist values, edge, total TD density and the percentage of screw dislocations.

	R374	**R489**	**R338**	**R593**	**R512**	**R135**	**R117**
a (Å)	3.508	3.489	3.496	3.492	3.498	3.526	3.530
Twist (rad)	0.0071	0.0114	0.0070	0.0061	0.0071	0.0079	0.0076
Edge and mixed component TD density (x10^{10} cm^{-2})	0.93	2.46	0.92	0.70	0.94	1.17	1.06
Screw component/edge component (%)	14.6	5.3	19.9	16.9	17.1	14.9	18.9

In our case, the R593 exhibits the least screw/mixed (1.18 x 10^9 cm^{-2}) and edge/mixed type dislocations (7 x 10^9 cm^{-2}), and it is the sample with highest strain (4.21 GPa).

3.3.4.2 *Screw and edge dislocation density*

Up to now, we have determined the dislocation density by HRXRD and we have to compare these results with the TEM observations. In order to observe the TD on the top surface of InN, a [0001] plan view sample of R117 was prepared. All TD density types (screw, edge and mixed) can be visible with a $<1\bar{2}1\bar{3}>$ zone axis at 31.4° away from <0001> zone axis under bright field conditions.[51] From plan view TEM observations (Fig 3.28), the density of TDs reaching the top surface of the InN film is about 7.8 x 10^{10} cm^{-2}. In Fig 3.28, the dislocations show up as small black segments.[51]

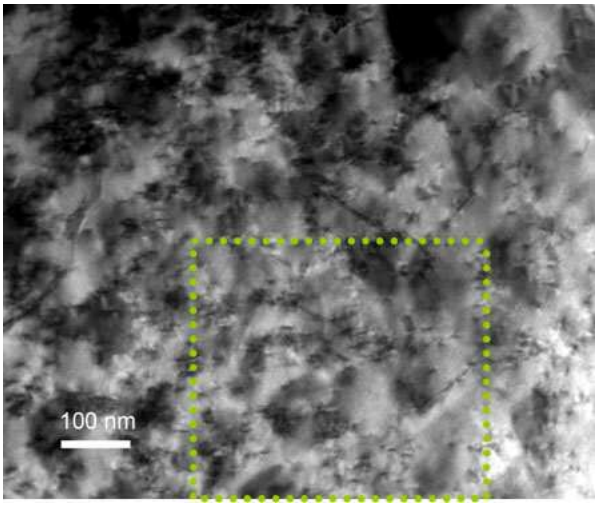

Fig 3.28 Plan-view TEM image of R117 sample.

In order to determine the percentage of each kind of dislocations the samples were prepared by cross section TEM. We have used the reflection conditions **g** = 0002, $\mathbf{g}=11\bar{2}0$, and $\mathbf{g} = 10\bar{1}0$ to characterize the dislocations types and then three corresponding TEM images were obtained and compared. With **g** = 0002 reflection, only the dislocations with Burgers vectors having a component along the *c* axis are visible whereas with a reflection in the basal plane, the visible

dislocations were those with *a* component in the basal plane. If the dislocations are visible in both images, then the dislocations possess mixed type (*a*+*c*) of Burger vector.[52]

Fig 3.29 shows g-3g weak beam TEM images taken in [$10\bar{1}0$] zone axis of InN/GaN (R593 sample) with three different diffraction vectors **g** (the orange square is a guide for the eye to check and compare the same area). Fig 3.29(a)-(b), with diffraction vector **g** = ($10\bar{1}0$) and **g** = ($11\bar{2}0$) make visible the *a*-type threading dislocation (edge dislocations) and mixed type *a*+*c* dislocations. The TD were noticed as bright lines propagating in a direction normal to the substrate surface and many dislocation lines in the near-interface InN/GaN region were oriented irregularly. According to the ***g*** ***b*** criteria described in *Chapter 2*, it can be concluded that the TD have Burgers vectors parallel to the substrate surface and therefore edge- and mixed type dislocations were the main dislocations observed.

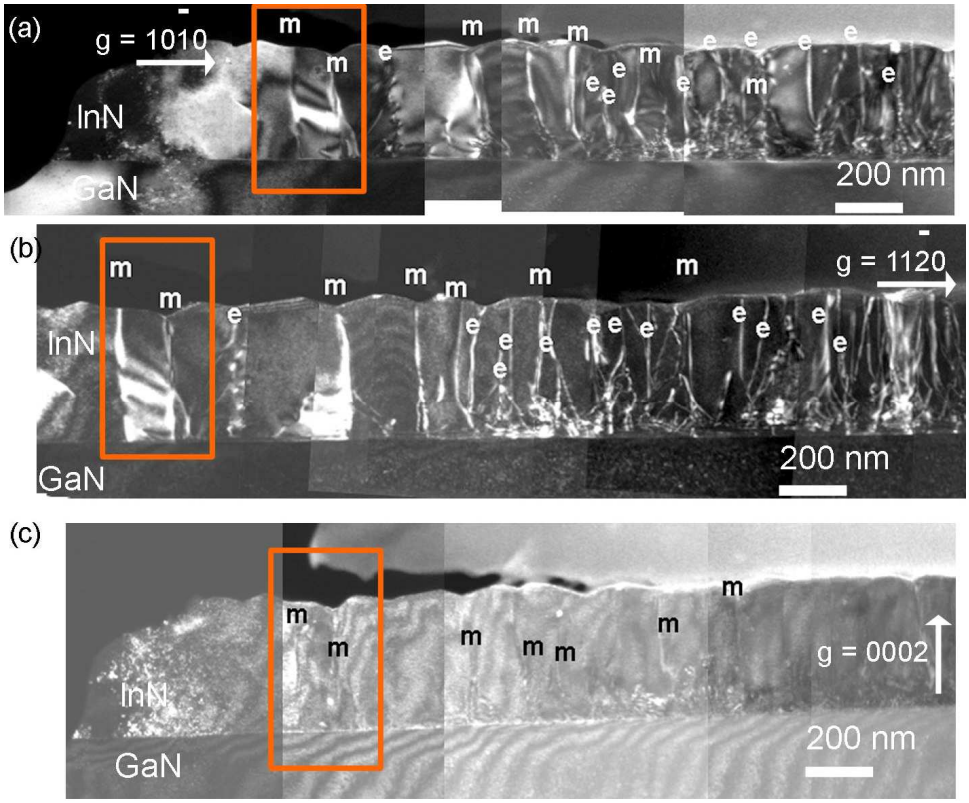

Fig 3.29 Cross-section TEM images of InN/GaN (R593) taken under (a) **g** = $10\bar{1}0$ dark field image (b) **g** = $11\bar{2}0$ dark field image and (c) g-3g weak beam with **g** = 0002 image diffraction conditions. Only edge (e) and mixed (m) TD density were identified on these micrographs.

Comparing the previous images with Fig 3.29(c), where the diffraction vector was **g** = (0002), we can notice that the dislocations observed in this condition are also present in the two other images, meaning that these dislocations are of mixed type. On the TEM images the dislocations types (e = edge, and m= mixed) are marked. On the other hand, pure screw dislocations were not observed in this sample area.

The cross sectional TEM images showed a wavy top surface, suggesting that the InN film has a 3D growth mode, in agreement with AFM observation where the rms roughness value was about 7.56 nm (Fig 3.10).

As we mentioned previously (*section 3.3.1)*, the samples grown in N-rich conditions have high rms roughness as well as 3D mode grown. If we take sample R117 grown on Si(111), it can be seen (Fig 3.30) that it exhibits also a wavy top surface InN similar to R593 (Fig 3.29).

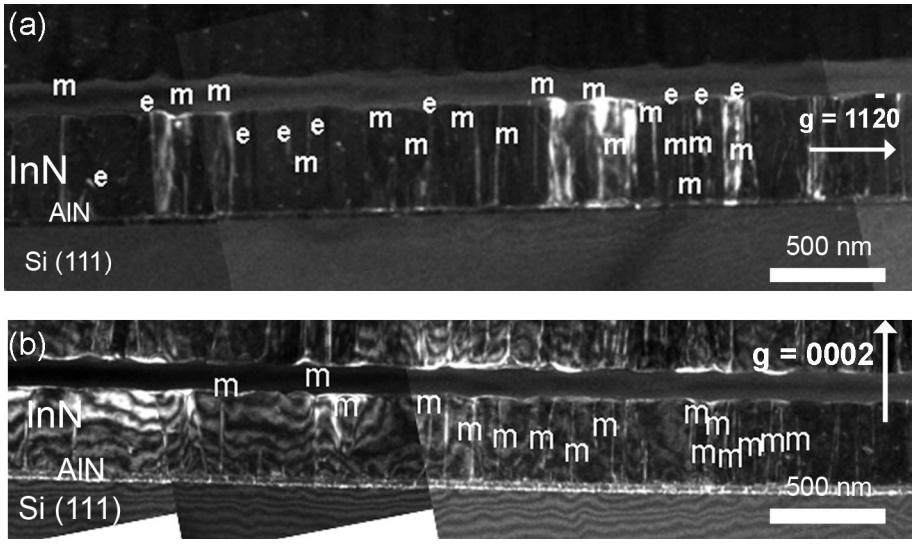

Fig 3.30 Cross-section micrograph of sample R117 (InN/AlN/Si (111)) taken under (a) **g** = $11\bar{2}0$ and (b) **g** = 0002, both in dark field mode. Mainly, mixed (m) and edge (e) dislocations are observed in these images, and no screw dislocations can be noticed.

The relative number of different types of TD (egde, mixed and screw) were investigated by recording dark field images under **g** = ($11\bar{2}0$) and **g** = (0002) reflections. In the first image (Fig 3.30(a)), only the edge and mixed-type dislocations are visible, whereas on the second one, only mixed-type dislocations are in contrast (Fig 3.30(b)). Therefore, as can be seen, the screw dislocations are

not visible in this area sample. At variance with the previous sample (R593), the TDs near to the interface InN/AlN region are oriented parallel to the *c*-axis.

If now we move to the samples grown in In rich conditions, choosing as an example R338, it can be seen that they exhibit a flat top surface (Fig 3.31), in agreement with the step growth morphology as pointed out by the AFM observations (the rms roughness is 0.79 nm). In this 0002 WBDF image, a few screw or mixed type dislocations can be noticed. The two TD lines denoted by 1 and 2 in GaN threaded into InN film. The defect (number 3) is a surface pinhole of ~ 92 nm diameter; such defects were also observed by AFM (Fig 3.9(b)).

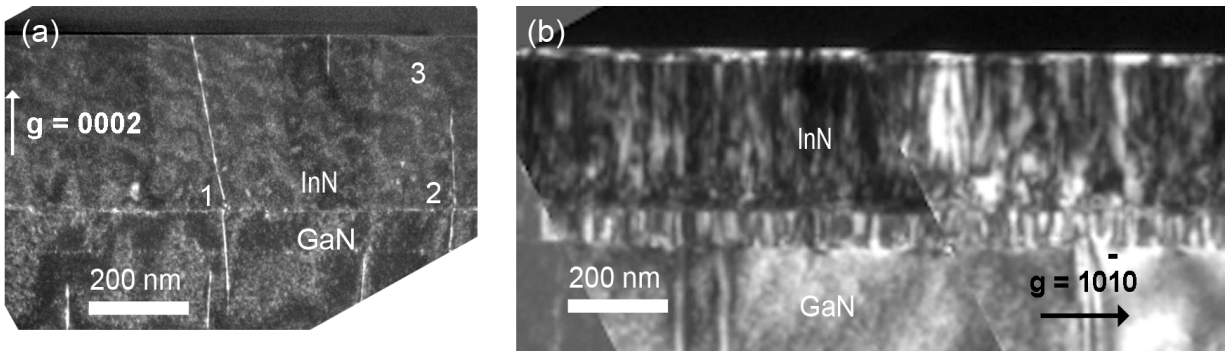

Fig 3.31 Cross-sectional dark field TEM image (a) **g** = 0002 and (b) **g** = $10\bar{1}0$ of InN film grown on GaN buffer layer (R338).

Up to now, we observed that the number of screw and mixed type dislocations was quite small in comparison with that of the edge type. During our observations, it was noticed that for R489 samples grown at 400 °C under In-rich conditions, the density of the mixed and screw type could be consistently increased. As shown in Fig 3.32(a)-(b), WBDF images taken with **g** = 0002 and **g** = $11\bar{2}0$ reflections, many dislocations with a screw component were generated at the InN/GaN interface and propagated inside the InN layer (in Fig 3.32(b) we have also new pure edge dislocations).

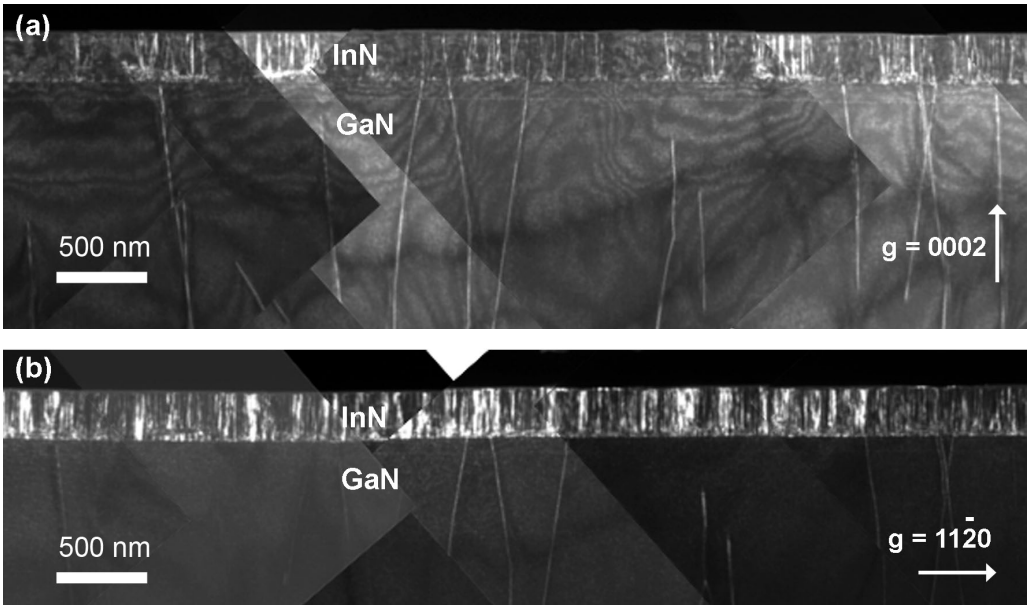

Fig 3.32 WBDF cross-sectional TEM images of R489: (a) g = 0002 (showing screw and mixed-types TDs) (b) g = 11$\bar{2}$0 (showing both edge- and mixed TDs).

On all samples we have carried out the same analysis to identify the dislocation types and their percentages; the results are given in Table 3.8 for the densities of threading dislocations inside the InN layers.

Table 3.8 Summary of dislocation types for all MBE-InN samples.

	Edge TD (%)	**Screw TD (%)**	**Mixed TD (%)**	**Total TD (x10^{10} cm^{-2})**
R374	72	---	28	4.0
R593	65	---	35	1.8
R489	50	---	50	5.4
R338	80	---	19	3.6
R512	>95			4.4
R117	50	<1	~ 49	2.2
R135	56	<1	~ 43	3.2

So, the edge-type dislocations are the predominant type in InN films, showing that the TEM results are in agreement with the HRXRD data and no or few screw dislocation are observed in the area analysed.

Previously, it was mentioned that using <1$\bar{2}$1$\bar{3}$> zone axis on plan view samples, all dislocations were visible (edge, screw and mixed).[51] On the other

hand, when the sample was tilted by about 18° away from <0001> zone axis under bright field conditions, the TEM image was provided using two-beam diffraction conditions with **g** = $(11\bar{2}0)$. In this way, it was possible to identify the edge and mixed dislocations, but screw dislocations were invisible.[53] With this method we can reveal the screw dislocations density comparing the total dislocation density of both images. In order to observe that difference, a plan view sample was prepared (R512). A plan view bright field image was taken under **g** = $<1\bar{2}1\bar{3}>$ diffraction condition and a high density of TD was displayed (Fig 3.33(a)). Counting the total dislocations density from a large area, a density of 3.85 x 10^{10} cm^{-2} was obtained. In Fig 3.33(b), the plan view image was taken under **g** = $<11\bar{2}0>$. Under these conditions, only the edge and mixed TD were visible with 2.38 x 10^{10} cm^{-2} density. This small difference may be due to the fact that under the $<11\bar{2}0>$ conditions, some edge or mixed type dislocation may be not visible as have pointed out Datta *et al.*[51] Therefore, as deduced from cross section observations, the number of screw dislocations is very low in our samples.

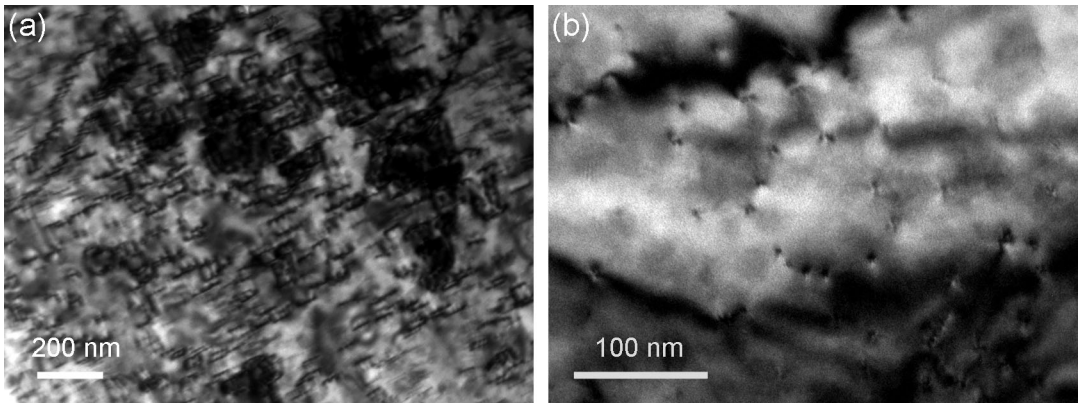

Fig 3.33 Plan view images on R512 sample: (a) bright field **g** =$<1\bar{2}1\bar{3}>$ zone axis image - all type dislocations are visible, (b) **g** = $<11\bar{2}0>$ zone axis - edge and mixed dislocations are visible.

These results are in the same range as other authors who used PA-MBE for InN layers in the same thickness range;[23] when much thicker layers have been grown, the density of dislocation could be reduced by more than one order of magnitude.[54] If now we try to compare the TEM results with those from HRXRD, we notice that the two densities of screw and edge component dislocations

obtained by HRXRD include the mixed type dislocations. However, as seen just above, the density of pure screw dislocations density should be negligibly small in comparison with the edge component plus the screw component dislocations. Therefore, in a first approximation, the total density of dislocations as measured by HRXRD are very close to the edge component ones and the measured screw/mixed density of dislocations corresponds only to mixed type dislocation.

As shown it Table 3.9, we notice that the dislocation density as measured by TEM and HRXRD vary from one sample to the next, and the TEM numbers are always higher than from XRD. The variation goes from about two to five times. In our calculations we have used a random distribution model for the dislocations, however, when looking at the sample investigated in plane view TEM (Fig 3.33), it can be seen that the distribution is most probably in the form of subgrain boundaries. This may probably be at the origin of the discrepancy, in agreement with Chierchia *et al*.[48]

Table 3.9 Comparison of the total dislocations by the two different techniques.

	R374	**R489**	**R338**	**R593**	**R512**	**R135**	**R117**
TOTAL TD by HRXRD ($x10^{10}$ cm^{-2})	0.93	2.46	0.92	0.70	0.94	1.17	1.06
TOTAL TD by TEM ($x10^{10}$ cm^{-2})	4.0	5.4	3.6	1.8	4.4	3.2	2.2

3.4 Discussion

If we compare the total TDs density extracted by HRXRD and that measured from TEM images (Fig. 3.34), in almost all the samples, the dislocation density appears to decrease with increasing thickness. However, for the thickest layer, the dislocation density is highest as measured by plan view TEM. In these HRXRD calculations, we have used the random distribution model, meaning that this model may not be applicable to the studied layers.

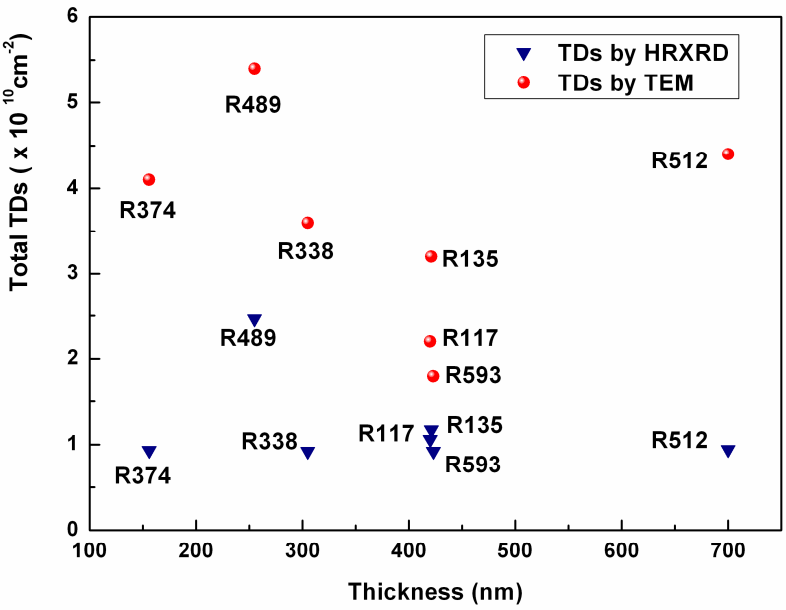

Fig. 3.34 Comparison of TDs determined by HRXRD using a random distribution model and TEM for the MBE-InN samples.

Indeed Chierchia *et al.*[48] as well as Liu *et al.*[50] reported that a good agreement between TEM, AFM and HRXRD, and between TEM and HRXRD respectively, can be achieved for the measurement of threading dislocations using the grain boundary dislocation mosaic model and when the lateral coherence length (grain diameter) is well known. More recently, Gallinat *et al.*[55], in their investigation of MBE InN layers, reported that fair agreement could be obtained if the grain average size was first determined by plan view TEM. So in our case we can focus on samples R512 (see Fig 3.33), the size of the exhibited subgrain is below 100 nm, this is more than 5 times smaller than the values obtained by Dimakis *et al.*[45] or Liu *et al.*[50] Assuming that the dislocations are piled inside such subgrains with an average size of 90 nm, the edge TDs are 4 x 10^{10} cm^{-2} in agreement with the plan view of the TEM observations (4.18 x 10^{10} cm^{-2}). So for our samples, the dislocations seem to be completely piled up in the grain boundaries in contrast to the observations of Dimakis *et al.*[45]

In the literature (Table 3.10), Komninou *et al.*[56], reported that in PA-MBE InN films on GaN/Al_2O_3 of thickness around 1 µm, the threading dislocations had a density in the range of 10^9-10^{10} cm^{-2} and the edge dislocation (2.3 x 10^{10} cm^{-2}) were one order the magnitude higher than both pure screw (1.1 x 10^9 cm^{-2}) and

mixed (2.7 x 10^9 cm^{-2}) type dislocations. In the case of thick InN (10 µm) grown on sapphire, Dimakis *et al*.[45] observed a decreased of edge (interface 1.55 x 10^{10} cm^{-2} and surface: 4.35 x 10^9 cm^{-2}) and mixed (interface: 1.69 x 10^9 cm^{-2} and surface: 1.20 x 10^9 cm^{-2}) type dislocation density from the interface to the surface, whereas the screw-type dislocation density remained constant (4.82 x 10^8 cm^{-2}).

Table 3.10 Comparison of TDs found in the literature and our data.

	Sample and thickness		**Threading dislocation by TEM**				**Threading dislocation by HRXRD**	
			Cross section			**Plan view**		
			Screw	Edge	mixed		Screw-component	Edge-component
Komninou *et al.*[56]	InN (1µm)		1.1 x 10^9	2.3 x 10^{10}	2.7 x 10^9		-----	------
Dimakis *et al.*[45]	InN/GaN (10 µm)		4.82 x 10^8	Interface: 1.55x 10^{10} Top: 4.35 x 10^9	Interface: 1.69x 10^9 Top: 1.20 x 10^9		1.29 x 10^9	Random: 2x10^{10} Piled up: 2.7 x10^9
Liu *et al.*[50]	InN (10 µm)		-----	-----	-----		3 x 10^8	Piled up: 4 x10^9
Gallinat *et al.*[55]	InN (1.5 µm)		3 x 10^8	Two orders of magnitude higher than screw		3x10^{10}	1.1 x10^9	Random: 3.5 x 10^{10}
Gherasoiu *et al.*[23]	InN (1µm – 8 samples)		-----	-----	-----		Range:2.3-6.7 x 10^9	Random,range: 6.1 – 13.8 x 10^{10}
O U R D A T A	**R374**	156	-----	2.88 x 10^{10}	1.12 x 10^{10}		1.36 x 10^9	9.3 x 10^9
	R489	255	-----	2.7 x 10^{10}	2.7 x 10^{10}		1.31 x 10^9	2.46 x 10^{10}
	R338	305	-----	2.88 x 10^{10}	6.8 x 10^9		1.83x 10^9	9.2 x 10^9
	R593	483	-----	1.17 x 10^{10}	4.1 x 10^9		1.18 x 10^9	7 x 10^9
	R512	700	-----	4.18 x 10^{10}	2.2 x 10^9	3.85x10^{10}	1.92x 10^9	9.4 x 10^9
	R117	420		1.1 x 10^{10}	1.78 x 10^{10}	7 x 10^{10}	1.74 10^9	1.17 x 10^{10}
	R135	421		1.18 x 10^{10}	1.38x 10^{10}		1.91 x 10^9	1.06 x 10^{10}

In Table 3.10, we show the mixed and edge dislocation type density for our samples; as can be seen, these values are in good agreement with those reported by the above two authors especially for the mixed type dislocations. For one of the samples (R489), the density of mixed type dislocation was one order of magnitude higher (2.7 x 10^{10} cm^{-2}), this may be probably explained by the fact that it was grown at the lowest used temperature (400 °C). Looking at the edge type dislocation density, we always have higher value, this probably can be explained by the fact that we have quite smaller thicknesses than the above authors.

If now we correlate the TDs density with the growth conditions, as can be seen in Fig 3.35, a trend that comes out is that the samples grown in N-rich conditions contain less dislocations.

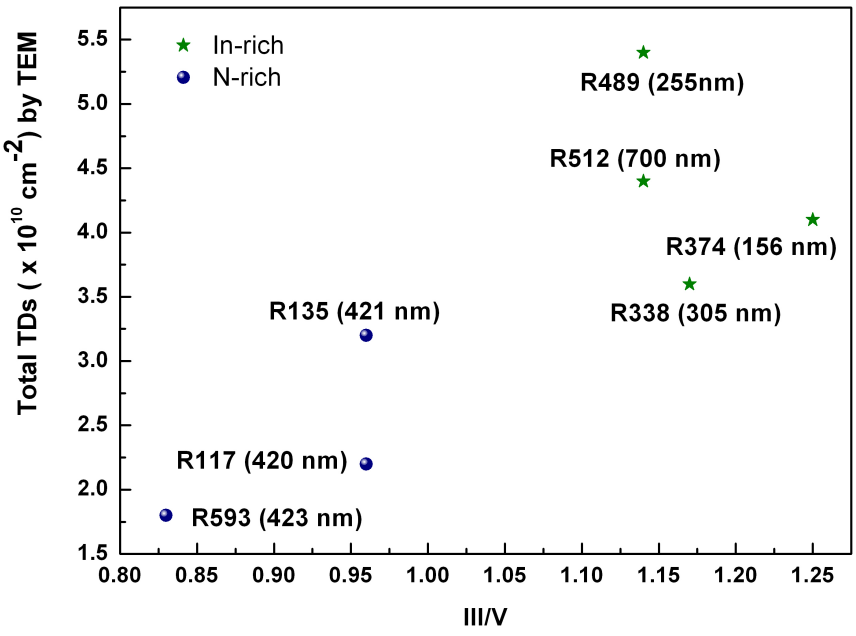

Fig 3.35 Total TDs versus III/V ratio for each sample.

One explanation may be sought in the morphology of the layers as seen by AFM. As may be recalled, the samples grown in N-rich conditions are in the form of large islands which may represented as subgrains, which probably means that each contains a small number of threading dislocations. Indeed, this was also noticed by Gallinat *et al*.[55] who reported that 3D islands decrease the threading dislocations. For these samples grown under N-rich (Table 3.11), we can observe

that those grown on Si substrate (R117 and R135) exhibit lower stress that the R593 grown on sapphire and this last sample has the lower TDs density. This means that the stress was better relieved through the generation of misfit dislocations at the interface between the epilayer and the substrate.[39,57]

Tabla 3.11 Summary of InN under In-rich and N-rich conditions.

	In-rich				N-rich		
	R374	**R489**	**R338**	**R512**	**R593**	**R135**	**R117**
Thickness (nm)	156	255	305	700	483	421	420
TOTAL TD by HRXRD ($x10^{10}$ cm^{-2})	0.93	2.46	0.92	0.94	0.70	1.17	1.06
TOTAL TD by TEM ($x10^{10}$ cm^{-2})	4.0	5.4	3.6	4.4	1.8	3.2	2.2
σ_{xx} (GPa)	-2.34	-3.63	-3.72	-3.62	-4.21	-0.92	-0.77
Carrier density ($x10^{18}$ cm^{-3})	3.2	4.3	1.5	2	3	8	17
N flux Φ_N (nm/min)	9	8.33	9	8.33	8.33	8.33	8.33

Looking at the carrier densities, we notice that samples R117 and R135 have the highest density of all the samples with a better value for R593 which has been grown at a more elevated temperature. Therefore, notwithstanding the better strain relaxation observed, it is possible that this island morphology and high carrier densities may not be optimal for device application.

Now moving to the samples grown in In rich conditions, we notice that at the lowest temperature (R489) we have the most complex morphology by AFM, and the highest density of dislocations (Fig. 3.35). This is agreement with Cuscó *et al.*[58] who reported that MBE-InN layers with most predominant pits exhibit highest carrier densities. For the other three samples, (R512, R338, R374), the TDs densities (4.4, 3.6, 4 x $10^9 cm^{-2}$) as well as the residual free carrier densities (2, 1.5, 3.2 x 10^{18} cm^{-3}) are comparable (Table 3.11). Looking at the growth temperatures of these samples, it should also be noticed that they are comparable if we take into

account the associated large error bars (see Fig 3.36). However, other parameters also appear to be important in determining the layer quality (Table 3.12).

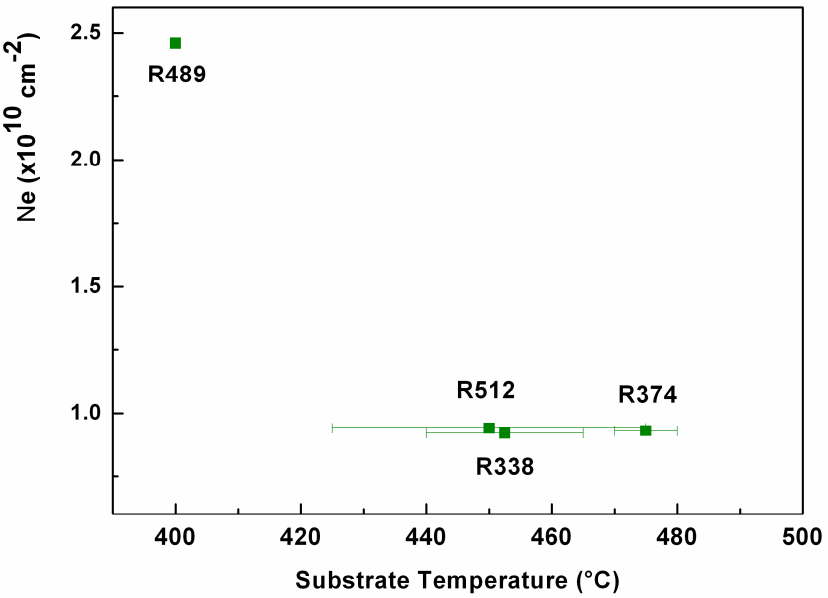

Fig 3.36 Calculated edge component-type TDs using equation (3.10) on In-rich samples. The TDs are analysed versus the substrate temperature.

In sample R374, the highest carrier concentration may be explained by remembering that this sample has been grown with the lowest V/III ratio of 0.8, whereas a higher one of 0.88 was used for sample R512.

Table 3.12 Results on R374, R512 and R338.

	R374	**R512**	**R338**
Thickness (nm)	156	700	305
Growth rate (nm/min)	7.5	8.3	8.8
V/III	0.8	0.88	0.86
Temperature (°C)	470-480	420-470	440-465
Carrier density (x 10 ^{18} cm^{-3})	3.2	2	1.5
TOTAL TD by TEM (x10^{10} cm^{-2})	4	4.4	3.6

Another interrelated parameter during the growth may also be the growth rate, we notice that the lowest carrier concentration was obtained at the highest growth rate of 8.8 nm/min. As reported by many authors (Gallinat *et al.*[55]) these

indium rich growth conditions lead to spiral growth for sample R374 and R512. This is probably at the origin of the closest measured dislocation density for the two samples, meaning that we are in the presence of similar mosaic blocks.

In summary, we have investigated InN films grown by three different methods. We have mainly focused on MBE-grown InN samples whose structural quality was the best as pointed out by the Raman measurements. For these samples, a non pure biaxial stress was observed and point defect analysis is an important result for understanding the presence of a hydrostatic component in the residual stress. The HRXRD calculated TD dislocation densities using a non random dislocation model (dislocation located at the grain boundaries) are in good agreement with the one determined by TEM. The corresponding densities are within the 10^{10} cm^{-2} range, in agreement with the results of the literature on MBE InN layers of comparable thicknesses. From these observations, it can be pointed out that obtaining high quality InN layers is a still complicated process, even by MBE. The best sample may not exhibit the perfect surface morphology, has In metallic and In oxide extra phases located in the top film part but interestingly, it shows the lowest carrier and dislocation densities.

Reference

[1] Y. Huang, H. Wang, Q. Sun, J. Chen, D. Y. Li, J. C. Zhang, J. F. Wanf, Y. T. Wang, H. Yang. *Evolution of mosaic structure in InN grown by metalorganic chemical vapor deposition.* J. Cryst. Growth **293**, 269 (2006).

[2] K.S.A. Butcher, M. Wintrebert-Fouquet, P. P.-T. Chen, T. L. Tansley, H. Dou, S. K. Shrestha, H. Timmers, M. Kuball, K.E.Prince, and J. E. Bradby. *Nitrogen-rich indium nitride.* J. Appl. Phys. **95**, 6124 (2004).

[3] Q. X. Guo, T. Tanaka, M. Nishio, H. Ogawa, X. D. Pu, and W. Z. Shen. *Observation of visible luminescence from indium nitride at room temperature.* Appl. Phys. Lett. **86**, 231913 (2005).

[4] Y. Kumagai, J. Kikuchi, Y. Nishizawa, H. Murakami, A. Koukitu. *Hydride vapor phase epitaxy of InN by the formation of $InCl_3$ using In metal and Cl_2.* J. Cryst. Growth **300**, 57 (2007).

[5] A. L. Syrkin, V. Ivantsov, A. Usikov, V. A. Dmitriev, G. Chambard, P. Ruterana, A. V. Davydov, S. G. Sundaresan, E. Lutsenko, A. V. Mudryi, E. D. Readinger, G. D. Chern-Metcalfe, and M. Wraback. *InN layers grown by the HVPE.* Phys. Stat. Sol. C **6**, 1792 (2008).

[6] F. Sotkker-Cheregi, A. Nedelcea, M. Filipescu, A. Moldovan, D. Colceag, V. Ion, R. Bîrjega, and M. Dinescu. *High temperature growth of InN on various substrates by plasma-assisted pulsed laser depositon.* Appl. Surface Science **257**, 5312 (2011).

[7] A. Pelli, K. Saarinen, F. Tuomisto, S. Ruffenach, and O. Briot. *Influence of V/III molar ratio on the formation of In vacancies in InN grown by metal-organic vapour-phase epitaxy.* Appl. Phys. Lett. **89**, 011911 (2006).

[8] Y. Nanishi, Y. Saito, and T. Yamaguchi. *RF- Molecular beam epitaxy growth and properties of InN and related alloys.* Jpn. J. Appl. Phys. **42**, 2549 (2003).

[9] X. Wang, S. Chen, W. Lin, S. Li, H. Chen, D. Liu, and J. Kang. *Structural properties of InN films grown in different conditions by metalorganic phase epitaxy.* J. of Material Research **26**, 775 (2011).

[10] P. Ruterana, A. L. Syrkin, E. Monroy, E. Valcheva, and K. Kirilov. *The microstructure and properties of InN layers.* Phys. Stat. Solidi **7**, 1301 (2010).

[11] V. Darakchieva, P. P. Paskov, T. Paskova, E. Valcheva, B. Monemar, and M. Heuken. *Lattice parameters of GaN layers grown on a-plane sapphire: Effect of in-plane strain anisotropy.* Appl. Phys. Lett. **82**, 703 (2003).

[12] C. A. Arguello, D. L. Rousseau, and S. P. S. Porto. *First-order Raman effect in Wurtzite-Type Crystals.* Phys. Rev. B **181**, 1351 (1969).

[13] C. Pinquier, F. Demangeot, J. Frandon, J. W. Pomery, M. Kuball, H.Hubel, N. W. A. van Uden, D. J. Dunstan, O. Briot, B. Maleyre, S. Ruffenach, and B. Gil. *Raman scattering in hexagonal InN under high pressure.* Phy. Rev. B **70**, 113202 (2004).

[14] V. Darakchieva, P. P. Paskov, E. Valcheva, T. Paskova, and B. Monemar. *Deformation potentials of the $E_1(TO)$ and E_2 modes of InN.* Appl. Phys. Lett. **84**, 3636 (2004).

[15] J. Arvanitidis, M. Katsikini, S. Vs, Th. Kehagias, Ph. Komninou, E. Dimakis, E. Iliopoulos, and A. Geogakilas. *Raman and transmission electron microscopy characterization of InN samples grown on GaN/Al_2O_3 by molecular beam epitaxy.* Phys. Stat. Sol B **243,** 1588 (2006).

[16] T. Kozawa, T. Kachi, H. Kano, Y. Taga, M. Hashimoto, N. Koide, K. Manabe. *Raman scattering from LO phonon-plasmon coupled modes in gallium nitride.* J. Appl. Phys. **75**, 1098 (1994).

[17] J. S. Thakur, D. Haddad, V. M. Naik, R. Naik, G. W. Auner, H. Lu, and W. Schaff. *A_1(LO) phonon structure in degenerate InN semiconductor films.* Phys. Rev. B **71**, 115203 (2005).

[18] C. Pinquier, F. Demangeot, J. Frandon, M. Gaio, O. Briot, B. Maleyre, S. Ruffenach, and B. Gil. Mater. Res. Soc. Symp. Proc. Vol. 831, E4.8.1 (2005).

[19] Y.-M. Chang, C. T. Chuang, C. T. Chia, K. T. Tsen, H. Lu, and W. J. Schaff. *Coherent longitudinal optical phonon and plasmon coupling in the near-surface region of InN.* Appl. Phys. Lett. **85**, 5224 (2004).

[20] M. Kuball, J. W. Pomeroy, M. Wintrebert-Fouquet, K. S. A. Butcher, H. Lu, W. J. Schaff. *A Raman spectroscopy study of InN.* J. Cryst. Growth. **269**, 59 (2004).

[21] C. Pinquier, F. Demangeot, J. Frandon, O. Briot, B. Maleyre, S. Ruffenach, B. Gil, J. Pomeroy, M. Kuball, H. Hubel, N. van Uden, and D. Dunstan. *Raman scattering in InN films and nanostructures.* Superlattices and Microstructures **36**, 581 (2004).

[22] K. Kim, W. R. L. Lambrecht, and B. Segall. *Elastic constants and related properties of tetrahedrally bonded BN, AlN, GaN, and InN.* Phys. Rev B **53**, 16310 (1996).

[23] I. Gherasoiu, M. O'Steen, T. Bird, D. Gotthold, A. Chandolu, D. Y. Song, S. X. Xu, M. Holt, S. A. Nikishin, and W. J. Schaff. *Characterization of high quality InN grown on production-style plasma assisted molecular beam epitaxy system.* J. Vac. Sci. Technol. A **23**, 399 (2008).

[24] Y. Saito, H. Harima, E. Kurimoto, T. Yamaguchi, N. Teraguchi, A. Sukuki, T. Araki, and Y. Nanishi. *Growth temperature dependence of Indium Nitride Crystalline quality grown by RF-MBE.* Phys. Stat. Sol b. **234**, 796 (2002).

[25] C. S. Gallinat, G. Koblmüller, J. S. Brown, S. Bernardis, J. S. Speck, G.D. Chern, E. D. Readinger, H. Shen, and M. Wraback. *In-polar InN grown by plasma-assisted molecular beam epitaxy.* Appl. Phys. Lett. **89**, 032109 (2006).

[26] G. Koblmüller, C. S. Gallinat, S. Bernardis, J. S. Speck, G.D. Chern, E. D. Readinger, H. Shen, and M. Wraback. *Optimization of the surface and structural quality of N-face InN grown by molecular beam epitaxy.* Appl. Phys. Lett. **89**, 071902 (2006).

[27] A. Vilalta-Clemente, G. R. Mutta, M. P. Chauvat, M. Morales, J. L. Doulan, P. Ruterana, J. Grandal, M. A. Sánchez-García, F. Calle, E. Valcheva, and K. Kirilov. *Investigation of InN layers grown by molecular beam epitaxy on GaN templates.* Phys. Status Solidi A **207**, 1079 (2010).

[28] C.S. Gallinat, G. Koblmüller, J. S. Brown, and J. S. Speck. *A growth diagram for plasma-assisted molecular beam epitaxy of In-face InN.* J. Appl. Phys. **102**, 064907 (2007).

[29] Y. F. Ng, Y. G. Cao, M. H. Xie, X. L. Wang, and S. Y. Tong. *Growth mode and strain evolution during InN growth on GaN (0001).* **81**, 3960 (2002).

[30] K. Kubota, Y. Kobayashi,and K. Fujimoto. *Preparation and properties of III-V nitride thin films.* J.Appl. Phys. **66**, 2984 (1989).

[31] W. Paszkowicz, *X-ray powder diffraction data for indium nitride.* Powder Diffraction **14**, 258 (1999).

[32] V. Y. Davydov, A. A. Klochikhin, R. P. Seisyan, V. V. Emtsev, S. V. Ivanov, F. Bechstedt, J. Furthmüller, H. Harima, A. V. Mudryi, J. Aderhold, O. Semchinova, and J. Graul. *Absorption and Emission of Hexagonal InN. Evidence of narrow Fundamental Band Gap*. Phys. Status Solidi B **229**, R1 (2002).

[33] E. Dimakis, K. Tsagaraki, E. Iliopoulos, Ph. Komninou, Th. Kehagias, A. Delimitis, and A. Georgakilas. *Correlation between nucleation, morphology and residual strain of InN grown on Ga-face GaN (0001).* J. Cryst. Growth **278**, 367 (2005).

[34] T. L. Tansley, and C. P. Foley. *Optical band gap of indium nitride.* J. Appl. Phys. **59**, 3241 (1986).

[35] A. F. Wright. *Elastic properties of zinc-blende and wurtzite AlN, GaN, and InN*. J. Appl. Phys. **82**, 2833 (1997).

[36] U. Sheleg, and V. A. Savastenko, Izv. Akad. Nauk SSSR, Neorg. Mater **15**, 1598 (1979).

[37] V. Cimalla, Ch. Förster, G. Kittler, I. Cimalla, R. Kosiba, G. Ecke, O. Ambacher, R. Goldhahn, S. Shokhovets, A. Georgakilas, H. Lu, and W. Schaff. *Correlation between strain, optical and electrical properties of InN grown by MBE.* Phys. Status Solidi C **0**, 2818 (2003).

[38] P. Specht, R. Armitage, J. Ho, E. Gunawan, Q. Yang, X. Xu, C. Kisielowski, and E. R. Weber. *The influence of structural properties on conductivity and luminescence of MBE grown InN*. J. Cryst. Growth **269**, 111 (2004).

[39] E. Dimakis, E. Iliopoulos, K. Tsagaraki, A. Adikimenakis, and A. Georgakilas. *Biaxial strain and lattice constants of InN(0001) films grown by plasma-assisted molecular beam epitaxy.* Appl. Phys. Lett. **88**, 191918 (2006).

[40] A. Kadir, T. Ganguli, R. Kumar, M. R. Gokhale, A. P. Shah, S. Ghosh, B. M. Arora, and A. Bhattacharya. *The role of hydrostatic stress in determining the bandgap of InN epilayers.* Appl. Phys. Lett. **91**, 111913 (2007).

[41] K. S.A. Butcher, A. J. Frenandes, P. P.-T. Chen, M. Wintrebert-Fouquet, H. Timmers, S.K. Shrestha, H. Hirshy, R. M. Perks, B. F. Usher. *The nature of nitrogen related point defects in common forms of InN.* **101**, 123702 (2007).

[42] R. Chierchia. *Strain and crystalline defects in epitaxial GaN layers studied by high-resolution X-ray diffraction* PhD Universität Bremen.(2007).

[43] T. Metzger, R. Höpler, E. Born, O. Ambacher, M. Stutzmann, R. Stömmer, M. Schuster, H. Göbel, S. Christiansen, M. Albrecht, and H. P. Strunk. *Defect structure of epitaxial GaN films determined by transmission electron microscopy and triple-axis X-ray diffractometry.* Philosophical Magazine A **77**, 1013 (1998).

[44] C. O. Dunn, and E. Koch. *Comparison of dislocation densities of primary and secondary recrystallization grains of Si-Fe.* Acta metall. **5**, 548(1957).

[45] E. Dimakis, J. Z. Domagala, A. Delimitidis, Ph. Komninou, A. Adikimenakis, E. Iliopoulos, A. Georgakilas. *Structural properties of 10 μm thick grown on sapphire (0001).* Superlattices and Microst. **40**, 246 (2006).

[46] M.A. Moram, and M. E. Vickers. *X-ray diffraction of III-nitrides.* Rep. Prog. Phys. **72**, 036502 (2009).

[47] G. K. Williamson, and W. H. Hall. *X-ray line broadening from filed aluminium and wolfram*. Acta Metal. **1**, 22 (1953).

[48] R. Chierchia, T. Böttcher, H. Heinke, S. Einfeldt, S. Figge, and D. Hommel. *Microstructure of heteroepitaxial GaN revealed by x-ray diffraction.* J. Appl. Phys. **93**, 8918 (2003).

[49] V. Holý, J. Kubìna, E. abramof, K. Lischka, A. Pesek, and E. Koppensteir. *X-ray double and triple crystal diffractometry of mosaic structure in heteroepitaxial layers.* J. Appl. Phys.**74**, 1736 (1993).

[50] B. Liu, R. Zhang, Z.L. Xie, H. Lu, Q. J. Liu, Z. Zhang, Y. Li, X. Q. Xiu, P. Chen, P. Han, S. L. Gu, Y.Shi, Y.D. Zheng, and W. J. Schaff. *Microstructure and dislocation of epitaxial InN films revealed by high resolution x-ray diffraction.* J. Appl. Phys. **103**, 023504 (2008).

[51] R. Datta, M. J. Kappers, J. S. Barnard, and C. Humphreys. *Revealing all types of threading dislocations in GaN with improved contrast is a single plan view image.* Appl. Phys. Lett. **85**, 3411 (2004).

[52] X.H. Wu, L. M. Brown, D. Kapolnek, S. Keller, B. Keller, S. P. DenBaars, and J. S. Speck. *Defect structure of metal-organic chemical vapor deposition-grown epitaxial (0001) GaN/Al_2O_3.*J. Appl. Phys. **80**, 3228 (1996).

[53] D. M. Follstaedt, N. A. Missert, D. D. Koleske, C. C. Mitchell, and K. C. Cross. *Plan-view image contrast of dislocations in GaN.* Appl. Phys. Lett. **83**, 4797 (2003).

[54] K. Wang, T. Kosel, and D. Jena. *Structural and transport properties of InN grown on GaN by MBE.* Phys; Stat. Sol C **6**, 1811 (2008).

[55] C. S. Gallinat, G. Koblmüller, F. Wu, and J. S. Speck. *Evaluation of threading dislocation densities in In- and N-face InN.* J. Appl. Phys. **107**, 053517 (2010).

[56] Ph. Komninou, Th. Kehagias, A. Delimitis, G. P. Dimitrakopulos, J. Kioseoglou, E. Dimakis, A. Geogakilas, Th. Karakostas. *Microstructural assessment of InN-on-GaN films grown by plasma-assisted MBE.* Superlattices and Microstructures **36**, 509 (2004).

[57] K. Aminer, A. Georgakilas, M. Androulidaki, K. Tsagaraki, M. Pavelescu, S. Mikroulis, G. Constantinidis, J. Arbiol, F. Peiro, A. Cornet, M. Calamiotou, J. Kuzmik, and V.Y. Davydov. *Study of the correlation between GaN material properties and the growth conditions of radio frequency plasma-assisted molecular beam epitaxy.* Mater. Sci. Eng. B **80**, 304 (2001).

[58] R. Cuscó, E. Alarcón-Lladó, J. Ibáñez, T. Yamaguchi, Y. Nanishi, and L. Artús. *Raman scattering study of backgroung electron density to the LO-phonon-plasmon-coupled modes.* J. Phys.: Condens. Matter. **21**, 415801 (2009).

Chapter 4

Characterization of InAlN heterostructures

In this chapter, we characterized two types of heterostructures: InAlN/AlN/GaN and InAlN/GaN for HEMTs applications. The layers were fabricated at different growth conditions (temperature, V/III ratio, gas fluxes, etc,…) in three Laboratories (Aixtron, EPFL and III-VLab).

4.1 Introduction

Conventionally for HEMTs applications, the AlGaN/GaN heterostructures exhibit a 2DEG close to the heterointerface of ~ 1.5 x 10^{13} cm^{-2} due to spontaneous and piezoelectric polarization, however the strain effects lead to a low reliability of the device.[1] In 2001, Kuzmík[2] proposed the use of an $In_xAl_{1-x}N$ barrier where at x=0.17-0.18 lattice-matching to GaN is attained, in order to produce strain free devices. The author reported also that, the InAlN brings about a better thermal stability than AlGaN barrier and the corresponding devices could be operated up to 1000 °C. However, this system exhibits low 2DEG density ($n_s/2$), and there is a decrease of mobility from 1500 cm^2/Vs to 120 cm^2/Vs due to alloy disorder scattering (Table 4.1). The introduction of a thin AlN layer at strained AlGaN/GaN interface[3] and lattice matched InAlN/GaN heterostructures has been observed to improve the carrier density, by reducing the alloy scattering of 2DEG and providing a better confinement of the electrons.[4,5] However, the 2DEG mobility and the average sheet resistance are sensitive to the thickness of the AlN interlayer as well as the barrier surface morphology (Fig 4.1).[6]

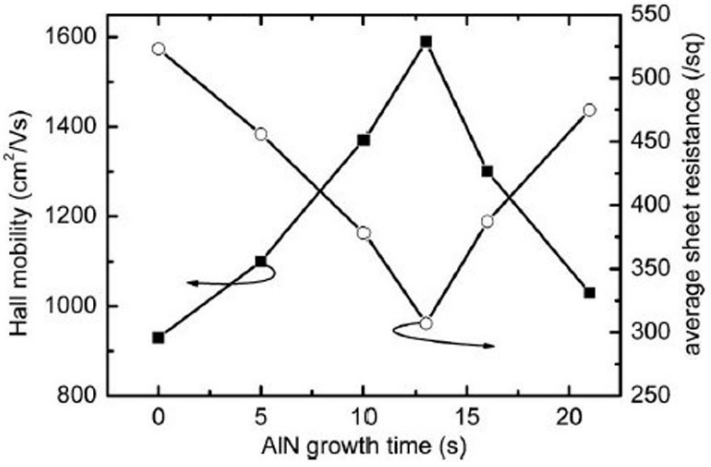

Fig 4.1 Dependence of Hall mobility and the average sheet resistance of $Al_{0.25}Ga_{0.75}N$/GaN herostructures on the growth time of the AlN interlayer.[6]

Gonschorek *et al.*[7] reported that the AlN interlayer thickness should have an optimum value of ~ 1 nm to avoid a reduced channel electron mobility. This is in good agreement with other investigations on AlGaN/GaN HEMT heterostructures, where an optimal AlN interlayer thickness of ~ 1 nm was also reported.[6] Table 4.1 summarizes the main electrical properties for the AlGaN/GaN, AlGaN/AlN/ GaN, InAlN/GaN, and InAlN/AlN/GaN systems.

However, the growth of InAlN alloys is more difficult due to the large structural differences between InN and AlN: the lattice parameter, bonding energies and growth temperatures. Indeed, AlN growth requires high temperature (~ 1000 °C), low pressure, and low ammonia flow rate, while InN growth needs low temperature (~ 500 °C), high ammonia partial pressure, and relatively high chamber pressure to increase In incorporation efficiency. Therefore phase separation and composition inhomogeneity are expected.[8]

Table 4.1 Experimental electrical properties of AlGaN/GaN, AlGaN/AlN/GaN, InAlN/GaN, and InAlN/AlN/GaN systems found in the literature.

	Electron mobility μ_e (cm^2/Vs) 300K	**Sheet carrier density n_s (cm^{-2}) 300K**	**Sheet resistance Rs (Ωsq^{-1}) 300K**	**Reference**
AlGaN/GaN	1500	1.5×10^{13}	250-350	9
$Al_{0.26}Ga_{0.74}N$/AlN (**1nm**)/GaN	2100	1×10^{13}	---	5
$Al_{0.37}Ga_{0.63}N$/AlN(**1 nm**)/GaN	1500	2.15×10^{13}	194	3
$In_{0.18}Al_{0.82}N$ /GaN	---	2.7×10^{13}	---	2
$In_{0.18}Al_{0.82}N$ /GaN	120	2.42×10^{13}	---	10
$In_{0.18}Al_{0.82}N$/AlN(**1.1nm)**/GaN	1550	1.16×10^{13}		10
$In_{0.18}Al_{0.82}N$/AlN(**1.1nm**)/GaN	1170	2.6×10^{13}	210	7
$In_{0.18}Al_{0.82}N$/AlN(**2.1nm**)/GaN	630	3.0×10^{13}	330	7
$In_{0.18}Al_{0.82}N$/AlN(**1 nm**)/GaN	1630	1.20×10^{13}	320	11
$In_{0.18}Al_{0.82}N$/AlN(**2 nm**)/GaN	1100	1.46×10^{13}	386	11
$In_{0.16}Al_{0.84}N$/GaN/Si (111)	406	3.2×10^{13}	---	12

The growth of InAlN/GaN heterostructures can be done using MBE, MOCVD and pulsed MOCVD.[13] Currently, phase separation and composition

inhomogeneity in InAlN has been reported in several works, normally linked to relaxation processes during the growth.[14,15,16]

Redondo-Cubero *et al*.[17] reported the composition inhomogeneity of InAlN/GaN grown close to lattice-matched conditions by RBS/C and XRD. They also mentioned that an initial pseudomorphic film was formed, with good single crystalline quality, nominal composition and a very low strain state. It seems that beyond a ~50 nm critical thickness, the InN molar fraction of the films drops to ~15 % and at the same time the single crystalline quality of the films degrades drastically.

Few TEM studies of MBE-grown InAlN lattice matched to GaN have revealed a microstructure indicative of phase separation. Zhou *et al*.[18] observed lateral nonuniformities in composition in InAlN epilayers with In composition between x = 0.128 and 0.175. A hexagonal honeycomb structure was reported using TEM, with cells of 5 to 10 nm in diameter, oriented parallel to the (0001) growth direction. STEM-HAADF was then used to show that the cell walls were In-rich. The authors concluded that this structure did not develop by spinodal decomposition. Instead, they proposed a mechanism in which compositional nonuniformities are initiated at the early stages of growth. In a later study of similar MBE-grown material, Sahonta *et al*.[19] observed similar honeycomb structures. The authors disagreed with the formation mechanism proposed by Zhou *et al*.[18], and instead suggested that the In composition modulations could be attributed to the initial formation of Al-rich platelets, due to the high sticking coefficients of Al on GaN at a lower growth temperatures. Incorporation of In is increased at platelet boundaries, leading to the honey structure.

For MOVPE InAlN layers, Kret *et al*.[20] reported that, in a 190 nm thick layer, there formed columns of same orientation, but with non uniform composition. In this instance, the maximum Al content was observed in the central part of the columns and with a highest In concentration toward the layer surface. Kehagias *et al*.[21] reported indium segregation on the apexes of the V-defects pyramids in $In_xAl_{1-x}N$ and explained its origin by strain relaxation along the dislocation lines and faster migration of In compared to Al. Mouti *et al*.[22] proposed that screw

component TDs shear stress was capable of inducing a local indium segregation in the core, and that at their top pits formed with indium-rich star shapes.

4.2 Sample description

The samples described in this chapter were grown by MOVPE in Aixtron 200RF horizontal reactors in two different laboratories: III-V Alcatel-Thales and EPFL, whereas the Aixtron samples have been grown in an Aixtron 3x2 inch Close Coupled Showerhead MOCVD reactor; in the following Table these have been identified as: AECi, Aii, and Aixiii, respectively.

The first sets were HEMTs heterostructures made of an InAlN barrier (thickness in the range 10-33 nm) and an AlN interlayer (thickness 0-7.5 nm) on GaN/Al_2O_3. The growth conditions for their InAlN/AlN/GaN HEMT heterostructures are presented in Table 4.2.

Table 4.2 Sample summary with main growth conditions, structural parameters, and the thickness of the layers measured by TEM.

	T_{growth} (°C)		**V/III**	**Pressure (mbar)**		**Thickness InAlN(nm)**	**Thickness AlN(nm)**	**Estimated In content (%)**	**Ns (x 10^{13} cm^{-2})**
	InAlN	**AlN**		**InAlN**	**AlN**	**Nominal /measured by STEM**	**Nominal /measured by STEM**		
Aix3234	790	790	5000	70	70	16/14.9	0/0	13.9	3.24 [23]
Aix3232	790	790	5000	70	70	33/33	1/1.4	12.7	3.34 [23]
Aix3233	790	790	5000	70	70	16/14.1	2.5/1.9	13.9	3.01 [23]
Aix3235	790	790	5000	70	70	16/14.9	7.5/6.9	13.9	2.05 [23]
AEC1681	865	1200	2200	70	50	10.8/7.6	1/3.6	18	1.29
AEC1778	865	1200	2200	70	50	14/9.2	1/4.5	18.5	1.20
AEC1769	865	1200	2200	70	50	10.9/7.9	1/4.6	19.9	1.16
AEC1770	865	1200	2200	70	50	10/4.8	1/3.1	18.9	1.27
AEC1849	865	1200	2200	70	50	10/4.8	4/3.9	17.6	1.50
A816	850	850	787	75	75	14/14	0/0	18	2.49 [7]
A856	850	850	787	75	75	14/14.2	0.6/1.4	18	2.72 [7]
A854	850	850	787	75	75	14/14.4	1.14/1.2	18	2.55 [7]
A852	850	850	787	75	75	14/13.5	2.08/3	18	2.98 [7]

For Aixtron samples the growth temperature on both InAlN and AlN layers was the same (790 °C), whereas for the AEC samples the AlN interlayer was grown at a higher temperature (1200 °C) and for InAlN layer the growth temperature was around 865 °C. The other different variables parameters between the samples were the V/III ratios (the ratio of the NH_3 molar flow versus group III molar flow). V/III ratio was 5000 in Aixtron samples, 2200 for AEC and lower ~ 790 for EPFL. The nominal thicknesses for the different samples (and the thicknesses measured by STEM) and the In content deduced from XRD rocking curves are shown in the Table 4.2. We also include the electron density of the 2DEG (Ns) as it is an important parameter for the HEMT heterostructures.

The second set consisted of heterostructures with different thicknesses of InAlN directly grown on GaN without deposition of an AlN interlayer. Table 4.3 summarizes the growth conditions such as the growth temperature for the InAlN layer, the V/III ratio and the pressure. This table also includes the nominal InAlN, TEM measured thicknesses and the estimated In content determined using XRD rocking curves. All these data have been supplied by the two laboratories (Thales and EPFL).[24,25] The range of growth temperatures for these samples was between 770-860 °C. For the AEC samples, the V/III ratio was 2500, whereas for sample A1583 it was 787, and the other EPFL samples the V/III ratio was in the 138–166 range.

Table 4.3 Summary of MOVPE growth parameters used for $In_xAl_{1-x}N$ on GaN template.

	T_{growth} InAlN (°C)	V/III	Pressure (mbar)	Nominal InAlN thickness (nm)	InAlN thickness measured by TEM (nm)	Estimated In content (%)
AEC1657	860	2500	70	100	90	16.26
AEC1655	860	2500	70	150	150	21
AEC1323	800	2500	70	225	260	----
A1583	850	787	75	30	30	18
A383	810	138	75	100	125	16
A1288	825	157	75	100	105	20
A1843	770	166	75	120	172	21
A1363	820	157	75	250	336	19

4.2.1 HEMT heterostructures

4.2.1.1 *Cross section InAlN/AlN observations and surface morphology*

In these types of heterostructures the top InAlN layer are the more important as the active part of the devices is here. So we focused on the InAlN/AlN interfacial area. The analysis of defects is necessary as they are detrimental to the device efficiency. Therefore, to study the InAlN structure and surface morphology we have chosen the four Aixtron samples with different nominal AlN thicknesses ranging from 0 to 7.5 nm.

Fig 4.2(a)-(d) shows cross sectional TEM images under weak beam conditions with **g** = 0002 reflections for Aix3234, 3232, 3233 and 3235. For samples with nominal AlN thicknesses larger than 1 nm, the AlN interlayer was clearly identified in the cross section TEM images. The measured TEM are respectively smaller and higher than the given nominal thickness for respectively Aix3232 (t_{AlN} = 1.8 nm) and samples Aix3233 (t_{AlN} = 2.1 nm) and Aix3235 (t_{AlN} = 6.9 nm). This interlayer was uniform for $t_{AlN} \leq$ 2.1 nm, whereas for the larger AlN thickness fluctuations were observed along AlN (Aix3235 sample).

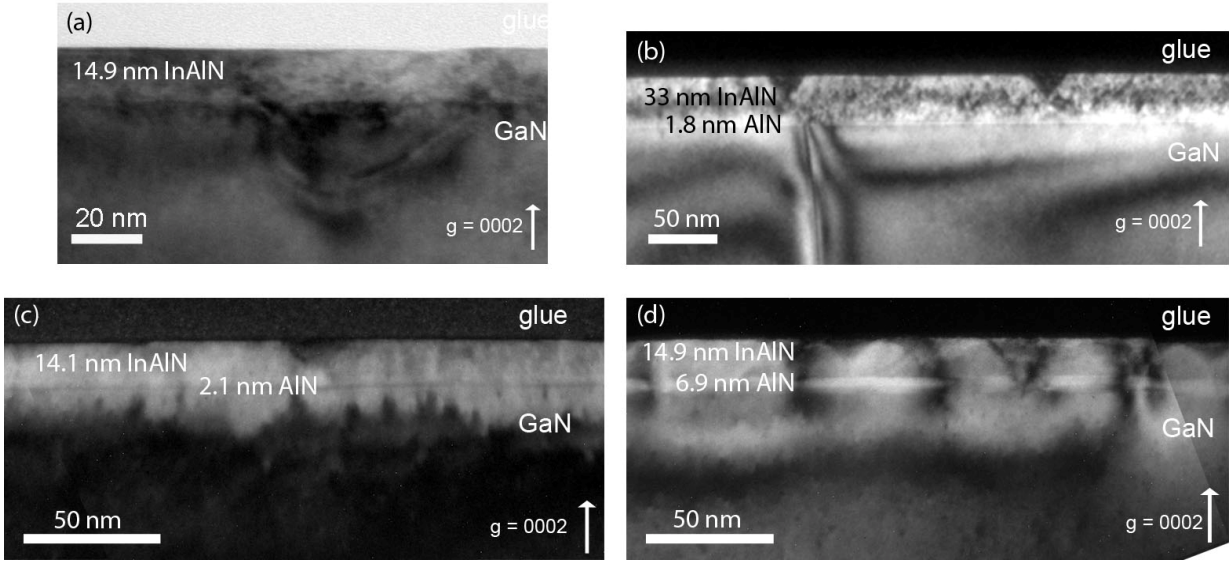

Fig 4.2 Weak beam cross section of Aixtron samples (a) 3234 (t_{AlN} = 0 nm), (b) 3232 (t_{AlN} = 1nm), (c) 3233 (t_{AlN} = 2.5 nm), and (d) 3235 (t_{AlN} = 7.5 nm). In the figure is included the InAlN and AlN thicknesses measured by TEM.

Concerning the InAlN layer, no defects were noticed for the sample without an AlN interlayer, whereas for the other three samples, v-shaped defects were observed. For the samples with thinner interlayers (Aix3232 and Aix3233), the v-shapes started in the middle of the InAlN layer, and the layer surface was flat between the pits. For both HEMT heterostructures (Aix3232 and Aix3233), the v-shapes density was 1 x 10^9 cm^{-2} and 8 x 10^8 cm^{-2}, respectively. This density difference could be attributed to the different thickness for the ternary layer (see the heterostructure at Table 4.2).

On Aix3235 (Fig 4.2(d)), the majority of the v-shapes originated from the AlN. At this magnification we observe a large number of v-shapes with diameters in the range 18–29 nm, and at a density of 4.4 x 10^9 cm^{-2}.

Fig 4.3 shows a weak beam dark field (g-5g) TEM micrograph taken with **g** =$11\bar{2}0$ reflection of the InAlN/AlN of sample Aix3235. On the image, moiré fringes can be seen inside the InAlN layer, and in the overlap area of AlN and InAlN. We observed that some the moiré fringes were closely spaced and others were widely spaced. The moiré fringes result from interference of the electron beam which has been travelling through at least two different superimposed layers.

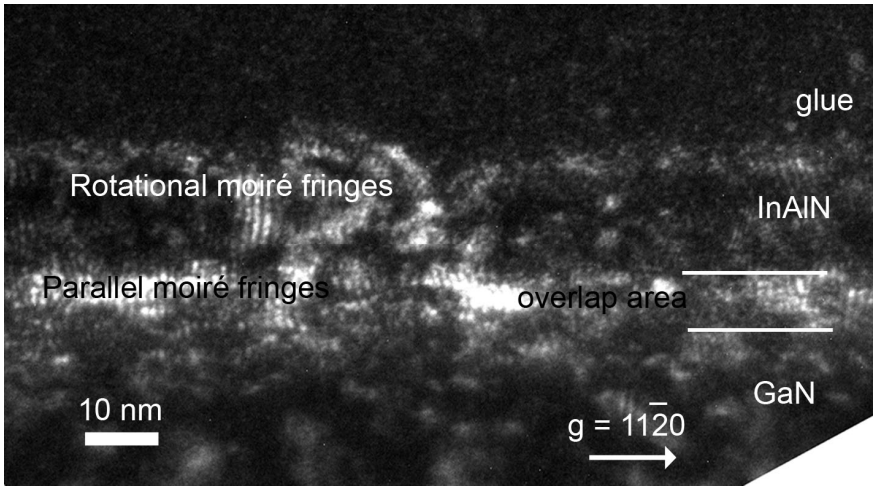

Fig 4.3 Moiré fringes in sample Aix3235 (t_{AlN} = 6.9 nm).

Moiré patterns can be categorised as follows:[26]

(a) Parallel: when the atomic lattice planes of superposed crystals are parallel, but different in lattice spacing.

(b) Twist or rotation of lattice planes.

(c) Mixed (the effects in (a) and (b) can be present at the same time).

In Fig 4.3, the moiré fringes observed at the interface are complex, in this area and taking into account that the sample has been tilted out of the $[11\bar{2}0]$ in order to obtain the $\mathbf{g} = 11\bar{2}0$ weak beam conditions, there is a possibility of partial or complete overlap between GaN, AlN and the InAlN barrier. Indeed their spacing varies from one area to the adjacent. Inside the InAlN layer, the observation of such fringes is quite strange as one would not expect foreign phases to be present. These most probably originate from misoriented grains along the InAlN which agrees with the fact that this layer contains the highest density of pinholes and probably trenches originating from the interface with GaN (see Fig 4.5(b)).

The surface morphology of these four samples is presented in Fig 4.4(a)-(d) using 5 μm x 5μm AFM micrographs. The surface becomes slightly smoother (rms ~ 0.33 nm) as the thickness of the AlN interlayer increases (from 0 to 2.1 nm), in agreement with Teke *et al.*[11] who showed that the surface becomes flat (from ~0.55 to ~0.34 nm) as the thickness of the AlN interlayer increases from 0 to 2.0 nm. However the roughness increases to 0.81 nm when the InAlN thickness increases to 33 nm, in agreement with the results obtained by TEM. However, for two InAlN layers, the surface exhibits low and rounded hillocks along with clear v-shaped defects (Aix3232 and Aix3233). In contrast, many micron-size irregular shaped morphology covered the entire layer for the fourth sample (Aix3235) extending the roughness to 8.46 nm

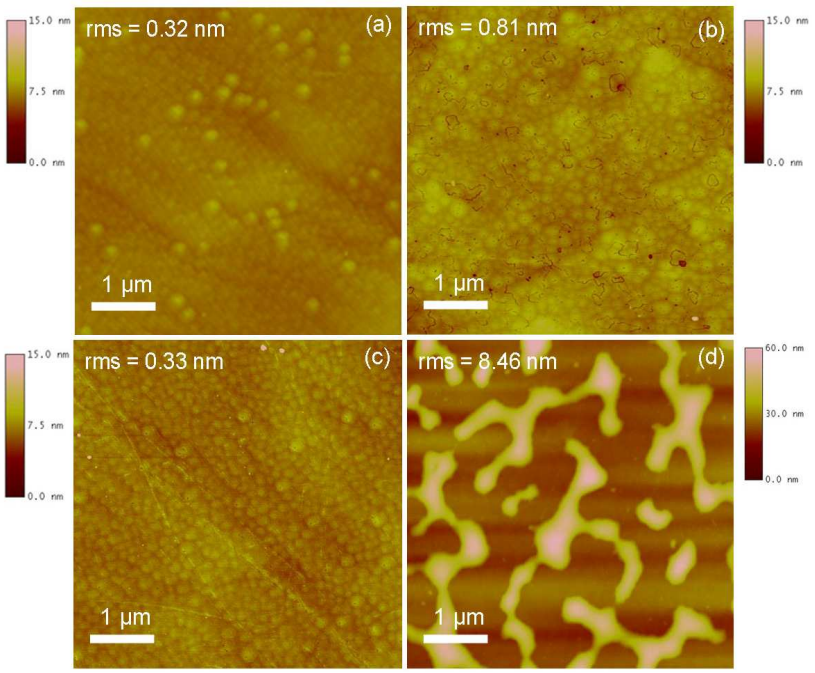

Fig 4.4 AFM micrographs of InAlN layers grown on (a) GaN, (b) 1.8 nm AlN, (c) 2.1 nm AlN, and (d) 6.9 nm AlN.

Sample Aix3235 was also analysed by electron channelling contrast imaging (ECCI) and scanning electron microscopy (SEM). Secondary electron (SE) images were recorded at 5 kV and 1.3 nA in order to probe the top few layers of the heterostructures. This study was done through the RAINBOW consortium in the University of Strathclyde (Glasgow) by Naresh Kumar. In Fig 4.5(a), one can see possible disruptions in the InAlN film, which probably start in the InAlN/AlN interface. We can see pits and trenches from high magnification SEM (Fig 4.5(b)) from which the pits density is calculated at 3.1 x 10^{10} cm^{-2}.

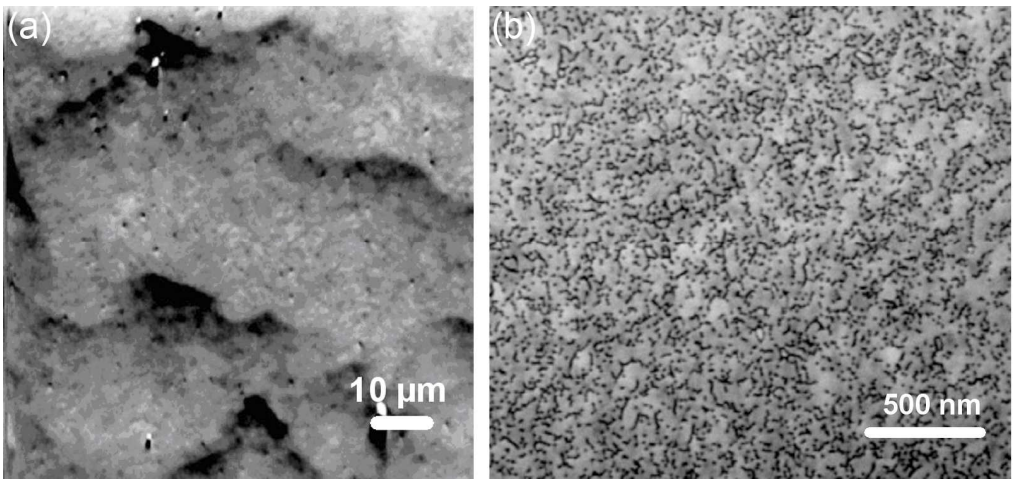

Fig 4.5 Aix3235 sample (a) ECCI (b) SEM image showing pits and trenches. (Courtesy of Naresh Kumar).

In summary, the AlN thickness has an important influence on the defect in InAlN as well as on the morphology.

4.2.1.2 *Influence of the AlN interlayer*

The sample Aix3235, as was mentioned before, exhibits structural degradation from the generation of dislocations and/or cracks in the interface. Thus, the InAlN surface was affected by the surface of the underlayer, in our case AlN film. The precise control of AlN thickness is an important factor in order to improve the InAlN crystalline quality. Consequently, critical thickness plays an important role for the limitation of the number of defects.

We have done a simple estimation for the critical thickness t_c according to the Fisher *et al*.[27] model. They reported an approach in equilibrium theory for strain relaxation in heteroepitaxial semiconductor structures. In this equilibrium theory, the elastic interaction between straight misfit dislocations was included and t_c was derived by setting the excess resolved shear stress required to produce misfit dislocations to zero.

The critical thickness t_c was given by the following equation:

$$\frac{(a_s - a_f)}{a_s} = \left(\frac{b\cos\lambda}{2t_c}\right) \times \left(1 + \left(\frac{1 - \nu\cos^2\theta}{4\pi(1+\nu)\cos^2\lambda}\right)\ln\left(\frac{t_c}{b}\right)\right) \qquad (4.1)$$

where a_f = 3.111 Å and a_s= 3.185 Å are the lattice constants of the fully relaxed film (AlN) and the substrate (GaN), respectively; λ = π/6 is the angle between the Burgers vector and the interface, θ = π/3 is the angle between the dislocation line and its Burgers vector,[28] ν = 0.27 is the AlN Poisson ratio,[29] and b = 3.185 Å is the length of the Burgers vector. Fig 4.6 shows that a t_c = 7.2 nm is expected at the onset of plastic relaxation and the formation of misfit dislocations for AlN grown on GaN.

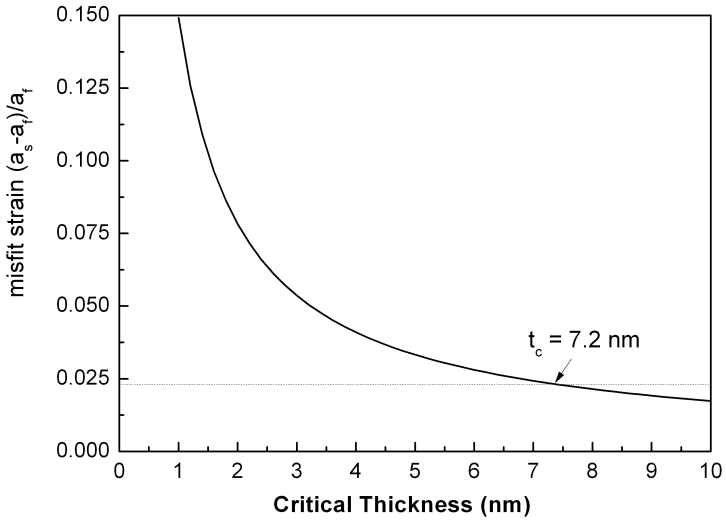

Fig 4.6 The calculated misfit strain against critical thickness for AlN/GaN system. The dashed line corresponds to a misfit strain of 2.3 %.

For our samples, only the AlN interlayer thickness in the Aix3235 sample was close to the critical thickness. In this sample, numerous defects have formed in the basal as well as in the prismatic planes leading to a disrupted layer with grains and cracks as observed in figures 4.3 and 4.5(b).

4.2.2 InAlN/GaN heterostructures

The details of surface morphology were assessed by AFM using 5 μm x 5 μm scans of four films with different InAlN thickness: (a) 30 nm (A1583), (b) 125 nm (A383), (c) 172nm (A1843), and (d) 336 nm (A1363). We can distinguish three different surface morphologies. Clearly the thinner InAlN (30 nm) has a much flatter morphology and the rms roughness value for this sample was 0.44 nm (Fig. 4.7(a)). When the thickness increased at 125 nm (Fig 4.7(b)), the topography image of the InAlN epitaxial layer revealed the presence of pits (also called v-shapes) with an average roughness of 0.65 nm. The same morphology was also presented by Sadler *et al.*[30] and by Miao *et al.*[31]. For our sample, the pit density was 189 pits from 5 μm x 5 μm scan, corresponding to 7.66 x 10^8 cm^{-2} density dislocations. The other two samples exhibit a granular morphology that covers all of the surface and

the larger grains are related to the thicker sample (Fig 4.7(c)-(d)). In general, the roughness of the InAlN increases with thickness.

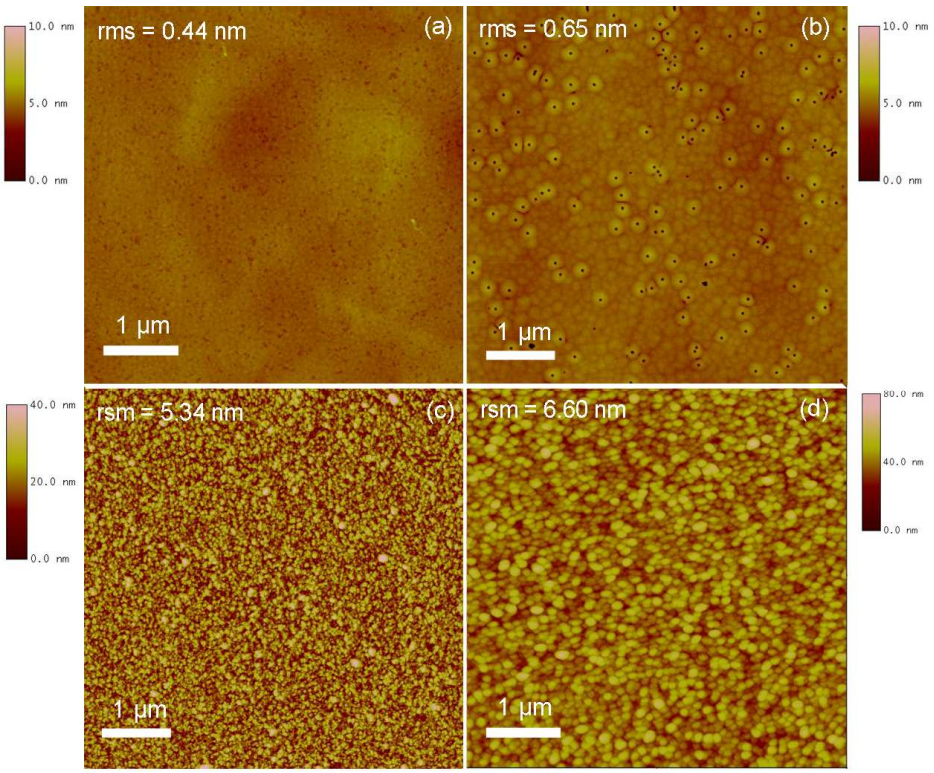

Fig 4.7 AFM images and the corresponding roughness for (a) A1583 (t_{InAlN} = 30 nm) (b) A383 (t_{InAlN} = 125 nm, (c) A1843 (t_{InAlN} = 172 nm) and (d) A1363 (t_{InAlN} = 336 nm).

These observations seem to indicate that the growth mode changes from 2D (A1583), through the formation of surface pits and then most probably to a 3D growth mode.

The microstructure of the InAlN along the *c*-axis was also investigated by conventional TEM. Cross-section TEM images of $In_xAl_{1-x}N$ (x = 0.18, 0.16, 0.21 and 0.19 corresponding to A1583, A383, A1843 and A1363, respectively) grown on GaN substrates are shown in Fig 4.8(a)-(d). All the micrographs were taken under two beam dark field diffraction conditions in **g** = 0002. The first two samples with lower In contents (Fig 4.8(a)-(b)) showed a flat InAlN surface, as already observed by AFM, with a roughness smaller than 0.7 nm. However in sample A1583 (lattice matched GaN) no defects have been observed in the InAlN film, it is not the same for the A383. For this second sample, v-shapes were observed and some of them can be seen at the end of mixed type dislocations.

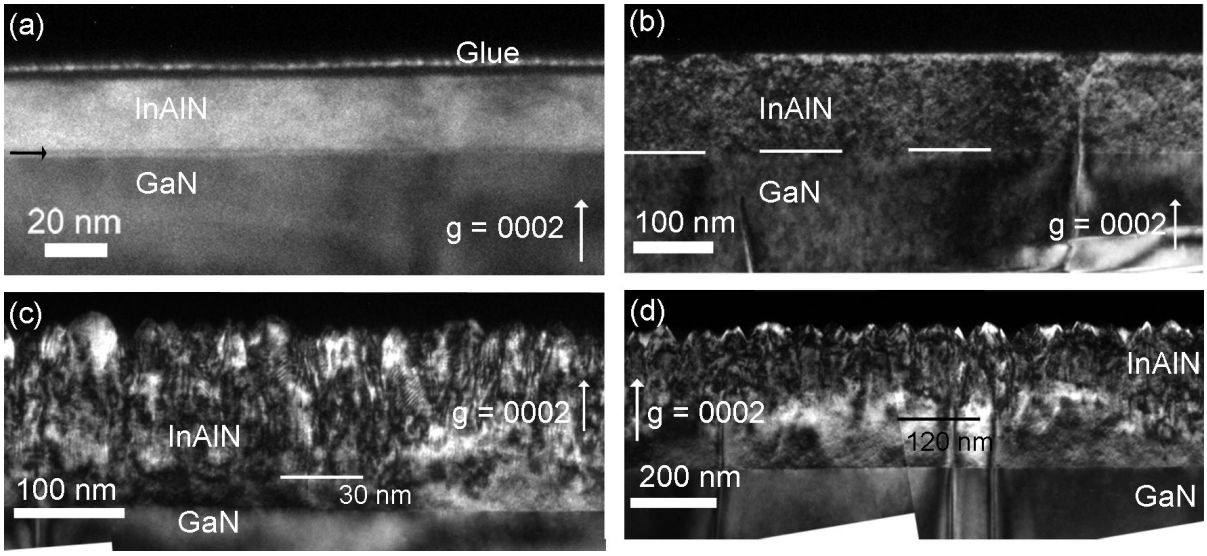

Fig 4.8 Cross section TEM images (a) A1583 (b) A383 (c) A1843 and (d) A1363.

The morphologies were completely different for the other two samples with higher In contents and larger thickness. In both samples, the surface morphology of the InAlN layer is rough, consistent with AFM roughness values of 5.34 and 6.60 nm, respectively. For the A1843, with the highest In content, columnar domains were noticeable at 30 nm from the InAlN/GaN interface (Fig 4.8(c)) and inside these columns is possible to identify moiré fringes. On Fig 4.8(d), we can nearly distinguish two different morphologies along the InAlN layer: the first ~ 120 nm showed good quality whereas the top area exhibits a columnar structure.

A particular microstructure was exhibited for the samples of thickness higher than 100 nm (except samples A383 and A1282). As shown for example at the sample AEC1323 (Fig. 4.9), numerous columns exist inside the InAlN. Looking the columns, we have observed that most of them were vertical at the interface, but also some of them were tilted.

To investigate the crystal structure of the InAlN/GaN, we performed selected area electron diffraction (SAED) measurements for the cross section of InAlN/GaN along the $[11\bar{2}0]$ zone axis. Fig 4.9(b)-(c) show SAED patterns taken on the InAlN and GaN layers, respectively.

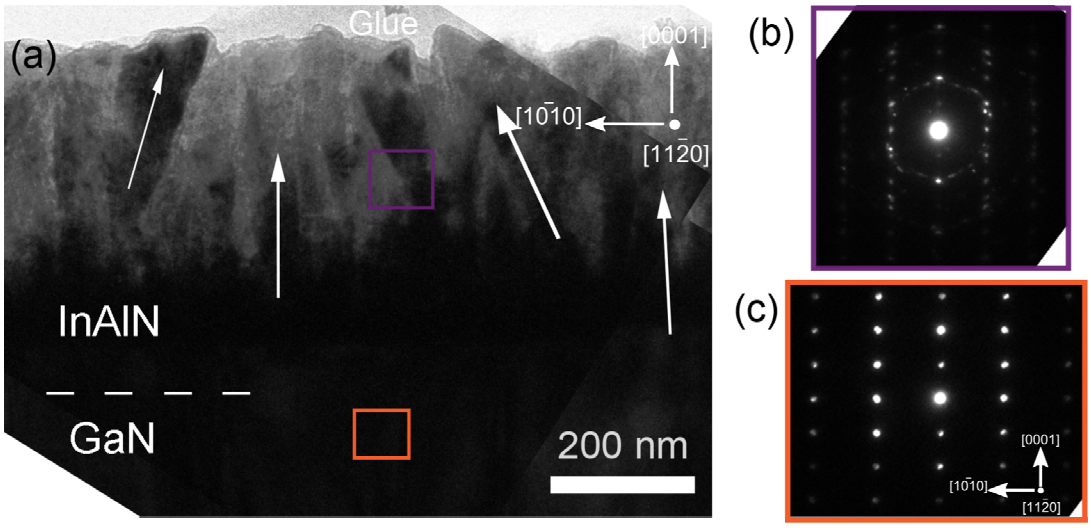

Fig 4.9 Sample AEC1323 (a) Cross section at the [11$\bar{2}$0] zone axis; (b) and (c) [11$\bar{2}$0] diffraction pattern taken from InAlN and GaN layer.

Fig 4.9(b) revealed a ring pattern corresponding to the polycrystalline structure of the InAlN film. Fig 4.9(c) displays strong spots corresponding to the single crystal structure of GaN. Kret *et al.*[20] also observed columns growing a few nanometers from the interface, but in their case all the columns preserve the same crystal orientation.

4.3 Composition analysis in InAlN/AlN/GaN and InAlN/GaN heterostructures

4.3.1 In content and strain analysis by HRXRD

HRXRD measurements were performed to determine the alloy composition and the strain using the (000ℓ) symmetric reflections since they correspond to the epitaxial growth direction.

A typical symmetric X-ray diffraction diagram from the sample Aix3232 with the heterostructure: InAlN/AlN/GaN/AlN(100nm)/Al_2O_3 is shown in Fig 4.10. In this diagram, the (000ℓ) peaks of the four layers are well identified allowing the determination of their *c* lattice parameters.

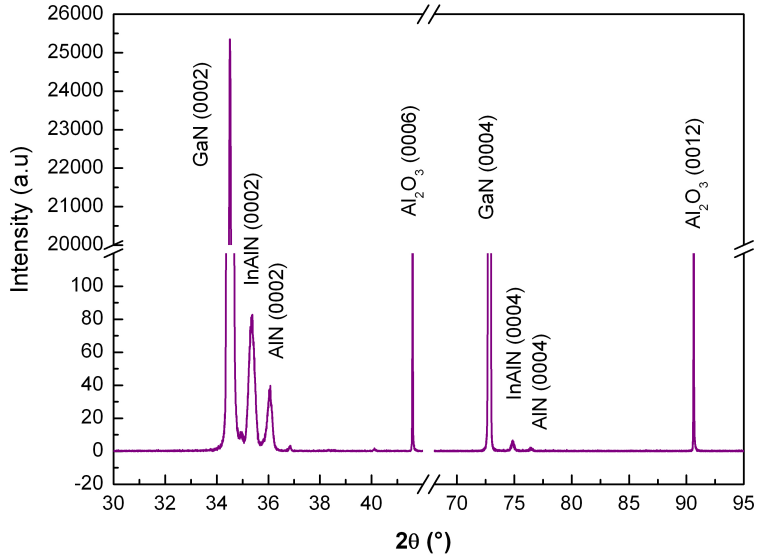

Fig 4.10 HRXRD θ-2θ diagram on InAlN/AlN/GaN/AlN on Al_2O_3 substrates (Aix3232).

However, in some samples (Fig 4.11(a)), there can be a strong overlap of the InAlN (0002) peak with that of GaN. In this case (Fig 4.11(a)), the InAlN *c* parameter (c^{InAlN}) cannot be extracted. Therefore, it is necessary to perform (000ℓ) symmetric reciprocal space maps (see *Chapter 2-Section 2.2.2.2* and *Chapter 3-Section 3.3.2*).

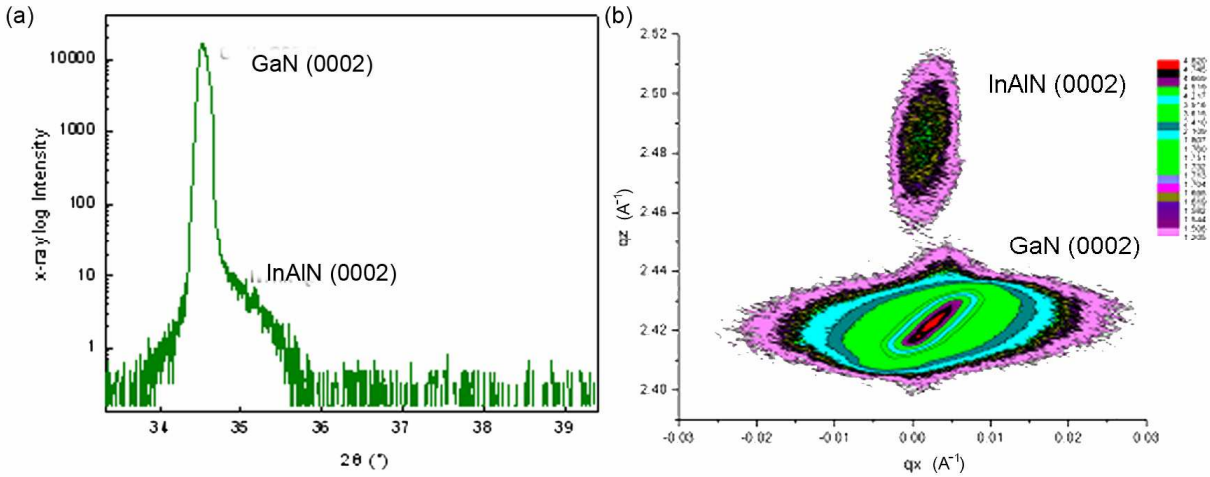

Fig 4.11 (a) (0002) θ-2θ diffraction scan and (b) (0002) reciprocal space map of the InAlN/AlN (Aix3234).

In Fig 4.11(b) is shown a RSM of the same InAlN/GaN sample. It exhibits well separated GaN and InAlN (0002) diffraction peaks. The corresponding c^{InAlN} lattice parameter was deduced from the (0002) symmetric position in order to

extract, respectively, the In content and the normal strain tensor component, ε_{zz} (Table 4.4).

Table 4.4 Results of c^{InAlN} lattice parameter and InN content measured by HRXRD using the corrected Vegard's law, and the in-plane residual stress (σ_{xx}). In the table is included the thickness of the layers.

	t_{InAlN} (nm)	t_{AlN} (nm)	c^{InAlN} (Å)	In (%)	σ_{xx} (GPa)
AEC1657	90	____	5.088	15.5	0.66
AEC1655	150	____	5.138	20.5	-1.44
AEC1769	7.9	4.6	5.089	17.7	0.92
AEC1770	4.8	4.8	5.114	18.4	-0.14
Aix3232	33	1.4	5.069	13.25	1.13
Aix3233	14.1	1.9	5.063	12.3	1.00
Aix3234	14.9	____	5.070	13.4	1.14
Aix3235	14.9	6.9	5.070	13.4	1.14

In strain free alloys, compositions can be derived using Vegard's law.[32] In our cases, the InAlN layers are under strain, and Vegard's law cannot be directly applied.[33,34] In our work, the In content was extracted from the corrected Vegard's law as proposed by Lorentz *et al.*[35] and deduced from combined HRXRD and RBS measurements. The latter gives the variation of the c^{InAlN} lattice parameter with the In content (x)

$$c^{InAlN} = x \cdot c_0^{InN} + (1-x) \cdot c_0^{AlN} - \partial_c \cdot x \cdot (1-x) \qquad (4.2)$$

where $\partial_c = 0.06 \pm 0.01$ is the non zero lattice constant bowing parameter and c_0^{InN} and c_0^{AlN} are the values of the unstrained lattice parameters respectively for InN and AlN reported in Table 1.2 of *Chapter 1*. For sample AEC1323, it was not possible to extract the In content or in-plane residual stress perhaps due to poor single crystalline quality.

Our results (green solid circles symbols) are plotted in Fig 4.12. They are compared with the simulation (square symbols) given by Dridi *et al.*[34], as can be seen they are in good agreement.

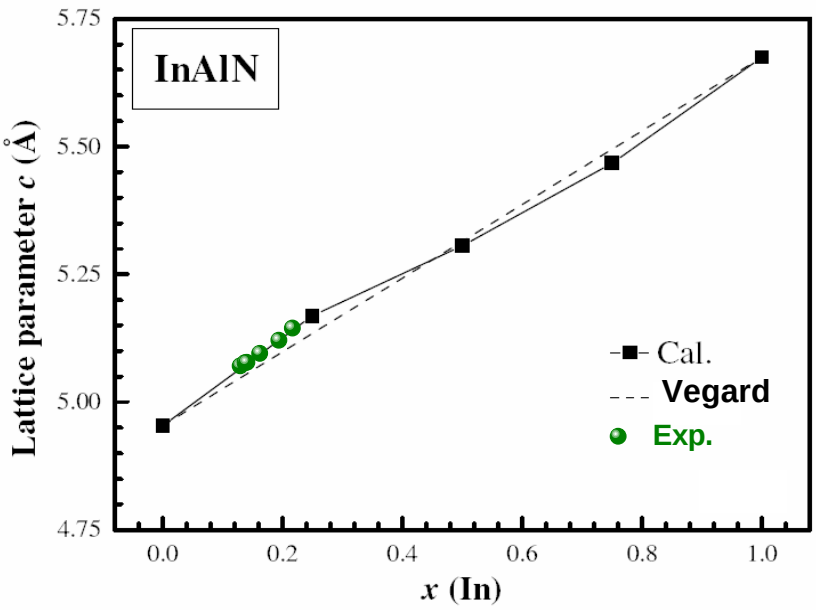

Fig 4.12 In content (green solid circle) and the data from Dridi *et al.*[34], the dashed line corresponds to the Vegard's law.

In Table 4.4, one can notice that the In content extracted using RSM presents some discrepancies with that given by the growers and extracted using a single ω-scan or rocking curves (RC). The differences observed between the two values are in the range 0.5-2.2%; these discrepancies can affect the corresponding *c* cell parameter as well as the in-plane residual stress values. As shown in *Chapter 2*, we must remember that recording a single RC corresponds to one dimensional diffracted intensity integration of the RLP. In epitaxial films, the 3D RLP extension is in general complex and the use of only one section of this RLP is not sufficient. This study shows that it is necessary to perform RSM in order to be able to reconstruct the corresponding 3D diffracted intensity profile.

Knowing the In content (x) from the c^{InAlN} lattice parameter (strained) extracted by RSM, and the c_0^{InAlN} parameter for relaxed InAlN derived from Vegard's law $\left(c_0^{InAlN} = x \cdot c_0^{InN} + (1-x) \cdot c_0^{AlN}\right)$, the normal ε_{zz} strain tensor components have been obtained from the equation:

$$\varepsilon_{zz} = \frac{c^{InAlN} - c_0^{InAlN}}{c_0^{InAlN}} \tag{4.3}$$

Under (0001) biaxial strain ($\sigma_{zz} = 0$), the in-plane residual stress σ_{xx} can be calculated using the equation

$$\sigma_{xx} = (-C_{33}^{InAlN} / (2C_{13}^{InAlN})(C_{11}^{InAlN} + C_{12}^{InAlN}) + C_{13}^{InAlN})\varepsilon_{zz} \tag{4.4}$$

where the C_{ij}^{InAlN} are stiffness coefficients linearly interpolated from the binary alloys AlN and InN given in Table 1. 1 (*Chapter 1*) and using:

$$C_{ij}^{InAlN} = x \cdot C_{ij}^{InN} + (1-x) \cdot C_{ij}^{AlN} \tag{4.5}$$

As has be seen in Table 4.4, the sign of the in-plane residual stress changes from tensile ($\sigma_{xx} > 0$) to compressive ($\sigma_{xx} < 0$) when x is larger than ~ 18 %, in agreement with the values predicted by the corrected Vegard's law.[35]

It should be noted that the values of the In content and residual stress for a given measured XRD lattice parameter are strongly affected by the uncertainties in the strain free lattice parameter and stiffness coefficients of InN and AlN as well the assumption of a pure biaxial strain.

4.3.2 In content and crystalline quality investigation by RBS/C

RBS/C in random and aligned geometries is another approach for assessing compositional and structural properties independently from the strain state of these crystalline materials. Besides, RBS is especially suitable for the compositional analysis of InAlN alloys in our case because the In signal is well separated from that of Ga (normally coming from the GaN template), thus providing a high sensitivity to the In concentration determination. Moreover, ion channelling has been used to check the crystalline quality. Thickness and composition information were extracted from the spectra using the SIMNRA software.

Fig 4.13(a)-(b) illustrates RBS/C random spectra (blue solid circles) and the corresponding fit (red line) for two selected samples with different thicknesses: (a) AEC1769 (7.9 nm InAlN) and (b) AEC1655 (150 nm InAlN). The In signal is found in the 1360-1390 keV energy range in the RBS spectrum whereas the Al signal is at 855-890 keV overlaps with the Ga signal (1270 KeV) from the template layer.

Different behaviour was observed by analysing the In signal for both samples. For AEC1769, with a thin InAlN layer, one layer modelling is sufficient to reproduce the In profile. Whereas the thicker InAlN must be modelled using two layers structure with different In compositions. The corresponding In contents found from SIMNRA simulations were cross checked with those evaluated by In peak integration using the surface approximation and a good agreement was obtained. These RBS In contents are listed in Table 4.5.

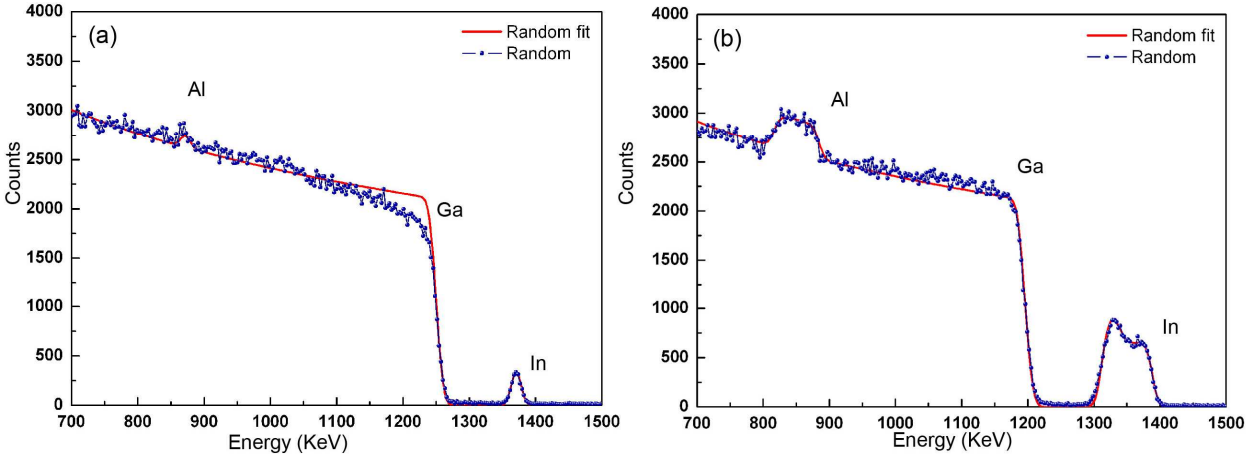

Fig 4.13 RBS random and fit spectra for the samples: (a) AEC1769 (b) AEC1657. The labels Al, Ga, In on the RBS spectrum indicate the signal of these elements.

From now on we focus on the analysis of the crystalline quality of the layers. Fig 4.14(a)-(b) is the random spectra for two thin samples, the first with 33 nm InAlN (Aix3232) and the second with a 14.9 nm InAlN layer (Aix3234). The <0001> aligned spectra have also been plotted.

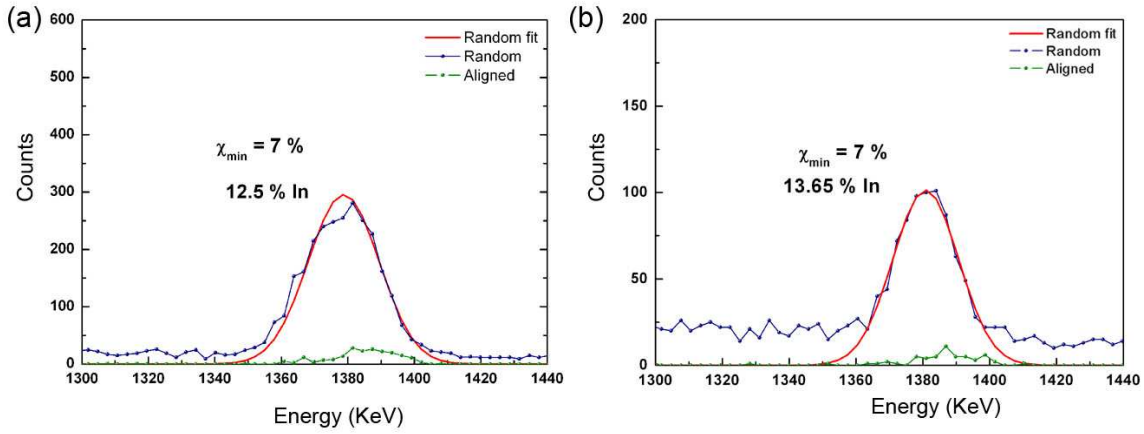

Fig 4.14 RBS/C random and <0001> aligned spectra for the In signal: (a) Aix3232, and (b) Aix3234.

As was explained in *Chapter* 2, the ratio between the <0001> aligned and the random yield in a given region, known as the minimum yield χ_{min}, has been used as an indicator of the film crystalline quality. The integrated energy regions of 1350 KeV to 1400 KeV backscattering corresponds to In atoms. For both samples, we found the same χ_{min} values of 7 %; this low value shows that for films up to 33 nm InAlN thickness, good single crystalline quality is achieved.

For samples deposited at 865 °C with a V/III ratio of 2000 and 1 nm AlN interlayer, the fitted RBS spectra shows that for thin layers, the In profile can be reproduced with one layer (Fig 4.15(a)) whereas for thick layers, (higher than 100 nm) two layers at least were necessary for reproducing the In profile in the corresponding RBS experimental spectra (Fig 4.15(b)-(d)). Nevertheless, we must notice that the introduction in the SIMNRA software of three or more layers also allows a good reproduction of the RBS In content for these thick layers. The thin InAlN layer exhibits a χ_{min} value of 31 % showing that the increase in temperature and reduction in V/III ratio led to an increase in χ_{min} of 24 % (χ_{min} = 7 % for Aix3232 and Aix3234). The larger channelling yield accompanied by a slight increase of the InAlN roughness at around 0.6 nm (AEC1769) may suggest the presence of In atom that are not incorporated on perfect substitutional sites.[35] With the increase of InAlN thickness a strong deterioration in crystalline quality is observed which starts systematically from the surface.

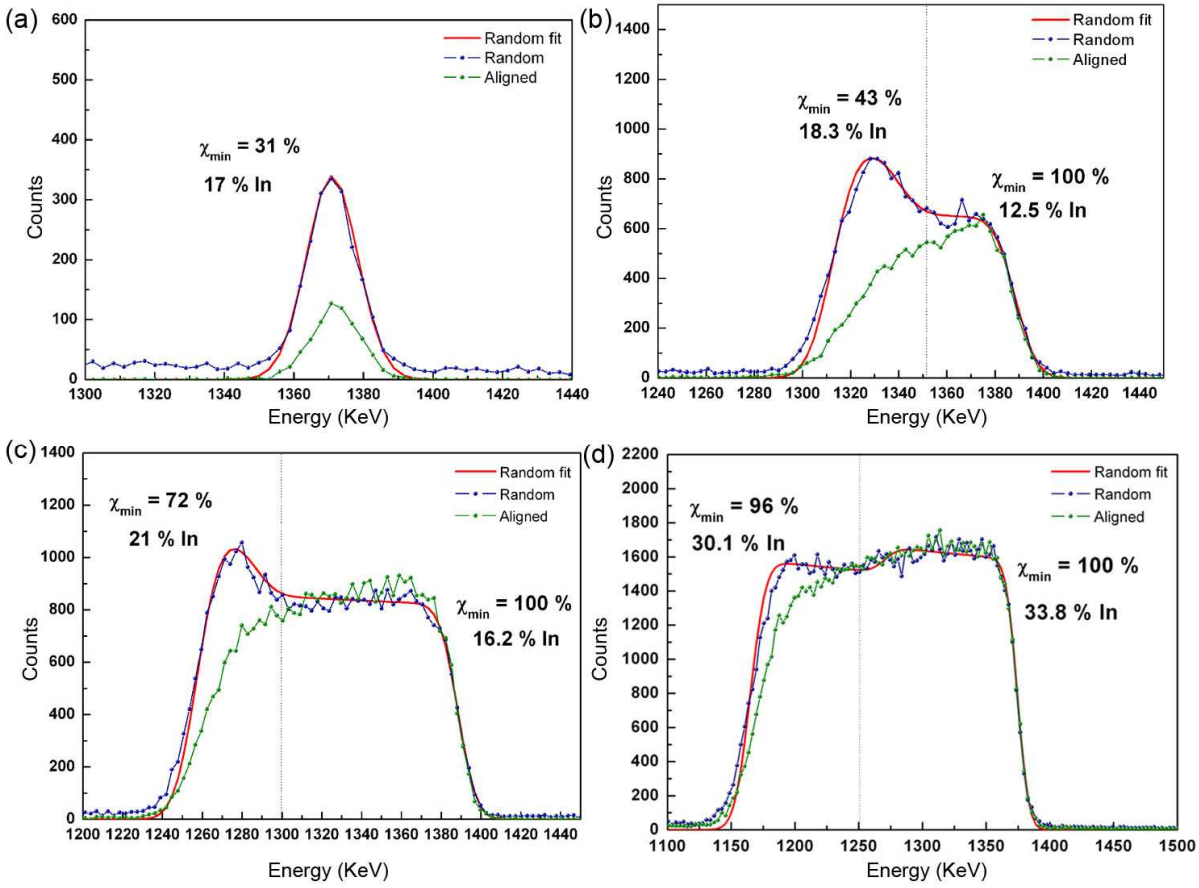

Fig 4.15 RBS random and <0001> aligned spectra of samples: (a) AEC1769, t_{InAlN} = 7.9 nm (b) AEC1657, t_{InAlN} = 100 nm (c) AEC1655, t_{InAlN} = 150 nm, and (d) AEC1323, t_{InAlN} = 260 nm. Vertical dashed line separates the two layers used in the fit with different composition.

Indeed, for the three samples, the top layer surface on InAlN exhibits a minimum yield χ_{min} of 100 % (the aligned spectrum is the same as the random) indicating that this layer is polycrystalline or amorphous. For the InAlN area close to the GaN, the χ_{min} were 43 %, 72 % and 96 % for the three samples AEC1657, AEC1655 and AEC1323, respectively (see Fig 4.15). Near the interface, the reduction of χ_{min} (43 %) in AEC1657 after the strong dechanneling induced by the top layer (χ_{min} = 100 %), implies that this layer is single crystalline. Checking the other two samples, the surface layer thickness is larger (112.5 nm and 173 nm), so the dechanneling induced by this layer must be reinforced; however, the measured χ_{min} values of 72 % and 96 % show that this interface layer is highly disordered. For the thickest sample (AEC1323, t_{InAlN} = 260 nm), the whole sample is almost polycrystalline explaining why it is not possible to use HRXRD to measure crystallinity. Of course, HRXRD is only sensitive to the single crystalline

part of the InAlN whereas using random RBS we are sensitive to the whole layer, independently of its crystalline character (polycrystalline, single, amorphous).

In the RBS spectra of Fig 4.15(b), the displayed two layers fit assumed a surface layer of thickness ~ 33 nm (i.e. one third of the total thickness) with an In content x = 12.5 %, followed by another layer, with a thickness of 66 nm (i.e. two thirds of the total), and with a higher In content of x = 18.3 % close to the GaN interface. For AEC1655 (Fig 4.15(c)), the InAlN area close to the GaN interface has the highest In content (21 %), with a refined thickness of around 37.5 nm (i.e. a quarter of the total), whereas the top layer has an In content of 16.2 % and a refined thickness of 112.5 nm (i.e. three quarters of the total). Thus, for $t_{InAlN} \leq 150$ nm, the highest In content is observed close to the GaN interface. For the thickest sample (Fig 4.15(d)), the two RBS refined layers display In contents higher than 30 % with the highest In content (33.8 %) representing only two thirds of the total InAlN thickness.

It was reported[17] earlier in similar layers that a critical thickness around 50 nm existed above which there was spontaneous decomposition of the InAlN into two InAlN layers, one lattice matched film close to the interface with high crystallinity and another layer of lower composition towards the surface. In our samples, for AEC1657 such an interfacial lattice matched layer was observed with a thickness of 66 nm with χ_{min} = 43 %. However, in contrast to the observations of Lorentz *et al.*[35], the lower InAlN layer thickness decreases when the total InAlN film thickness increases, with an increase of its In content close to 30 %. So in our thick samples, the crystalline quality deterioration seems to be also strongly correlated to the larger In content incorporated.

4.3.3 HAADF investigation and local In content by EDS

X-ray diffraction is commonly used to determine the In content of the ternary alloys via measuring the lattice parameters. The RBS measurements indicate clearly a possible different In layer composition for the samples with a thickness larger than 100 nm. However, there is no information directly available from X-ray or RBS spectra about any changes in the local composition. For this

reason, we are used STEM-HAADF together with EDS microanalysis on our samples. We have divided this section in two different parts: (1) elemental distribution in the HEMT structures and (2) structural degradation and chemical distribution.

4.3.3.1 *Elemental distribution in HEMT structures*

The investigated samples are divided into three sets identified by the deposition temperature of the AlN interlayer and/or the InAlN barrier. The first series is made of four InAlN/AlN/GaN samples, with AlN interlayer thicknesses of 0, 1.8, 2.1 and 6.9 nm, respectively. Both the InAlN layer and the AlN interlayer were grown at the same temperature (790 °C) at 70 mbar reactor pressure. In Fig 4.16, the Aix3234 HAADF image shows two different regions, the first one with dark contrast (InAlN) and a second with bright contrast (GaN).

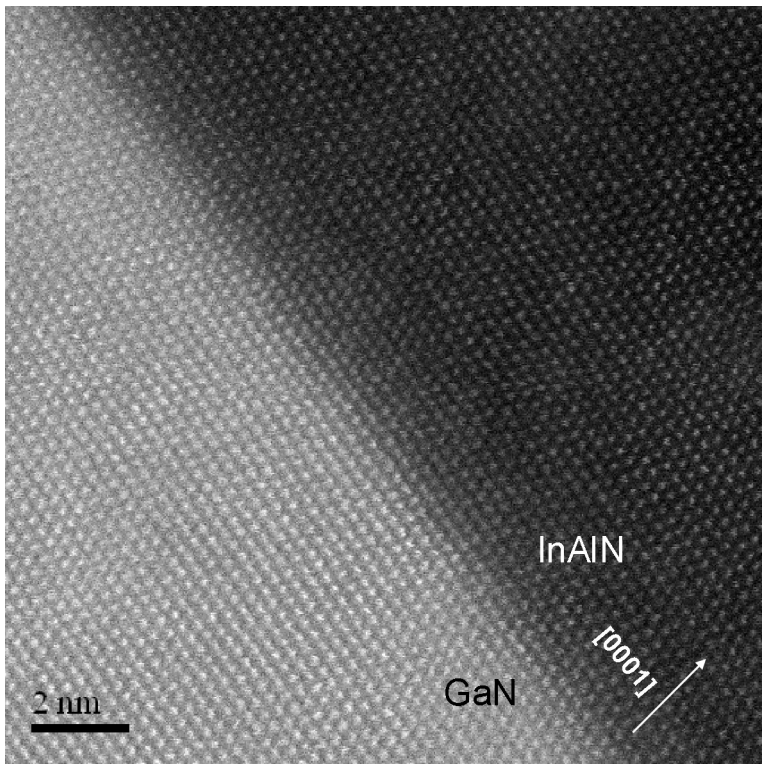

Fig 4.16 STEM-HAADF image of InAlN/GaN (Aix3234).

In Fig 4.17, three layers are clearly visible corresponding to InAlN, AlN and GaN (Aix3232). The intended nominal AlN interlayer was 1 nm and there is an

abrupt transition from GaN to AlN within one monolayer. The AlN layer thickness is measured between 1.2 and 1.4 nm.

As compared to Fig 4.16, we notice that the contrast inside the InAlN layer exhibits randomly distributed bright atomic columns. This means that such columns contain a larger number of heavy atoms (~ In).

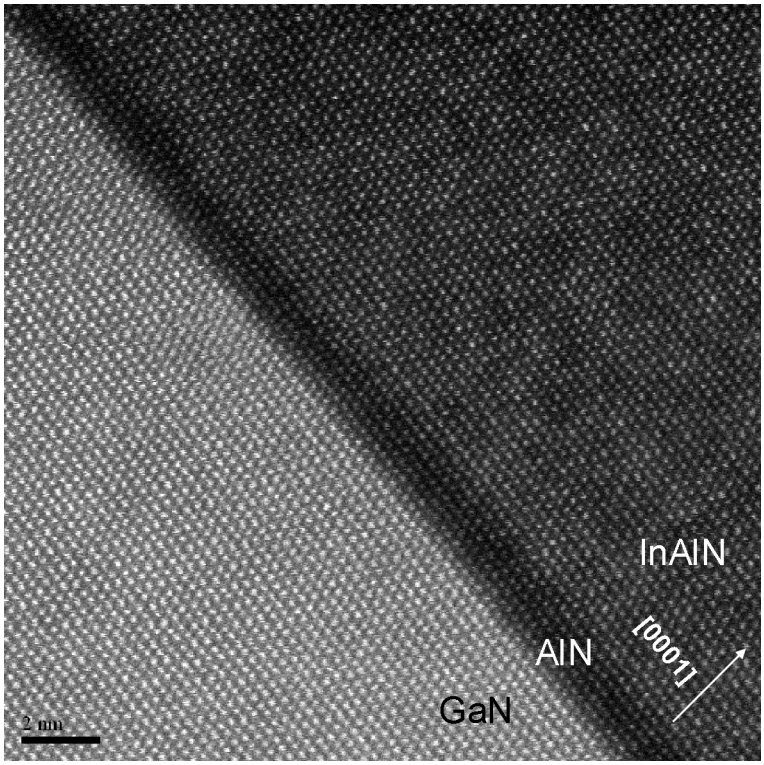

Fig 4.17 STEM-HAADF image of InAlN/AlN (1 nm)/GaN (Aix3232).

In sample Aix3235 with the nominal 7.5 nm AlN interlayer, Fig 4.18 reveals clearly four regions with different composition. Especially, two interlayers are present on top of the GaN (marked as 1 and 2). It also can be noticed that a v-defect starts in the interlayer as was earlier observed by conventional TEM (Fig 4.2(d)). In order to clarify the composition of both interlayers, EDS (LG12) was performed in the corresponding area. The cyan scan line shows the probe positions during the EDS acquisition; 9 points were analysed along about 20 nm, obviously, almost no In was present in this area (Fig 4.18(b)).

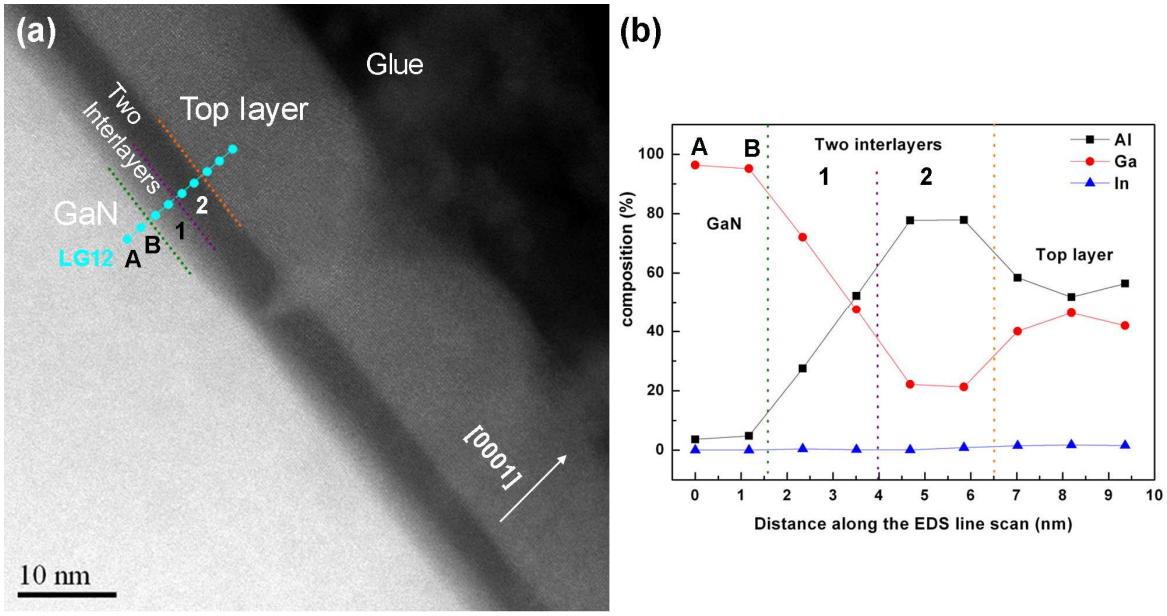

Fig 4.18 STEM-HAADF image of Aix3235: a) image and EDS scan line, LG12 indicates the EDS line from the substrate to the surface, (b) the EDS line scan profile showing Ga, Al and In composition as a function of position. A and B are the starting positions for EDS analysis. 1 and 2 show the two interlayers.

In Fig 4.18(b), the two first points (called A and B) correspond to highest Ga content, therefore they are located in the GaN layer. For the two following positions, we obtain ~72 and 48 % for Ga and the Al content is increasing (~28 % and 52 %), implying that the interlayer is a Ga rich AlGaN with a non constant composition. In the darkest layer, the two EDS positions show a sudden increase of Al up to 80 % and a decrease of Ga (to 20 %). Inside the top layer, the Al content decreases and at the same time the Ga content increases and both can be seen to oscillate around 50 %.

Following their investigation of $Al_xGa_{1-x}N$ layers, Rosenauer *et al.*[36] have reported that the intensity in HAADF images can be related to the local (x) composition (Fig 4.19). They showed that with a known reference material, the intensity ratio is given by

$$R = I_x/I_{ref} \tag{4.6}$$

where I_x corresponds to the normalized intensity in the area of interest and I_{ref} the normalized intensity in the reference. As is shown in Fig 4.19, this is valid

for a large window of TEM sample thicknesses and in these conditions: the intensity ratio varies from 1 to 0.47 when the Al content goes from 0 to 1.

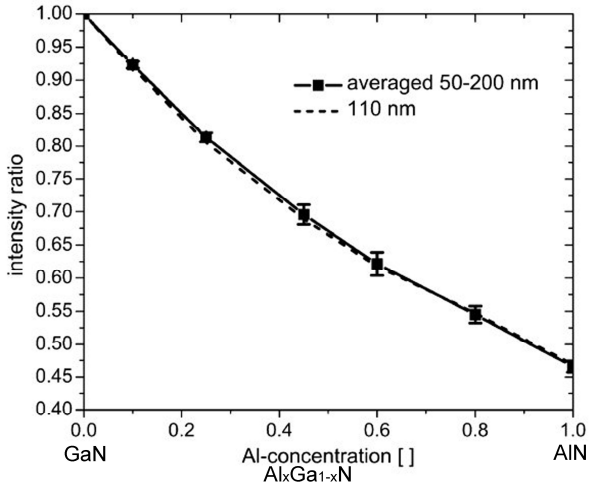

Fig 4.19 Ratio of simulated normalized intensity plotted versus the Al-concentration x in $Al_xGa_{1-x}N$. The dashed line was extracted at a specimen thickness of 110 nm, and the solid line was obtained by averaging intensity ratios for TEM foils between 50 and 220 nm thickness.[36]

In their work, Rosenauer *et al*.[36] used a FEI microscope in which the reference intensities are easily measured on the HAADF detector.[37] In this work, as mentioned in *Chapter 2*, the HAADF work was carried out on a JEOL 2200FS STEM microscope, and up to now no procedure has been published for the measurement of the intensity on detector. Therefore, in the following, we have used the GaN layer contrast as the reference and the intensity through the vacuum as the background, indeed the results may not be as accurate, but the interest was to determine the trends. Indeed, for sample Aix3235, the aim was to see if the HAADF contrast could be related to the measured chemical composition. As can be seen in Fig 4.20(a), the rectangle on the HAADF image shows the area where the intensity profile was integrated (Fig 4.20(b)). Obviously, a constant minimum is reached in the area 2, whereas the contrast steadily decreases in area 1. As can be seen in the figure, the intensity in interlayer 1 is larger than in interlayer 2. Calculating the ratios, we obtain $I_x/I_{GaN} = 0.37$ in layer 2, lower that the theoretical value of 0.47. A possible explanation of this discrepancy may be the local strain as seen in TEM. However in layer 1, we have values that extend from pure GaN to

0.57 corresponding to around 70 % Al, in agreement with the measurement by EDS (Fig 4.18(b)).

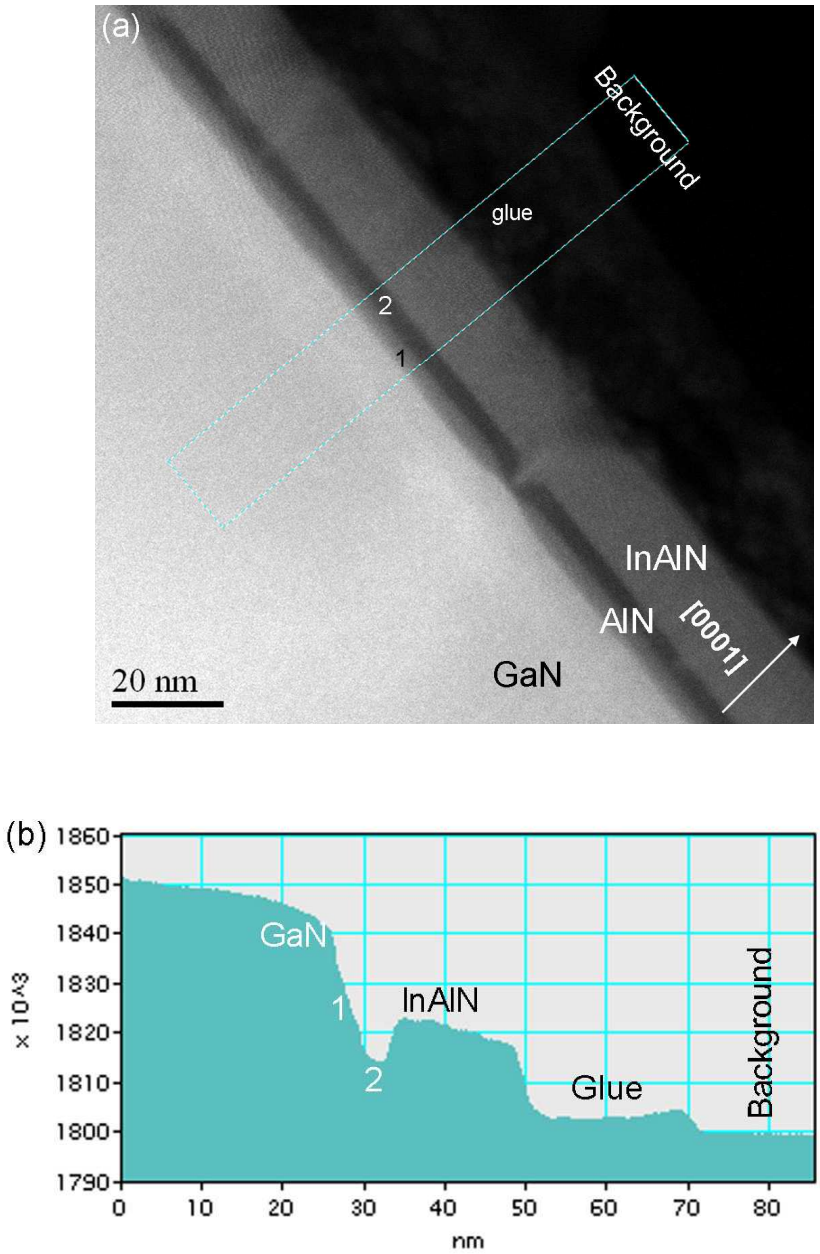

Fig 4.20 Aix3235 (a) HAADF image, the rectangle where the intensity profile is integrated (b) Intensity profile versus distance.

Following this observation of Ga inside the barrier, we performed EDS on all the Aixtron samples in order to check for Ga inside the InAlN layers. For this investigation, we used different line scans inside the InAlN layers, parallel to the interface, and at different distances from it. For the four samples the line scans were as follows:

♦ Aix3232: two line scans at 5.9 nm and 15.4 nm from the interface, and 15 points/line. The length of the line was 50 nm.

♦ Aix3233: two line scans at 2.5 nm and 7 nm from the interface and 15 points/line with the same line length as the previous sample.

♦ Aix3234: two line scans at 4.6 nm and 12.8 nm from the interface and 7 points/line. The length of the line was 60 nm.

♦ Aix3235: one line at 11.3 nm from the interface and 5 points/line. The length of the line was 20 nm.

The quantitative composition of the line scans are collected in Table 4.5 for all the samples.

Table 4.5 EDS microanalysis results for the Aixtron samples. The distance from the interface for the EDS analysis, Al, Ga and In content by EDS. In content by HRXRD and RBS are listed.

Sample and thickness (nm)	**Distance from interface (nm)**	**Al (%)**	**Ga (%)**	**In (%)**	**$In_xAl_{1-x}N$**	
					In (%) by HRXRD	**In (%) by RBS**
Aix 3232	5.9	36.06 – 46.62	47.70 – 55.29	3.34 – 10.52	13.25	12.5
$t_{InAlN = 33}$	15.4	39.37 – 48.53	42.68 – 49.46	8.47– 13.46		
Aix 3233	2.5	53.91 – 57.95	38.92 – 41.62	3.14 – 5.08	12.3	11.93
$t_{InAlN = 14.1}$	7.0	54.15 – 58.67	36.85 – 41.72	3.42 – 4.56		
Aix 3234	4.6	47.33 – 55.91	41.60 – 49.67	1.82 – 4.52	13.4	13.65
$t_{InAlN = 14.9}$	12.8	52.83 – 55.77	41.25 – 43.14	2.15 – 4.03		
Aix 3235	11.3	56.09 – 59.39	34.92–39.01	4.32 – 5.69	13.4	13.27
$t_{InAlN = 14.9}$						

As an example, we show one of the line scans (LG4) for Aix3232 (Fig 4.21(a)). For the three elements (Al, In and Ga), the data are plotted in Fig 4.21(b). As can be noticed, we end up with the same trend as Aix3235 sample above: there is a large amount of Ga content (~ 45 %). The three different profiles for each element show also fluctuations along the InAlN barrier (10 %), such an amplitude

is much higher than the error bar of the EDS measurements in our working conditions (1-2 %).

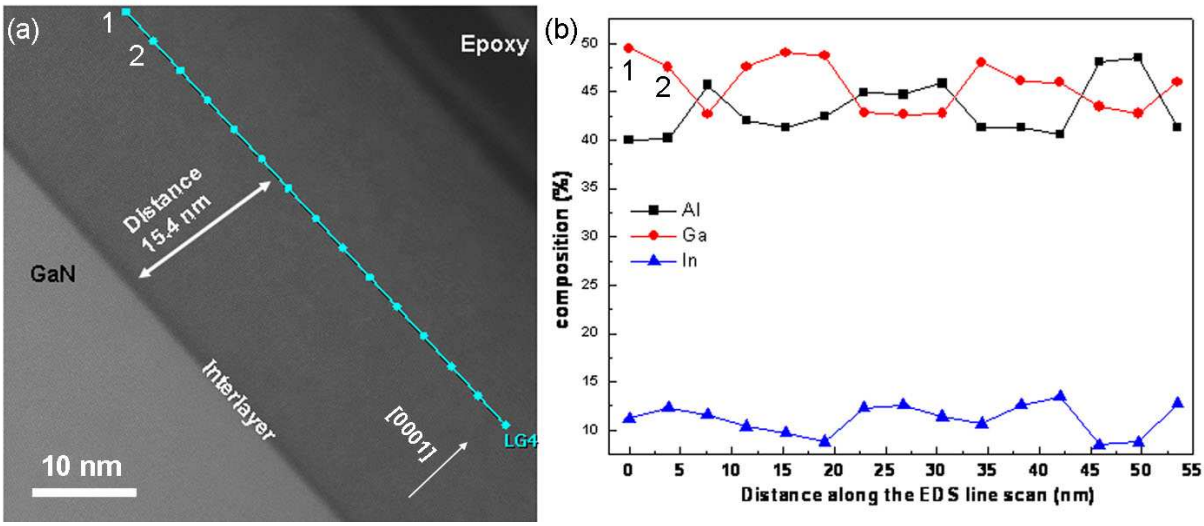

Fig 4.21 Aix3232 (a) HAADF image where the line (LG12) indicates the EDS line scans at 15.4 nm from the interface, and (b) the EDS line scan profile shows composition of Ga, Al and In as a function of position. The numbers (1, 2) are to identify the EDS analysis with the position on the graph.

As can be seen in Table 4.5, the indium content fluctuates between 8 % and 13 %. The indium content determined by HRXRD and RBS was 13.25 and 12.4 %, respectively (Table 4.5), it may be concluded that, at this local scale, we have composition fluctuations around a ~ 10 % In mean content. For the thinnest barriers, as can be seen in Table 4.6, the In content is around 4 times lower than extracted from XRD and RBS. Interestingly, for sample Aix3232, the In local composition measured by EDS matched the RBS and HRXRD when measured far from the interface. Therefore, it was of interest to see if there was any indium migration to the v-shaped defects as has been claimed by other authors.[21] As can be seen in Fig 4.22, threading dislocations cross the interface and terminate as v-shapes at the top of the InAlN barrier. A close examination of the v-defects shows that there is no change in contrast around their walls (bright contrast), this is an indication that there is no gross accumulation of indium in these pyramidal shaped defects. However, this may not be considered as a definite conclusion as we did not carry out plan view TEM analysis as reported in reference 21.

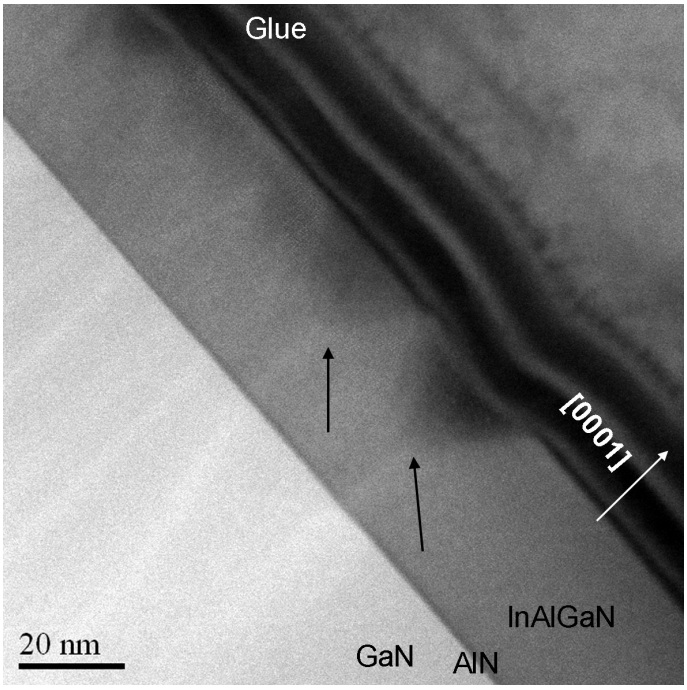

Fig 4.22 HAADF-STEM image revealing the v-shapes connected at the end with threading dislocation (black arrows) in Aix3232.

In the second set of samples (Aii) the deposition was carried out at 850 °C for both the AlN interlayer and the InAlN barriers. The corresponding HAADF and EDS results are collected in Table 4.6.

Table 4.6 EDS results for EPFL and Thales samples. The distance from the interface for EDS analysis and Al, Ga and In content are shown.

Sample and thickness (nm)	**Distance from interface (nm)**	**Al (%)**	**Ga (%)**	**In (%)**	**$In_xAl_{1-x}N$ In (%) by HRXRD**
AEC1778 t_{InAlN} = 9.2	3.85	81.82-89.45	1.07-7.12	9.47-13.40	18.5
A852 t_{InAlN} = 13.5	3.2	70.75-82.35	0 (only one point has 1.42 %)	17.65-27.83	18
	7.0	75.49-85.02	0	14.98-24.51	
A816 t_{InAlN} = 14	4.0	79.05-83.52	0-1.06	15.88-20.09	18
A856 t_{InAlN} = 14.2	5.45	71.05-75.96	1.35-4.19	18.24-25.95	18
A1583 t_{InAlN} = 30	11.5	73.80-78.87	1.54-4.61	19.58-22.95	18
	17.5	73.60-78.84	0.82-2.81	18.35-25.58	
AEC1657 t_{InAlN} = 100	6.25	79.22-84.90	1.12-2.85	12.25-18.68	15.5
	83.0	72.32-93.15	1.07-5.74 (one point 10.27 %)	5.07-18.01	

Considering only the EDS for Ga content, it is obvious that in these samples, the Ga incorporation inside the InAlN layer is at most low. For the EPFL samples, the Ga incorporation was less than 1.3-4.19 % and 1.5-4.61 % for A856 and A1583, respectively. In the case of A816 and A852, only traces of Ga were detected in the InAlN caplayer. In this case the investigated HEMT structures had undergone a complete electrical characterization.[7] As can be seen in Fig 4.23, the samples (A816, A856, A854, and A852) have an increasing nominal AlN thickness from 0 to 2.08 nm. The 2DEG is maximum for sample A854, and then it is decreased for sample A852. In reference 7, this behaviour has been correlated with the sample surface roughness as well as the AlN interlayer thickness. The AlN interlayer of ~ 1 nm was shown to be ideal in terms of alloys scattering for the increased the 2DEG. The degradation of the transport properties was attributed to the accelerated generation of defects when the AlN thickness was increased above 1.5 nm, as correlated to a parallel increase of the surface roughness.

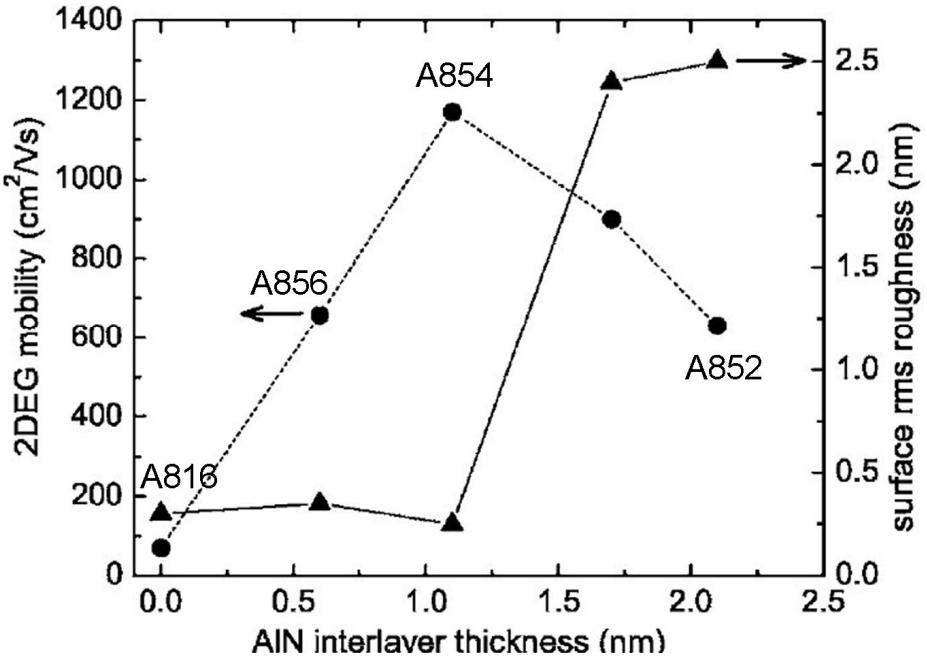

Fig 4.23 Mobility and root mean square roughness versus AlN thickness (samples A816, A856, A854 and A852).[7]

The HAADF investigation shows that for sample A816 (no nominal AlN interlayer) there is a small interlayer of about 1.4 nm (denoted by *) with an Al

content close to 90 %; the corresponding intensity ratio is 0.51 (Fig 4.24(a)-(b)). When the nominal AlN interlayer thickness was 0.6 nm (A856), we could only notice a non continuous bright fringe located at 1.2 nm from the GaN surface.

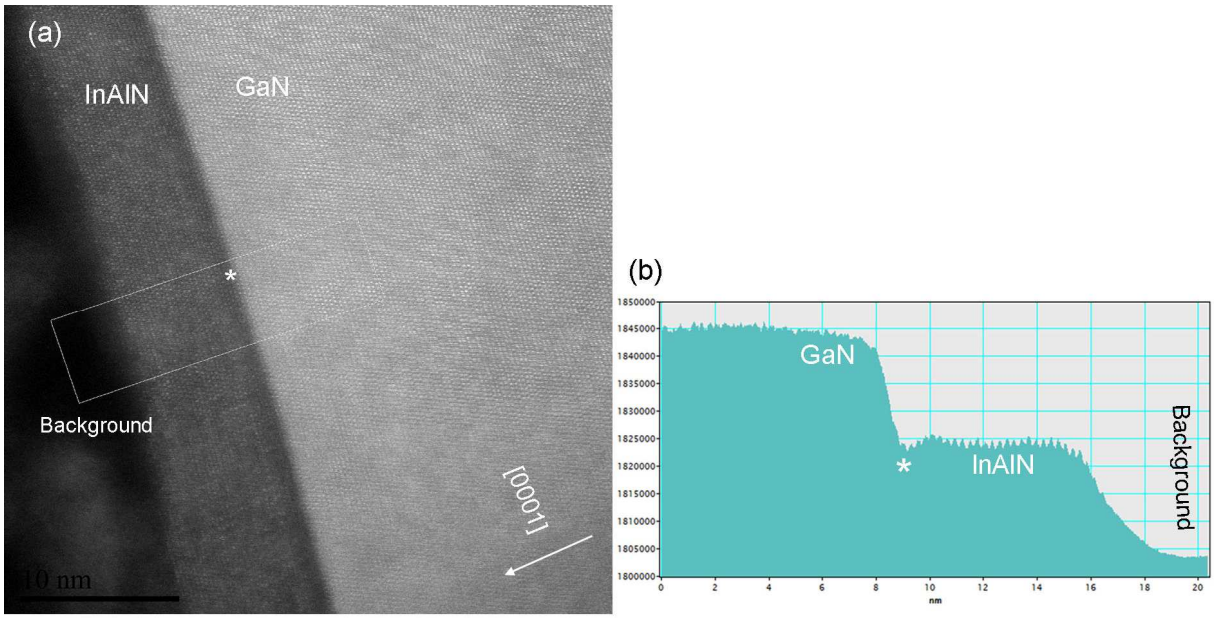

Fig 4.24 Sample A816 (a) HAADF image, the asterisk marks the dark interlayer (b) Intensity profile versus distance.

Taking the HAADF image profile, it is not easy to correlate such area with an increase in Al content. For the sample (A854) with a nominal AlN interlayer of 1.14 nm and best electrical properties, we end up with a ratio of 0.54, meaning that the Al content was close to 80 % within an interlayer of 1.2 nm, in agreement with the nominal thickness (1.14 nm).

In sample A852 with the nominal 2.08 nm AlN interlayer, Fig 4.25 reveals clearly two interlayers (arrow) between the GaN and InAlN, with 1.5 nm thickness for each one. As noticed in the sample Aix3235 grown at 790 °C, this first layer exhibits a graded intensity meaning that we have a varying Ga content inside. An estimation from the profile shows that, at the lowest point of this layer, we end up with an Al content of 70 % (Fig 4.25(b)). In the darker interlayer, the calculated intensity ratio is 0.39 also lower than the 0.47 expected for AlN. This discrepancy is not at the moment completely understood, and complementary work is needed in order to clarify.

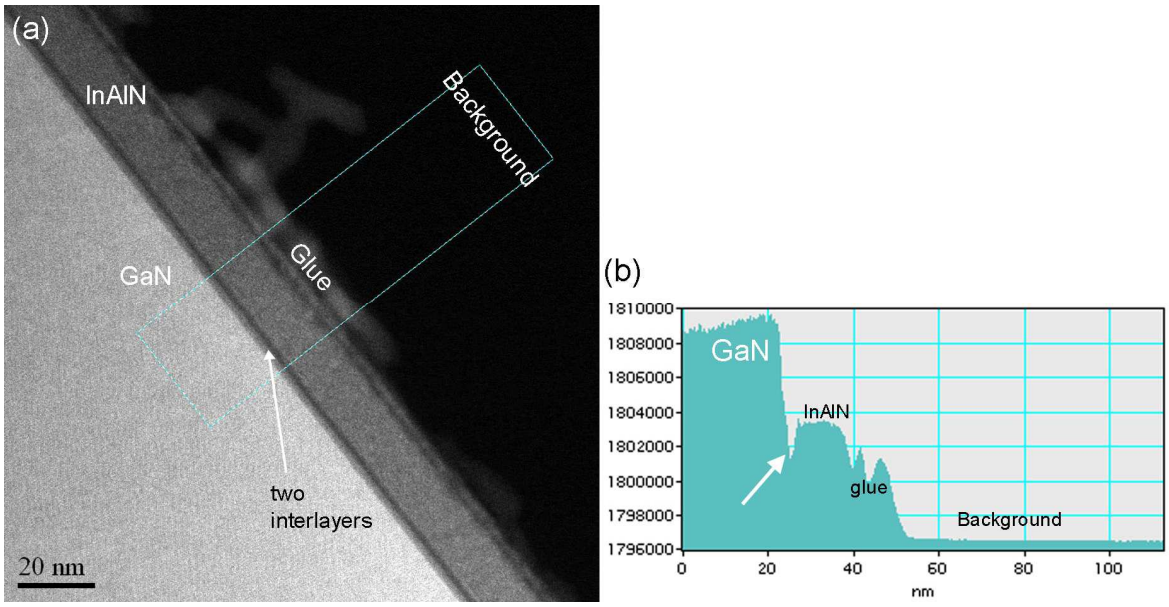

Fig 4.25 Sample A852 (a) HAADF image, the arrow shows the two interlayers (b) intensity profile versus distance.

In contrast to the Aix samples series, the EDS shows a rapid drop in the Ga content for all the samples, at 3.5 nm from the GaN surface, the detected Ga is ≤ 4% which may be considered as background.

In the samples where the interlayer was deposited at 1200 °C, the measured interlayer thickness was larger than the nominal one for instance in AEC1778 (Fig 4.26(a)), the exhibited thickness for the interlayer is ~ 4.5 nm. When EDS was carried out, as can be seen in Fig 4.26(b), the interlayer is rich in Ga, with a gradient from ~80 % at the interface with GaN, to ~20 % at the top of the interlayer. In Fig 4.26(c), the intensity ratio in the HAADF image gives (0.7) which corresponds to an Al composition of 40 % in agreement with the EDS which shows a change in Ga content from 70 % to around 20 % (Fig 4.26(b)). In AEC samples, at 5 nm from the interface, the detected highest Ga content was less than 3 %. It is then clear that, in this set of InAlN barriers, there was no Ga incorporation.

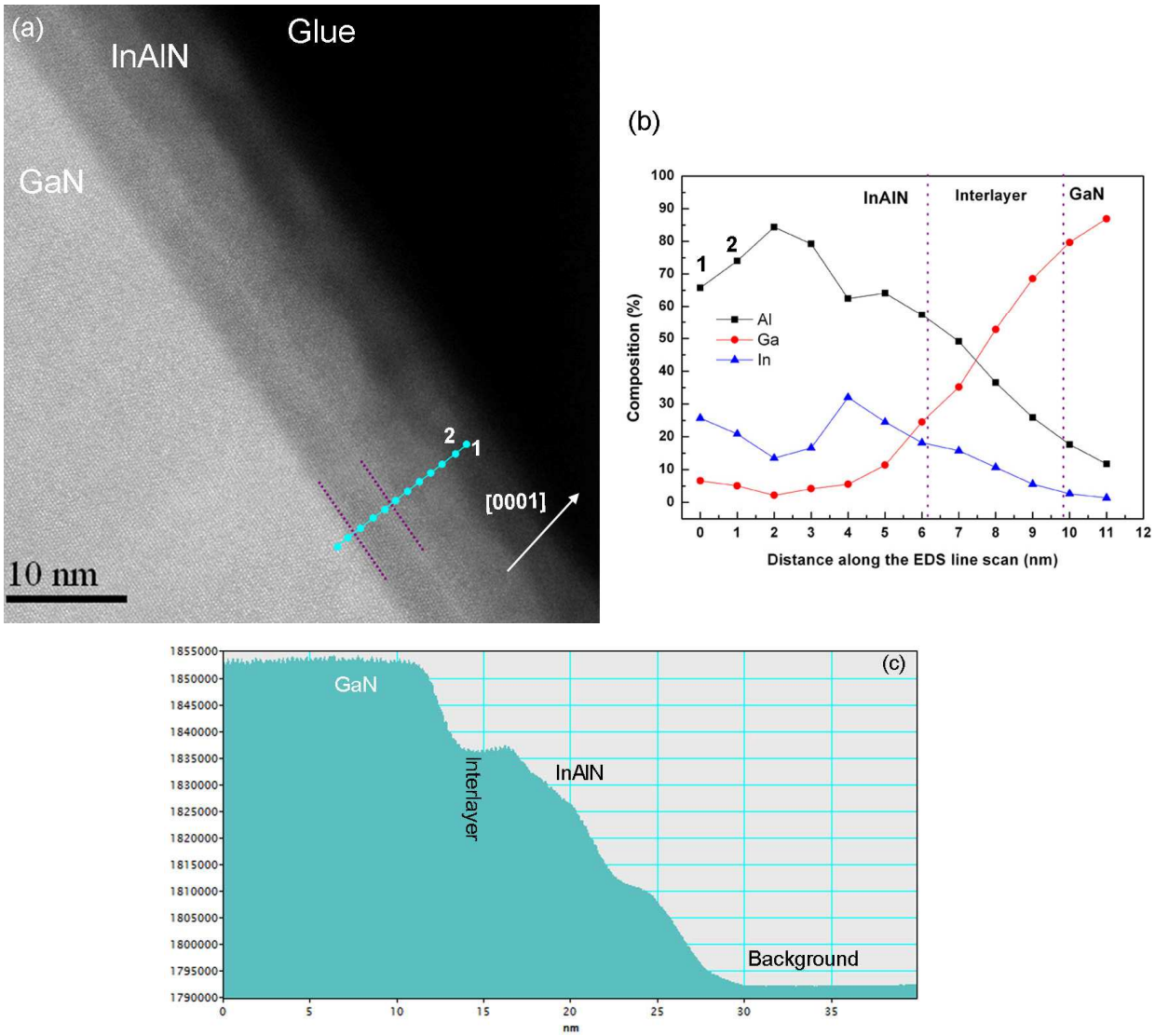

Fig 4.26 Sample AEC1778 (a) HAADF image with the cyan line indicating EDS analysis, the purple dashed line represents the interface (b) EDS data for Al, Ga and In content. The numbers (1, 2) are to identify the EDS analysis with the position on the graph (c) Intensity profile versus distance.

In summary, the above results show that when the deposition has been done at 790 °C, we have a strong incorporation of Ga in the barrier, and mostly low indium content, except for one sample, where indium content fluctuation was observed to take place between 8 and 13 %. For the HEMT structures grown at 850 °C, it is seen that the degradation of the transport properties mainly correlates with the generation of defects when the interlayer thickness is increased. At the lower deposition temperatures (790 °C, 850 °C), an attempt to grow thick AlN interlayers is shown to lead to the formation of a double layer.

4.3.3.2 *Structural degradation and chemical distribution*

For this section we have selected four InAlN/GaN heterostructures, with thickness from 15 to 260 nm. The goal was to determine the In distribution inside the InAlN layers as a function of film thickness and to analyse in detail the In content in order to see possible correlation with RBS (*section 4.3.2).*

Starting with the thin A816 and A1583 samples of nominal thickness of 14 and 30 nm InAlN (Fig 4.27(a)-(b)), we see a very thin interlayer (1.4 nm) on top of the GaN. As can be seen in Tables 4.2 and 4.3, the two heterostructures have been deposited using the same growth conditions. Comparing the two images, it can be noticed that the two interlayers have different contrast. In sample A816 (Fig 4.27 (a)), the interlayer is darker, this means that the layer contains more Al. For the upper InAlN layers, the overall contrast seems to be homogeneous. However, when an EDS scan is taken laterally as indicated by the arrow (L1), as in Fig 4.27(c), it can be noticed that the In content is laterally varying between 16 %-20 % in this area. The changes are more pronounced in the thicker A1583 InAlN layer. We performed two EDS line scans at 11.5 nm (L2) and 17.5 nm (L3) from the InAlN/GaN interface (indicated by arrows). Fig 4.27(d) displays the In composition of the two EDS profiles. The scan line at 11.5 nm from the interface shows In concentration between 20 % and 23 %. When a line scan at 7.5 nm from the GaN is performed, the fluctuations are more pronounced (18 % - 26 %).

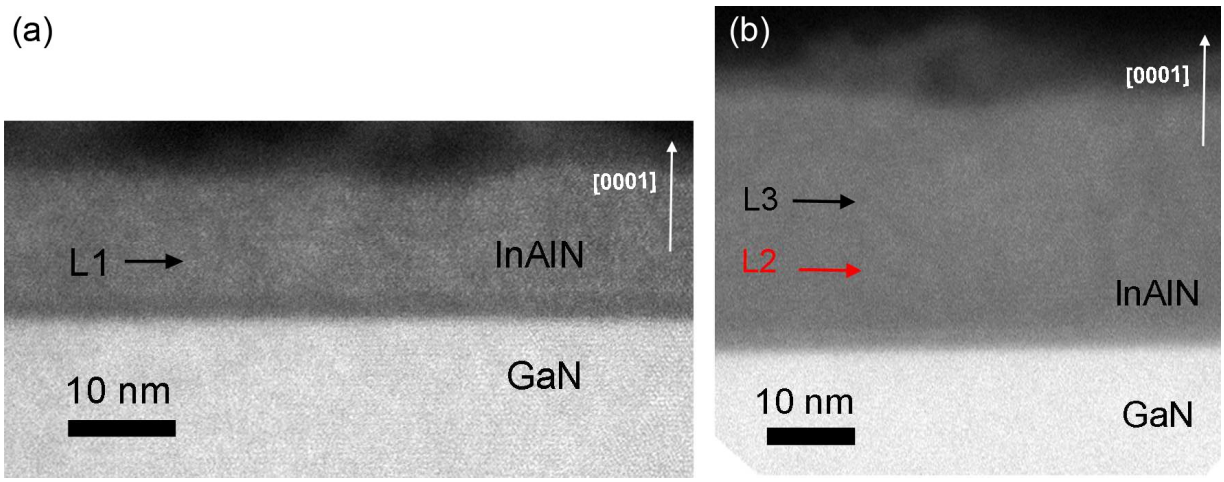

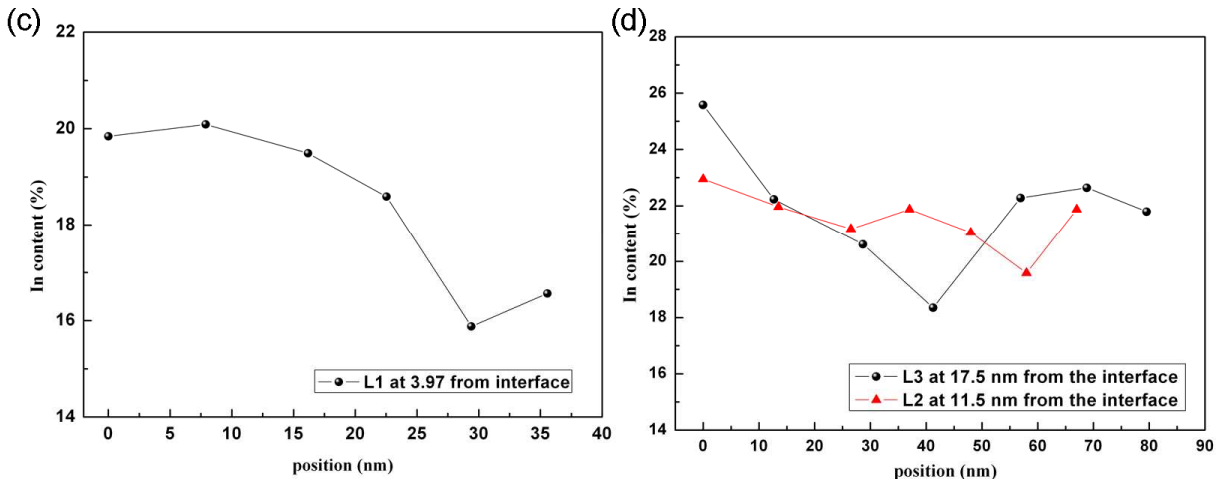

Fig 4.27 (a) Cross section HAADF image of A816 sample, a dark interlayer (1.4 nm) is visible between the GaN and InAlN, the arrow (L1) indicates the position of EDS line scan (b) Sample A1583: the interlayer exhibits a lighter contrast, two EDS line position are shown (L2 and L3) (c) the In content variation as a function of position along L1 (d) the In composition variations along the two scan lines L2 and L3.

When the InAlN layers become thicker as was shown in *section* 4.2.2, columnar growth takes place. The question is if there is any relation between the observed structural disruption (*section* 4.2.2) and the local chemical composition. To this end, we have investigated in detail two samples with InAlN thickness of 100 nm (AEC1657) and 260 nm (AEC1323).

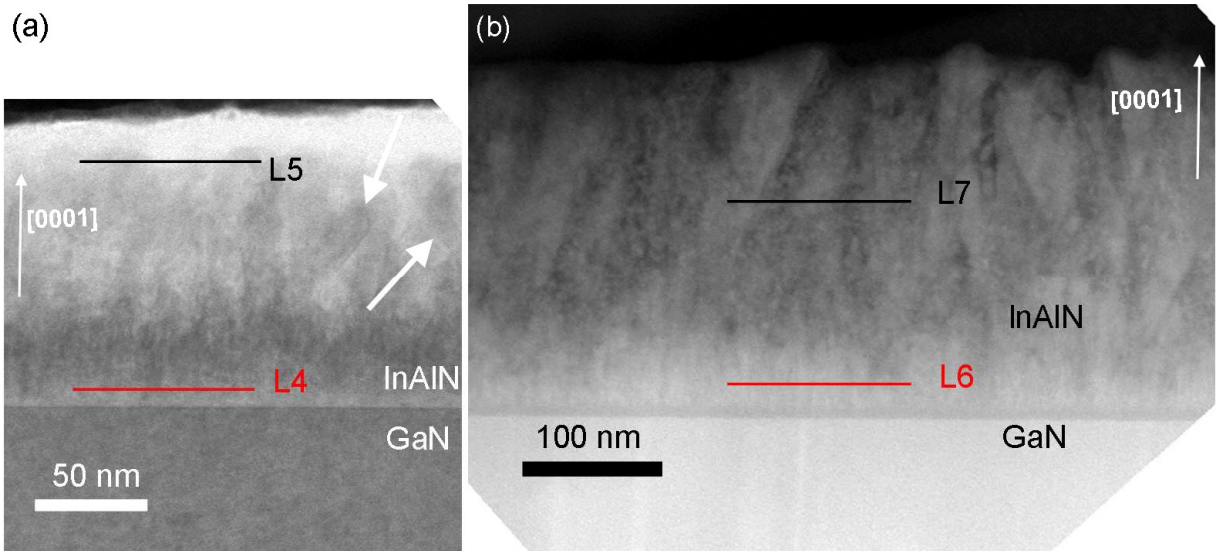

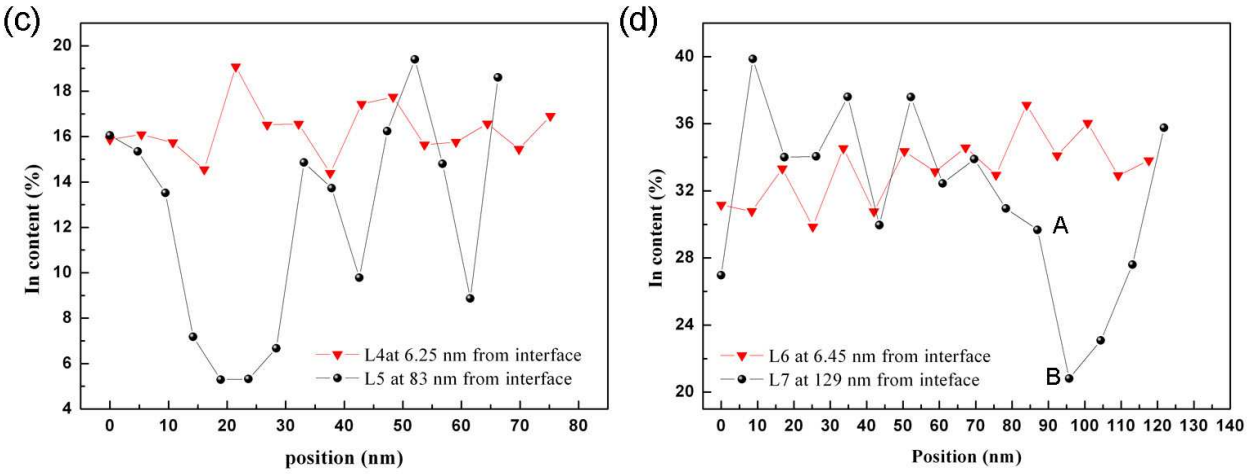

Fig 4.28 (a) Sample AEC1657: Cross section HAADF image, the white arrows show the highly inclined columns (b) In composition fluctuation for the sample AEC1657 (c) Sample AEC1323: HAADF image (L4 and L5 indicate the position for the EDS profile); and (d) Two EDS line profiles at 6.45 nm and 129 nm (L6 and L7) from InAlN/GaN interface (AEC1323).

The cross sectional STEM-HAADF images for both samples (Fig 4.28(a)-(b) exhibit clearly columnar structures as was expected (vertical and highly inclined columns, especially for AEC1323). However, the columns appear to have different shapes: for sample AEC1657, the columns have the same diameter along the whole layer thickness. Indeed, as can be seen in Fig 4.28(b) such uniform diameter does not hold in sample AEC1323. For both samples, the columns do not start directly from the interface with the GaN. Instead, as shown in Fig 4.29, there first form an irregular shaped layer, with a high roughness (as indicated by the yellow arrows) and uniform contrast. One wavy bright region is observed on the top of GaN. This initial layer has a different average thickness for the two samples and it is smaller (15 nm) in the thickest AEC1323 sample.

Two EDS scans are presented for each sample (Fig 4.28(c)-(d)), the first inside the uniform region close to the interface, and the second towards the surface, inside the polycrystalline area. For sample AEC1657, the line scans were located at 6.25 nm and 83 nm (Fig 4.28(a)), and in AEC1323, they were at 6.45 nm and 129 nm (Fig 4.28(b)), from the InAlN/GaN interface respectively. For both samples, the In composition close to the interface is between 15-19 % and 31-37 % in AEC1657 and AEC1323, respectively. Closer to the InAlN layer surface, the

fluctuations in the In content are larger: we observe In content variations from 5 % to 19 %, and 21 % to 40 % In compositions in AEC1657 and AEC1323, respectively. In the EDS plots (Fig 4.28(c)-(d)), there may be strong jumps in In composition between two adjacent positions (*e.g.* in AEC1323, from 30 % to 20 % at positions A and B).

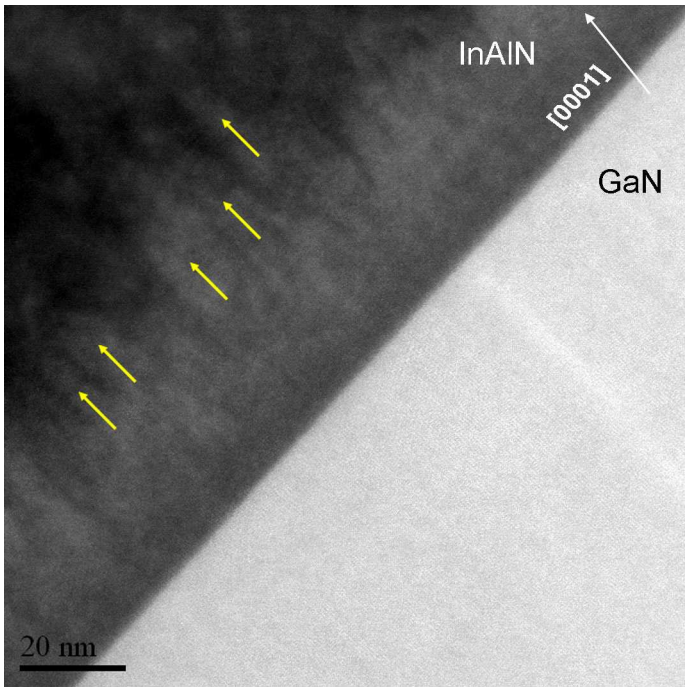

Fig 4.29 AEC1657 sample. The average thickness is 20nm.

Polycrystalline InAlN films have been previously grown by magnetron sputter deposition for In contents above 10 % on TiN and ZrN substrates.[38]At 600 °C on ZrN/MgO substrates columns were seen to develop after some 50–60 nm of the initial two-dimensional epitaxial growth. During MBE growth, columnar domains have also been reported.[18,19] Zhou *et al.*[18] suggested that the columnar structure could result from a horizontal phase separation initiated by random compositional non uniformities at the very early stages of growth. From the above results, we can point out that starting at the interface with GaN, the indium composition is not uniform, and this is in agreement with these other reports.

4.4 Discussion

From the above results on the HEMT heterostructures (Table 4.7) the three samples sets follows different trends. The common feature is that when the AlN interlayer thickness is increased past 1 nm, we observe the formation of v-shapes the density of which increases with the interlayer thickness in agreement with the literature.[7] It needs to be underlined that the real situation can be much more complex. We notice that the interface layer can be different from the nominal composition. In sample Aix3234, no interlayer has formed as expected whereas in A816 a 1.5 nm thin layer is clearly evidenced by HAADF. Moreover, two samples exhibit a double composition interlayer which is rich in Ga when close to the GaN interface.

Now, we notice a lower 2DEG density in AEC heterostructures in comparison to the EPFL set. No v-defects have been observed in the AEC sample set where the interlayer is made of AlGaN and not AlN. Recently, thin AlGaN interlayers have been used to produce InAlN layers with smooth surfaces and low v-shaped defects density.[38] Moreover in this work, they observe a 2DEG density decreased, in agreement with our observation.[39] The most intriguing part of our observations can be noticed from the Aixtron sample series. From the literature, the highest 2DEG density may be attained with ternary InAlN barriers. In these layers, we are measuring high Ga concentration up to around 50 %, and mainly low indium concentration except in Aix3232, where we have a more acceptable In composition (~ 13 %).

Concerning the composition of the samples, the combination of HRXRD and RBS techniques has allowed the determination of the In content in the InAlN barrier. Table 4.8 shows the In content in seven different heterostructures (using HRXRD and RBS) as well as their χ_{min} values: four thin samples with InAlN caplayer thickness below 33 nm, and three samples with the InAlN layer thickness larger than 100 nm.

Table 4.7 Summary: Growth temperature, thickness of the layers, N_S and roughness.

	T_{growth} (°C)		AlN (estimated thickness)	AlN (thickness measured by STEM)	Ns (cm^{-2})	Roughness (nm)	Observations
	InAlN	AlN					
Aix3234	790	790	0	0	3.24×10^{13}	0.32	No v-shapes
Aix3232	790	790	1	1.4	3.34×10^{13}	0.81	v-shapes
Aix3233	790	790	2.5	1.9	3.31×10^{13}	0.33	v-shapes
Aix3235	790	790	7.5	6.5 (*)	2.05×10^{13}	8.46	v-shapes
A816	850	850	0	---	2.49×10^{13}	0.39	Thinner dark interlayer
A856	850	850	0.6	1.4	2.72×10^{13}	0.41	v-shapes
A854	850	850	1.14	1.2	2.55×10^{13}	0.41	v-shapes
A852	850	850	2.08	3 (*)	2.98×10^{13}	0.6	v-shapes
AEC1681	865	1200	1	3.6	1.29×10^{13}	0.56	No v-shapes
AEC1778	865	1200	1	4.5	$1.20x\ 10^{13}$	0.42	No v-shapes
AEC1769	865	1200	1	4.6	1.16×10^{13}	0.72	No v-shapes
AEC1770	865	1200	1	3.1	1.27×10^{13}	0.58	No v-shapes
AEC1849	865	1200	4	3.9	1.50×10^{13}	0.9	No v-shapes

(*) Two interlayer are observed

Table 4.8 Comparison of In composition by HRXRD and RBS. The χ_{min} of the samples is also shown. For the thickest samples, we have also indicated in parentheses the In content for each layer and the weighted one for all the InAlN.

	Heterostructure	In content (HR-XRD) (%)	In content (RBS)(%)	X_{min} (%)
Aix3232	InAlN(33 nm)/AlN(1.4nm)/GaN	13.25	12.5	7
Aix3234	InAlN (14.9 nm)/GaN	13.4	13.65	7
AEC1770	InAlN(15.5nm)/AlN(3.1nm)/GaN	18.4	18.47	30
AEC1769	InAlN(8.6nm)/AlN(4.6nm)/GaN	17.7	17	31
AEC1657	InAlN(90nm)/GaN	15.5	(18.3/12.5) 14.5	(43/100)
AEC1655	InAlN(150nm)/GaN	20.5	(21/16.3) 17.3	(72/100)
AEC1323	InAlN(260nm)/GaN	(*)	(30.1/33.8) 31.9	(96/100)

(*) No possible determine

For the thinner heterostructures exhibiting $\chi_{min} \leq 31$ % good agreement between the In contents determined using both techniques is observed. We have larger discrepancies between HRXRD and RBS for the thicker samples with a two layers structure and different In contents; in this case, the χ_{min} values (range: 43 %-100 %) is large and there is poor single crystalline quality. However, we must keep in mind that HRXRD is only sensitive to the single crystalline part of the two-layer of the InAlN structure, i.e. to the lower InAlN (Table 4.8) whereas using random RBS, the refined In content is representative of the whole layer independently of its state (polycrystalline, single crystalline or amorphous). Taking into account these effects, small discrepancies between HRXRD In content (15.5 %) and the RBS (14.5 %) of samples AEC1657 (in which only a quarter of the surface is polycrystalline) is observed. This fact can be explained by lateral and vertical In inhomogeneity, as was observed by EDS (Fig 4.28(c)) and to the non homogeneous profile of <0001> aligned RBS spectra (Fig 4.15). For sample AEC1655 in which more than three quarters of the layer is polycrystalline, the HRXRD In content (20.5 %) is in a good agreement with the RBS In composition of the better quality interfacial layer (21 %). The upper region of the InAlN film has higher incorporation of indium and to a strong structural deterioration of the whole caplayer (Fig 4.15(d)). Comparing EDS composition profiles along the *c*-axis, there appear to be large fluctuations in In content sample AEC1778 whereas none are visible for sample Aix3232. This may explain the large χ_{min} difference (7-30 %) between these two layers.

Let's now focus on the samples with the best crystallinity in this instance Aix3232. As shown in Fig 4.30(a), we have carried EDS analysis along the growth direction through the whole InAlN layer, and the elemental composition is presented in Fig 4.30(b). Evidently, we have a homogeneous distribution with Al/Ga around 45% and In around 10% ($Al_{0.44}Ga_{0.43}In_{0.13}N$).

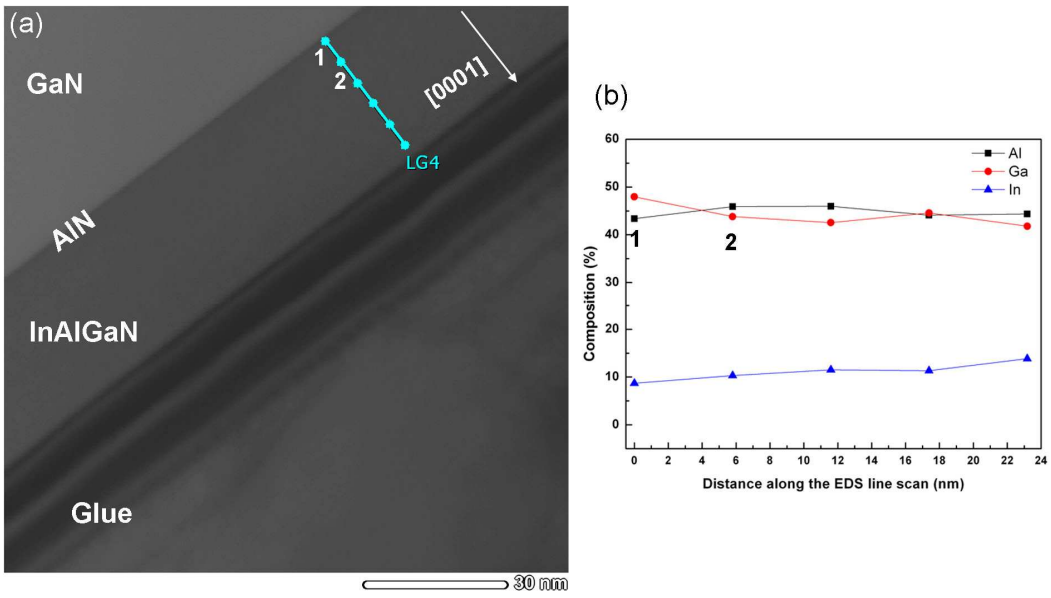

Fig 4.30 Sample Aix3232 (a) HAADF image (b) EDS profiles for Al, Ga, and In along the heterostructure. The numbers (1, 2) are to identify the EDS analysis with the position on the graph.

In the RBS experimental spectrum, focusing of the Ga signal (Fig 4.31), it can be noticed that there is a small change in the slope. As evidenced in the simulated spectra using InAlN/GaN structure model, this latter can be correlated with the presence of Ga in the InAlN. Such a change in slope at around 1250 KeV energy was not observed in similar but thinner layers (~ 16 nm), probably because of their smallest thickness.

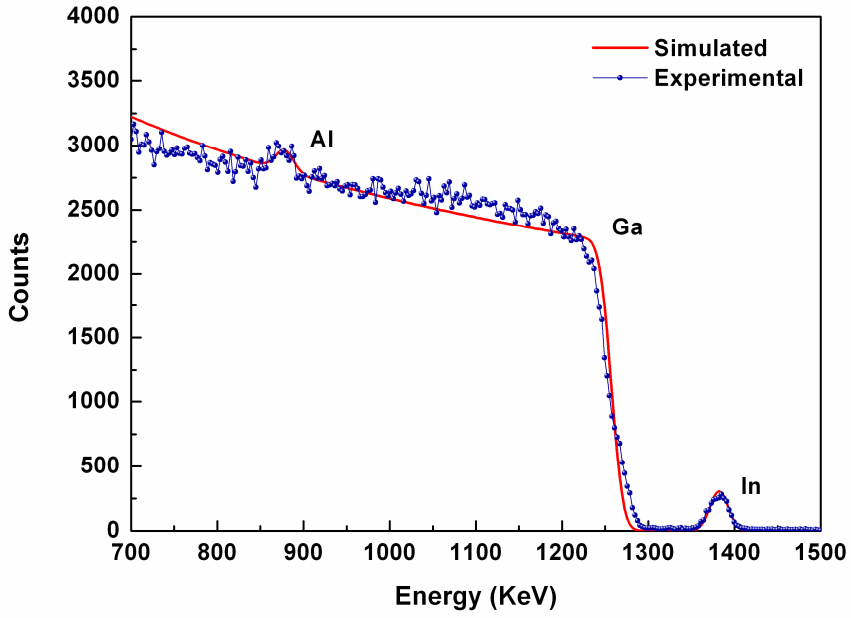

Fig 4.31 RBS experimental and simulated spectra using $In_{0.06}Al_{0.42}N_{0.52}$/GaN heterostructure for Aix3232.

In Fig 4.32 an RBS fit for Aix3232 sample with the introduction of a two layer structure (with a layer surface layer consisting of InAlGaN and the lower interface layer made of InAlN) are presented. As evidenced, a good agreement between experimental and simulated spectra is achieved with a relatively good reproduction of the Ga slope. The corresponding In refined contents are 9.2 % and 6.2 % for the quaternary and ternary, respectively and with a Ga content of 66.8 % in the top film quaternary layer. Moreover, tacking into account the EDS observations, various attempts to simulate the Aix3232 experimental spectrum have been also made with : (i) two InAlN layers with different Ga contents and (ii) only one layer with Ga inside the InAlN. As evidenced for example in Fig 4.33 this kind of layer model not succeeded to make a good fit of this spectrum.

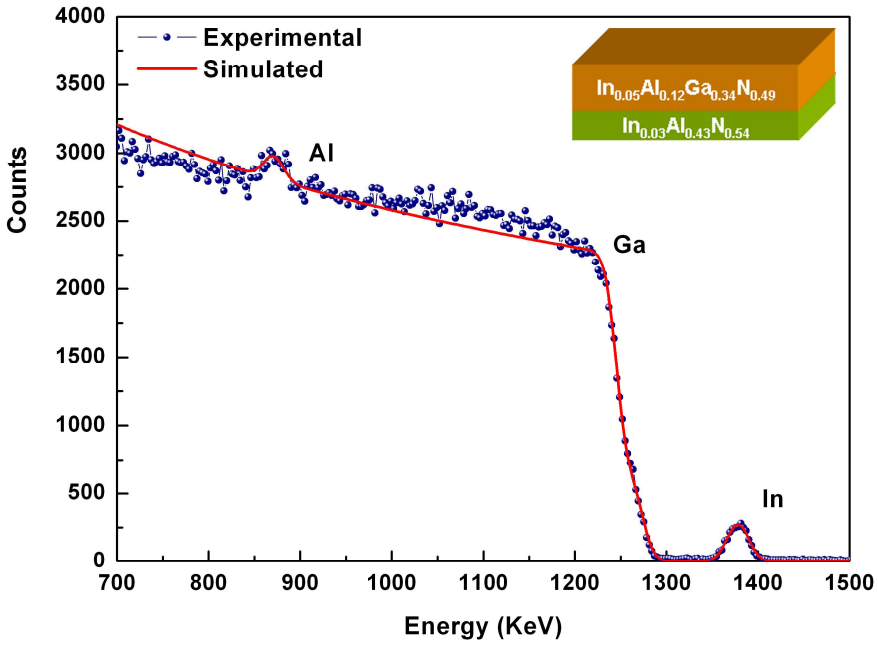

Fig 4.32 RBS spectra and simulated including two different layers, the first one InAlN and the second InAlGaN and schematic structure of the two different layers fitted in SIMNRA is also shown.

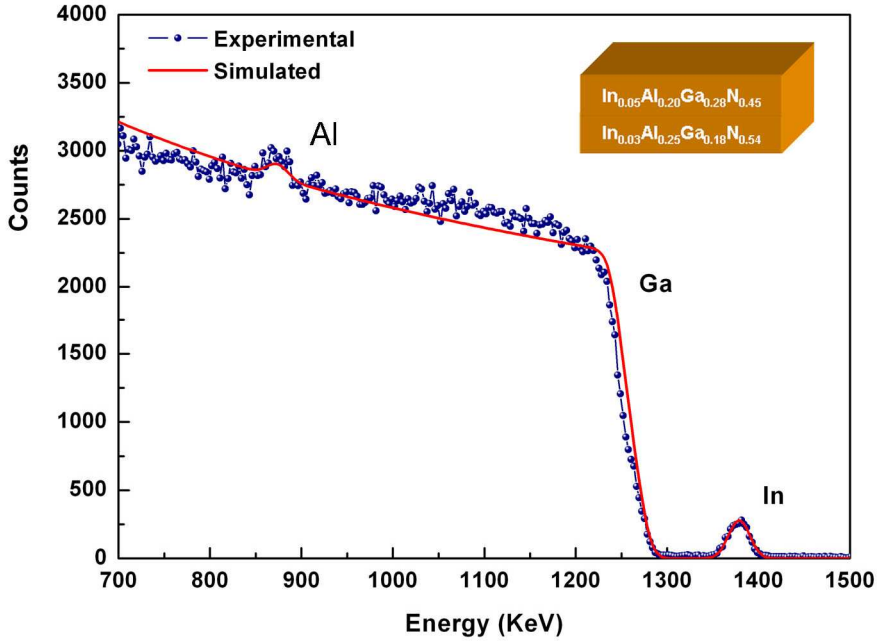

Fig 4.33 RBS spectra and simulated including Ga in the caplayer. Schematic structure of the two InAlGaN layers fitted in SIMNRA is also given.

So these simulations show that the two-layer structure with a quaternary alloy at the film surface and with ternary InAlN towards the GaN interface is a best fit to the observed RBS spectrum. This is in contrast to the EDS, where Ga was found in the whole InAlN layer thickness. A possible explanation may be that sample could be highly inhomogeneous in composition.

In contrast, samples grown at 860 °C with a V/III ratio around 790 show negligible Ga incorporation inside the InAlN layer (< 4 %). However, when the AlN was grown at 1200 °C, the resulting interlayer was AlGaN, and some Ga was also incorporated for a few monolayers inside the InAlN is observed. Closely examining the growth conditions of our samples, we notice that between the A series and AEC ones, the only change is the V/III ratio. According to the results reported by Sakai *et al.*[40], a reduction of V/III ratio leads to higher and more uniform In incorporation, in agreement with our observations. The EDS shows that the In composition is most uniform in the Aiii series. For the growth of thick InAlN (> 100 nm), we can notice that this reduction in V/III ratio may not be sufficient; indeed the InAlN layers progressively lose the crystalline quality as

they grow. However, for lower V/III conditions, the loss in crystalline quality happens more slowly (Fig 4.8 and Fig 4.9).

In summary, we have investigated InAlN/AlN heterostructures grown in three different conditions. As can be noticed, it is not straightforward to grow optimal quality layers. Using HRXRD, RBS/C and HRTEM techniques, we assess out the structure and composition at a range of length scales. It is clear that the results obtained from only one technique may not give a fair description of this complex system, of course, more extensive work is necessary if we want to build a growth diagram for InAlN by MOVPE.

References

[1] R. Tülek, A. Ilgaz, S. Gökden, A. Teke, M. K Öztük, M. Kasap, S. Özçelik, E. Arslan, and E. Özbay. *Comparison of the transport properties of high quality AlGaN/AlN/GaN and AlInN/AlN/GaN two-dimensional electron gas heterostructures.* J. Appl. Phys. **105**, 013707 (2009).

[2] J. Kuzmík. *Power electronics on InAlN/(In)GaN: Prospect for a record performance.* IEEE Electron Devices Lett. **22**, 510 (2001).

[3] I.P.Smorchkova, L. Chen, T. Mates, L. Shen, S. Heikman, B. Moran, S. Keller, S. P. DenBaars, J. S. Speck, and U. K. Mishra. *AlN/GaN and (Al,Ga)N/Al/GaN two-dimensional electron gas structures grown by plasma-assisted molecular-beam epitaxy.* J. Appl. Phys. **90**, 5196 (2001).

[4] M. Gonschorek, J.-F. Carlin, E. Feltin, M. A. Py, N. Grandjean, V. Darakchieva, B. Monemar, M. Lorenz, and G. Ramm. *Two-dimensional electron gas density in $Al_{1-x}In_xN$/AlN/GaN heterostructures ($0.03 \leq x \leq 0.23$)*. J. Appl. Phys. **103**, 093714 (2008).

[5] M. Miyoshi, H. Ishikawa, T. Egawa, K. Asai, M. Mouri, T. Shibata, M. Tanaka, and O. Oda. *High-electron-mobility AlGaN/AlN/GaN heterostructures grown on 100-mm-diam epitaxial AlN/sapphire templates by metalorganic vapour phase epitaxy.* Appl. Phys. Lett. **85**, 1710 (2004).

[6] J. Song, F. J. Xu, Z. L. Miao, Y. Wang, X. Q. Wang, and B. Shen. *Influence of ultrathin AlN interlayer on the microstructure and electrical transport properties of $Al_xGa_{1-x}N$/GaN heterostructures.* J. Appl. Phys. **106**, 083711 (2009).

[7] M. Gonschorek, J.-F. Carlin, E.Feltin, M. A. Py, and N. Grandjean. *High electron mobility lattice-matched AlInN/GaN field-effect transistor heterostructures.* Appl. Phys. Lett. **89**, 062106 (2006).

[8] S. Fernández-Garrido, Ž. Gačević, and E. Calleja. *A comprehensive diagram to grow InAlN alloys by plasma-assisted molecular beam epitaxy.* Appl. Phys. Lett. **93**, 191907 (2008).

[9] T. Palacios, S. Rajan, A. Chakraborty, S. Heikman, S. Keller, S. P. DenBaars, and U. K. Mishra. *Influence of the dynamic access resistance in the g_m and f_t linearity AlGaN/GaN HEMTs.* IEEE Trans. Electron Devices **52**, 2117 (2005).

[10] J. Xie, X. Ni, M. Wu, J. H. Leach, Ü. Özgür, and H. Morkoç. *High electron mobility in nearly lattice-matched AlInN/AlN/GaN heterostructures field effect transistors.* Appl. Phys. Lett. **91**, 132116 (2007).

[11] A. Teke, S. Gökden, R. Tülek, J. H. Leach, Q. Fan, J. Xie, Ü. Özgür, H. Morkoç, S. B. Lisesivdin, and E. Özbay. *The effect of AlN interlayer thicknesses on scattering processes in lattice-matched AlInN/GaN two-dimensional electron gas heterostructures.* New J. of Phys. **11**, 063031 (20009).

[12]A. Dadgar, F. Schulze, J. Bläsing, A. Diez, A. Krost, N. Neuburger, E; Kohn, I. Daumiller, and M. Kunze. *High-sheet-charge-carrier-density AlInN/GaN field-effect transistors on Si(111).* Appl. Phys. Lett. **85**, 5400 (2004).

[13] J. Xue, Y. Hao, J. Zhang, X. Zhou, X. Zhou, Z. Liu, J. Ma, and Z. Lin. *Nearly lattice-matched InAlN/GaN high electron mobility ransistors grown on SiC substrate by pulsed metal organic chemical vapor deposition.* Appl. Phys. Lett. **98**, 113504 (2011).

[14] K. Lorenz, N. Franco, E. Alves, S. Pereira, I. M. Watson, R. W. Martin, and K. P. O'Donnell. *Relaxation of compressively strained AlInN on GaN.* J. Cryst. Growth **310**, 4058 (2008).

[15] V. Darakchieva, M. Beckers, M.-Y. Xie, L. Hultman, B. Monemar, J.-F. Carlin, E. Feltin, M. Gonschorek, and N. Grandjean. *Effects of strain and composition on the lattice parameters and applicability of Vegard's rule in Al-rich $Al_{1-x}In_xN$ films grown on sapphire.* J. Appl. Phys. **103**, 103513 (2008).

[16] C. Hums, J. Bläsing, A. Dadgar, A. Diez, T. Hempel, J. Christen, A. Krost, K. Lorenz, and E. Alves. *Metal-organic vapor phase epitaxy and properties of AlInN in the whole compositional range.* Appl. Phys. Lett. **90**, 022105 (2007).

[17] A. Redondo-Cbero, K. Lorenz, R. Gago, N. Franco, M-A di Forte Poisson, E. Alves, and E. Muñoz. *Depth-resolved analysis of spontaneous phase separation in the growth of lattice-matched AlInN.* J. Phys. D: Appl. Phys. **43**, 1 (2010).

[18] L. Zhou, D. J. Smith, M. R. McCartney, D. S. Katzer, and D. F. Storm. *Observation of vertical honeycomb structure in InAlN/GaN heterostructures due to lateral phase separation.* Appl. Phys. Lett. **90**, 081917 (2007).

[19] S.-L. Sahonta, G. P. Dimitrakopulos, Th. Kehagias, J. Kioseoglou, A. Adikimenakis, E. Iliopoulos, A. Georgakilas, H. Kirmse, W. Neumann, and Ph. Komninou. *Mechanism of compositional modulations in epitaxial InAlN films grown by molecular beam epitaxy.* Appl. Phys. Lett. **95**, 021913 (2009).

[20] S. Kret, A. Wolska, M. T. Klepka, A. Letrouit. F. Ivaldi, A. Szczepańska, J-F Carlin, N.A.K. Kaufmann, and N. Grandjean. *TEM and XANES study of MOVPE grown InAlN layers with different indium content.* Journal of physics: Conference Series **326**, 012013 (2011).

[21] Th. Kehagias, G. P. Dimitrakopulos, J. Kioseoglou, H. Kirmse, C. Giesen, M. Heuken, A. Georgakilas, W. Neumann, Th. Karakostas, and Ph. Komninou. *Indium migration paths in V-defects of InAlN grown by metal-organic vapour phase epitaxy.* Appl. Phys. Lett. **95**, 071905 (2009).

[22] A. Mouti, J-L. Rouvière, M. Cantoni, J.-F. Carlin, E. Feltin, N. Grandjean, and P. Stadelmann. *Stress-modulated composition in the vicinity of dislocations in nearly lattice mtached $Al_xIn_{1-x}N$/GaN heterostructures: A possible explanation of density intensity.* Phys. Rev. B **83**, 195309 (2011).

[23] S. Pandey, B. Fraboni, D. Cavalcoli, A. Minj, A. Cavallini. *Two-dimensional electron gas properties by current voltage analyses of $Al_{0.86}In_{0.14}N$/AlN/GaN heterostructures.* Appl. Phys. Lett. **99**, 012111 (2011).

[24] N. Sarrazin. *HEMTs à base de nitrure de Gallium: évolution vers un nouveau système de matériaux, une nouvelle génération de composants*. Thèse Doctorat de l'Université des Sciences et Technique de Lille, N°4028 (2007).

[25] 4th Rainbow Workshop Bolognia (2011). Internal communication.

[26] P. B. Hirsch, A. Howie, R. B. Nicholson, D. W. Pashley, M. J. Whelan. *Electron Microscopy of Thin Crystals.* Ed. Butterworths (1965).

[27] A. Fisher, H. Kühne, and H. Richter. *New Approach in Equilibrium Theory for Strained Layer Relaxation.* Phys. Rev. Lett. **73**, 2712 (1994).

[28] A. M. Sánchez Fuentes. C*ontribución al estudio de la Estructura de Defectos en GaN Heteroepitaxial mediante Técnicas de Haces de Electrones*. PhD Universidad de Cádiz (2001).

[29] L. E. McNeil, M. Grimsditch, and R. H. French. *Vibrational Spectroscopy of Aluminum Nitride*. J. Am. Ceram. Soc. **76**, 1132 (1993).

[30] T.C. Sadler, M. J. Kappers, and R. A. Oliver. *Investigation of optimum growth conditions of InAlN for application in distributed Bragg reflectors.* J. Phys: Conf. Series **209**, 012015 (2010).

[31] Z. L. Miao, T. J. Yu, F. J. Xu, J. Song, L. Lu, C. C. Huang, Z. J. Yang, X. Q. Wang, G. Y. Zhang, X. P. Zhang, D. P. Yu, and B. Shen. *Strain effects on In_xAl_{1-x} crystalline quality grown on GaN templates by metalorganic chemical vapor deposition.* J. Appl. Phys. **107**, 043515 (2010).

[32] L. Vegards. *Vegard's law.* Z. Phys. **5**, 17 (1921).

[33] V. Darakchieva, M. –Y. Xie, F. Tasnádi, I. A. Abrikosov, L. Hultman, B. Monemar, J. Kamimura, and K. Kishino. *Lattice parameters, deviations from Vegard's rule, and E_2 phonons in InAlN.* Appl. Phys. Lett. **93**, 261908 (2008).

[34] Z. Dridi, B. Bouhafs, and P. Ruterana. *First-principles investigation of lattice constants and bowing parameters in wurtzite $Al_xGa_{1-x}N$, $InGa_{1-x}N$ and$Inl_xAl_{1-x}N$ alloys.* Semicond. Sci. Technol. **18**, 850 (2003).

[35] K. Lorenz, N. Franco, E. Alves, I. M. Watson, R. W. Martin, and K. P. O'Donnell. *Anomalous Ion channeling in AlInN/GaN Bilayers: Determination of the strain state.* Phys. Rev. lett. **97**, 085501 (2006).

[36] A. Rosenauer, K. Gries, K. Müller, A. Pretorious, M. Schowalter, A. Avramescu, K. Engl, and Stephan Lutgen. *Measurements of specimen thickness and composition in $Al_xGa_{1-x}N$/GaN using high-angle annular dark field images.* Ultramicroscopy **109**, 1171 (2009).

[37] J. M. LeBeau, and S. Stemmer *Experimental quantification of annular dark-field images in scanning transmission electron microscopy*. Ultramicroscopy **108,** 653 (2008).

[38] T. Seppänen, P. O. A. Persson, L. Hultman, J. Birch, G. Z. Radnóczi. *Magnetron sputter epitaxy of wurtzite $Al_{1-x}In_xN$ ($0.1 < x < 0.9$) by dual reactive dc magnetron sputter deposition.* J. Appl. Phys. **97**, 083503 (2005).

[39] X. Dong, Z.H. Li, Z. Y. Li, J. J. Zhou, L. Li, Y. Li, L. Zhang, X-J. Xu, X. Xuan, C-L. Han. *Effects of AlN and AlGaN interlayer on properties of InAlN/GaN Heterostructures.* Chin. Phys. Lett. **27**, 3 (2010).

[40] Y. Sakai, P. C. Khai, and T. Egawa. *Effect of metal-precursor gas ratio on AlInN/GaN structures for high efficiency ultraviolet photdiodes.* J. Appl. Phys. **110**, 103523 (2011)

Conclusions and Perspectives

The scientific and technological objectives of the RAINBOW project were to address fundamental materials issues in order to accelerate the possibility of production of InN-based devices using the three main growth technologies of nitride semiconductors: Plasma Assisted Molecular Beam Epitaxy (PAMBE), Hydride Vapour Phase Epitaxy (HVPE), and Metalorganic Vapour Phase Epitaxy (MOVPE). Our structural analysis was mainly to support two of the RAINBOW objectives:

a) *Growth of high-quality InN materials and its alloys by PAMBE, MOVPE and HVPE.*

b) *Growth and properties of InN-based quantum wells and heterostructures.*

With the defect density reduction achieved under these objectives, significant progress is expected towards the realization of InN-based heterostructures for optoelectronic and electronic applications, such as high efficiency LEDs or HEMTs.

In our work, five complementary techniques (AFM, IBA, Raman, TEM, XRD) have been used for the characterization of InN layers (UPM, TUB, EPFL) and InAlN/GaN and InAlN/AlN/GaN heterostructures (III-VLabs, Aixtron, EPFL) with the aim of helping towards the optimization of the processes. In the following, the major contributions are summarized.

The InN layers

We have determined that the MBE-InN samples exhibit the best crystalline quality with reasonable residual carrier densities. Their surface topography, strain state and threading dislocation have been investigated versus the growth conditions (V/III ratio, growth rate, temperature, In-rich and N-rich conditions). All the samples have been found to have two residual strain components: a biaxial and a hydrostatic one, the latter may be correlated to point defects. Moreover, two typical trends have been found, in N-rich growth conditions, we always end up with a 3D growth morphology (rms roughness ~7nm) and the highest residual carrier densities (8 and 17 x 10^{18} cm^{-3}). On the silicon substrate, this complex island growth results in layers with observed smallest residual stress correlated with the lowest dislocation densities (1.8-3.2 x 10^{10} cm^{-2}). This particular structure could be detrimental for device fabrication.

For the samples deposited under In-rich conditions, a step flow growth has been reached (rms roughness <1 nm). In this instance, we have noticed a critical role of the growth temperature: for the lowest temperature (T = 400 ^{o}C), the measured TDs density is the highest (5.5 x 10^{10} cm^{-2}) as well as the residual carrier density for this set. For the rest of samples (with temperature in a range 420-480 ^{o}C), the TDs were comparable (3.6-4.4 x 10^{10} cm^{-2}) as well as the surface morphology (2D mode). We have noticed that the sample grown under V/III = 0.86 ratio and with a growth rate 8.8 nm/min exhibits the lowest dislocation density (3.6 x 10^{10} cm^{-2}) of the set and smallest carrier density (1.5 x 10^{18} cm^{-3}).

The InAlN layers

In parallel, we investigated two sets of MOVPE heterostructures grown by MOVPE: InAlN/AlN/GaN/sapphire and InAlN/GaN.

We have observed that when an AlN interlayer is grown, v-shaped defects are generated in the InAlN, their density increases with the AlN thickness. Moreover, inside the two samples with the largest thickness of the AlN interlayer (3 and 6.9 nm), we have noticed the formation of a double layer, where the part

closest to the interface is rich in Ga. In this instance, the deposition was carried out at 850 and 790 °C respectively. In the case where the growth of the interlayer was carried out at 1200 °C, we systematically end up with a Ga rich interlayer, of graded composition with thicknesses ranging from 3 to 4.6 nm and no v-shaped defects have been observed. When the AlN and InAlN was grown at the lowest temperature (790 ^{o}C), we have measured high Ga concentration around 50 % inside the InAlN barrier.

In the samples with an AlGaN interlayer the 2DEG density (1.16-1.50 x 10^{13} cm^{-2}) is slightly lower that when the interlayer is AlN (2.49-2.98 x 10^{13} cm^{-2}). In the samples grown at 790°C, the highest 2DEG densities were measured (2.05-3.34 x 10^{13} cm^{-2})

For the thinnest InAlN barriers (t_{InAlN} < 33 nm), the layers exhibit a good crystallinity with χ_{min}=7-30 % depending on the growth conditions. When thick barriers (t_{InAlN} > 90 nm) were deposited, we have observed that the InAlN film has two layers structure and different In content. The top layer of InAlN reveals a χ_{min} of 100 % indicating that it is polycrystalline and this degradation progresses towards the interface with GaN when the barrier thickness is further increased.

This structural degradation was then explained by the local composition analysis. Indeed, we have found local composition fluctuations at the nanometer scale starting already at the interface with the GaN. The amplitude of this fluctuation is small at the interface, it highly increase toward the surface of the barriers.

Future work

For the growth of InN layers, we have only investigated samples fabricated during the first setting up of these techniques, therefore, there is much room for materials improvement. One suggestion which is still to be tested by the growers is the use of N polar substrates which have proven some success for the growth of InN by MBE.

The growth in N-rich conditions should be avoided, as it results in highest residual carrier densities. The results obtained by MBE-InN layers are quite interesting in In-rich growth conditions. A correlation was noticed between the residual carrier density and the threading dislocations. Indeed, the lowest attained carrier density is still quite high, therefore, there is still much work needed for improvement. To this end he following tasks can be suggested:

♦ The investigated samples were grown within a large range of temperature (up to 50° C possible change during the layer growth). It is clear that a much tighter control of the growth temperature stability should be the first step to be taken.

♦ As was pointed out, the samples grown with a V/III = 0.8-0.88 ratio exhibit 2D growth. Observing our data, appears that further improvement should come from an investigation of the growth rate.

In the case of the InAlN heterostructures three different growth conditions were investigated, it is clear that in order to improve the quality of InAlN layer, more work is needed:

♦ At lowest deposition temperature, we have observed the incorporation of Ga of ~ 43 % inside the InAlN, and this sample has the best crystal quality, such conditions should be investigated further by devices fabrication and characterization in order to know accurately the performances.

♦ When the AlN interlayer was grown at 1200 ^{o}C and V/III = 2200, the Ga was incorporated in AlN and no v-shapes defects were observed in InAlN layer. This result may help to the growth of a new heterostructures with a reduced density of defects. For instance, it would be good to test the growth a double interlayer AlGaN/AlN.

♦ In all the cases the uniformity of the InAlN need further investigation.

Publications and contributions to conference

Publications

1. ***Defect evolution and interplay in n-type InN***. C. Rauch, F. Tuomisto, **A. Vilalta-Clemente**, B. Lacroix, P. Ruterana, S. Kraeusel, T. Veal, and W. J. Schaff. *Applied Physics Letters* **100**, 091907 (2012).

2. ***Imaging and identifying defects in nitride semiconductor thin films using a scanning electron microscope.*** G. Naresh-Kumar, B. Hourahine, **A. Vilalta-Clemente**, P. Ruterana, P. Gamarra, C. Lacam, M. Tordjman, M. A. Di Forte-Poisson, P. J. Parbrook, A. P. Day, G. England, and C. Trager-Cowan. *Physica Status Solidi A* **209**, No. 3, 424-426 (2012).

3. ***AlGaN/GaN HEMTs on large area silicon wafers: growth, physicsl characterisation and devices results***. P. Gamarra, **A. Vilalta-Clemente**, P. Ruterana, M. Charles, P. Gergaud, P. Renaud, C. Lacam, M. Magis, M. Tordjman, and M. A. di Forte-Poisson. Proceedings of European Workshop on Metalorganic Vapor Phase Epitaxy. Wroclaw. Poland (2011).

4. ***Evidence of charge carrier number fluctuations in InN thin films?***. G.R. Mutta, B. Guillet, L. Méchin, **A. Vilalta-Clemente**, J. Grandal, M. A. Sánchez-García, S. Martin, F. Calle, P. Ruterana, and J.-M. Routoure.

Proceedings of ICNF 2011-21st International Conference on Noise and Fluctuations (ICNF) *Toronto, Canada*. 12-16 June, 483 (2011).

5. ***The structure of InAlN/GaN heterostructures for high electron mobility transistors*.A. Vilalta-Clemente**, M.A. Poisson, H. Behmenburg, C. Giesen, M. Heuken, and P. Ruterana. *Physica Status Solidi A* **207**, 1105-1108 (2010).

6. ***Investigation of InN layers grown by molecular beam epitaxy on GaN templates***. **A. Vilalta-Clemente**, G. R. Mutta, M. P. Chauvat, M. Morales, J. L. Doualan, P. Ruterana, J. Grandal, M. A. Sánchez-García, F. Calle, E. Valcheva, and K. Krilov. *Physica Status Solidi A* **207**, 1079-1082 (2010).

7. ***Optical properties of InN grown on Si (111) substrates***. E. Sakalauskas, P. Schley, J. Räthel, T. A. Klar, R. Müller, J. Pezoldt, K. Tonisch, J. Grandal, M. A. Sánchez-García, F. Calle, **A. Vilalta-Clemente**, P. Ruterana, and R. Goldhahn. *Physica Status Solidi A* **207**, 1066-1069 (2010).

8. ***Transmission electron microscopy and XRD investigations of InAlN/GaN thin heterostructures for HEMT applications.*Vilalta-Clemente A.**, Morales M., Chauvat M. P., Arroyo-Rojas Dasilva, Poisson M. A., Heuken M., Giesen C. and Ruterana P. Proceedings of SPIE -- Gallium Nitride Materials and Devices V- *Conference 7602: Photonic west OPTO: Gallium Nitride Materials and Devices V, United States* (2010).

Contributions to conferences

1. An oral presentation on *Structural, luminescence and electrical characterisation of InAlN/AlN/GaN heterostructures*. N. Kumar, C. Trager-Cowan, **A. Vilalta-Clemente**, M. Morales, P. Ruterana, H. Behmenburg, M. Heuken, F. Ivaldi, A. Letrouit, S. Kret, S. Pandey, A. Minj, A. Cavallini., in MRS fall meeting, November 2011, Boston, USA.
2. An poster presentation on *Structural analysis of InAlN heterostructures using electron channelling constrast imaging in a scanning electron microscope.* N. Kumar, P. Gamarra, **A. Vilalta-Clemente,** P. Ruterana, M. A. di Forte-Poisson, C. Trager-Cowan, in ICNS 9 (International conference on nitride semiconductor), 10-15 july, 2011, Glasgow, Scotland.
3. An oral presentation on *Structural and microstructural characterization of InAlN layers for HEMTs applications*. M. Morales, **A. Vilalta-Clemente**, P. Ruterana, M. A di Forte-Poisson, P. Gamarra, M. Heuken, and C. Giesen, in European Workshop on Metalorganic Vapor Phase epitaxy, 5-8 June, 2011, Wroclaw, Poland.
4. An poster presentation on *AlGaN/GaN HEMTs on large area silicon wafers: growth, physical characterisation and device results*. P. Gamarra, **A. Vilalta-Clemente**, P. Ruterana, M. Charles, P. Gergaud, P. Renaud, C. Lacam, M. Magis, M. Tordjman, and M. A. di Forte-Poisson, in European Workshop on Matalorganic Vapor Phase epitaxy, 5-8 June, 2011, Wroclaw, Poland.
5. An oral presentation on *Structural characterization of InAlN/AlN/GaN and InAlN/GaN heterostructures for HEMTs*. **A.Vilalta-Clemente**, M. Morales, P. Gamarra, M. A. di Forte-Poisson, I. Vickridge, and P. Ruterana, in EMRS spring meeting, 9-12 May 2011, Nice, France.
6. An oral presentation on *X-ray diffraction and Transmission Electron Microscopy analysis of threading dislocations and strain in MBE-grown InN layers*. M. Morales, **A. Vilalta-Clemente**, P. Ruterana, J. Grandal, S. Albert,

M. A. Sánchez-García, and F. Calle, in EMRS spring meeting, 9-12 May 2011, Nice, France.

7. An oral presentation on *Structural analysis of InAlN heterostructures using electron channelling contrast imaging in a scanning electron microscope.* N. Kumar, P. Gamarra, M. A. di Forte-Poisson, **A. Vilalta-Clemente**, P. Ruterana, and C. Trager-Cowan in EMRS spring meeting, 9-12 May 2011, Nice, France.

8. An oral presentation on *InN-based material devices for infrared photodetection.* T. Brazzini, J. grandal, A. Del Prado, **A. Vilalta-Clemente**, F. Calle. 19th European Workshop on Heerostructure Technology, 18-20 October 2010, Fodele, Crete, Greece.

9. An oral presentation on *MBE growth and characterization of InN/InGaN thin films and nonostructures on GaN templates and Si(111) substrates.* A. Steven, J. Grandal, M. A. Sánchez-García, P. Lefebvre, J. Ristic, E. Calleja, **A. Vilalta-Clemente**, B. Lacroix, P. Ruterana, E. Luna, U. Jahn, A. Trampert. 16th International Conference on Molecular Beam Epitaxy (MBE 2010), Augost 2010, Berlin, Germany.

10. An oral presentation on *Structural analysis of InAlN/AlN/GaN heterostructures and m-plane GaN using electron channelling contrast imaging, atomic force microscopy and transmission electron microscopy.* N. Kumar, P. R. Edwards, B. Hourahine, **A. Vilalta-Clemente**, P. Ruterana, Y. A-R Dasilva, C. Giesen, M. Heuken, H. Behmenburg, C. Mauder, H. Kalisch, R. H. Jansen, A. P. Day, A. Winkelmann, C. England, and C. Trager-Cowan in BIAMS (Beam induced assessment of microstructure), July 2010, Halle, Germany.

11. An poster presentation on *From material to illumination* in Marie Curie Satellite Event, 1-2 July 2010, Torino, Italy.

12. An oral presentation on *Structural properties of InAlN thin layers for HEMT applications*, **A. Vilalta-Clemente**, M. Morales, M. A. di Forte-Poisson, M. Heuken, C. Giesen, and P. Ruterana in EMRS spring meeting, 7-11 June 2010, Strasbourg, France.

13. An oral presentation on *Structural study of InN layers with compressive strain*, M. Morales, **A. Vilalta-Clemente,** G. R. Mutta, M. P. Chauvat, J. L. Doualan, P. Ruterana, J. Grandal, M. A. Sánchez-García, and F. Calle in EMRS spring meeting, 7-11 June 2010, Strasbourg, France.
14. An oral presentation on *Transmission electron microscopy and XRD investigations of InAlN/GaN thin heterostructures for HEMT applications*, **A. Vilalta-Clemente**, M. Morales, M. P. Chauvat, Y. Arroyo-Rojas Dasilva, M. A. di Forte-Poisson Poisson, M. Heuken, C. Giesen, and P. Ruterana in SPIE Photonics West 2010, 25-28 January 2010, San Francisco, California, United Stated.
15. An oral presentation on *Investigation of InN layers grown by molecular beam epitaxy on GaN templates*, **A. Vilalta-Clemente**, G. R. Mutta, M. P. Chauvat, M. Morales, J. L. Doualan, P. Ruterana, J. Grandal, M. A. Sánchez-García, F. Calle, E. Valcheva, and K. Krilov in EMRS fall meeting, 14-16 September 2009, Warsaw, Poland.
16. An poster presentation on *The structure of InAlN/GaN heterostructures for High Electron Mobility Transistors*, **A. Vilalta-Clemente**, M.A. di Forte-Poisson, H. Behmenburg, C. Giesen, M. Heuken and P. Ruterana in EMRS fall meeting , 14-16 September 2009,Warsaw, Poland. Recognition of the best poster presentation in symposium A (InN material and alloys).

Structure des couches d'InN et d'alliages (In,Al)N

Résumé:

En raison de leurs applications prometteuses dans les domaines de l'optoélectronique et de l'électronique, les semiconducteurs III-V à base d'azote: les nitrures (AlN, GaN, InN) et leurs alliages (InAlN, InGaN, AlGaN), font l'objet, depuis les années 1990, d'une activité intense en recherche et développement.

Dans ce travail, nous avons étudié les propriétés structurales des couches d'InN et de l'alliage InAlN dans les hétérostructures InAlN/AlN/GaN et InAlN/GaN en combinant les techniques AFM, IBA, DRXHR, Raman et MET.

L'étude des couches d'InN a été menée par DRX afin de déterminer la contrainte résiduelle, et on a cherché à faire une corrélation avec la morphologie des surfaces par AFM. Les contraintes résiduelles obtenues par DRX ont été comparées aux résultats de spectroscopie Raman, et on a pu montrer que toutes les couches avaient une contrainte résiduelle qui n'est pas purement bi-axiale.

Les hétérostructures InAlN pour transistors à haute mobilité électronique (HEMTs) sont des couches ultraminces de quelques monocouches atomiques à plusieurs dizaines de nanomètres d'épaisseur. De plus, leur structure peut être assez complexe dans le but d'optimiser le gaz d'électrons généré dans le canal du transistor. Dans l'idéal, on utilise une concentration en indium autour de 17%, qui est celle de l'accord de paramètres cristallins avec le GaN. Nos travaux ont mis en évidence qu'il n'est pas facile de contrôler la composition locale; en effet la structure et morphologie des couches sont très sensibles aux conditions de croissance.

Mots clés: InN, InAlN, MBE, MOVPE, déformation, contraintes, dislocations, contenu d'indium, fluctuations de composition

The structure of InN layers and (In, Al) alloys

Abstract

Due to their promising optoelectronic and electronic applications, nitrogen based III-V compound semiconductors (AlN, GaN, InN) and their alloys (InAlN, InGaN, AlGaN) have received a large research interest since the early 90's.

In this work, we have investigated the structural behaviour of InN layers and InAlN alloys in InAlN/AlN/GaN and InAlN/GaN heterostructures using complementary techniques: AFM, IBA, HRXRD, Raman and TEM.

The study of InN layers has been carried out by HRXRD in order to determine the residual stress and the results were correlated with the morphology as investigated by AFM. The residual stress obtained by HRXRD has been compared with the Raman results, showing that all the layers were characterized by a non pure biaxial stress.

The InAlN heterostructures for high electron mobility transistors (HEMTs) are ultra thin layers ranging from a few atomic monolayers to dozens of nanometers. Moreover, their structure can be quite complex in order to optimize the electron gas (2DEG) generated in the transistor channel. We have investigated InAlN layers with In content around 17 % which corresponds to the lattice-match to GaN. In this work, we have shown that it is not easy to control the local composition together with the structure and morphology, meaning that the InAlN layers quality is very sensitive to the growth conditions.

Keywords: InN, InAlN, MBE, MOVPE, strain, stress, dislocations, In content, composition fluctuations